



Cardiff
Catalysis Institute

Sefydliad Catalysis
Caerdydd

Solvothermal stability studies of porous inorganic and metal-organic materials

Thesis submitted in accordance with the requirements of Cardiff
University for the degree of Doctor of Philosophy by

Justyna Minkiewicz

School of Chemistry
Cardiff University
2021

Supervisor
Dr Ceri Hammond

ACKNOWLEDGEMENTS

“Keep away from people who try to belittle your ambitions. Small people always do that, but the really great make you feel that you, too, can become great.”

— Mark Twain

Firstly, I would like to thank my supervisor Dr Ceri Hammond for valuable support and assistance during my PhD journey. I would like to thank Cardiff University School of Chemistry for giving me the opportunity and tools to accomplish my work.

A big thank you to the whole Hammond group and those who contributed to my work directly by training and guiding me throughout the 3 years of my PhD.

A special thank you to those, who were of great support in and outside the laboratory - Alba, Anna, Leti and Michał.

Dziękuję rodzicom – Danucie i Krzysztofowi, za miłość, wsparcie i wiarę w moje możliwości.

Dziękuję Grzesiek, że mogę zawsze na Ciebie liczyć. Dzięki Tobie jestem silna.

ABSTRACT

The increasing interest of green chemistry in the use of greener solvents, has led to a surge in the need of solid materials stable in liquid phase processes. In particular, the use of porous materials such as zeolites and their related Metal Organic Framework (MOF) counterparts as catalysts or membranes has drawn great attention. Yet even though zeolites are already widely used in petrochemical applications, their commercialisation in liquid phase operations has not yet been achieved. A major reason for this is that the stability of zeolites and MOFs in water has not yet been fully evaluated and understood.

In order to tackle the (in)stability challenge, various points call for attention. This mainly includes identification of porous materials that possess sufficient stability in solvent media. As such, the aim of this thesis is to present a detailed investigation of the stability of various porous materials in water and organic solvents. Detailed understanding of material degradation upon direct contact with solvents at elevated temperatures is provided, by focusing on different analytical techniques and spectroscopic studies. This work begins in Chapter 3, by exploring how different zeolite structures of various framework densities, pore volumes and aluminium contents are modified upon water treatment in continuous flow reactors (CFR) at elevated temperature and pressure. Chapter 4 focuses on the investigation of the MFI framework and the role of aluminium content in hydrothermal stability in CFR. Subsequently, in Chapter 5, the stability of MOF structures as analogues to zeolites is investigated in CFR. Preliminary investigations led to the selection of UiO-66(Zr)-H structure as the most robust in water. Subsequently, the choice of metal, linker and operational conditions are determined regarding MOF (in)stability. In closing, Chapter 6 evaluates the findings of this study and describes the potential further questions that raise.

GLOSSARY

Å	Angstrom (10^{-10} meters)
a.u.	Arbitrary units
β or Beta	Zeolite Beta (Zeolite β)
BET	Brauner, Emmet and Teller
CHA	Chabazite, <i>i.e.</i> , SSZ-13, SAPO-34
CFR	Continuous flow reactors
cm	Centimetre
cm ⁻¹	Reciprocal Centimetre
°C	Degrees Celsius
DDR	Deca-dodecasil 3R zeolite
eV	Electron Volts
FAU	Faujasite, <i>i.e.</i> , zeolite Y
FER	Zeolite – Ferrierite
FTIR	Fourier transform infrared spectroscopy
g	Gram
h	Hours
H ₂ O/water	Deionized Water
ICP-MS	Inductively Coupled Plasma Mass Spectroscopy
IE	Ion Exchange
IUPAC	International Union of Pure and Applied Chemistry
LTA	Zeolite A, <i>i.e.</i> , NaA, KA, CaA
M	Molar
m	Moles
mg	Milligrams

mL	Millilitres
mL min ⁻¹	Flow rate, millilitres per minute
MOF	Metal Organic Framework
MP-AES	Microwave Plasma Atomic Emission Spectroscopy
N ₂	Nitrogen, gas
NLDFT	Non-linear discrete Fourier transform
NMR	Nuclear Magnetic Resonance
R. C. (%)	Relative crystallinity in %
R. M. (%)	Relative microporosity in %
rpm	Revolutions per minute
SEM	Scanning Electron Microscope
SiO ₂ /Al ₂ O ₃	Molar ratio given in parenthesis, X moles of SiO ₂ to 1 mole of Al ₂ O ₃ in a zeolite
SS	Stainless Steel
T	Temperature
TGA	Thermogravimetric Analysis
TPD	Temperature-Programmed Desorption
UiO-66	Universitetet i Oslo, MOF
UV-VIS	Ultraviolet–Visible Spectroscopy
% v/v	Percent Volume/Volume
wt. %	Weight percent
XRD	X-ray powder diffraction
Y	Zeolite Y
ZSM-5	Zeolite ZSM-5

TABLE OF CONTENTS

1	Introduction	1
1.1	Zeolites – structure, properties and applications.....	1
1.1.1	Structure	1
1.1.2	Framework density (FD _{Si}).....	4
1.1.3	Physicochemical properties of zeolites	7
1.1.4	Zeolite industrial applications and future prospects.....	9
1.1.4.1	Catalytic hydrocracking.....	10
1.1.4.2	Biomass conversion	10
1.1.4.3	Solvent dehydration systems	11
1.1.4.4	Desalination	13
1.1.4.5	Gas separation systems	15
1.1.5	Zeolite deactivation mechanisms and solubility in liquid media.....	17
1.1.5.1	Reversible deactivation mechanisms	17
1.1.5.2	Irreversible deactivation mechanisms.....	18
1.1.5.3	Solubility in water.....	19
1.1.5.4	Vapour and organic solvent uptake	22
1.2	Metal Organic Frameworks – structure, properties and applications	24
1.2.1	General structure	24
1.2.1.1	ZIF-8	26
1.2.1.2	MIL-53.....	27
1.2.1.3	HKUST-1 (Cu-BTC)	28
1.2.1.4	UiO-66	29
1.2.2	Potential prospect commercial applications.....	31
1.2.2.1	Water harvesting	31
1.2.2.2	Catalysis.....	32

1.3	Aims and objective.....	33
1.4	References	35
2	Experimental and characterisation techniques.....	41
2.1	List of reagents.....	41
2.2	Synthesis procedures	43
2.2.1	Zeolite synthesis.....	43
2.2.1.1	One-pot synthesis of Silicalite-1.....	43
2.2.1.2	One-pot synthesis of HZSM-5.....	43
2.2.2	MOF synthesis	44
2.2.2.1	UiO-66(Zr)-X (X = H, NH ₂).....	44
2.2.2.2	UiO-66(Hf)-H	44
2.2.2.3	ZIF-8	45
2.3	Zeolite post-synthesis procedures	45
2.3.1	Organic template removal.....	45
2.3.2	Protonation of as-synthesised materials.....	45
2.3.3	Protonation of commercial zeolites.....	46
2.3.4	Alkali ion-exchange of commercial materials	46
2.4	Relative values determination.....	47
2.4.1	Relative crystallinity determination.....	47
2.4.2	Relative microporosity determination.....	47
2.5	Zeolite and MOFs solvothermal testing.....	48
2.5.1	Stability tests in continuous flow	48
2.5.2	Stability tests in round bottom flask	49
2.6	Materials characterisation techniques	50
2.6.1	Powder X-Ray diffraction (pXRD).....	50
2.6.2	Nitrogen physisorption.....	51
2.6.3	Water vapour isotherms	53

2.6.4	Thermogravimetric analysis (TGA).....	53
2.6.5	Temperature-Programmed Desorption (TPD)	54
2.6.6	UV-VIS absorption spectroscopy	56
2.6.7	Transform Infrared Spectroscopy (FTIR)	56
2.6.8	Scanning Electron Microscopy (SEM)	59
2.6.9	Energy Dispersive X-ray Spectroscopy (EDX)	61
2.6.10	Nuclear Magnetic Resonance (NMR) spectroscopy	62
2.6.10.1	Theoretical background	62
2.6.10.2	Magic Angle Spinning (MAS) in Solid state NMR.....	64
2.6.10.3	Single Pulse ²⁷ Al MAS NMR spectroscopy	66
2.6.10.4	Single Pulse ²⁹ Si MAS NMR spectroscopy	66
2.6.10.5	Cross Polarisation ¹³ C MAS NMR spectroscopy	67
2.6.11	Microwave Plasma-Atomic Emission Spectrometer (MP-AES)	67
2.7	References	69
3	Hydrothermal stability of selected commercial zeolites	71
3.1	Introduction	71
3.2	Results and discussion	73
3.2.1	Characterisation of untreated parent zeolites	73
3.2.2	Pre-screening of high aluminium content commercial zeolites	75
3.2.3	General effect of aluminium content.....	79
3.2.4	Influence of temperature and time on FAU type zeolite.....	82
3.2.5	Influence of Na ion exchange on commercial ZSM-5.....	88
3.2.6	Alkali ion exchange on commercial β (38) zeolite	92
3.2.7	LTA zeolite stability	96
3.2.8	Framework density considerations.....	99
3.3	Conclusions	101
3.4	References	103

4	Influence of aluminium content on the stability of high framework density zeolites	105
4.1	Introduction	105
4.2	Results and discussion	107
4.2.1	Characterisation of one-pot synthesised H-ZSM-5 zeolites.....	107
4.2.2	Influence of water on crystallinity and porosity	110
4.2.3	Comparison study between post-synthetic treated and one-pot synthesised HZSM-5 zeolites	112
4.2.4	Medium aluminium content HZSM-5 (80) HT stability with time.....	115
4.2.5	High aluminium content HZSM-5 (30) stability.....	119
4.2.5.1	Influence of extended water contact on stability	119
4.2.5.2	Influence of water temperature on stability	122
4.2.5.3	Influence of testing conditions on stability.....	127
4.2.5.4	High density frameworks and water contact.....	131
4.3	Conclusions	135
4.4	References	138
5	Stability of MOFs	140
5.1	Introduction	140
5.2	Initial MOF screening	142
5.3	UiO-66(Zr)-H and its amino analogue, UiO-66(Zr)-NH ₂	151
5.3.1	Materials characterisation	151
5.3.2	CFR stability testing.....	156
5.4	High temperature testing of Hf and Zr UiO-66.....	165
5.4.1	UiO-66(Hf)-H	165
5.4.1.1	Material characterisation.....	165
5.4.1.2	CFR stability testing	166
5.4.2	UiO-66(Zr)-H.....	170

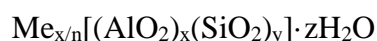
5.4.2.1	CFR stability testing	170
5.5	Conclusions	173
5.6	References	176
6	Conclusions and prospective challenges	179
6.1	Conclusions	179
6.2	Challenges and final remarks	183
6.3	References	186

1 Introduction

1.1 Zeolites – structure, properties and applications

1.1.1 Structure

The term zeolite refers to a variety of crystalline, microporous, 3-dimensional aluminosilicates. They occur naturally, and can also be made synthetically, and have been studied for more than 300 years. The general chemical formula of natural zeolites stands as follows:



Where: Me – compensating (or extra-framework) cations such as Na^+ , K^+ , Ca^{2+} , Mg^{2+} , or related ions of positive charge,

n – the charge balancing the cation (Me),

z – number of water molecules per unit cell,

x/y – silicon to aluminium molar ratio.

The framework of a zeolite can accommodate a wide variety of charge compensating cations (Me) that are located in cavities and channels. This occurs as for every silicon (Si) replaced with aluminium (Al), a negative charge is introduced into the framework, which is compensated with an equivalent number of cations or ions of positive charge (*i.e.*, H^+ , NH_4^+).

The conventional Löwensteinian linkages rule states that if an oxygen bridge links two tetrahedra and an aluminium atom occupies one, the other must be occupied by silicon. Therefore, the x/y ratio, which is the Si/Al ratio, is dictated to be a number between 1 and infinity. However, since 1954 when the rule was conceptualised, several publications provided solid evidence for existence of non-Löwensteinian linkages in some protonated zeolite frameworks. Detailed periodic density functional theory (DFT) calculations have given evidence of thermodynamic preference for Al^{3+} atoms to be bridged one another by a hydroxyl group.¹ This concept challenges the generally agreed assumption of how atoms are arranged in zeolites.

There are 67 different known natural zeolites, which are divided into 28 different framework types.¹⁶ The synthetic man-made zeolites cover more than 200 structures, out of which some are pure silica, aluminium free and doped silica materials, *i.e.* silicalite-1,² SSZ-24,³ ITQ-9,⁴ all-silica zeolite β ⁵ and their derivatives such as titanium silicalite-1⁶ and all silica Sn- β ,⁷ which can be directly bottom-up synthesised or require post-synthetic methods to be achieved.

Zeolites are specific hierarchical structures formed by linked tetrahedral building blocks with a uniform subnanometre or nanometre scale pores network. These internal tetrahedral blocks are so called primary building units (PBU) – corner-sharing TO_4 tetrahedra. Furthermore, PBU are most often $[\text{SiO}_4]$ and $[\text{AlO}_4]^-$ units linked by oxygen bonding creating ring type secondary building units (SBU). Linked SBU units create the whole zeolite 3-dimensional framework. What is more, the SBU units are used to organise all of the zeolites structures according to the IUPAC rules of nomenclature of microporous materials.⁸ For instance, an important class of zeolites are MFI structures, of which the most well-known member is ZSM-5. The MFI-type structure is built up from oxygen bridged pentasil unit chains. A single pentasil unit consists of eight five-membered rings. A different example of a structure is an LTA-type structure built of a sodalite cage (or β -cage), consisting of 24 T atoms (six 4-membered rings, four 6-membered rings, three 6-2 units or four 1-4-1 units), as presented in Figure 1.1.

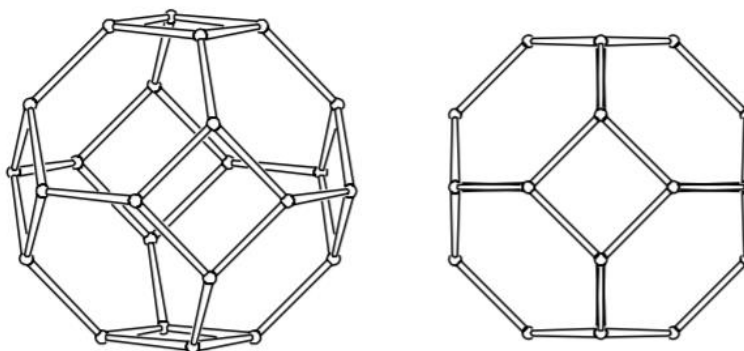


Figure 1.1 A perspective and parallel view of a sodalite cage.¹⁶

A 3-dimensional cubic framework is built by linking the 8 sodalite cages through double 4-membered rings creating a α -cavity (diameter $\approx 11.2 \text{ \AA}$) inside, as presented in Figure 1.2.

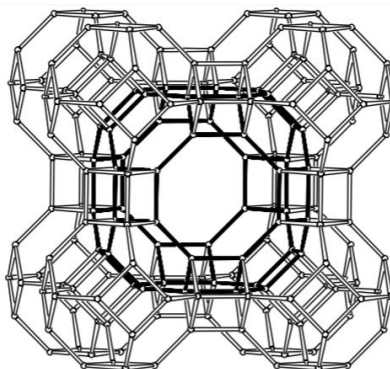


Figure 1.2 The 8-sodalite cages connected through double 4-membered rings creating an inside α -cavity (bold black).¹⁶

In a sodium LTA, the α -cavity linked through the 8-membered rings of 4.1 Å diameter, creates a 3-dimensional system of channels. These channels are widely known as the zeolite pore system or porosity. The effective 4.1 Å diameter window size is subject to change by the presence of exchangeable extra-framework cations, which partially block the pore. The eight α -cages building the LTA unit have 12 negative charges that must be compensated by these ions. In this way the LTA structure forms so called 3 Å (K^+ -form), 4 Å (Na^+ -form) and 5 Å ($\text{Ca}^{2+}/\text{Na}^+$ -form) molecular sieves. The 3 Å and 5 Å are formed by replacing the sodium via a post-synthesis ion-exchange procedure.

Porosity is the most significant feature of porous crystalline structures. According to the IUPAC classification, micropores are characterised by diameters of less than 20 Å, mesopores are those with diameters from 20 to 500 Å, and macropores are those larger than 500 Å.⁹ In the case of zeolites, the pores are molecular dimensions, and form highly regular and coordinated network. Most of the zeolites are classified as microporous materials, as the pore diameters created by PBU are smaller than 20 Å. As mentioned before, the three-dimensional frameworks are made up of a series of rings. Zeolites can therefore be classified according to their T-atom ring sizes as:

- small pore (3.5 – 4.5 Å, *i.e.*, LTA),
- medium pore (4.5 – 6.0 Å, *i.e.*, MFI),
- large pore (6.0 – 7.5 Å, *i.e.*, FAU, MOR).

These pore dimensions enable zeolites to act as molecular sieves in selective ion permeability (membrane processes) and as shape-selective catalysts in heterogeneous

catalysis. For example, the MFI type framework has a three-dimensional pore system built up of two interconnected parallel straight and sinusoidal 10-membered ring channels. Those channels create an overall high internal active surface area.¹⁰

New micro- or mesopores in the crystalline structure can be introduced by two approaches, including bottom-up methods, such as hard templating, soft templating and non-templating, or top-down methods, such as demetalation or delamination and assembly.¹¹ The bottom-up approach is present during the crystallisation of a zeolite and is linked to the use of organic structure-directing templates (OSDAs) and mineralising agents, such as *e.g.* HF. Post-synthetic methods include metal extraction, such as dealumination and desilication or aggregation of already existing zeolite particles. Demetalation is based on extraction of one or more framework atoms (Si, Al, Ti) from the crystalline zeolite structure through strong acid or alkali treatment. In contrast to zeolite dealumination, desilication does not significantly affect the acidity and the crystalline structure of zeolites.¹¹

1.1.2 Framework density (FD_{Si})

Application in ion exchange, catalysis, and sorption strongly depends on the size and orientation of the internal pores and channels. For ion sorption, the total pore volume is also important. In general, pores are related to the Framework density (FD_{Si}), which is the number of silicon tetrahedral atoms per 1000 \AA^3 . Back in 1989, Brunner and Meier found a relationship between zeolite framework densities, porosity and the smallest rings in their framework, based on theoretical studies.¹² They have shown that the FD_{Si} value depends on the number and type of the smallest rings in the tetrahedral structure. The lowest density frameworks are those with a maximum number of 4-membered rings (*e.g.*, FAU type framework, $FD_{Si} = 13.3$, smallest ring – 4). Also, as reported in their work, highly porous structures built of 5- and 6-membered rings, as smallest rings, were unlikely to occur. However, they also found out that 3- and 4-membered rings were much less stable than 5- and 6-membered ones. Furthermore, they also proposed that the successful synthesis of very low FD_{Si} , extra-large pore and highly porous zeolite structure would be unlikely to happen in the case of pure silica structures. According to Moliner *et al.*, a way to produce stable large-pore zeolites for catalytical applications is the use of relatively large and rigid OSDAs.¹³

Frameworks with lowest FD_{Si} , such as the FAU structure, are predominantly built of 4-membered rings. What is more, the framework lacks 5-membered rings subunits, in contrast to the MFI structure. Therefore, to obtain same volumes and sizes of mesopores less time is required to remove atoms (through demetalation) from a less dense FAU structure than from a much denser MFI structure.

In nearly all known cases, the general observation is that the higher the FD_{Si} value, the lower the zeolite pore openings and pore volumes. However, there is great interest in finding stable zeolites with high FD_{Si} and extra-large pores that allow diffusion of bulky reactants. Despite efforts made up recently by industrial and academic research, only a few zeolites with more than 12-ring channels have been successfully synthesised. Examples of these are SSZ-53, SSZ-59, ECR-34 and OSO-1.¹⁴ As mentioned before, the FD_{Si} does not reflect the size of the pore openings, which is crucial for catalytic activity and sieving properties. This is why some zeolites possess similar or same FD_{Si} and smallest ring sizes (here 4), but different pore openings *i.e.*, ETR (15.4 T/1000 Å³) and BEA (15.3 T/1000 Å³) structures, pore openings of 10.05 Å and 6.7 Å, respectively. Subsequently, larger pore opening mean larger pore volumes of the zeolite. However, this observation is valid only for few novel structures, which are not yet used industrially.

Channel dimensions and orientations are significant in various applications. Medium (MFI) and large (FAU) pore materials dominate in catalytic processes in petrochemical industry (*i.e.*, cracking, isomerisation and reforming). On the other hand, small pore structures (*i.e.*, CHA, LTA) have found application in gas separation, humidity sensors, ethanol dehydration or as adsorbents/desiccants.¹⁵

Table 1.1 summarises structural features of some of the most common zeolites used in industrial application. The 5 first framework types are the so-called “big five”: MFI, BEA, MOR, FAU, and FER. All those structures and their application are discussed further in this chapter, in Section 1.1.4.

Table 1.1 Summary of structural features of structures dominating in industrial processes.¹⁶

Framework	Zeolite	No. tetrahedra in ring	Pore dimensions Å (orientation) ^(a)	Framework density (FD _{Si}) ^(b) T/1000 Å ³
MOR	Mordenite	12 8	6.5 x 7.0 (c)* ↔ 2.6 x 5.7 (c)**	17.0
FER	Ferrierite	10 8	4.2 x 5.4 (c)* ↔ 3.5 x 4.8 (b)*	17.6
FAU	Zeolite Y	12	7.4 x 7.4 <111>***	13.3
BEA	Zeolite β	12 12	6.6 x 6.7 <100>** ↔ 5.6 x 5.6 (c)*	15.3
MFI	ZSM-5	10 10	5.1 x 5.5 (a)*** ↔ 5.4 x 5.6 (b)***	18.4
LTA	Zeolite A	8	4.1 x 4.1 <100>***	14.2
CHA	SAPO-34	8	3.8 x 3.8 (c)***	15.1
DDR	ZSM-58	8	3.6 x 4.4 (c)**	17.6

^(a) Orientation examples: (c) parallel to [001], <111> parallel to all crystallographically equivalent (x, y, z) axes of the cubic structure. The number of asterisks * indicates the channel system being 1-, 2- or 3-dimensional; ↔ interconnecting channel systems.

^(b) Framework density, calculated for an idealised SiO₂ composition in the highest possible space group.

The sorption capacity strongly depends on the width of the channels. This means that larger molecules will only be able to enter and diffuse through wider channels. Cations located within the voids can also affect the total pore volume and sorption properties. Since it is possible to synthesise zeolites of different SiO₂/Al₂O₃ molar ratios and different doping metals, the micropore volume might vary even for the same crystalline structure. These changes alter the properties and have a huge impact on sieving and catalytic properties. As an example, the LTA type (SiO₂/Al₂O₃ = 2) zeolite is most commonly balanced by an alkali ion (*i.e.*, Na⁺, K⁺, Ca²⁺). The counterbalancing cation has a major influence on the pore opening size. The primary sodium form has a 3-dimensional channel system of a 3.8 Å diameter opening. When sodium is exchanged to larger potassium, the pore is compressed to 3.2 Å. Therefore, K-LTA (or K-A zeolite) is also called the 3 Å molecular sieve. It is possible to exchange the sodium ion for a divalent calcium one, and as there are only half of the cations present in the structure, some pores open up to 5 Å diameter.²³

1.1.3 Physicochemical properties of zeolites

Zeolites belong to the group of cationic exchangers due to the negatively charged surface, which is a result of the isomorphous replacement of Si by Al in the tetrahedral framework.¹⁷ Charge-balancing cations can be easily, partially or fully, exchanged as these are interacting with the lattice through only Coulombic forces. The existing Lewis and Brønsted acid sites in zeolites are presented in Figure 1.3.

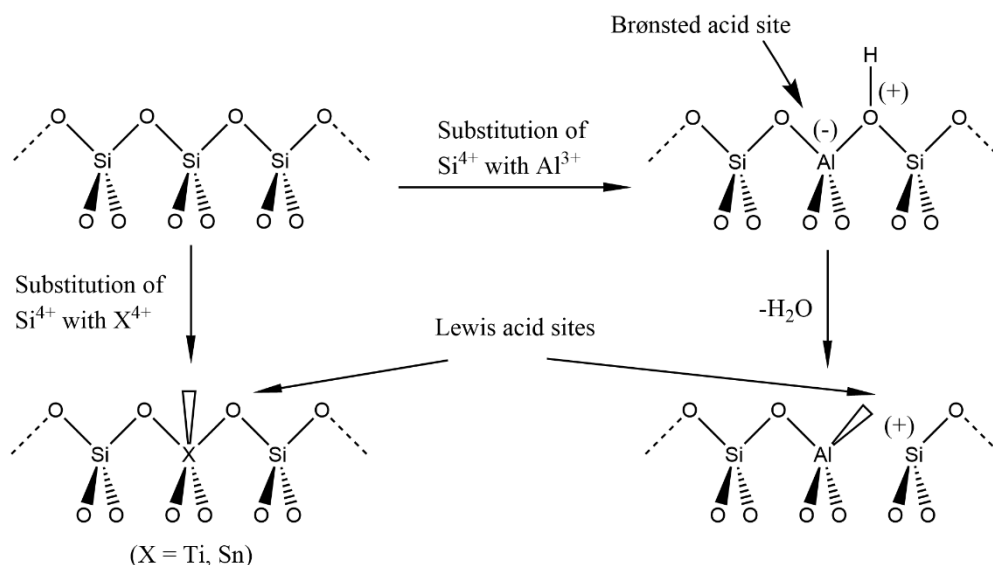


Figure 1.3 Representation of the Brønsted and Lewis acid sites in zeolites.

One of two acidity sites present in a zeolite are the Lewis acid sites, usually generated by the framework and extra-framework Al (EFAl) species.¹⁸ Lewis acidity can be also generated by substitution of Si with other tetravalent heteroatoms (*i.e.*, Sn⁴⁺, Ti⁴⁺, Zr⁴⁺) in the zeolite framework.¹⁹ The second type of zeolite acid sites are the Brønsted acid sites associated with the bridging hydroxyl groups (OH group) in the Si–(OH)–Al unit of the framework tetrahedra. All protonic form (H⁺, *i.e.*, H-ZSM-5) zeolites are so called solid Brønsted acids.

The metal atoms located in the framework positions can undergo partial or total relocation to extra-framework positions when heated to high temperatures. For instance, an FTIR study by Lee *et al.*, demonstrated that in a protonated Ga-ZSM-5 zeolite, gallium was located in framework positions.²⁰ However, at temperatures above 500°C, a strong relocation tendency was observed. This relocation caused the generation of strong Lewis acid sites of unsaturated extra-framework gallium centres. Yu *et al.* observed a similar trend for the H-Y zeolite after high temperature calcination (above 600°C).²¹ The relocation of Al generated five- and

six-coordinated EFAl species. Same observations were made by Li *et al.*, in the case of a dealuminated and rehydrated zeolite H-Y.²²

The SiO₂/Al₂O₃ molar ratio of the zeolite determines the acidity as well as other physical properties such as the hydrophobic or hydrophilic character of the structure. A high content of Al in the zeolite framework tunes the zeolite hydrophilicity, thermally stability but also makes it unsuitable for acidic conditions.²³ Aluminium rich structures are used for solvent dehydration due to strong adsorption of polar molecules, while high and all-silica structures are non-polar adsorbents. The higher the content of Si, the more hydrophobic the structure. The inclusion of Al in the zeolite imparts so called hydrophilic point defects in the structure. It has been generally accepted that the presence of silanol nests (hydrophilic defects) and their concentration and distribution correlate with the zeolites increased hydrophilic behaviour.²⁴ What is more, since water uptake is much favourable, water molecules share the void spaces with the charge compensating cations. Both water and the cations are mobile within the framework and can undergo an unlimited number of reversible ion-exchange, dehydration and rehydration cycles.⁸

The ultimate physical and chemical properties of zeolites can be tailored in several different ways. The zeolite lifetime strongly depends on its synthesis route. For example, large crystals in which the pore channels are oriented along the longest crystal dimension tend to be prone towards increased coke formation. Coke is defined as carbonaceous deposits formed in catalytic processes and deposited on active sites, in zeolite pores, external or internal zeolite surfaces, *e.g.*, hydrocarbon molecules deposition in the pores of a HZSM-5 catalyst after ethanol conversion reactions, which led to temporary deactivation of the catalyst.^{25,26} Relatedly, it has been shown that ultrathin MFI-type zeolite crystals found to be much more catalytically active and stable comparing to a commercial sample.²⁷ Tailoring of the shape and dimensions can be achieved by controlling the temperature, water content, molar composition, use of OSDAs, hydroxyl media and fluoride media.^{28,29} Fluoride ions have a profound impact on silica mineralisation and compensate positive charge linked to the use of OSDAs. As a result, crystalline materials with lower structural defect density are achieved.²⁹ Furthermore, it has been reported that silicalite-1 prepared with the use of F⁻ medium contained significantly fewer structural defects.³⁰ Since this structure is an all-silica type, the focus was on the surface where silanol groups (Si-OH) were undesired. As a result, the densities of polar Si-OH groups were much lower in comparison to a sample crystallised

with the use of OH⁻ medium and therefore a higher pH of the initial synthesis gel. However, Nabavi *et al.* reported that zeolite crystals achieved by fluoride routes were of much larger sizes, which is particularly undesired in catalytic applications due to high mass transfer resistance.³¹

It is important to note that the use of fluoride media sources is also rather undesirable due to their highly toxicity, with HF being particularly most dangerous to handle.³² In order to eliminate problematic surface silanol groups and suppress degradation, low cost silanisation (also known as silylation)³³ and other methods of surface modification, such as polydopamine polymerisation³⁴ and amine functionalisation³⁵ are employed. Silanisation is a process of covering a surface with organosilane (*i.e.*, chlorosilane, octadecyltrichlorosilane, 3-aminopropyltriethoxysilane) molecules which replace terminal OH groups through formation of covalent Si-O-Si bonding. As an example, Zapata *et al.* reported surface treatment of an H-Y (SiO₂/Al₂O₃ = 60) catalyst with octadecyltrichlorosilane (OTS) for the biofuel upgrading reactions in water/oil emulsions.³⁶ This method led to hydrophobisation of the external surface as well as enhanced hydrostability.

1.1.4 Zeolite industrial applications and future prospects

In this section, different existing industrial applications and possible future uses of zeolites are discussed. Due to possibility of extended contact with water and/or organic solvents, the solvent stability is critical. Since it is still not fully understood what makes certain zeolite structures more or less stable, the solubility and possible rapid deactivation mechanisms are described in a later section, section 1.1.5.

It is worth mentioning here that, among more than 200 existing zeolite frameworks, less than 10 are used in industrial processes, and only 5 structures dominate the catalyst production (FAU, MFI, MOR, FER, and BEA).³⁷ A major reason for this is lack of understanding why they are such differences in structural stability among different zeolite frameworks. The choice of framework is even narrower in water purification systems, where LTA and CHA type zeolites are mostly explored.^{23,38} Additionally, pure silica commercial DDR type zeolite membranes have been patented in gas separation selectivity processes.³⁸ One of the main

reason for this limitation is mainly the cost of novel zeolite preparation; this is the need for expensive OSDAs, which facilitate the formation of molecule cages and channels.³⁹

1.1.4.1 Catalytic hydrocracking

As mentioned previously, medium (MFI) and large (FAU) pore aluminosilicates are widely used in the petrochemical industry. One of the most important process utilising zeolite catalysts is hydrocracking, which is a two-step process of (1) breaking of long-chain hydrocarbons into smaller ones (cracking) and (2) hydrogenation, at both elevated temperatures and pressures. Hydrocracking processes are done in a continuous flow regime with the use of fixed-bed or ebullated-bed reactors (hydrocrackers). As the process name suggests, constant flow of hydrogen is required to prevent alkene adsorption (coke formation) in the pores. This provides much longer on-stream times, as the frequent catalyst regeneration is not necessary. In conventional Fluid Catalytic Cracking (FCC), hydrogen is not required. However, coke formation is significant when zeolites are used, hence for this application noble metal catalysts on metal oxide supports are being widely employed.⁴⁰

Among zeolites, partially dealuminated high-silica zeolite Y is most frequently used in industrial hydrocracking.⁴¹ However, it is necessary to reduce water content of the fresh feed, ideally to less than 25 ppm, as at elevated temperatures (290-400°C) and pressures (8,275-15,200 kPa) water vapour (steam) causes the crystalline structure to collapse as demetalation and/or agglomeration takes place. In some processes such as Unicracking (UOP LCC) and GOFining (Exxon Mobil) water content is tolerated up to 500 ppm.⁴²

1.1.4.2 Biomass conversion

Much of researchers' attention has recently turned towards catalytic conversion of biomass to valuable chemicals and energy (*i.e.*, valorisation). One of the reasons why catalytic biomass conversion has not yet been commercialised is that zeolites may not be stable in the liquid phase, such as hot liquid water.⁴³ Hence, the evaluation of their stability and the need of development is crucial. However, it is still worth mentioning, due to high interest in biomass use especially for production of energy from renewable sources. The use of renewable biomass feedstock instead of fossil fuels from petrochemical industry would revolutionise today's world by limiting greenhouse gasses (*i.e.*, CO₂ and NO_x) emissions

and hereafter help with the global warming. These environmental problems are also pushing green chemistry interest towards the use of water instead of harmful and toxic organic solvents for catalytic reactions.⁴⁴

Carbohydrates (sugars and starches) represent a large part of the biomass feedstock. One of these, lignocellulose, composed of cellulose (9%-80%), hemicellulose (10%-50%), and lignin (5%-35%), is an attractive and challenging substrate for bioethanol production.⁴⁵ Cellulose is a linear polysaccharide build of hundreds to thousands monosaccharide units joined by glycosidic linkages. Cellulosic bioethanol fuel can be produced from catalytic hydrolysis of cellulose to glucose. However, zeolites seem not to have same importance in biomass conversion as in the petrochemical industry, but they can be used in further transformations of deconstructed lignocellulose.⁴⁶ Although, moisture content of biomass ranges from 5 to 35% and after drying at 100-200°C drops to <5%. The use of water stable zeolite catalyst could help bypass the energetically and economically intensive biomass dehydration steps and open a new pathway of lower catalytic reaction temperatures.^{47,48} This is why high temperature; liquid phase stable inorganic catalysts are needed to be developed. The major step to achieve this is to understand the weak points causing zeolite degradation in liquid phase. As an example of a catalyst development, Moliner *et al.* presented that isomerisation of glucose can be achieved with all silica, aluminium free (prepared with use of HF), Sn- β catalyst. Batch reaction (10 wt. % glucose in water) was performed for 30 min at 110°C and 12 min at 140°C. Both reactions given product yields of approximately 46 wt. % of glucose, 31 wt. % of fructose and 9 wt. % of mannose.⁴⁹

1.1.4.3 Solvent dehydration systems

The first zeolite membranes used in industry on a commercial scale were zeolite Na-A membranes produced in 1999 by Mitsui Engineering & Shipbuilding Co., Japan, used for organic solvent dehydration.²³ In 2011, a German company, GFT Membrane Systems, constructed five plants for high scale ethanol dehydration, utilising LTA coated four-channel alumina tubes.⁵⁰ Until now, several companies produced zeolite coated ceramic membranes mostly for application in pervaporation (PV) and/or vapour permeation (VP) separation processes.

Pervaporation is a membrane-based process in which separation of constant boiling point (azeotropes) or close-boiling organic mixtures occurs. Pervaporation is used when standard distillation fails, *e.g.*, for separating mixtures of xylene isomers.⁵¹ In principle, liquid phase flow is being placed in contact with a membrane on the feed side and by applying vacuum permeate is removed as vapour phase.⁵² Cold traps provide surfaces chilled by liquid N₂ and are used to trap condensable vapours and prevent the vapour reaching vacuum pump. The most important features differentiating pervaporation from distillation are lower operating temperatures, lower pressures, and the ability to separate mixtures with low energy consumption. Furthermore, separation takes place in one-step, as the mechanism does not rely on the volatility of the mixture components. It is based on the molecule absorption/diffusion properties and the permselectivity of the inorganic membrane.⁵³

In a paper by Gallego-Lizon *et al.*, commercially available polymeric, silica and zeolite pervaporation membranes were investigated towards t-butanol dehydration from water mixtures.⁵⁴ Herein, at 60°C and 10 wt. % water content, Na-A membrane (SMART Chemical Company Ltd., UK, dissolved in early 2020) obtained lower fluxes than the microporous silica unit, while water selectivity was 4.5 times higher.

Table 1.2 presents commercially available zeolite membranes. All systems were used in PV and/or VP for solvent dehydration. All mentioned companies are on the market and actively produce membranes as of May 2021.

Table 1.2 Chosen industrial zeolite membranes for liquid separation (PV/VP) applications

Company	Name	Zeolite type	Coating side, substrate	Application
Mitsubishi Chemical Co., Japan ⁵⁵	Zebrex™	CHA	Outer, ceramic tube	Bioethanol and solvent dehydration
	KonKer™	CHA		Beverage concentration
Hitachi Zosen Co., Japan ⁵⁶	HDS®	LTA (Na-A)	Outer, α -Al ₂ O ₃ tube	Ethanol dehydration
	HDS®	FAU (Na-Y)		
Mitsui Engineering & Shipbuilding Co., Ltd. (Japan) ⁵⁷	-	LTA (Na-A)	Outer, ceramic tube	Bioethanol dehydration
	-	T-type (zeolite T)		
Jiangsu Nine Heaven Hi-Tech Co., China ⁵⁸	-	LTA (Na-A)	Outer, α -Al ₂ O ₃ tube	Solvent dehydration
Pervatech BV, Netherlands ⁵⁹	-	LTA (Na-A)	Inner, α -Al ₂ O ₃ tube	Ethanol (>90%) dehydration
Fraunhofer, IKTS, Germany ⁶⁰	-	LTA (Na-A)	Outer, α -Al ₂ O ₃ tube	Solvent dehydration

In 2008, Hitachi Zosen Co. delivered Japan's first large-scale bioethanol dehydration plant with the production capacity of 50,000 L day⁻¹. It was reported that The Hitachi Zosen membrane (HDS[®]), which is a Na-A zeolite thin film deposited on outer surface of the Al₂O₃ porous support tube, was stable under the pervaporation dehydration operations at 130°C.⁶¹ However, even though for these zeolite membranes swelling did not occur, other issues were reported, such as framework degradation, dealumination and solubility in acidic solutions. What is more, hydrothermal stability issues were observed. When the Na-A zeolite membrane was in contact with feed of higher water contents, *i.e.*, 50 to 80 wt. %, it was reported that the membrane was severely damaged just after 6 h of operation at 70°C.⁶² This includes decrease in relative crystallinity, cracks and large pinholes observed by SEM.

1.1.4.4 Desalination

According to the World Health Organisation (WHO), the occurrence of sodium in drinking water at levels above 0.2 g L⁻¹ affects the taste of it. Knowing this, the lowest acceptable salt (NaCl) rejection rate is 99.5% if seawater (3.5% salinity) is to be converted into drinking water. This is because long-term exposure to excess of sodium chloride happens to increase blood pressure with age. All the recommendations and requirements for drinking water quality are collected in the open access WHO Guidelines for Drinking-water Quality (GDWQ) document.⁶³

Since LTA zeolite membranes have demonstrated excellent performance in solvent pervaporation separation, they are also believed to be suitable for desalination process.^{23,64} However, as described in the previous section, Na-A zeolite coated PV dehydration membrane failed when the feed water content was greater than 50%.⁶² One of the methods of overcoming limitations on the synthesis of zeolite thin films on ceramic tubes was the development of the Mixed Matrix Membrane (MMM).⁶⁵ In principle, the MMM is supposed to combine the benefits of polymeric matrix and inorganic nanoparticles. Nanoparticles (inorganic fillers) were expected to be dispersed in a continuous polymer phase. However, so far none of the designed MMMs systems has been commercially used. Unfortunately, in most cases there were issues with physical and chemical compatibility and the possibility of large-scale fabrication.⁶⁶

However, one of the prospect inorganic-polymer membrane examples would be the thin film nanocomposite (TFN) membrane. In this case, the inorganic-polymer layer creates a thin coating on top of a porous polymer support. Researchers from the Hoek group at the University of California at Los Angeles (UCLA) designed and patented such a reverse osmosis (RO) membrane (QuantumFlux, NanoH₂O Inc., since 2014 a part of LG Chem, Korea) for seawater desalination. The membrane is built out of 3 elements – non-woven polyester fabric, porous polysulfone film and the nanocomposite (Na-A zeolite nanoparticles-polyamide) thin film.^{67,68} A single unit has an active area of 37 m², water permeate flow rate of 34 m³ day⁻¹ and minimum NaCl and boron rejection of 99.75% and 93.00%, respectively.⁶⁹

Table 1.3 presents chosen membranes tested in laboratory scale. All systems were used in PV and/or VP desalination.

Table 1.3 Prospective zeolite membranes and their performance in pervaporation application for desalination.

Zeolite - Support	NaCl (g L ⁻¹)	Conditions on feed side	Conditions on permeate side	Thickness (µm)	Flux (kg m ⁻² h ⁻¹)	Rejection (%)
Na-A – glass ceramic tube ⁷³	Seawater, pH 8	69°C, 30 L h ⁻¹	Vacuum, 133 Pa	-	1.9 (4 h)	99.9
	31	77°C, 30 L h ⁻¹		-	4.9 (4 h)	99.9
Silicate-1 - α-Al ₂ O ₃ tube ⁷⁴	3.5	21°C, 2.4 L h ⁻¹	Vacuum, 0.1 MPa	6.0	1.9 (100 h)	99.0
ZSM-5 - α-Al ₂ O ₃ tube ⁷⁴				3.3	2.0 (100 h)	99.0
ZSM-5 - α-Al ₂ O ₃ tube ⁷⁰	3.8	80°C	Vacuum, 7 MPa feed pressure	-	0.85 (N/A)	99.0
ZSM-5 - α-Al ₂ O ₃ tube ⁷¹	3.0	90°C 21°C	Vacuum, 7 MPa feed pressure	3.0	~14.3 ~7.0 (90 h)	75.0 82.0
FAU - APTES-modified α-Al ₂ O ₃ tube ⁷²	Seawater, 3.5%	75°C	Vacuum 10 kPa	2.3	3.25 (120 h)	99.8

As described before, in order to overcome limitations for commercial membranes use, many different studies were conducted on alternative zeolite type membranes. In all cases, the major challenge was to find stable solutions for heavy metal water purification and seawater desalination, where high water content is present. A particular focus has been placed on MFI structure, as the ZSM-5 zeolite can be synthesised in a wide range of SiO₂/Al₂O₃ molar ratio, has a medium range of 3-dimensional interconnecting channels (5.1-5.6 Å) network and a

high framework density ($18.4 \text{ T}/1000 \text{ \AA}^3$), which makes it a potentially stable and suitable candidate for a desalination membrane.

The paper by Cho *et al.* reported an excellent performance of a Na-A membrane in seawater desalination.⁷³ The membrane rejected more than 99.9% seawater ions such as Na^+ , K^+ , Mg^{2+} , Ca^{2+} , Sr^{2+} , F^- , Cl^- , Br^- , SO_4^{2-} , PO_4^{2-} , NO_3^- , except for charge neutral boron, $\text{B}(\text{OH})_3$. Boron rejection was on the level of 79.2% at 69°C , while the flux was relatively low ($1.9 \text{ kg m}^{-2} \text{ h}^{-1}$). However, the paper failed to consider the long-term experiments and presented observations after only 4 h of desalination. Because of this, the performance and stability of those membranes after extended periods of operation are unknown.

However, the paper by Drobek *et al.* presented a 560 h desalination test in pervaporation mode.⁷⁴ The main aim of this study was to show the decrease of the two zeolite based (ZSM-5 and Silicalite-1) membranes performance in time. During the long-term experiment, the NaCl concentration increased from 3.5% to 7.5% and a decrease in performance was observed for both membranes. Salt rejection dropped from 99.9% to below 30% and 96% to 82% for ZSM-5 and Silicalite-1, respectively. This was most probably due to Na ion exchange and dissolution mechanisms. However, these pervaporation tests were done in a cyclic change of temperature and sea salt concentration without any previous regeneration of the membranes.

1.1.4.5 Gas separation systems

Nowadays, gas separation systems are applicable in many industrial processes such as hydrogen recovery, CO_2 storage, natural gas upgrading, alkenes recovery, air purification and other.⁷⁵ In particular, separation of CO_2 and CH_4 is important in *e.g.*, anaerobic digestion of plant and animal derived biomass. Opposite to catalytic hydrocracking, CO_2 separation takes place at low temperatures but requires elevated pressures. This is why stable inorganic membranes are much more favourable than polymer ones for this application.

Table 1.4 presents commercially available zeolite gas separation membranes used in CO_2/CH_4 mixture separation processes.

Table 1.4 Chosen industrial zeolite membranes for gas separation applications

Company	Name	Zeolite type	Coating side, substrate type	Application
Hitachi Zosen Co., Japan ⁵⁶	Hitz CO ₂	LTA	Outer, α -Al ₂ O ₃ tube	CO ₂ separation
		FAU		CO ₂ separation
NGK Insulators, Japan ⁷⁶	-	DDR	Inner, α -Al ₂ O ₃ honeycomb tube	CO ₂ separation from methane

In February 2019, two Japanese companies started the construction of a gas separation facility at a Texas-based petroleum site. Daily, during production at the site, approximately 85,000 m³ of associated gas was generated. In 2020 it was announced that the facility would be testing large-scale (0.18 m diameter, 1.0 m length) DDR-type membranes (NGK Insulators, Japan). The role of the membranes is the removal of CO₂ from the associated gas. So far, initial tests were carried out only on a laboratory scale (0.03 m diameter, 0.16 m length) but under conditions similar to real-life ones. These were as follows: 65-71 mol % CO₂ and 29-35 mol % CH₄ gas mixture, 58-60°C, transmembrane pressure difference of 7.4-7.7 MPa and up to 140 h testing time. As a result, the separation factor of CO₂/CH₄ was high and relative gas permeability was stable (~1) throughout the test, which is considered as a success.⁷⁷

In addition, NGK Insulators performed their first gas separation tests. Simple DDR type membranes were prepared by hydrothermal synthesis on the outer wall of a porous α -Al₂O₃ tube (active area of 8.7 cm²).⁷⁸ The best results were reported for the DDR membrane in a 1:1 CO₂/CH₄ gas system, at 25°C and transmembrane pressure difference of 0.1 MPa.⁷⁸ Higher temperatures (up to 100°C) and pressure differences resulted in lower CO₂ permeance and separation. Furthermore, in order to check the effect of humidity on gas permeation and DDR stability, a CO₂/CH₄ gas mixture containing water vapour (up to 3% H₂O) was introduced to the feed after stabilising the membrane with a dry mixture for 4 h at 25°C. Because of the introduced vapour, the CO₂ permeance and the separation selectivity decreased by 56% and 50% their initial values, respectively. Yet, the CH₄ permeance was the same as during stabilisation. Both permeance and selectivity were recovered to initial values as soon as vapour was switched back to the dry mixture. Contrarily, the presence of 3% N₂ had no effect on both CO₂ permeance and selectivity.

According to Hitachi Zosen Co., the Hitz CO₂ membrane separation element is able to reduce CO₂ concentration from around 400 ppm (in atmospheric air) to less than 80 ppm.

Furthermore, the element can extract 97% of the CO₂ from engine combustion exhaust, which typically contains 20-30% of the gas.⁵⁶

Small pore zeolites frameworks such as LTT, CHA and DDR are the main interest of researchers for gas separation, as these zeolites possess pores of a sizes similar to that of the CH₄ (3.8 Å), but larger than the CO₂ molecule (3.3 Å). However, despite excellent testing results and scale-up possibilities, the industrial production of SAPO-34 (CHA type) and zeolite T (LTT type) membranes for gas separation has not yet come to realisation.⁷⁹

1.1.5 Zeolite deactivation mechanisms and solubility in liquid media

1.1.5.1 Reversible deactivation mechanisms

As described previously, in section, 1.1.4, two of the major problems prohibiting the use of zeolite catalysts for biomass conversion and other liquid phase applications are the rapid rates of deactivation and framework collapse observed upon use in the liquid phase. Due to those phenomena, the use of zeolites is still limited in those industrial applications. There have been several reasons identified for the zeolite deactivation in liquid phase catalysis, most of which are reversible. Understanding the stability and overcoming these deactivation mechanisms would open the possibility of using a wider variety of zeolite frameworks in industry. Reversible mechanisms are ones including fouling (coking) and poisoning.⁸⁰

The first deactivation cause, fouling, is associated with site blockage by physisorbed reaction by-products. This is very common when heavy hydrocarbons are produced, *i.e.*, during hydrocracking. That is why constant flow of hydrogen is needed to avoid this phenomenon. However, fouling might also occur in liquid phase biomass conversion.⁸¹ The process causes a decrease in specific surface area and porosity, and results in reduced conversion activity and selectivity of the catalyst. This process is reversible and regeneration can be achieved by simple calcination (over 550°C) procedure.⁸² The ultimate aim of this is to remove the material that blocks access of the reactants from pores and voids in order to reuse the catalyst.

Poisoning refers to strong chemisorption of various adsorbates, which block the active sites. This is associated with various components present in the feed or with by-products formed during the catalytic reaction. Similar to fouling, partial regeneration is possible by thermal treatment.⁸³ However, prevention by removal of contaminants from the feed is much more beneficial due to the ability of the catalyst to operate for longer times without need of

intermittent regeneration. Other ways to prevent chemisorption are the optimisation of zeolite pore structure and/or adding additives that selectively adsorb the contaminants causing poisoning.⁸⁴

1.1.5.2 Irreversible deactivation mechanisms

There are three known irreversible processes causing the catalyst deactivation and one associated with mechanical disorder. These are of chemical (leaching, dissolution and active site reorganisation) and physical nature (mechanical alteration).

Leaching is the solubilisation of particular components of the catalyst while in reaction medium.⁸⁰ It is irreversible and might be a consequence of active site reorganisation. The process can be detected by the liquid phase analysis such as ICP-MS and MP-AES methods. Contact time between the liquid and solid phases might play a critical role in the leaching process. Britton *et al.* previously reported that reactions done under continuous flow regime offer multiple advantages over batch reactions in terms of catalyst lifetime and its activity.⁸⁵ However, it should be noted that postsynthetic metal leaching (*e.g.*, demetalation) is occasionally targeted in order to stimulate the formation of mesopores. For this process, acids and bases are used in a controlled time and temperature process. One of the ways of producing mesopores is by controlled desilication. Groen *et al.* published initial findings in this field and Pérez-Ramírez *et al.* further expanded the topic.^{86,87} These authors also emphasise the need for sustainable zeolite synthesis route and note that most bottom-up approaches use larger amounts of toxic organic templates.

The (solvo)thermal dissolution is associated with the structural destruction or dissolution of the solid when in contact with a hot solvent. For zeolites, it means amorphisation or formation of new phases.⁸⁰ This process can be identified through common techniques used for the characterisation of powders such as powder X-Ray diffraction (pXRD).

Active site reorganisation (sintering) is associated with agglomeration of active sites, which results in reduction of specific surface area and accessible active site area. This process is strongly temperature dependent and most likely occurs due to (solvo)thermal reactions.⁸⁸ Since atoms within the zeolite framework can move to extra-framework positions this process might be a precursor to leaching, which is irreversible. Reorganisation might be

regenerated by silylation. This process is associated with covering the external surface with organosilanes, which also enhances hydrophobicity of the zeolite.⁸⁹

A mechanism not strictly associated with deactivation, but causing multiple problems, is mechanical alternation of the material *i.e.*, size reduction or breakup of particles. The mechanism is especially important when operating in continuous flow regime as liquid media might cause abrasion to the solid material. This process might be problematic when performing reactions in fixed-bed reactors under continuous flow regime. Because of mechanical alternation, smaller particles are formed. This causes pressure build-up in the continuous flow reactor.⁹⁰

To overcome the irreversible deactivation and complete degradation of the material, two approaches are possible. The first is to try and avoid possible causes by minimising parameters initiating deactivation, this is by feed purification or tuning the framework.⁹¹ Second approach is to carefully monitor of the parameters in the synthesis process, such as presence of silanol nests and accept partial deactivation. In order to avoid chances of mechanical alternation, the temperature and pressure must be chosen in such a way, which avoids severe gradients in the reactor. This problem often occurs in catalytic fixed-bed reactors as mentioned above.

1.1.5.3 Solubility in water

As discussed in Section 1.1.4, solvent dehydration processes are performed at temperatures up to 130°C, while desalination is typically performed in a lower temperature regime, ranging from 30°C to 100°C. It has been observed that the lower the water content, the higher process temperatures are tolerated by the zeolite structure.⁹² To add, at elevated temperatures (up to 400°C) catalytic processes can be achieved only if the water concentrations are below 25 ppm. In high temperature hydrocracking, steam acts as a “poison”, causing not only deactivation of the catalyst, but also a general collapse of the whole structure. However, it is not clearly known what makes certain zeolite structures more stable and less prone to irreversible deactivation mechanisms.

Studies show that steaming process differs from standard water treatment. However, steam treatment is a conventional method of zeolite dealumination. Since the 1970s, dealuminated Y zeolites were used as Fluid Catalytic Cracking (FCC) catalysts.

Dealumination by steam is preferred since high silica zeolite Y, of $\text{SiO}_2/\text{Al}_2\text{O}_3$ molar ratio >6 , cannot be synthesised in a traditional bottom-up way. Thus, commercial zeolites are post-synthetically treated with steam ($>400^\circ\text{C}$) to achieve dealumination and therefore higher Si content.^{92,93} As an example, a commercial NaY zeolite (CBV 100, $\text{SiO}_2/\text{Al}_2\text{O}_3 = 5.1$, Zeolyst) is steamed and ion-exchanged to achieve high silica content, of $\text{SiO}_2/\text{Al}_2\text{O}_3$ up to 80 (*i.e.*, CBV 780) for commercial uses.

However, when using liquid water under autogenic pressure, Ravenelle *et al.* suggested that the main degradation mechanism of the HY and HZSM-5 zeolites was the hydrolysis of Si-O-Si (siloxane) bonds.⁹⁴ This phenomenon was observed in contrast to dealumination, which dominated while steam applied. Steam treatment of the HY zeolite led to an increase in the $\text{SiO}_2/\text{Al}_2\text{O}_3$ and complete amorphisation within 6 h at $250\text{-}300^\circ\text{C}$. Another study that focused on the impact of steaming on BEA type zeolite has shown that after applying 100% steam for 14 h at 480°C , 14% of all framework Al atoms moved to EFAl positions.⁹⁵ The dealumination lead to a decrease of Brønsted acid sites concentration to a number much lower than expected. So far, it was accepted, that the high temperature steaming always leads to hydrolysis of the Si-O-Al bonds, formation of EFAl species and observation of hydroxide species on the zeolite surface.

It is a well-known fact that high alumina zeolites are more soluble in aqueous acidic media and high silica ones are more soluble in aqueous alkali.⁹⁶ In a neutral value of pH (pH ~ 7) the overall zeolite solubility in water at room temperature is known to be low and nearly non-existent. However, when higher temperature is involved the stability in neutral pH differs.

Table 1.5 presents observations on different zeolite type structures behaviour when in contact with water when samples were tested in Teflon lined stainless steel autoclaves under autogenic pressure.

Table 1.5 Examples of chosen zeolite structures hydrothermal stability studies in recent years.

Structure	Zeolite	Commercial? Y/N	Test method	T (°C)	Time (h)	SiO ₂ /Al ₂ O ₃	Result/ Change: ^(a)
BEA ⁹⁷	H β	Y (Clariant)	300 mL SS autoclave reactor, 1 g zeolite in 80 mL of water	160	48	25	Pore volume: T+ MS+ M-, Si/Al: N, Crystallinity: significant decrease
						150	Pore volume: MS+ M-, Si/Al: Y- Crystallinity: slight decrease
				300		25	Pore volume: T- MS- M- Si/Al: N Crystallinity: completely lost
				150		Pore volume: T+ MS+ M-, Si/Al: Y-, Crystallinity: completely lost	
BEA ⁹⁸	H β	Y (Zeolyst)	50 mL Teflon lined SS autoclave, 0.5 g	200	6	25	Crystallinity: 6%-
MFI ⁹⁸	HZSM-5					23	Crystallinity: 35%-
TON ⁹⁹	HZSM- 22	N	200 mL Teflon lined SS autoclave, 0.3 g zeolite in 200 mL of water	250	144	92	Pore volume: T- MS- M- Si/Al: Y- Crystallinity: no change BET area: 81% -
				100	72	92	Pore volume: T- MS- Si/Al: Y- BET area: 6% -
				200		Pore volume: T- MS- M- Si/Al: Y- BET area: 26% -	
MFI ⁹⁴	HZSM-5	Y (Zeolyst)	Teflon lined SS autoclave, 1 g zeolite in 20 mL water	200	6	30	Pore volume: MS+ Crystallinity: no change ²⁷ Al NMR: octahedral Al peak disappeared
FAU ⁹⁴	HY					50	
						80	
						12	Pore volume: MS+ M- Crystallinity: 34% -
						30	Pore volume: MS+ M- Crystallinity: 65% -
						80	Pore volume: MS+ M- Crystallinity: completely lost

^(a) (Y) – changed; (N) – no change observed; (T) – total pore volume; (MS) - mesopores volume; (M) – micropore volume; (+) – increase in value; (-) – decrease in value. All values compared to untreated samples.

The experimental investigations, highlighted in Table 1.5, of various zeolite hydrothermal stability provides useful data. For example, a number of reports have focused on the stability of FAU, MFI and BEA type frameworks. In contrast, the only data considering the MOR structure reported only the change in relative crystallinity without focusing on other features such as pore volume, EFAI appearance or change in other textural properties. However, a few conclusions can be made after analysing the presented dataset. First of all, in aqueous environment, it is clear that the higher the temperature, the larger the damage to the structure of a particular zeolite material. The induced structural damage was mainly observed as a significant loss of framework integrity, evidenced by a loss of relative crystallinity and (micro)pore volume. Secondly, in elevated temperatures (200°C) the MFI structure, in particular the HZSM-5 zeolite ($\text{SiO}_2/\text{Al}_2\text{O}_3$ range 23-80), showed relatively better stability than the FAU structure. Thirdly, the lower the aluminium content, the larger the damage to the FAU structure. Ravenelle *et al.* observed that the low aluminium zeolite Y was completely amorphous after only 6 h of treatment in the autoclave.⁹⁴ Lastly, both BEA structures of high and low aluminium content completely lost crystallinity after contact with water at 300°C. This observation might indicate that at some point, the temperature is high enough to damage the zeolite structure, after only a few hours, no matter how durable and stable it would be at lower temperature (160°C).

Despite these findings, it is clear that all the studies presented thus far have focused on the stability of zeolites under autogenous pressure in Teflon-lined autoclaves, and none of them were done under other conditions, such as high pressure or continuous regime. Consequently, direct extrapolation of these findings to the use of zeolites in continuous flow liquid-phase applications is not straightforward. Accordingly, it is clear that further knowledge regarding the chemistry of zeolite materials in liquid phase media is required for improved performance in heterogeneous catalysis or separation processes to be obtained.

1.1.5.4 Vapour and organic solvent uptake

Hydrophobic zeolites of high silica content do have an organophilic nature, which might find application in *e.g.*, solvent-phased catalysis or in solvent separation applications.

While, as expected, water vapour uptake is increased in hydrophilic high Al content zeolites, ethanol sorption isotherms revealed a different behaviour. In particular, a similarly high level

of ethanol vapour uptake among high alumina (H-ZSM-5, $\text{SiO}_2/\text{Al}_2\text{O}_3=30$, Zeolyst) and no alumina (Silicalite-1) samples was observed.¹⁰⁰ At 35°C, two Silicalite-1 samples synthesised in hydroxyl and fluoride media resulted the same values of ethanol uptake ($\sim 2.4 \text{ mmol g}^{-1}$). This would mean that the concentration of structural silanol defects had no influence on ethanol sorption abilities. However, the H-ZSM-5 (30) sample had a slightly higher ethanol uptake of $\sim 3.0 \text{ mmol g}^{-1}$ under the same temperature testing conditions.

Another study, by Hunger *et al.* focused on the influence of methanol on acid sites of HZSM-5 and NaZSM-5 (both commercial, $\text{SiO}_2/\text{Al}_2\text{O}_3 = 30$, Chemiewerk Bad Köstritz).¹⁰¹ Two types of experiments were done - adsorption isotherms of methanol vapour at 25°C and TPD chemisorption in the range of 27-377°C. Methanol vapour isotherms showed that the adsorption on HZSM-5 is always higher than on its Na-form. However, in the case of both samples the coverage was in a similar range of $3.0\text{-}3.5 \text{ mmol g}^{-1}$.

After comparing both studies, it can be concluded that the adsorption capacity of both solvents (methanol and ethanol) over the H-ZSM-5 zeolite is comparable. In addition, the kinetic diameter of methanol and ethanol are 3.6 \AA and 4.3 \AA , respectively.¹⁰²

According to own analysis and gathered data, an HZSM 5 (30) sample is capable of absorbing 135 mL g^{-1} of water vapour (at 25°C). This means that the vapour sorption capacity is approximately 770 times higher than in the case of ethanol and methanol sorption. Water is more polar than most used organic solvents. Since the critical diameter of water molecules is 2.8 \AA , these molecules can penetrate the structural zeolite channels much easier, while larger molecules such as ethanol and methanol are excluded. Recently it was found that the zeolite stability might be directly correlated with the concentration of internal structural defects and the number of intraporous water molecules absorbed into the structure.¹⁰³ However, these assumptions have not yet been proved and evidence-based research is needed. Comparison studies between different structures call for attention since it is not clearly known what enhances hydrolysis (framework degradation) and if it applies to all types of zeolites.

1.2 Metal Organic Frameworks – structure, properties and applications

1.2.1 General structure

Metal Organic Frameworks (MOFs), which are usually referred to as analogues to zeolites, are built up of metal ions or clusters coordinated with organic mono-, di-, tri- or tetravalent ligands, usually referred as organic linkers.¹⁰⁴ MOF structures may be organised by repeating coordination into 1-, 2- or 3-dimensional frameworks. However, only the general idea of structural building units makes MOFs and zeolites similar. The choice of metal ion or cluster and the organic linker is flexible but dictates the overall structure and most of the properties, such as cavity size, pore volume, specific surface area, acidity, hydrophilicity, and thermal stability.¹⁰⁵

In 1989 Hoskins and Robson proposed a new class of polymeric materials, new infinite polymeric frameworks consisting of three dimensionally linked rod-like units.¹⁰⁶ In early papers, Robson proposed a series of predictions about these structures, all of which have been experimentally confirmed. However, it was the development of the first MOFs (in 1995) which turned out to be a milestone in porous artificial crystal science.¹⁰⁷ One of the most well-known and widely researched MOF structures is the so-called IRMOF-1 (or MOF-5).¹⁰⁸ This MOF is composed of oxygen-centred Zn_4O clusters and a terephthalate dianion linker between.¹⁰⁹ It was synthesised for the first time in 1999 by the Yaghi group. Its derivative, IRMOF-3, differs by only a single amino group on its carboxylate linker. The use of 2-aminoterephthalic acid (NH_2BDC) introduces the said amino group. This slight difference in the structure influences various properties such as thermal and solvent stability.¹¹⁰

Same as in the case of zeolites, various MOF topologies are successfully synthesised by varying the arrangement of linker and metal-containing SBU units (*i.e.*, linear, triangle, square, cubic etc.).¹¹¹ These arrangements have been classified and it has been recommended that for network topologies three letter codes from the Reticular Chemistry Structure Resource (RCSR) would be used, as presented in Figure 1.4. It should be mentioned, that currently (as of November 2021) there are more than the full Cambridge Structural Database (CSD) contains over 100,000 known MOFs.¹¹²

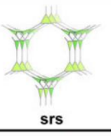
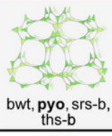
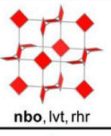
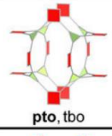
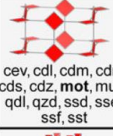
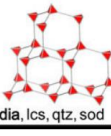
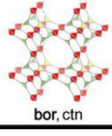
Building unit 1 \ Building unit 2	2-c Linear	3-c Triangle	4-c Square
3-c Triangle	 srs	 bwt, pyo, srs-b, ths-b	 fjh, fmj, gee, iab, yac, yao
4-c Square	 nbo, lvt, rhr	 pto, tbo	 cev, cdl, cdm, cdn, cds, cdz, mot, muo, qdl, qzd, ssd, sse, ssf, sst
4-c tet	 dia, lcs, qtz, sod	 bor, ctn	 fgl, mog, pds, pth, pti, ptr, ptt

Figure 1.4 A small part of a table of suggested possible binary metal-organic frameworks arrangement. All data shown are taken from the Reticular Chemistry Structure Resource (RCSR). Adapted from Kalmutzki *et al.* work published in Science Advances.¹¹³

The naming for the network topologies was adapted from zeolite science. As an example, the abbreviation *dia* comes from the four-connected net of a diamond. A MOF structure may also have its derivatives and in this case a suffix is added when *i.e.*, the original vertices are replaced by tetrahedron ones (-a).¹¹¹

Most of the early-developed MOFs had poor chemical stability, which resulted in degradation of the frameworks even under ambient conditions.¹¹⁴ Poor stability has thus initially prohibited the use of MOFs in applications such as catalysis and membrane separation, even though their chemical structure and functionality, such as their porous nature and tuneable structure, suggest high suitability for these applications.¹¹⁵ Recently, more and more water-stable MOFs have been developed and many applications in water have been investigated and reported.^{116,117,118}

Similar to the case of zeolites, the water stability of MOFs might be post-synthetically improved. Burch *et al.* observed that the stability could be improved by the incorporation of hydrophobic fluorinated and alkyl functional groups on the ligand.¹¹⁹ This mechanism is related to two types of hydrophobicity. In the first case, water is being prevented from adsorbing into the inner pores. In the second case, water can still adsorb in the pores but cannot cluster around the metal centre.

1.2.1.1 ZIF-8

Zeolite Imidazolate Frameworks (ZIFs) are a subset of the Metal-Organic Frameworks and are isomorphic with zeolites. ZIFs are composed of tetrahedrally coordinated transition metal ions (*e.g.*, Fe, Co, Cu, Zn) connected by imidazolate or imidazolate-type linkers.¹²⁰ The basic repetitive units of metals (M) are similar to Si and Al ions in zeolites, same as imidazolates (IM) are in place of linking O atoms. The 145° angle between the M-IM-M makes them similar to zeolites in terms of framework construction.¹²¹

The most well-known ZIF structure is the sodalite (sod) type ZIF-8, built with zinc ions coordinated by four imidazole rings.¹²⁴ The coordination is same as in the case of silicon and aluminium atoms covalently joined by bridging oxygen ions in zeolites.¹²⁰ The structure is known for its large cavities with a diameter of 11.6 \AA , which are connected through small pore channels of 3.4 \AA diameters. The crystal structure of ZIF-8 is presented in Figure 1.5.

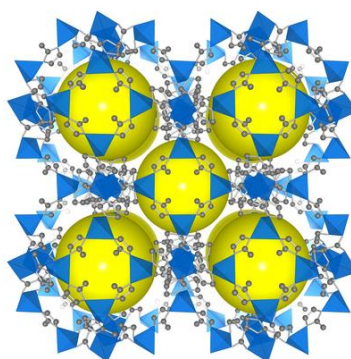


Figure 1.5 Crystal structure of ZIF-8, where: ZnN - blue tetrahedra; carbon - grey balls; large cavities - yellow spheres. The figure was adapted from a published article by Fujie *et al.*¹²²

The ZIFs group differs from other MOF subgroups by exhibiting hydrophobic properties.¹²³ Generally, ZIF-8 is known for high porosity, high specific surface area, hydrophobic nature, open metal sites and water stability.¹²⁴

Stability studies were conducted by Park *et al.* and revealed that amongst twelve tested zeolite imidazole frameworks only Zn(II) ZIF-8 found to be water insoluble.¹²⁵ The structure maintained its crystal structure after being kept 7 days in boiling water (100°C) and organic solvents. Furthermore, the structure remained unchanged after boiling (100°C) it for 24 h in 0.1 M and 8 M aqueous NaOH.¹²⁵ Unfortunately, the paper failed to provide data on the acid stability of the tested ZIFs.

Preliminary studies confirmed that ZIF-8 remained structurally unchanged after immersing in boiling water or steaming at 300°C by demonstrating data on the crystalline structure and specific surface area.¹²⁶ Bhattacharyya *et al.* reported that the acid gas (*i.e.*, SO₂ and in humid air) causes irreversible degradation mechanism, this research was supported by a computational study.¹²⁷ Also, an in-detailed EDX and FTIR study on ZIF-8 hydrolysis showed that water attack might take place to a certain extent and hydrolysis is observed after prolonged water treatment at high temperatures.¹²⁸ The described degradation mechanism involved partial cleavage of the Zn-N bond in the building unit, leading to a formation of hydrolysed clusters in water.

The ZIF-8 as a commercial product is produced under the name Basolite™ Z1200 (BASF).

1.2.1.2 MIL-53

A typical MIL-53 structure consists of interconnected (via OH groups) corner-sharing AlO₄(OH)₂ octahedra bridged by 1,4-benzenedicarboxylate (H₂BDC) linkers. For each metal centre, four of the oxygen atoms originate from four different carboxylate groups of the linker. The remaining two oxygen atoms belong to two different μ-OH groups, which bridge neighbouring metal clusters.¹²⁹ The structure is presented in Figure 1.6.

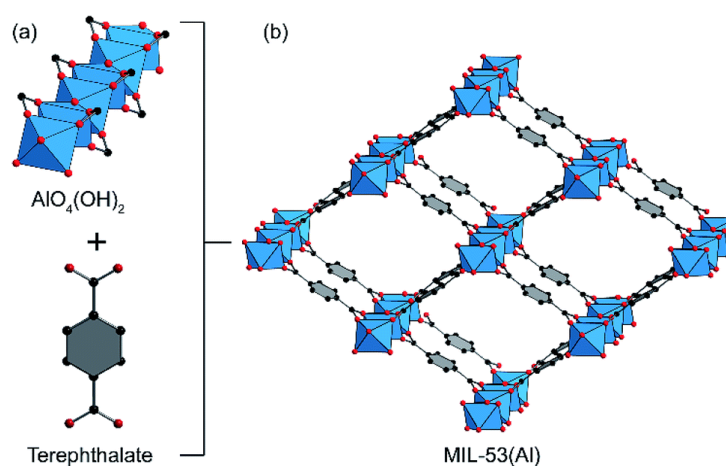


Figure 1.6 (a) octahedral metal building units and the H₂BDC linker forming (b) a 3D structure with 1D rhombic channels. Atom colours: C, black; O, red; Al, blue. Figure was adapted from a published article by Nguyen *et al.*¹³⁰

The MIL-53 structure is characteristic for its 3D structure and 1D diamond shape channels of 8.5 Å (anhydrous) along the [100] crystallographic direction. This MOF is praised for its remarkable thermal stability (up to 500°C, in air), high microporosity and high specific surface area.¹³¹ Due to its structure, MIL-53(Al) has exceptional potential in catalysis, as it possesses Brønsted-type and Lewis-type acid sites. Recently, MIL-53(Al) was used in catalysis such as alkylation, cycloaddition, Mannich reaction and cellulose transformation.¹³⁰ Furthermore, MIL-53(Al) and MIL-53(Al)-NH₂ modified α -alumina membranes showed an excellent efficiency and performance in terms of separating a hazardous organic dye from methanol and isopropanol solutions at an extremely high concentration of 200 mg L⁻¹.¹³²

However, prolonged testing of MIL-53(Al) under static conditions, in boiling water under reflux, has shown that surface degradation of the MOF particles might occur. The particles might become covered with a thick amorphous shell of γ -AlO(OH) and exhibit a large number of protrusions.¹³³

The ultramicroporous MIL-53(Al) MOF is commercially produced under the name Basolite™ A100 (BASF).

1.2.1.3 HKUST-1 (Cu-BTC)

The HKUST-1, also known as Cu-BTC, was first described in 1999 as an open-framework metal-coordination polymer with a molecular-sieve character and thermal stability up to 240°C in air.¹³⁴

Studies on water sorption abilities have shown that HKUST-1 is strongly hydrophilic and that the Cu²⁺ metal sites were the primary adsorption sites for water and other polar molecules.^{135,136,137} In contrast to previously described structures, HKUST-1 is built of metal copper nodes interconnected by 1,3,5-benzenetricarboxylic acid (BTC), which is a tritopic linker. The crystal structure of HKUST-1, a copper-based paddle wheel topology, is presented in Figure 1.7.

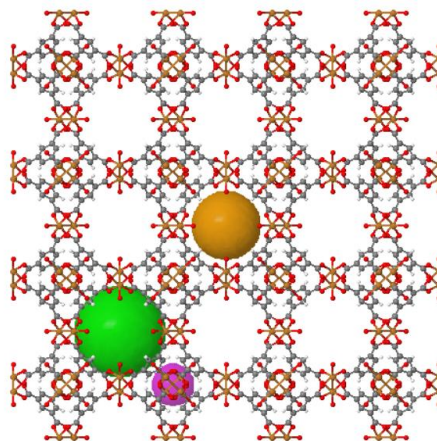


Figure 1.7 Crystal structure of HKUST-1 where: primary pore size (green ball); pore size (large brown ball); secondary pore size (pink ball); hydrogen (white ball and stick); linker struts (grey ball and stick); copper nodes (small brown ball and stick); oxygen (red ball and stick) are indicated. Figure was prepared and adapted from Chemtube 3D.¹³⁸

The HKUST-1 structure was found to possess moderate steam stability and high efficiency in reversible sorption of CO₂.¹³⁹ It was also found to be highly stable in steam but with significant decrease in its specific surface area and water capacity after primary water adsorption.¹⁴⁰ Another water vapour adsorption study, under dynamic non-equilibrium conditions simulating scenarios of carbon capture from natural gas, showed that water vapour did not cause the decomposition of Cu-BTC (25°C, 15 and 120 min exposure time, 5.6 mbar partial pressure).¹⁴¹

The ultramicroporous MOF is commercially produced under the name Basolite™ A300 (BASF).

1.2.1.4 UiO-66

The structure of a model UiO-66 structure is built out of octahedrons consisting of zirconium (Zr), hafnium (Hf) or cerium (Ce) atoms.¹⁴² As an example, in a UiO-66(Zr), the Zr atoms are capped by μ 3-oxo and μ 3-hydroxy groups occurring repeatedly, creating [Zr₆O₄(OH)₄] clusters. Octahedral edges are linked all together with carboxylate groups originating from the organic linker, 1,4-benzenedicarboxylate (H₂BDC) or its functionalised analogue. This results in a formation of the UiO-66 structure presented in Figure 1.8.

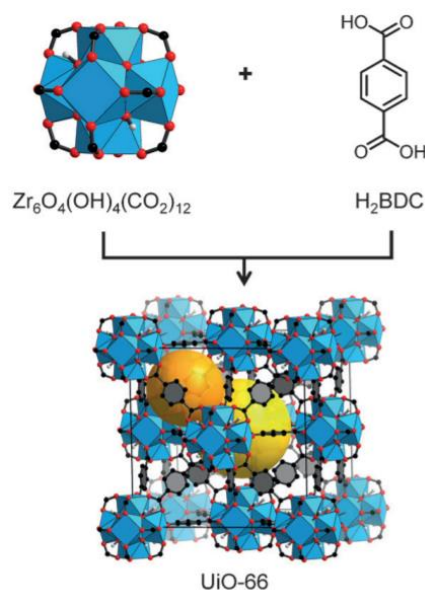


Figure 1.8 A representation of a defect-free structure of UiO-66 with 12-coordinated Zr-based metal clusters interconnected by the 1,4-benzenedicarboxylate (H_2BDC) linker in a face-centered cubic array. Atom labelling scheme: C, black; O, red; Zr, blue polyhedra; H, white; tetrahedral cavity, orange; octahedral cavity, yellow.¹⁴³

Depending on the linker variation, the MOF derivatives are named with added suffixes, as follows, *i.e.*, -H (H_2BDC); - NH_2 (NH_2BDC); -OH (OH-BDC); -COOH (BDC-COOH). The UiO-66(Zr)-H is characteristic for having a pore size of 6 Å along with tetrahedral and octahedral cavities of 7.4 Å and 8.4 Å diameter, respectively.¹⁴⁴

Along with thermal stability up to 350°C, the most intriguing property of this particular MOF is its reported solvent stability at room temperature among commonly used solvents *i.e.*, acetone, chloroform, isopropanol, methanol and water.¹⁴⁵ These could prove the potential for applications such as gas sorption and separation, solvent separation and catalysis.

It was reported by DeCoste *et al.* that both UiO-66(Zr)-H and - NH_2 showed structural stability towards organic solvents, water and 0.1 M HCl after testing the stability at room temperature for 24 h.¹⁴⁵ However, a structural breakdown was observed when both were exposed to 0.1 M NaOH. The complete degradation of the structure was indicated by observation of an amorphous XRD pattern.

In a work by Caratelli *et al.*, a multistep computational modelling approach was used to explore the influence of water and methanol (MeOH) on active sites of a UiO-66 structure.¹⁴⁶ It was found that water had a beneficial effect on reactivity as it provided extra Brønsted

sites through hydrogen bonding. On the other hand, methanol molecules were located at the active sites and linked by hydrogen bonds. Methanol was believed to assist in proton transfer between active sites and charged intermediates in the solution. In this case, methanol was believed to stabilize the active site charge.

The post-synthetic ligand exchange (PSE) reported by Marreiros *et al.* showed that the role of MeOH was to aid stabilisation of dangling linkers.¹⁴⁷ However, a strong interaction was found between MeOH solvent species and the inorganic clusters as ¹H NMR detected signals from MeOH. The chemisorption of MeOH was observed even though the sample was washed with EtOH and dried at 100°C before the NMR analysis. Previously, Shearer *et al.* reported a decrease in the linker content of a UiO-66 structure washed with MeOH.¹⁴⁸ These observations showed that the excess use of MeOH might generate structural defects such as missing linker and/or cluster.

Furthermore, an IRMOF-3 [Zn₄O(BDC-NH₂)₃], which is a zinc analogue of a UiO-66-NH₂ structure has shown poor stability towards MeOH.¹⁴⁹ A degree of crystal degradation, broadening of peaks and reduced intensities, were observed by pXRD after formation of methoxymethyl amine groups by the reaction with paraformaldehyde and MeOH after only 24 h at 50°C.

1.2.2 Potential prospect commercial applications

1.2.2.1 Water harvesting

Water harvesting is one of the MOF applications that is currently attracting interest. The Yaghi group have designed a novel MOF water-harvester prototype in 2017.¹⁵⁰ The general idea was to generate fresh water out of air under any conditions. The device is powered by sun, under ambient sunlight and a condenser was used to recover water vapour absorbed inside a MOF-801(Zr).¹⁵⁰ As the project gained attention, the group shifted their focus from zirconium type MOF to newly designed aluminium MOF-303(Al). The search for a new material was driven by the need for a hydrolytic stable MOF material.¹⁵¹ Apart from the synthesis, there are also more challenges and objectives to achieve, such as stability towards airborne contaminants, optimised heat and mass transport and efficient sunlight utilisation.

This selection of the aluminium MOF-303(Al) in the optimised system presented sorption abilities 10 times higher than when the Zr-MOF was previously used. What is more, the

synthesis was done in a much greener way, with use of only water as solvent.¹⁵² In 2018, a larger device with dimensions similar to a microwave was tested in the driest place in USA, the Mojave desert. The authors of the project have shown that even if the relative humidity and temperature were at the level of 10% and 27°C, respectively, the recovery of water was 0.7 L day⁻¹ kg_{MOF}⁻¹.¹⁵² It was initially planned that by the end of 2019 the group would be able to produce a new device with harvesting capacity of 7-10 L day⁻¹ kg⁻¹ of pure drinkable water.

1.2.2.2 Catalysis

Metal-organic frameworks have rapidly gained interest as analogues to zeolites. Their degree of structure flexibility, variety of topologies, pore sizes and supposed stability across a wide range of pH and temperatures makes them superior candidates towards the use in heterogeneous catalysis.¹⁵³ Furthermore, their unique structure may be of bifunctional nature as the unsaturated metal sites and weakly coordinated moieties could function as Lewis and Brønsted acid sites.¹⁵⁴ Their catalytic activity originates from the uncoordinated metal centres and functional groups attached to the linkers of the framework.¹⁵⁵ The use of these structures in catalysis has not yet reached industrial scale due to their complexity, and a lack of fundamental understanding of the structures.

Several studies show that MOFs have a potential in solvent-based catalysis.¹⁵⁶ This is mainly due to the pore sizes and topology of the framework, which can be finely tuned by selecting appropriate linkers and metal nodes. As an example, Bakuru *et al.* presented that isostructural UiO-66 structures (Hf, Zr, and Ce) exhibited varying degree of acidity.¹⁵⁷ The acidity order was found to be Hf>Ce>Zr, in accordance with their oxophilicity order.

However, there are still a lot of challenges and objectives to overcome such as understanding the structure and reactivity relationship, establishing sustainable reaction protocols and validating the materials in scale-up scenarios.¹⁵⁸

1.3 Aims and objective

Water stability of materials used in catalysis and separation processes has clearly become a topic of research interest over the last decade. However, to date, many challenges have still not been completely overcome. One of these is the understanding of hydrolysis and other processes leading to complete structural degradation of the materials. Answering the questions of why some materials are prone to water damage while others not, is one of the scopes of this thesis research. As an example, all zeolites are built of same atoms but the arrangements of those are different in each of the 250 known structures. Building units create different 3-dimensional frameworks of which some are highly resistant to water damage, while others undergo structural failure. Similar observation can be made for the case of MOF structures.

Based on this, the main aim of this thesis is to develop experimental protocols to investigate and further evaluate the stability of chosen zeolite and MOF structures in contact with solvents. Of primary interest is the evaluation of the stability of these materials under real operational conditions *i.e.*, in the presence of a solvent at elevated temperature and pressure, in continuous flow. The thesis starts from testing commercially available materials. Later experiments focus on the solvent stability of synthesised structures, in order to compare the trends generated to those obtained for the commercial ones, whilst gaining greater control over the composition and structure of the materials. In all cases, relative crystallinity and microporosity are the first indicators of internal changes, although complex spectroscopic studies as well as simple methods are also employed to prove and understand the observed structural changes, such as leaching and/or dissolution.

To summarise, the studies that will be covered in this thesis are as follows:

- In Chapter 3, preliminary studies are done focusing only on chosen commercial zeolites (FAU, BEA, MFI, MOR, FER, and LTA framework types) in order to gain understanding on the stability of different structures in water. Continuous flow experiments in a fixed-bed reactor are employed due to ease of sample and effluent evaluation, and to provide realistic mechanistic information. The relation between framework density, decrease in crystallinity and (micro)pore volume of various zeolite frameworks is investigated.
- In Chapter 4, the effect of aluminium loading in the MFI type zeolite on its water stability is investigated. Differences and similarities between own-synthesised and

commercially available samples are covered. High alumina content HZSM-5 samples are also compared to commercial mordenite (MOR) and ferrierite (FER) samples of the same aluminium loading. The degree of desilication is evaluated by MP-AES analysis.

- In Chapter 5, the focus is switched to four chosen MOF structures as analogues to zeolites. All structures (ZIF-8, HKUST-1, MIL53 and UiO-66) are investigated for their thermal and hydrothermal stability. Further, the effect of linker and metal choice in a UiO-66 MOF structure is explored. The effect of solvents such as ethanol, methanol and water on the structure at elevated temperatures (110-160°C) is evaluated. Characterisation techniques, in particular XRD, DRIFTS and ^{13}C CP-MAS NMR, are used to understand hydrolysis processes in the Zr MOF.

1.4 References

- 1 R. E. Fletcher, S. Ling, B. Slater, *Chem. Sci.* 2017, **8**, 7483-7491
- 2 J. Zhang, X. Li, J. Liu, C. Wang, *Catalysts* 2019, **9**, 13
- 3 R. Bialek, W. M. Meier, M. Davis, M. J. Annen, *Zeolites* 1991, **11**, 438-442
- 4 L. A. Villaescusa, P. A. Barrett, M. A. Camblor, *Chem. Commun.* 1998, **21**, 2329-2330
- 5 T. Lu, L. Zhu, X. Wang, W. Yan, W. Shi, R. Xua, *Inorg. Chem. Front.* 2018, **5**, 1640-1645
- 6 T. Zhang, Y. Zuo, M. Liu, C. Song, X. Guo, *ACS Omega* 2016, **1**, 1034-1040
- 7 X. Yang, Y. Liu, X. Li, J. Ren, L. Zhou, T. Lu, Y. Su, *ACS Sus. Chem. Eng.* 2018, **6**, 8256-8265
- 8 D. W. Breck, *Zeolite Molecular Sieves: Structure, Chemistry and Use*, John Wiley & Sons, New York-London-Sydney-Toronto, 1974
- 9 IUPAC *Manual of symbols and terminology for physicochemical quantities and units*, Butterworths, London, 1972
- 10 C. Baerlocher, W. M. Meier, D. H. Olson, *Atlas of Zeolite Framework types*, Elsevier, Oxford, 2007
- 11 W. Schwieger, A. Gonche Machoke, T. Weissenberger, A. Inayat, T. Selvam, M. Klumpp, A. Inayat, *Chem. Soc. Rev.* 2016, **45**, 3353-3376
- 12 G. O. Brunner, W. M. Meier, *Nature* 1989, **337**, 146-147
- 13 M. Moliner, F. Rey, A. Corma, *Angew. Chem.* 2013, **52**, 13880-13889
- 14 A. Corma, M. J. Díaz-Cabañas, F. Rey, S. Nicolopoulos, K. Boulahya, *Chem. Commun.*, 2004, **10**, 1356-1357
- 15 M. Dusselier, M. E. Davis, *Chem. Rev.* 2018, **118**, 5265-5329
- 16 C. Baerlocher, L. McCusker, *Database of Zeolite Structures* [Available from: www.iza-structure.org/databases/]
- 17 R. T. Yang, *Adsorbents: Fundamentals and application*, Wiley Interscience, New Jersey, 2003
- 18 S. De, S. Dutta, B. Saha, *Catal. Sci. Technol.*, 2016, **6**, 7364-7385
- 19 M. Ravi, V. L. Sushkevich, J. A. van Bokhoven, *Nat. Mater.*, 2020, **19**, 1047-1056
- 20 G. S. Lee, Y.-J. Lee, K. B. Yoon, *J. Am. Chem. Soc.* 2001, **123**, 9769-9779
- 21 Z. Yu, A. Zheng, Q. Wang, L. Chen, J. Xu, J. P. Amoureux, F. Deng, *Angew. Chem. Int. Ed.* 2010, **49**, 8657-8661
- 22 S. Li, A. Zheng, Y. Su, H. Fang, W. Shen, Z. Yu, L. Chen, F. Deng, *Phys. Chem. Chem. Phys.* 2010, **12**, 3895-3903
- 23 I. G. Wenten, P. T. Dharmawijaya, P. T. P. Aryanti, R. R. Mukti, Khoiruddin, *RSC Adv.* 2017, **7**, 29520-29539
- 24 M. Fasano, A. Bevilacqua, E. Chiavazzo, T. Humplik, P. Asinari, *Sci Rep.*, 2019, **9**, 18429
- 25 M. A. Uguina, D.P. Serrano, R. V. Grieken, S. Vènes, *Appl. Catal. A* 1993, **99**, 97-113
- 26 A. Devaraj, M. Vijayakumar, J. Bao, M. F. Guo, M. A. Derewinski, Z. Xu, M. J. Gray, S. Prodinger, K. K. Ramasamy, *Sci. Rep.*, 2016, **6**, 37586
- 27 M. Choi, K. Na, J. Kim, Y. Sakamoto, O. Terasaki and R. Ryoo, *Nature* 2009, **461**, 246-249
- 28 E. A. Eilertsen, B. Arstad, S. Svelle and K. P. Lillerud, *Micropor. Mesopor. Mat.* 2012, **153**, 94-99

- 29 A. Corma, M. E. Davis, *Chem. Phys. Chem.* 2004, **5**, 304–313.
- 30 A. Farzaneh, M. Zhou, O. N. Antzutkin, Z. Bacsik, J. Hedlund A. Holmgren, M. Grahn, *Langmuir* 2016, **32**, 11789-11798
- 31 M. S. Nabavi, M. Zhou, J. Mouzon, M. Grahn, J. Hedlund, *Micropor. Mesopor. Mat.* 2019, **278**, 167-174
- 32 F-S. Xiao, X. Meng *Zeolites in Sustainable Chemistry: Synthesis, Characterization and Catalytic Applications*, Springer 2015
- 33 C. T. O'Connor, K. P. Möller, H. Manstein, *CATTECH* 2001, **5**, 172–182
- 34 Z. Wu, C. Zhang, L. Peng, X. Wang, Q. Kong, X. Gu, *ASC Appl. Mater. Interfaces* 2018, **10**, 3175-3180
- 35 T. Custódio dos Santos, S. Bourrelly, P. L. Llewellyn, J. Walkimar de M. Carneiro, C. Machado Ronconi, *Phys. Chem. Chem. Phys.* 2015, **17**, 11095-11102
- 36 P. A. Zapata, J. Faria, M. P. Ruiz, R. E. Jentoft, D. E. Resasco, *J. Am. Chem. Soc.* 2012, **134**, 8570-8578
- 37 R. E. Morris, J. Cejka, P. Nachtigall, *Zeolites in Catalysis: Properties and Applications*, Royal Society of Chemistry, 2017
- 38 K. Araki, H. Sakai, *IOP Conf. Series: Materials Science and Engineering* 2011, **18**, 012001
- 39 J. D. Rimer, M. Kumar, R. Li, A. I. Lupulescu, M. D. Oleksiak, *Catal. Sci. Technol.* 2014, **4**, 3762–3771
- 40 S. Biswas, A. Pal, T. Pal, *RSC Adv.*, 2020, **10**, 35449-35472
- 41 J. G. Speight, *The Refinery of the Future*, Elsevier, 2010
- 42 J. H. Gary, G. E. Handwerk, M. J. Kaiser, *Petroleum Refining: Technology and Economics*, Fifth Edition, CRC Press, 2007
- 43 T. Ennaert, J. Geboers, E. Gobechiya, C. M. Courtin, M. Kurttepel, K. Houthoofd, C. E.A. Kirschhock, P. C. M. M. Magusin, S. Bals, P. A. Jacobs, B. F. Sels, *ASC Catal.*, 2015, **5**, 754-768
- 44 T. Welton, *Proc. R. Soc. A* 2015, **471**, 20150502
- 45 L. Yang, F. Xu, X. Ge, Y. Li, *Renew. Sustain. Energy Rev.* 2015, **44**, 824–834
- 46 C. Perego, A. Bosetti, *Micropor. Mesopor. Mat.* 2011, **144**, 28-39
- 47 A. T. Aguayo, A. G. Gayubo, A. Atutxa, M. Olazar, J. Bilbao, *Ind. Eng. Chem. Res.* 2002, **41**, 4216-4224
- 48 A. Kruse, N. Dahmen, *J. Supercrit. Fluids* 2015, **96**, 36-45
- 49 M. Moliner, Y. Román-Leshkov, M. E. Davis, *PNAS* 2010, **107**, 6164–6168
- 50 A. Huang, N. Wang and J. Caro, *Micropor. Mesopor. Mat.* 2012, **164**, 294-301
- 51 T. C. Bowen, R. D. Noble, J. L. Falconer, *J. Membr. Sci.* 2004, **245**, 1-33
- 52 M. Mulder, *Basic Principle of Membrane Technology*, Kluwer Academic Publisher, Netherlands, 1996.
- 53 N. Wynn, *Chemical Engineering Progress*, 2001, **97**, 66–72
- 54 T. Gallego-Lizon, E. Edwards, G. Lobiundo, L. Freitas dos Santos, *J. Membr. Sci.* 2002, **197**, 309–319
- 55 Mitsubishi Chemical Co. (Japan), *Alumina Fiber / Inorganic Products*. Retrieved from <https://www.m-chemical.co.jp>
- 56 Hitachi Zosen Co. (Japan), *Hitz Dehydration System HDS® by Zeolite Membrane Element*. Retrieved from <https://www.hitachizosen.co.jp>
- 57 Mitsui Engineering & Shipbuilding Co. (Japan), *Zeolite Membrane (*PV / VP Separation)*. Retrieved from <https://www.mes.co.jp>
- 58 Jiangsu Nine-Heaven Co. (China), *Molecular sieve membrane technology*. Retrieved from <https://www.en-cphi.cn/company-HEAVEN>

- 59 PERVATECH BV (Netherlands), *Zeolite NaA Membranes 2017*. Retrieved from <http://pervaporation-membranes.com>
- 60 Fraunhofer IKTS (Germany), *NaA Zeolite membranes for vapour permeation*. Retrieved from <https://www.ikts.fraunhofer.de>
- 61 M. Aizawa, S. Fujita, Y. Takaki, K. Yano, T. Shimizu, Y. Asari, J. Yano, K. Shinoya, *Development of Hitz zeolite membrane dehydration system for bio-Ethanol production*; AIChE annual meeting; Salt Lake City, UT, 2010
- 62 Y. Li, H. Zhou, G. Zhu, J. Liu, W. Yang, *J. Membr. Sci.* 2007, **297**, 10-15
- 63 WHO, *Guidelines for drinking-water quality*, 4th edition, 2011
- 64 Q. Wang, N. Li, B. Bolto, M. Hoang, Z. Xie, *Desalination*, 2016, **387**, 46-60
- 65 N. Jusoh, Y. F. Yeong, T. L. Chew, K. K. Lau, A. M. Shariff, *Sep. Purif. Rev.*, 2016, **45**, 321-344
- 66 G. Dong, H. Li, V. Chen, *J. Mater. Chem. A*, 2013, **1**, 4610-4630
- 67 B.-H. Jeong, E. M.V. Hoek, Y. Yan, A. Subramani, X. Huang, G. Hurwitz, A. K. Ghosh, A. Jawor, *J. Membr. Sci.* 2007, **294**, 1-7
- 68 M. L. Lind, A. K. Ghosh, A. Jawor, X. Huang, W. Hou, Y. Yang, E. M. V. Hoek, *Langmuir* 2009, **25**, 10139-10145
- 69 QuantumFlux (Qfx) *Seawater Reverse Osmosis (RO) Element Qfx SW 400 R* product datasheet. Retrieved from <https://www.lenntech.com>
- 70 M. C. Duke, J. O'Brien-Abraham, N. Milne, B. Zhu, J. Y. Lin, J. C. D. da Costa, *Sep. Purif.* 2009, **68**, 343-350
- 71 B. Zhu, J. H. Kim, Y. H. Na, I. S. Moon, G. Connor, S. Maeda, G. Morris, S. Gray, M. Duke, *Membranes* 2013, **3**, 155-168.
- 72 C. Zhou, J. Zhou, A. Huang, *Micropor. Mesopor. Mat.* 2016, **234**, 377-383
- 73 C. H. Cho, K. Y. Oh, S. K. Kim, J. G. Yeo, P. Sharma, *Int. J. Mol. Sci.* 2011, **371**, 226-238
- 74 M. Drobek, C. Yacou, J. Motuzas, A. Julbe, L. Ding, J. C. D. da Costa, *Int. J. Mol. Sci.* 2012, **415-416**, 816-823.
- 75 X. Zou, G. Zhu, *Microporous Materials for Separation Membranes*, Wiley-VCH Verlag GmbH & Co. KGaA, Weinheim, Germany, 2019
- 76 NGK, Insulators ltd. (Japan), *NGK's Large Ceramic Membrane to Be Used in Demonstration Test for CO₂ Recovery from Associated Gas during Oil Production*. Retrieved from <https://www.ngk-insulators.com>
- 77 J. Okazaki, H. Hasegawa, N. Chikamatsu, K. Yajima, K. Shimizu, M. Niino, *Sep. Purif.* 2019, **218**, 200-205
- 78 S. Himeno, T. Tomita, K. Suzuki, K. Nakayama, K. Yajima, S. Yoshida, *Ind. Eng. Chem. Res.* 2007, **46**, 6989-6997
- 79 N. Rangnekar, N. Mittal, B. Elyassi, J. Caro, M. Tsapatsis, *Chem. Soc. Rev.* 2015, **44**, 7128-7154
- 80 C. Hammond, *Green Chem.*, 2017, **19**, 2711-2728
- 81 E. F. Iliopoulou K. S. Triantafyllidis A. A. Lappas, *WIREs Energy Environ*, 2018, **8**, 8:e322
- 82 D. Padovan, C. Parsons, M. Simplicio Grasina, C. Hammond, *Green Chem.*, 2016, **18**, 5041-5049
- 83 D. Padovan, S. Tolborg, L. Botti, E. Taarning, I. Sadaba, C. Hammond, *React. Chem. Eng.*, 2018, **3**, 155-163
- 84 M. D. Argyle, C. H. Bartholomew, *Catalysts*, 2015, **5**, 145-269
- 85 J. Britton, C. L. Raston, *Chem. Soc. Rev.*, 2017, **46**, 1250-1271

- 86 J. C. Groen, L. A. A. Peffer, J. A. Moulijn, J. Pérez-Ramírez, *Micropor. Mesopor. Mat.*, 2004, **69**, 29-34
- 87 D. Verboekend, J. Pérez-Ramírez, *ChemSusChem*, 2014, **7**, 753-764
- 88 C. H. Bartholomew, *Appl. Catal., A*, 2001, **212**, 17-60
- 89 P. A. Zapata, J. Faria, M. P. Ruiz, R. E. Jentoft, D. E. Resasco, *J. Am. Chem. Soc.*, 2012, **134**, 8570-8578
- 90 I. Sadaba, M. L. Granados, A. Riisager, E. Taarning, *Green Chem.*, 2015, **17**, 4133-4145
- 91 J. A. Moulijn, A.E. van Diepen, F. Kapteijn, *Appl. Catal., A: Gen.*, 2001, **212**, 3-16
- 92 C. J. Heard, L. Grajciar, F. Uhlík, M. Shamzhy, M. Opanasenko, J. Čejka, P. Nachtigall, *Adv. Mater.*, 2020, **32**, 2003264
- 93 R. Zhang, S. Xu, D. Raja, N. B. Khusni, J. Liu, J. Zhang, S. Abdulridha, H. Xiang, S. Jiang, Y. Guan, Y. Jiao, X. Fan, *Micropor. Mesopor. Mat.*, 2019, **278**, 297-306
- 94 R. M. Ravenelle, F. Schüßler, A. D'Amico, N. Danilina, J. A. van Bokhoven, J. A. Lercher, C. W. Jones, C. Sievers, *J. Phys. Chem. C*, 2014, **114**, 19582-19595
- 95 S. M. Maier, A. Jentys, J. A. Lercher, *J. Phys. Chem. C* 2011, **115**, 8005-8013
- 96 R. L. Hartman, H. S. Fogler, *Langmuir*, 2007, **23**, 5477-5484
- 97 A. Vjunov, J. L. Fulton, D. M. Camaioni, J. Z. Hu, S. D. Burton, I. Arslan, J. A. Lercher, *Chem. Mater.*, 2015, **27**, 3533-3545
- 98 L. Zhang, K. Chen, B. Chen, J. L. White, D. E. Resasco, *J. Am. Chem. Soc.* 2015, **137**, 11810-11819
- 99 A. K. Jamil, O. Muraza, R. Osuga E. N. Shafei, K-H. Choi, Z. H. Yamani, A. Somali, T. Yokoi, *J. Phys. Chem. C* 2016, **120**, 22918-22926
- 100 K. Zhang, R. P. Lively, J. D. Noel, M. E. Dose, B. A. McCool, R. R. Chance, W. J. Koros, *Langmuir* 2012, **28**, 8664-8673
- 101 B. Hunger, S. Matysik, M. Heuchel, W.-D. Einicke, *Langmuir* 1997, **13**, 6249-6254
- 102 Y. Tang, D. Dubbeldam, S. Tanase, *ACS Appl Mater Interfaces*, 2019, **11**, 41383-41393
- 103 S. Prodinge, M. A. Derewinski, *Pet. Chem.*, 2020, **60**, 420-436
- 104 Y. Cao, X. Mi, X. Li, B. Wang, *Front Chem.*, 2021, **9**, 673738
- 105 N. Aljammal, C. Jabbour, S. Chaemchuen, T. Juzsakova, F. Verpoort, *Catalysts* 2019, **9**, 512
- 106 B. F. Hoskins, R. Robson, *J. Am. Chem. Soc.*, 1989, **111**, 5962-5964
- 107 O. M. Yaghi, G. Li, H. Li, *Nature* 1995, **378**, 703-706
- 108 S. Wang, X. Xie, W. Xia, J. Cui, S. Zhang, X. Du, *High Temp. Mater. Proc.*, 2020, **39**, 171-177
- 109 V. V. Butova, M. A. Soldatov, A. A. Guda, K. A. Lomachenko, C. Lamberti, *Russ. Chem. Rev.* 2016, **85**, 280-307.
- 110 S. J. Lyle, R. W. Flaig, K. E. Cordova, O. M. Yaghi, *J. Chem. Educ.* 2018, **95**, 1512-1519
- 111 M. O'Keeffe, M. A. Peskov, S. J. Ramsden, O. M. Yaghi, *Acc. Chem. Res.* 2008, **41**, 1782-1789
- 112 S. Wiggin (2020). Classifying metal-organic frameworks MOFs for search and screening. Retrieved from <https://www.ccdc.cam.ac.uk/Community/blog/MOF-classification-search-screen>
- 113 M. J. Kalmutzki, N. Hanikel, O. M. Yaghi, *Science Advances* 2018, **4**, eaat9180
- 114 M. Ding, X. Cai, H-L. Jiang, *Chem. Sci.*, 2019, **10**, 10209-10230
- 115 R. Ricco, C. Pfeiffer, K. Sumida, C. J. Sumby, P. Falcaro, S. Furukawa, N. R. Champness, C. J. Doonan, *CrystEngComm*, 2016, **18**, 6532-6542

- 116** H. Yu, M. Fan, Q. Liu, Z. Su, X. Li, Q. Pan, X. Hu, *Inorg. Chem.*, 2020, **59**, 2005-2010
- 117** B. Liu, K. Vikrant, K-H. Kim, V. Kumar, S. K. Kailasa, *Environ. Sci.: Nano*, 2020, **7**, 1319-1347
- 118** M. Feng, P. Zhang, H-C. Zhou, V. K. Sharma, *Chemosphere*, 2018, **209**, 783-800
- 119** N. C. Burtch, H. Jasuja, K. S. Walton, *Chem. Rev.* 2014, **114**, 10575-10612
- 120** R. Banerjee, A. Phan, B. Wang, C. Knobler, H. Furukawa, M. O'Keeffe, O. M. Yaghi, *Science* 2008, **319**, 939-943
- 121** C. Gao, S. Liu, L. Xie, C. Sun, J. Cao, Y. Ren, D. Fenga, Z. Sua, *CrystEngComm*, 2009, **11**, 177-182
- 122** K. Fujie, K. Otsubo, R. Ikeda, T. Yamada, H. Kitagawa, *Chem. Sci.* 2015, **6**, 4306-4310
- 123** E. E. Sann, Y. Pan, Z. Gao, S. Zhan, F. Xia, *Separation and Purification Technology*, 2018, **206**, 186-191
- 124** M. Bergaoui, M. Khalfaoui, A. Awadallah-F, S. A. Al-Muhtaseb, *Journal of Natural Gas Science and Engineering*, 2021, **96**, 104289
- 125** K. S. Park, Z. Ni, A. P. Côté, J. Y. Choi, R. Huang, F. J. Uribe-Romo, H. K. Chae, M. O'Keeffe, O. M. Yaghi, *PNAS* 2016, **103**, 10186-10191
- 126** J. J. Low, A. I. Benin, P. Jakubczak, J. F. Abrahamian, S. A. Faheem, R. R. Willis, *J. Am. Chem. Soc.*, 2009, **131**, 15834-15842
- 127** S. Bhattacharyya, S. H. Pang, M. R. Dutzer, R. P. Lively, K. S. Walton, D. S. Sholl, S. Nair, *J. Phys. Chem. C* 2016, **120**, 27221– 27229
- 128** H. Zhang, M. Zhao, Y. Yang, Y. S. Lin, *Micropor. Mesopor. Mat.* 2019, **288**, 109568
- 129** F. Millange, R. I. Walton, *Isr. J. Chem.* 2018, **58**, 1019-1035
- 130** H. T. Nguyen, L. H. T. Nguyen, T. L. H. Doan, P. H. Tran, *RSC Adv.* 2019, **9**, 9093-9098
- 131** T. Loiseau, C. Serre, C. Huguenard, G. Fink, F. Taulelle, M. Henry, T. Bataille, G. Ferey, *Chem. Eur. J.*, 2004, **10**, 1373-1382
- 132** M. Amirilargani, R. B. Merlet, P. Hedayati, A. Nijmeijer, L. Winnubst, L. C. P. M. de Smet, E. J. R. Sudhölter, *Chem. Commun.* 2019, **55**, 4119-4122
- 133** I. Bezverkhyy, G. Ortiz, G. Chaplais, C. Marichal, G. Weber, J-P. Bellat, *Micropor. Mesopor. Mat.* 2014, **183**, 156-161
- 134** S. S.-Y. Chui, S. M.-F. Lo, J. P. H. Charmant, A. G. Orpen, I. D. Williams, *Science*, 1999, **283**, 1148-1150
- 135** P. Küsgens, M. Rose, I. Senkovska, H. Fröde, A. Henschel, S. Siegle, S. Kaskel, *Micropor. Mesopor. Mat.* 2009, **120**, 325-330
- 136** P. M. Schoenecker, C. G. Carson, H. Jasuja, C. J. J. Flemming, K. S. Walton, *Ind. Eng. Chem. Res.* 2012, **51**, 6513-6519
- 137** J. M. Castillo, T. J. H. Vlugt, S. Calero, *J. Phys. Chem. C* 2008, **112**, 15934-15939
- 138** <https://www.chemtube3d.com>
- 139** G. Majano, O. Martin, M. Hammes, S. Smeets, C. Baerlocher, J. Pérez-Ramírez, *Adv. Funct. Mater.* 2014, **24**, 3855–3865
- 140** J. L. C. Rowsell, O. M. Yaghi, *J. Am. Chem. Soc.*, 2006, 128, 1304.
- 141** N. Al-Janabi, V. Martis, N. Servi, F. R. Siperstein, X. Fan, *Chem. Eng. J.* 2018, **333**, 594-602
- 142** S. Waitschat, D. Fröhlich, H. Reinsch, H. Terraschke, K. A. Lomachenko, C. Lamberti, H. Kummer, T. Helling, M. Baumgartner, S. Henninger, N. Stock, *Dalton Trans.* 2018, **47**, 1062-1070

- 143** C. A. Trickett, K. J. Gagnon, S. Lee, F. Gandara, H-B. Birgi, O. M. Yaghi, *Angew. Chem. Int. Ed.* 2015, **54**, 11162–11167
- 144** H. Furukawa, F. Gandara, Y-B. Zhang, J. Jiang, W. L. Queen, M. R. Hudson, O. M. Yaghi, *J. Am. Chem. Soc.* 2014, **136**, 4369–4381
- 145** J. B. DeCoste, G. W. Peterson, H. Jasuja, T. G. Glover, Y-G Huang, K. S. Walton, *J. Mater. Chem. A* 2013, **1**, 5642-5650
- 146** C. Caratelli, J. Hajek, S. M. J. Rogge, S. Vandenbrande, E. J. Meijer, M. Waroquier, V. Van Speybroeck, *Chem. Psych. Chem.* 2018, **19**, 420-429
- 147** J. Marreiros, C. Caratelli, J. Hajek, A. Krajnc, G. Fleury, B. Bueken, D. E. De Vos, G. Mali, M. B. J. Roeffaers, V. Van Speybroeck, R. Ameloot, *Chem. Mater.* 2019, **31**, 1359-1369
- 148** G. C. Shearer, S. Chavan, J. Ethiraj, J. G. Vitillo, S. Svelle, U. Olsbye, C. Lamberti, S. Bordiga, K. P. Lillerud, *Chem. Mater.* 2014, **26**, 4068–4071
- 149** H. Amer Hamzah, W. J. Gee, P. R. Raithby, S. J. Teat, M. F. Mahon, A. D. Burrows *Chem. Eur.J.* 2018, **24**, 11094 –11102
- 150** H. Kim, S. Yang, S. R. Rao, S. Narayanan, E. A. Kapustin, H. Furukawa, A. S. Umans, O. M. Yaghi, E. N. Wang, *Science* 2017, **356**, 430-434
- 151** N. Hanikel, M. S. Prevot, O. M. Yaghi, *Nat. Nanotechnol.* 2020, **15**, 348–355
- 152** N. Hanikel, M. S. Prevot, F. Fathieh, E. A. Kapustin, H. Lyu, H. Wang, N. J. Diercks, T. G. Glover, O. M. Yaghi, *ASC Cent. Sci.* 2019, **5**, 1699–1706
- 153** V. Pascanu, G. G. Miera, A. K. Inge, B. Martín-Matute, *J. Am. Chem. Soc.* 2019, **141**, 7223–7234
- 154** Y. Qin, J. Guo, M. Zhao, *Trans. Tianjin Univ.*, 2021, **27**, 434–449
- 155** M. L. Hu, V. Safarifard, E. Doustkhah, S. Rostamnia, A. Morsali, N. Nouruzi, S. Beheshti, K. Akhbari, *Micropor. Mesopor. Mat.*, 2018, **256**, 111–127
- 156** Q. Wang, D. Astruc, *Chem. Rev.*, 2020, **120**, 1438–1511
- 157** V. R. Bakuru, S. R. Churipard, S. P. Maradur, S. B. Kalidindi, *Dalton Trans.*, 2019, **48**, 843-847
- 158** H. Konnerth, B. M. Matsagar, S. S. Chen, M. H.G. Prechtel, F. K. Shieh, K. C. W. Wu, *Coord. Chem. Rev.*, 2020, **416**, 213319

2 Experimental and characterisation techniques

2.1 List of reagents

The following reagents listed were used in this project. All reagents were used as received, without further purification, unless otherwise stated:

- Ethanol (Absolute, Sigma Aldrich)
- N,N-Dimethylformamide, DMF (99%, Alfa Aesar)
- Methanol ($\geq 99.5\%$, Fisher Scientific)
- Zeolite ZSM-5 ($\text{SiO}_2/\text{Al}_2\text{O}_3 = 23, 30, 50, 80, 280$, Zeolyst)
- Zeolite Beta ($\text{SiO}_2/\text{Al}_2\text{O}_3 = 25, 38, 300$, Zeolyst)
- Zeolite Y ($\text{SiO}_2/\text{Al}_2\text{O}_3 = 5.1, 30, 80$, Zeolyst)
- Mordenite ($\text{SiO}_2/\text{Al}_2\text{O}_3 = 20$, Zeolyst)
- Ferrierite ($\text{SiO}_2/\text{Al}_2\text{O}_3 = 20$, Zeolyst)
- Zeolite A (Linde type A, BCR-705, $\text{SiO}_2/\text{Al}_2\text{O}_3 = 2$)
- Basolite[®] Z1200 (Sigma-Aldrich)
- Basolite[®] C300 (Sigma-Aldrich)
- Basolite[®] A100 (Sigma-Aldrich)
- Tetraethyl orthosilicate, TEOS ($\geq 99.0\%$ GC, Sigma-Aldrich)
- Tetrapropylammonium hydroxide, TPAOH (1 M in H_2O , Sigma Aldrich)
- Sodium aluminate, NaAlO_2 (Technical, anhydrous, Sigma Aldrich)
- Zirconium chloride, ZrCl_4 ($\geq 99.5\%$, Sigma Aldrich)
- Hafnium chloride, HfCl_4 (98%, Sigma Aldrich)
- Acetic acid (glacial), AA ($\geq 99.99\%$ trace metals basis, Sigma Aldrich)
- Potassium nitrate, KNO_3 ($> 99\%$, Sigma Aldrich)
- Sodium nitrate, NaNO_3 ($> 97\%$, Sigma Aldrich)
- Ammonium nitrate, NH_4NO_3 ($\geq 98\%$, Honeywell Fluka)
- Zinc nitratehexahydrate, $\text{Zn}(\text{NO}_3)_2 \cdot 6\text{H}_2\text{O}$ (98%, Arcos Organics)
- 2-Methylimidazole, HMIM (99%, Sigma Aldrich)
- Terephthalic acid, H_2BDC (98%, Sigma Aldrich)
- 2-Aminoterephthalic acid, NH_2BDC (99%, Sigma Aldrich)
- Aluminium, Reference Standard Solution (1000 ppm $\pm 1\%$, Fisher Scientific)

- Silicon, Reference Standard Solution (1000 ppm \pm 1%, Fisher Scientific)
- Ammonia (10% NH₃ in Ar, BOC gases)

2.2 Synthesis procedures

2.2.1 Zeolite synthesis

2.2.1.1 One-pot synthesis of Silicalite-1

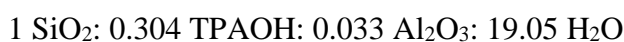
The synthesis of Silicalite-1 was done as follows;¹ TEOS (10.24 g, 49.4 mmol) was added dropwise to TPAOH (15 g, 1 M in H₂O, 15.0 mmol). The resulting solution was left stirring and homogenised for 1 h at room temperature, prior to addition of H₂O (5 mL, 278 mmol; total H₂O: 941 mmol). The solution was then left stirring at room temperature, the final homogeneous clear gel had the following composition:



The resulting gel was homogenised for 3 h and crystallised (72 h at 175°C) in a Teflon-lined stainless steel Parr autoclave. The as-synthesised material was later recovered by centrifugation (4300 rpm, 5 min), washed with deionised water at least 3 times and dried in a benchtop oven (at 110°C, 16 h, static air).

2.2.1.2 One-pot synthesis of HZSM-5

The preparation of HZSM-5 (MFI type) of SiO₂/Al₂O₃ molar ratio equal 30 was done as follows;¹ TEOS (10.24 g, 49.4 mmol) was added dropwise to TPAOH (15 g, 1 M in H₂O, 15.0 mmol). The resulting solution was left stirring and homogenised for 1 h at room temperature prior to addition of NaAlO₂ (0.291 g, 1.63 mmol of Al₂O₃) dissolved in H₂O (5 mL, 278 mmol; total H₂O: 941 mmol). The solution was then left stirring at room temperature, the final homogeneous clear gel had the following composition:



The resulting gel was homogenised for 3 h and crystallised (72 h at 175°C) in a Teflon-lined stainless steel Parr autoclave. The as-synthesised material was later recovered by centrifugation (4300 rpm, 5 min), washed with deionised water at least 3 times and dried in a benchtop oven (at 110°C, 16 h, static air).

For all other HZSM-5 samples used in this study, the amount of added NaAlO₂ was recalculated in accordance with a desired SiO₂/Al₂O₃ molar ratio (80-300).

2.2.2 MOF synthesis

2.2.2.1 UiO-66(Zr)-X (X = H, NH₂)

The method was adapted and modified from a published paper by Ma *et al.* as follows:² In a round bottom flask, Acetic Acid (2.223 mL, 38.87 mmol) was added to DMF (20 mL, 258.3 mmol) at room temperature under stirring. To the solution, ZrCl₄ (0.1776 g, 0.762 mmol) and the linker was added as follows:

- 0.1266 g of H₂BDC (0.762 mmol) for UiO-66(Zr)-H;
- 0.1380 g of NH₂BDC (0.762 mmol) for UiO-66(Zr)-NH₂;

The solution was aged for 10 min stirring in room temperature prior to transferral into a Teflon lined stainless steel Parr autoclave. The final homogeneous clear gel had the following composition:

1 ZrCl₄: 1 H₂BDC/NH₂BDC: 51 Acetic Acid: 339 DMF

The autoclave was then heated up to 120°C for a desired time (24-48 h). The as-synthesised material was later recovered by centrifugation (4300 rpm, 15 min), washed with ethanol at least 3 times and dried in air overnight (at 110°C, 16 h, static air). To completely remove the solvent residue trapped in the pores of UiO-66(Zr) the powder was dried under vacuum (at 110°C, 6 h).

2.2.2.2 UiO-66(Hf)-H

The method was similar as described in Section 2.2.2.1, with only one difference. Instead of ZrCl₄, HfCl₄ was used, as follows:

- 0.1266 g of H₂BDC (0.762 mmol);
- 0.2441 g of HfCl₄ (0.762 mmol);

The solution was aged for 10 min stirring at room temperature prior to transferral into a Teflon lined stainless steel Parr autoclave. The final homogeneous clear gel had the following composition:

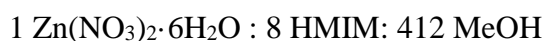
1 HfCl₄: 1 H₂BDC: 51 Acetic Acid: 339 DMF

The autoclave was then heated up to 120°C for a desired time (24-48 h). The as-synthesised material was later recovered by centrifugation (4300 rpm, 15 min), washed with ethanol at

least 3 times and dried in air overnight (110°C, 16 h, static air). To completely remove the solvent residue trapped in the pores of UiO-66(Hf)-H the powder was dried under vacuum (110°C, 6 h).

2.2.2.3 ZIF-8

Two separate solutions were prepared. In the first round bottom flask $\text{Zn}(\text{NO}_3)_2 \cdot 6\text{H}_2\text{O}$ (0.89 g, 3 mmol) was dissolved in methanol (30 mL, 742 mmol). The second solution, in a round bottom flask HMIM (1.97 g, 24 mmol) was dissolved in methanol (20 mL, 494 mmol). The solutions were mixed with stirring at room temperature. The final homogeneous clear gel had the following composition:



The solution was left stirring for another 24 h and the resulting white precipitate was collected by centrifugation (4300 rpm, 15 min), washed 3 times with methanol and dried in a benchtop oven (at 110°C, 16 h, static air).

2.3 Zeolite post-synthesis procedures

2.3.1 Organic template removal

The as-synthesised zeolite sample was grounded in a mortar, transferred into a ceramic calcination boat and placed into a quartz tube inside a high temperature combustion furnace. The tube was then sealed on both sides and the furnace was heated up to 550°C, at a heating rate of 1°C min⁻¹. The sample was held for 3 h in flowing air (80 mL min⁻¹) to allow the organic template to be removed. The sample was left to cool down to room temperature prior to use.

2.3.2 Protonation of as-synthesised materials

Following the template removal, the one-pot synthesised zeolites were converted to the NH_4^+ form by ion exchange with an aqueous solution of NH_4NO_3 (1 M) as follows;

Per 1 g of zeolite, 30 mL of the 1 M solution was added in a round bottom flask. The flask was heated up to 100°C and left for 6 h under reflux. After this time, the flask was cooled

down and the zeolite was then filtered and dried in a benchtop oven (110°C, 16 h, static air). The procedure has been repeated 3 times. Following this procedure, the ion exchanged powder was placed on a ceramic calcination boat in a combustion furnace. Heated up to 550°C, at heating rate of 10°C min⁻¹ in static air. The sample was held at 550°C for 3 h and later left to cool down to room temperature prior to use.

A one-pot laboratory synthesised MFI type ZSM-5 zeolite sample after activation, possessing a SiO₂/Al₂O₃ molar ratio of 30, was denoted as HZSM-5 (30) HT.

2.3.3 Protonation of commercial zeolites

Commercial (NH₄⁺ form) and the one-pot synthesised zeolite samples were activated prior to use. The activation led to a conversion into their acid form (H⁺). The procedure, given for NH₄-ZSM-5 (280) and any other NH₄⁺ zeolite, was as follows;

The NH₄-ZSM-5 (SiO₂/Al₂O₃ = 280) was transferred to a ceramic calcination boat and placed inside a high temperature combustion furnace. The furnace was heated up to 550°C, heating rate of 10°C min⁻¹. The sample was held for 3 h in static air at the desired temperature (550°C) and allowed to cool down to room temperature prior to use.

A commercial zeolite sample, *e.g.*, commercial BEA type zeolite β sample after activation, possessing a SiO₂/Al₂O₃ molar ratio of 25, was denoted as Hβ (25) C.

2.3.4 Alkali ion-exchange of commercial materials

For some tests zeolites of H⁺ form have been further converted to Na, K or other cation forms by ion exchange with aqueous solutions of chosen nitrate *e.g.*, NaNO₃ (1 M) as follows;

For every 1 g of zeolite 30 mL of the solution (1 M NaNO₃) was added in a round bottom flask. The flask was then heated up to 85°C for 6 h under reflux.³ The flask was then cooled and the zeolite filtered and dried in a benchtop oven (at 110°C, 16 h, static air). The procedure was repeated 3 times. Following this procedure, the ion-exchanged powder was placed on a combustion boat in a combustion furnace. The furnace was heated up to 550°C, at heating rate of 10°C min⁻¹. The sample was held for 3 h in the desired temperature (550°C) in static air.

2.4 Relative values determination

2.4.1 Relative crystallinity determination

The relative crystallinity (X_{rel}) was determined by comparing the Integrated Peak Area (Table 2.1) from the pXRD diffraction pattern of the treated (X_{tr}) and untreated sample, where the untreated (X_{untr}) samples were denoted as 100% crystalline, as described by the equation:

$$X_{rel} = \frac{X_{tr}}{X_{untr}} \times 100\%$$

In general, the relative (%) crystallinity is equal to the sum of areas of characteristic peaks (Table 2.1) of the treated sample to the sum of areas of characteristic peaks of the parent reference sample, multiplied by 100%.

Table 2.1 Peak areas taken to determine the relative crystallinity

Zeolite structure	MOR	FER	FAU	BEA	MFI	LTA
Peak area	18.5°-29.5°	21.5°-27.5°	18.0°-28.5°	21.0°-24.0°	21.5°-25.0°	10.0°-35.0°

Preferred orientation and textures are the most common cause of intensity variations in pXRD powder analysis. Therefore, the peak intensity is very sensitive to the sample preparation method. Each sample for analysis was prepared on the same sample holder and was analysed 5 times in order to guarantee that the relative crystallinity is calculated with high accuracy. It was observed that the middle range of the diffraction pattern was most comparable between runs. It was decided that for the purpose of the relative crystallinity determination the low angle peaks would be omitted. Relative crystallinity error bars represented the standard deviation of the Integrated Peak Area after 5 samples examination.

2.4.2 Relative microporosity determination

Micropore volumes (V_{mc} , pores of a diameter $<2\text{nm}$) were derived using the simulation methods provided by the Quantachrome Instruments software. The calculation was done by

the non-local density functional theory (NLDFT) of N₂ - silica equilibrium transition kernel at 77 K based on a cylindrical pore model.

All values were determined in rel. %, where the volume or area of a tested sample was compared to an untreated one. As an example, relative microporosity calculation is given as the micropore volume of tested (V_{mctr}) sample was divided by the value of an untreated (V_{mcuntr}) one and multiplied by 100%, and described by the equation:

$$V_{\text{mc}} = \frac{V_{\text{mctr}}}{V_{\text{mcuntr}}} \times 100\%$$

2.5 Zeolite and MOFs solvothermal testing

2.5.1 Stability tests in continuous flow

The solvent stability tests were carried out in a fixed-bed continuous flow reactor (CFR) in presence of water or another solvent (ethanol, methanol) flow. The setup is presented on Figure 2.1.

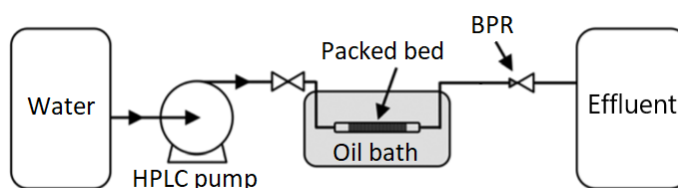


Figure 2.1 Scheme of the reactor used in continuous flow operation

The tests were performed with the use of deionised water and organic solvents such as ethanol and methanol under mild inlet pressure (25-50 bar). The temperature was ranging from room temperature up to 160°C, depending on the test. The inlet solvent flow was set to 0.3 mL min⁻¹ by the means of an HPLC pump.

One of the projects within the research group focused on addition of small amounts of water (1< x <10% w/w) to methanol for glucose to fructose isomerisation at low temperatures (110°C), and the conversion of fructose into methyl lactate at higher temperatures (160°C) over an Sn- β zeolite.⁴ Due to similarities in experiments, it was decided to perform most of the tests at 110°C. However, temperature of 160°C was later also used to test MOF samples for their solvothermal stability.

In the case of zeolites, each powder was pelletised and sieved to retain particles between 63-77 μm in diameter.⁵ Pelletisation and sieving are important in catalysis and in particular when using continuous flow systems, due to minimisation of backmixing and for maintaining a low pressure drop.⁶ The sieved sample (0.2 g) was placed in between two plugs of quartz wool in the fixed-bed CFR. In the case of MOFs, the powders were not pelletised due to probability of structure damage.⁷ The real testing system is presented on Figure 2.2.

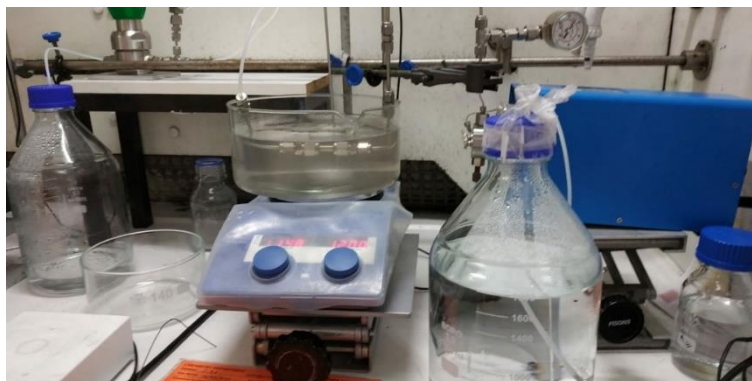


Figure 2.2 Photograph of the real-life testing system in a continuous flow operation. The packed fixed-bed CFR reactor was immersed in an oil bath.

The reactor was built with the use of the 316 Stainless Steel Swagelok[®] tube fittings. The tested material was packed into a ¼” stainless steel tube (35 mm long) and a frit of 0.5 μm was placed at the reactor exit. The prepared stainless-steel reactor was then immersed in an oil bath and the system was heated to a desired temperature. Pressure in the system was controlled by means of a back pressure regulator (BPR). The BPR is commonly used to prevent reagent boiling and allow operations above the boiling point. The BPR was set to 10 bar for tests with water and 20 bar for tests for with ethanol and methanol. The solvent was pumped into the system by the use of a Cole-Parmer Single Head Piston Pump (316 stainless steel fluid path).

2.5.2 Stability tests in round bottom flask

The zeolite hydrothermal (Batch) stability tests were carried out in a round bottom flask of 250 mL capacity. The sieved zeolite sample (0.2 g) was placed in the flask and 250 mL of water was added. The flask was placed in an oil bath, heated until boiling and kept under

reflux up. The flask was left under stirring for 120 h. The samples were recovered by centrifugation and dried in a benchtop oven (110°C, 16 h, static air).

2.6 Materials characterisation techniques

2.6.1 Powder X-Ray diffraction (pXRD)

The powder X-Ray diffraction (pXRD) technique allows the characterisation of bulk structure of solid materials in order to explore their crystal structure, phase composition, phase purity, residual strain, orientation, size and the shape of unit cells. Nearly all of solid materials can be characterised by this method. Every solid crystalline material owns its own unique ordered microscopic structure, called the crystal lattice, which has a unique individual X-ray powder pattern ('fingerprint'). A diffraction pattern is generated when the incident X-rays interacts with the material.

X-rays are generated by bombarding a copper cathode ray tube with accelerated high-energy electrons. Controlling the current and voltage results in the emission of a specific X-Ray wavelength. The monochromatic K_{α} radiation filtered through a nickel plate is collimated to concentrate into a beam and directed towards the sample. The peaks recorded on an experimental diffraction pattern are a visual translation of the atom scattering within a specific plane of an ordered lattice. This is explained by the Bragg's Law:⁸

$$n\lambda = 2d_{hkl} \sin\theta$$

Where: n – order of diffraction (1,2..),

d_{hkl} – spacing between diffracting planes (nm),

θ – incident angle (°),

λ – wavelength of the Cu beam (nm).

In a crystalline material, diffraction occurs for any lattice or direction that satisfies Bragg's law. This occurs when the X-Rays interacts with the atoms in two lattice planes as presented on Figure 2.3.

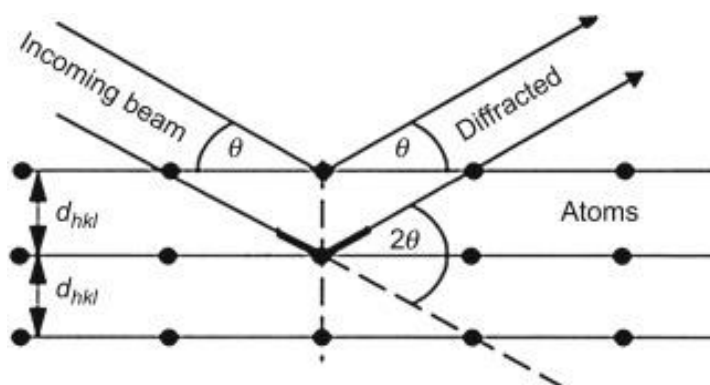


Figure 2.3 A scheme of X-Ray diffraction interacting with the crystal lattice plane according to the Bragg law equation.⁹

The experimental diffraction patterns can be compared with standard reference patterns collected in open databases. In the case of zeolites, such database is provided online by the International Zeolite Association (IZA).¹⁰ Crystallite sizes may be determined knowing the peak width through the Scherrer equation; however, the latter is limited to species with particle sizes of greater than 5 nm. If the particles are too small (< 3 nm), the peak broadening might become so severe that in some cases it would not be even detected.¹¹

The XRD technique is essential to analyse the crystalline structure of solid materials. Here it was used to confirm phase purity of zeolite and MOF samples. This technique was utilised at every step of powder processing, *i.e.*, after synthesis, ion exchange, thermal activation. After running a stability test, the technique was used to confirm undergoing changes in the crystal structure of tested materials.

Powder X-ray diffraction (XRD) patterns were measured with the use of a PANalytical X'PertPRO diffractometer equipped with a CuK α radiation source (40 kV and 40 mA). Diffraction patterns were recorded between 5-60° 2 θ (step size 0.0167°, total time 38 min). All measurements were done under ambient conditions.

2.6.2 Nitrogen physisorption

N₂-physisorption method is a common method used in identification of specific surface area and pore volume of solid materials. The analysis proceeds through the adsorption and desorption of a N₂ monolayer onto and from a solid sample. This process is done at low

partial pressure at -196°C (77 K), which is the boiling point for liquid nitrogen. Determining the surface area can be done by computing the monolayer capacity of a sample.¹²

For nonporous materials, the Brunauer-Emmett-Teller (BET) equation is the most widely used for surface area analysis and it relies on relative pressure (P/P_0) between 0.05 and 0.35.¹³ In this range the BET theory suggests the adsorption isotherm should form a straight line.

$$\frac{1}{V \left(\frac{P_0}{P} - 1 \right)} = \frac{1}{V_m C} + \frac{C - 1}{V_m C} \left(\frac{P}{P_0} \right)$$

Where: P – equilibrium pressure (kPa),

P_0 – saturation pressure (kPa),

V – volume of adsorbed gas (cm^3),

V_m – volume of gas required to create a monolayer (cm^3),

C – constant related to the heat of adsorption.

However, the BET concept is not reliable for calculating surface areas of microporous materials since the second and further layers of nitrogen are already built up prior to the completion of the primary monolayer.¹⁴ In order to provide a more realistic information on adsorption, pore sizes and pore volumes, other methods such as BJH and NLDFT are applied. Although, BJH is a method based on the Kelvin equation it is used to determine porosity (cylindrical pores) and pore size distribution of only mesoporous solids. To determine the pore volume and surface area of a microporous material, a more modern non-local density functional theory (NLDFT) method is used as it is based on complex pore models, such as cylindrical, spherical, slit and other.

Total pore volume (V_t), mesopore volume (V_{ms}), micropore volume (V_{mc}), pore size distribution and specific surface area (S_{DFT}) values were determined with the use of the non-local density functional theory (NLDFT) of the N_2 - silica equilibrium transition kernel at 77 K based on a cylindrical pore model. The measurements were conducted in this study to gain information about the pore volumes, pore size distribution and specific surface area of the tested zeolite and MOF samples before and after solvothermal stability tests.

The N₂-physisorption analysis was performed at -196°C (77 K) on a Quantachrome Autosorb IQ unit. Prior to analysis, zeolite samples were degassed at 300°C (6 h, 10⁻⁶ bar pressure) and MOF samples at 160°C (6 h, 10⁻⁶ bar pressure) to remove all residual water or solvents from internal pores.

2.6.3 Water vapour isotherms

Water vapour adsorption isotherms were determined by vapour physisorption analysis in the circulation bath temperature of 25°C in a Quantachrome Autosorb IQ unit. Prior to analysis, samples were degassed at 300°C (6 h, 10⁻⁶ bar pressure) and MOF samples at 160°C (6 h, 10⁻⁶ bar pressure). Data was collected in order to determine the total adsorption volume which was taken from the topmost data point of the isotherm ($P/P_0 = 0.95$).¹⁵ Isotherms were collected in order to compare the shape of isotherm and the final values of vapour sorption among the analysed samples. By knowing the final values of water sorption capacity hydrophilicity of the samples was determined. This technique was primarily used due to a need of determining the relationship between the aluminium content and/or ion exchange and the water vapour sorption capacity of the tested zeolites.

2.6.4 Thermogravimetric analysis (TGA)

Thermogravimetric Analysis (TGA) determines the weight change (wt. %) of a given sample as a function of temperature. The TGA is equipped with a precise analytical quartz crystal microbalance placed inside a combustion furnace. The decomposition reactions are monitored by the change in the sample weight as the furnace is heated in an inert environment. To achieve that, the combustion crucible is held under a constant flow of an inert gas (nitrogen or argon) in order to remove gaseous decomposition products and to prevent condensation of water vapour on the inner walls of the instrument. The identification of peaks in weight change is performed by the first derivative (derivative thermogravimetry, DTG) of the weight loss curve with respect to temperature. The DTG analysis gives information useful in determination of the *e.g.*, phase changes, dehydration, desorption or degassing processes.¹⁶

TGA was primarily used to monitor the changes in sample weight as the furnace temperature changed and to determine the overall thermal decomposition temperature of the samples.

These changes might include physisorbed effluent evaporation from the sample, linker decomposition, recrystallisation and other mechanisms.

The Thermogravimetric Analysis was performed on a Perkin Elmer TGA 4000 unit. Analysis was done on samples of around 10 mg in the range of room temperature to 800°C at a rate of 10°C min⁻¹ under a constant nitrogen purge (30 mL min⁻¹).

2.6.5 Temperature-Programmed Desorption (TPD)

Ammonia TPD is a measurement of desorption of chemisorbed ammonia (NH₃), as a function of temperature. Samples are pre-treated in order to remove all solvent residue or water vapour from the surface and inner pores. This process is done under inert conditions with the use of a steady gas flow through a glass U-cell and for this application helium is used. Desorption of the chemisorbed NH₃ is measured using a Thermal Conductivity Detector (TCD).

The detector measures changes in the thermal conductivity of the gas stream, where the conductivity is proportional to the molecular gas concentration. The concentration is referenced to a NH₃ calibration curve, which is prepared by injecting known volumes (0.2-0.4 mL) of pure NH₃ directly into the TCD sampling loop and recording the signal (Figure 2.4).

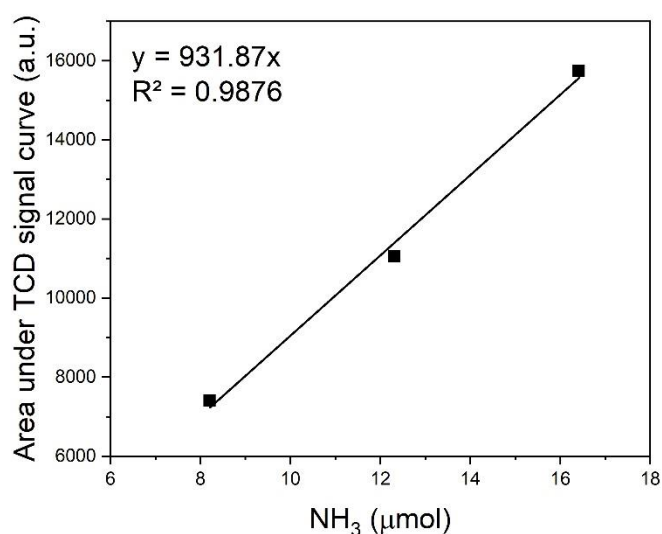


Figure 2.4 TPD calibration curve. Known volumes of NH₃ (0.2-0.4 mL) were injected into the system and the signal was reported. The area values are an average of 4 TCD signals for each injected volume.

The number of moles of NH₃ was calculated from the Ideal Gas Law equation:

$$PV = nRT$$

Where: P – pressure of the gas (Pa),
V – volume of the gas (m³),
n – amount of substance of gas (mol),
R – ideal gas constant equal to 8.315 (J K⁻¹ mol⁻¹),
T – absolute temperature of the gas (K).

The TCD signal plotted versus temperature is used to calculate the volume of total ammonia consumed based on the integrated area from the plot and sample mass. Blank runs are performed for each material to determine the TCD signal resulting from the degradation of the material or loss of compensating anions during heating. The ammonia capacity for each material is calculated by finding the difference in peak area for the NH₃-TPD curve and the blank curve. The temperature and the quantity of gas desorbed provide information on active sites, their strength and possibility of sample regeneration.¹⁷

Ammonia TPD was used in this work in order to probe different MOF structures with ammonia to determine the distribution of weak and strong acid sites. In order to obtain the proper ammonia sorption capacity two different measurements were performed for the same sample. One measurement was done for the sample without chemisorbed ammonia. This was used to subtract the background from the data obtained through analysis with NH₃ saturation. This was specifically needed for the UiO-66(Zr)-NH₂ in order to differentiate the coordinated ammonia from the decomposed MOF structure. The TPD profiles were plotted as TCD signal versus temperature in order to determine the distribution of these acid sites. Quantitative analysis allowed for comparison of the synthesised MOF acidities, which might find use in liquid phase heterogeneous catalysts.

The ammonia desorption analysis was performed on a Quantachrome ChemBET 3000 TPR/TPD/TPO unit. The sample was pre-treated for 120 min at 160°C, heating rate 10°C min⁻¹, in a flow of helium (80 mL min⁻¹). After 20 min of ammonia (10% NH₃ in Ar) saturation the system was heated for 1 h at 100°C, heating rate 10°C min⁻¹, under a helium flow (80 mL min⁻¹) in order to remove the physisorbed ammonia. Chemisorbed ammonia

was desorbed by heating the sample up to 500°C, at a heating rate 10°C min⁻¹, in helium flow (80 mL min⁻¹). Desorbed ammonia was monitored using a thermal conductivity detector (TCD), set to a current of 180 mV, attenuation 1.

TPD calibration curve presented on Figure 2.4 was provided by Takudzwa Bere from Cardiff Catalysis Institute (Cardiff University). The calibration of the Quantachrome ChemBET 3000 was done by Cardiff Catalysis Institute (Cardiff University).

2.6.6 UV-VIS absorption spectroscopy

The Ultraviolet-Visible spectroscopy (UV-VIS) uses light beam in the visible and near ultraviolet range (200-800 nm wavelength range). In this technique, light is partially absorbed by the molecules when the beam passes through the sample. At specific wavelengths, the internal valence electrons of the molecule undergo energy excitation to higher anti-bonding molecular orbitals.¹⁸

In the case of MOFs, the light being absorbed at a particular wavelength is corresponding to the difference of energy between the highest occupied molecular orbital (HOMO) and the LUMO (lowest unoccupied molecular orbital) of the organic linker.¹⁹ The UV-VIS spectrophotometer measures the intensity of the light before and after passing through the sample and compares the difference between them.

The spectra obtained in this work present bands that are of UiO-66 materials. These spectra allow the identification of metal node coordination and absorption edges. It is accepted that a standard UiO-66 shows an absorption edge at 330 nm in the UV region.²⁰

A solid-state UV-VIS spectrophotometer Cary 4000 was used to monitor the changes in absorbance. A UV-VIS changeover wavelength of 260 nm was present. The wavelength range of 200-800 nm was utilised at scan rate of 200 nm min⁻¹. Background scans were taken using a high purity PTFE disc. Prior to analysis, samples were ground to fine powder using an Agate pestle and mortar.

2.6.7 Transform Infrared Spectroscopy (FTIR)

The Fourier Transform Infrared spectroscopy (FTIR) is a technique used to obtain absorption spectra based on the vibrations of the atomic bonds within a molecule. The Fourier transform

is required to convert the obtained raw data into the actual vibrational spectrum. The infrared incident radiation passing through the molecule is absorbed at a particular energy. The molecule is then transitioned to a higher energy vibrational state. The absorbed energy (infrared radiation) corresponds to the frequency vibration of a molecule and a peak in the spectrum appears.²¹

Chemical bonds vibrate in different motions as they absorb energy at varying intensities and frequencies, they stretch, bend, scissor, rock and twist.²² The energy required to change the vibration of a chemical bond is also fixed. This is primarily because the absorption of infrared radiation is a quantised process. A molecule absorbs only specific energy of infrared radiation. During the absorption process only the frequencies of radiation that are equal to the natural vibrational frequencies of the specific molecule are absorbed. However, only the bonds that possess a dipole moment, which changes as a function of time, can absorb the infrared radiation.²³ In organic chemistry, vibrational bands (stretching and bending) are allocated in specific regions of the infrared spectrum and tables describing characteristic IR absorption regions can be found online. This is because each type of bond has a different natural frequency of vibration.

The FTIR technique allows light absorption measurements in a wide range of frequencies (4000-400 cm^{-1}).²⁴ It is a very efficient, non-destructive and cheap method of analysing solids. Moreover, this method is complementary for the NMR technique. This is because both spectroscopy techniques are based on the interaction between electromagnetic energy. FTIR spectroscopy is used to define the presence or absence of functional groups based on their vibration modes at different infrared wave numbers. These can be easily monitored by analysing the position and intensity of the different infrared absorption bands. Also, can be used to quantitatively determine concentrations of organic molecules within a sample. Whereas NMR spectroscopy is used to identify the chemical structure, its content and purity.²⁵ The technique is much more complex and is used to determine the type and number of *e.g.*, carbon atoms in a molecule. In the case of inorganic solids, this technique is used to determine the coordination and type of bonding in materials.

There are various sampling techniques used in conjunction with FTIR such as Diffuse Reflectance Infrared Fourier Transform Spectroscopy (DRIFTS) and the Attenuated Total Reflection (ATR). Both are used for fine bulk powders without any special preparation or pre-treatment.

DRIFTS uses a sample cup that needs to be filled in with the bulk sample. The IR beam interacts with the particles in one of several ways. Radiation can be reflected without penetration of the sample; the light can undergo multiple reflections off particle surface or can be scattered after the incident radiation penetrates the particle. Scattering is how the true diffuse reflectance results.²⁶ The output mirror controls the direction of the scattered energy into the detector of the spectrometer (Figure 2.5).

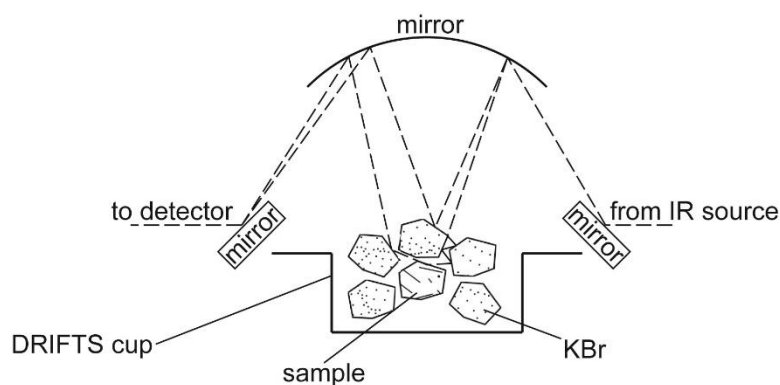


Figure 2.5 A scheme of the FTIR DRIFTS experiment.²⁷

The ATR operates on an accessory provided with a hard crystal that possesses a high refractive index at a certain angle. Those are most usually polished diamond, zinc selenide and germanium crystals. In contrast to the DRIFTS method, here the light is not reflected directly on the surface. This part of the light internally penetrating the sample is called the evanescent wave. The depth of penetration depends on the light beam entering angle, wavelength, the refractive index of the crystal and the sample. After total internal reflection, the light beam exits the crystal and is directed to the IR-detector (Figure 2.6). The method does not require the use of finely grounded KBr as background sample.

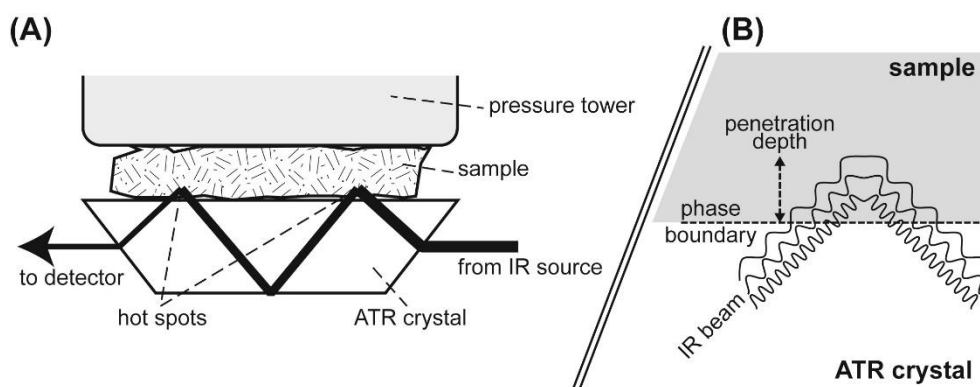


Figure 2.6 Scheme of the FTIR ATR experiments (left, A); sample is pressed on the crystal surface. The penetration depth (right, B) depends on wavelength.²¹

Both techniques, DRIFTS and ATR were used in this work in order to obtain the infrared spectra of untreated and solvent treated zeolite and MOF samples. These spectra were used in the characterisation of the structure of these materials, *i.e.*, intensity and position of the OH stretching vibrations, framework and extra-framework positions of aluminium.

The DRIFTS spectra were recorded on a Bruker Tensor II spectrometer fitted with a liquid N₂ cooled Mercury Cadmium Telluride (MCT) detector over a range of 4000-600 cm⁻¹ at a resolution of 2 cm⁻¹ frequency and 16 scans. Background scans were taken using finely ground KBr.

The ATR spectra were recorded on a Bruker Vertex 70 spectrometer fitted with a liquid N₂ cooled Mercury Cadmium Telluride (MCT) detector and a diamond ATR cell. Scans were collected across the range 4000-400 cm⁻¹, at a resolution of 2 cm⁻¹ frequency and 32 scans.

DRIFTS analysis from Chapter 5 (Figure 5.19 and Figure 5.22) was prepared by Dr Giulia Tarantino from Imperial College London.

2.6.8 Scanning Electron Microscopy (SEM)

SEM is a characterisation technique, which is based upon the utilisation of a high-energy electron beam over a solid material and where the detection of the backscattering and secondary electrons is the main mechanism of observing images. The method is widely used in materials science as it allows the observation of surface topography and microstructure.

The collimated electron beam is emitted from by an electron gun fitted with a tungsten filament cathode. During the scan, the X-Ray interacts with electrons in discrete orbitals of

atoms in the sample producing different signals. To create images signals emitted from the materials surface must be identified by the inbuilt detector. Typically, two out of three types of signals, depending on the interaction volume, are studied during the scan - back scattered electrons and secondary electrons (Figure 2.7).

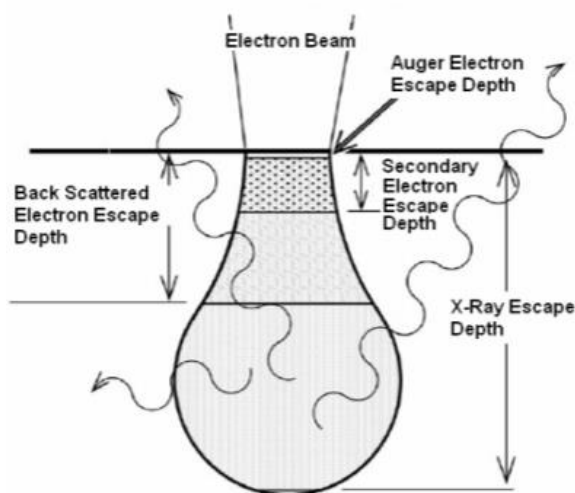


Figure 2.7 Scheme of the teardrop-shaped volume of the sample known as the interaction volume.²⁸

As described on the figure, three types of interactions can be studied in order to characterise the sample. Secondary electrons (SE) originate from the sample surface or the near-surface (up to 10 \AA depth) of the material.²⁹ The incident beam knocks out the electrons of their outer orbital shell and the atoms become ionised. They are reflected from the sample by low intensity (less than 50 eV) inelastic scattering. The emission does not depend on the accelerating voltage values. This type of interaction provides valuable information on the morphology and topography of the particles.

Backscattered electrons (BSE) originate from high intensity (from 50 eV to incident beam energy) electrons that are reflected or backscattered by elastic scattering interactions out of the sample (up to $1 \text{ }\mu\text{m}$ depth). The intensity and brightness of the image depends on the atomic number and the acceleration voltage of the primary beam, the higher the brighter. This type of interaction is primarily used for detection of high atomic number elements to provide useful information on the elemental composition of the particles.

The emission of characteristic Auger electrons may occur when the amount of energy to be released is larger than in the inner state. If the X-ray is to be emitted, a single outer electron falls into the inner shell vacancy. The energy of the X-ray is the difference between the

energies of the two excited states and this is characteristic of the particular atomic species. The energy of these electrons is generally low, of few kV.

In this study, Scanning Electron Microscope (SEM) technique was used to provide direct information about topography of the as-synthesised and tested zeolite and MOF materials. The material zeolite and MOF materials were placed on a holder inside a chamber and the chamber was evacuated prior analysis. Carbon-taped and copper-taped stainless-steel holders were used in examination of the solids.

Back scattered electron (BSE) imaging was primarily used in this study. A Hitachi Tabletop TM3030 scanning electron microscope operating with accelerating voltages of 5 kV and 15 kV was used.

2.6.9 Energy Dispersive X-ray Spectroscopy (EDX)

Energy Dispersive X-ray (EDX) spectroscopy is an X-ray technique used to perform the elemental composition analysis of solid-state materials. The detector is coupled with a Scanning Electron Microscope (SEM) and data generated during the analysis is in a form of a spectrum with peaks of different intensities corresponding to the elements making up the composition of the mapped area. The non-destructive analysis can be performed on a point, line, or area of a chosen sample. The multi-approach EDX is a complementary tool for all other materials analysis techniques. An example of a spectrum is presented on Figure 2.8.

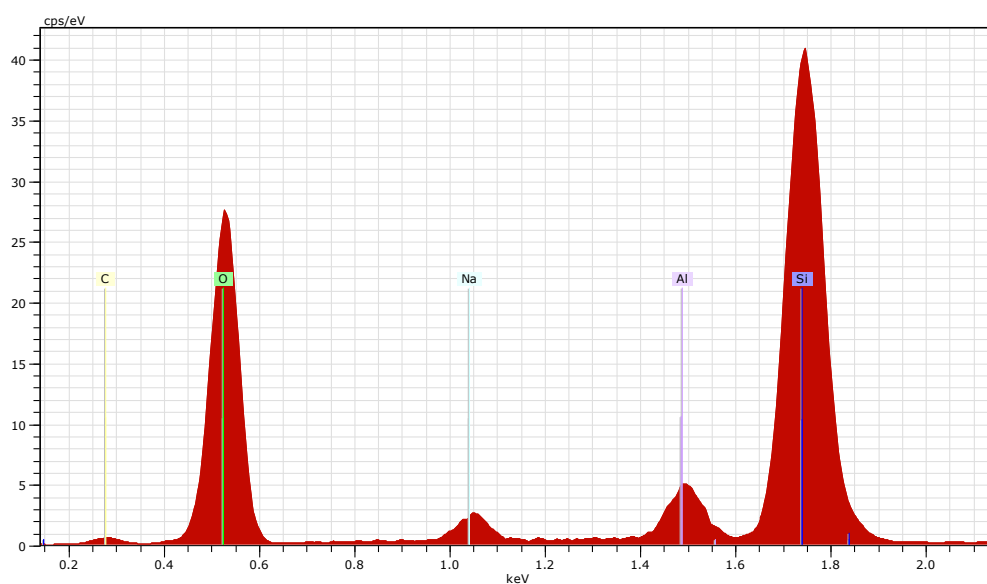


Figure 2.8 Energy dispersive X-ray analysis (EDX) spectrum of an untreated HZSM-5 (30) HT sample.

When the incident beam hits the Silicon Drift Detector (SDD) it creates a charge pulse proportional to the X-ray energy. The pulse is converted to a voltage pulse by an amplifier. The energy of all incident X-rays is determined from the voltage measurements and sent to the computer for further evaluation. The identification of elements in an EDX spectrum is based on energy of the X-rays versus the number of counts emitted by atoms electrons as those transfer from high to low energy shells.³⁰

Since the Scanning Electron Microscopy (SEM) coupled with an Energy Dispersive X-ray (EDX) detector is able to perform elemental analysis, in this work EDX analysis was primarily used to analyse the chemical composition of the zeolites before and after water stability tests. EDX analysis was performed with a Hitachi Tabletop TM3030 scanning electron microscope coupled with a BRUKER Quantax XFlash® 6 detector. All values presented in this work are an average of 10 areas of different parts of the analysed sample.

2.6.10 Nuclear Magnetic Resonance (NMR) spectroscopy

2.6.10.1 Theoretical background

Nuclear Magnetic Resonance (NMR) spectroscopy is an ideal method in materials characterisation as it is a powerful tool providing detailed structural information on molecule and its atoms arrangements. The experiments are performed on the nuclei of an atom and the overall number of neutrons and protons must be odd, so the nucleus has a half-integer spin, which is described by the quantum number I , *i.e.*, $1/2$, $3/2$, $5/2$. When an external static magnetic field is applied, an energy transfer between low and high energy levels is possible. The quantum number I and the gyromagnetic ratio γ (constant property of each nucleus) are associated with the magnetic moment called μ and defined as:

$$\mu = I \gamma$$

The magnetic moment of the nuclei can be aligned with (low energy) or against (high energy) the direction of the external magnetic field (B_0). When the nucleus is exposed to external magnetic field the atomic energy levels are split into different levels. This splitting is called as the Zeeman Effect, the spin quantum number is renamed as m and each energy level is therefore defined as:

$$E = \pm m \hbar \gamma B_0$$

When the quantum number m is $\pm 1/2$, two nuclear degenerate spin energy levels (Figure 2.9) are formed and the difference between these levels is expressed as:

$$\Delta E = \hbar\gamma B_0$$

Where: \hbar – reduced Planck constant (J s^{-1}),

γ – gyromagnetic ratio (MHz T^{-1}),

B_0 – external magnetic field (T).

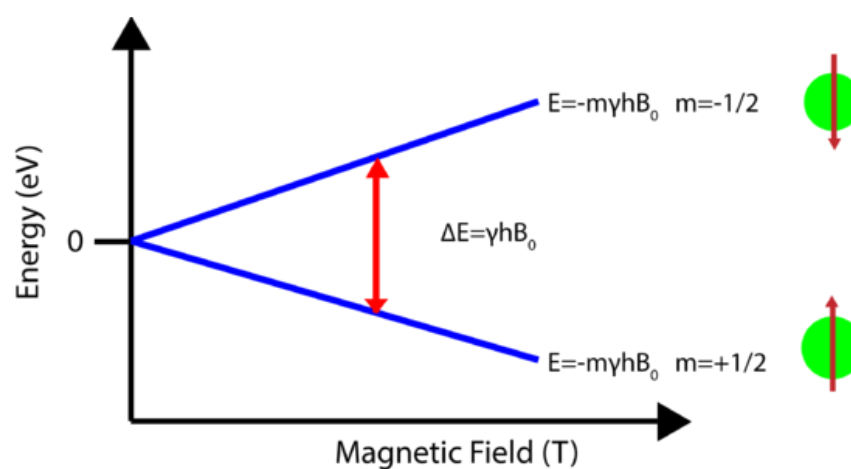


Figure 2.9 Schematic representation of the splitting of the degenerate nuclear energy levels under an applied magnetic field. The green spheres represent atomic nuclei which are either aligned with (low energy) or against (high energy) the magnetic field.

The energy transfer takes place at a wavelength corresponding to a radiofrequency radiation and after relaxation time, when higher energy state return to the lower state, the absorbed energy is emitted at the same frequency.³¹ Radiofrequency radiation of hundreds of MHz or GHz is required for the absorption to occur.

Protons in a molecule have different resonance at the same frequency. This is a result of protons being surrounded by a different number of electrons (valence-shell electron densities vary) and their existence in slightly different magnetic environments from one another. When a molecule is exposed to a magnetic field the shielding electrons start to circulate. The circulation, known as the diamagnetic current, generates a counter magnetic field that opposes the applied magnetic field. This effect is known as diamagnetic shielding. The greater the electron density around a nucleus, the greater the induced counter field.

Various functional groups are located in different places of the NMR spectrum, as they need different external magnetic fields to bring them in to resonance at a particular radio frequency. The active nuclei in the sample resonate at different frequencies that are called resonance frequencies. The Chemical shift (δ), given in ppm, is the resonant frequency of a nucleus relative to a standard in a magnetic field. As an example, a peak at chemical shift of 2 ppm means that a nucleus needs a magnetic field two millionths less than the field needed by the external reference sample to produce resonance. The signals emitted by the atoms sample are received by the detector and Fourier transformed by the spectrometer (Figure 2.10).

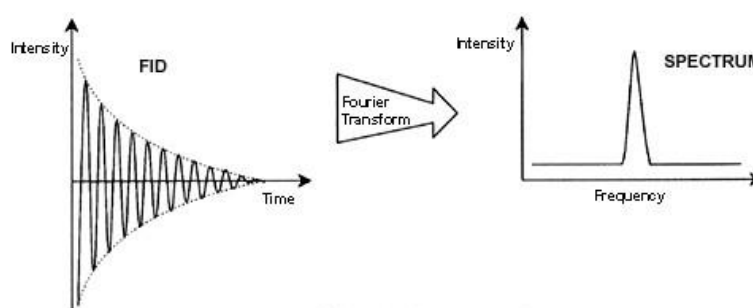


Figure 2.10 Fourier transformation of the raw FID into a spectrum.³²

The process of signal receiving is called an acquisition. When an acquisition is carried out, the yet non-transformed data is acquired and the received signal is called an FID (Free Induction Decay). Through Fourier transformation, the FID is transformed into a frequency spectrum.

2.6.10.2 Magic Angle Spinning (MAS) in Solid state NMR

The Magic Angle Spinning (MAS) is used to perform experiments in solid-state NMR spectroscopy. The principle of this method is the elimination of anisotropic magnetic susceptibility effect by spinning a cylindrical sample with its axis at the 'magic angle' ($\theta_m=54.7^\circ$) to the static magnetic field B_0 (Figure 2.11).

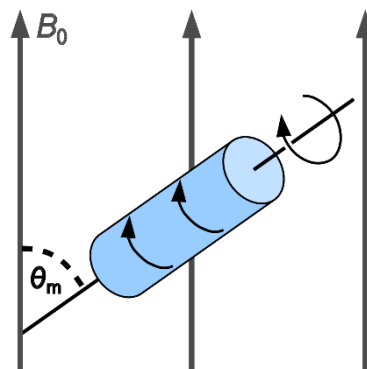


Figure 2.11 Magic-angle spinning: the 4 mm zirconia rotor (blue) is rotating with high frequency inside the main magnetic field (B_0). The axis of rotation is tilted by the magic angle θ_m (54.7°) with respect to the direction of B_0 .

Spinning is necessary as it helps narrowing the lines and so it is used for accurate chemical shift measurements.³³ It has been found that if the solid sample is spun at rates 1 to 35 kHz at the angle of 54.7° , with respect to the magnetic field B_0 , the random molecular motion and anisotropic dipolar interactions are reduced. When the sample is spun presence of spinning sidebands may occur. These signals result from the modulation of the magnetic field at the spinning frequency.

Different pulse sequences are used for different isotopes in order to acquire the NMR spectrum. Cross polarisation is commonly used for routine studies in carbon environment examination, such as of MOF structures, as it is more sensitive in comparison to the single pulse method. Although, single pulse provides higher level of quantitation for organic samples, but sample analysis takes longer times.³⁴ The single pulse sequence is much often used for high ionic strength samples when the proton probe channel is disrupted, *e.g.*, analysis of graphene or carbon nanotubes.³⁵

Solid State MAS NMR analysis was performed on a Bruker Avance III HD 400 MHz unit. Between 50 to 100 mg of solid sample was packed in a 4 mm zirconia rotor and spun at 10 kHz.

Training and settings, as well as any help needed, were provided by Dr Nia Richards from Cardiff Catalysis Institute (Cardiff University).

2.6.10.3 Single Pulse ^{27}Al MAS NMR spectroscopy

Aluminium MAS NMR is performed using single pulse sequence with MAS. Most often the ^{27}Al ($I = 5/2$) chemical shifts are used to differentiate two aluminium coordination the tetrahedral framework aluminium (Brønsted acid sites) and octahedral extraframework aluminium (EFAl, Lewis acid sites). Tetrahedral aluminium ranges between 100 and 50 ppm and octahedral between 20 and -10 ppm.³⁵ In some cases penta-coordinated aluminium (AlO_5) can be observed in the range between 20 and 52 ppm.³⁶ The natural high abundance of ^{27}Al (100%) reduces the analysis time significantly.

In this work, ^{27}Al spectra were analysed due to the need of investigating and understanding the framework and extra-framework (EFAl) positions of aluminium in the zeolite structure. Since MAS NMR spectroscopy gives the ability to examine solid state materials, it became the most reliable method of analysing zeolites. By analysing and interpretation of the spectra it became clear that this method is the most accurate in determining the amount of EFAl.

The ^{27}Al SP spectra were recorded with 8192 scans and a recycle delay between scans of 0.2 s. The operating frequency was 104.28 MHz. Aluminium chemical shift was referenced to an external standard reference $\text{Al}(\text{NO}_3)_3$ with an intense peak signal at 0 ppm.

2.6.10.4 Single Pulse ^{29}Si MAS NMR spectroscopy

The silicon NMR was performed using single pulse sequence with MAS. The analysis of ^{29}Si ($I = 1/2$) isotope required extended acquisition times to obtain spectra as it is the only stable natural isotope with mean abundance of 4.67%.

In this work, ^{29}Si spectra were used in order to investigate the framework positions of silicon in the zeolite structure before and after performing hydrothermal stability tests in the CFR. Typically, in a zeolite, silicon atoms can reside in five possible coordination environments – $\text{Si}(\text{nAl})$ units, where $n=0, 1, 2, 3, 4$. The n number means the distribution of Al atoms around the central SiO_4 unit. Alternatively, the more common naming follows the Q notation – so called Q^n sites, where n denotes the number of linked SiO_4 tetrahedra [$\text{Q}^4 = \text{Si}(\text{0Al})$], as shown on Figure 2.12.

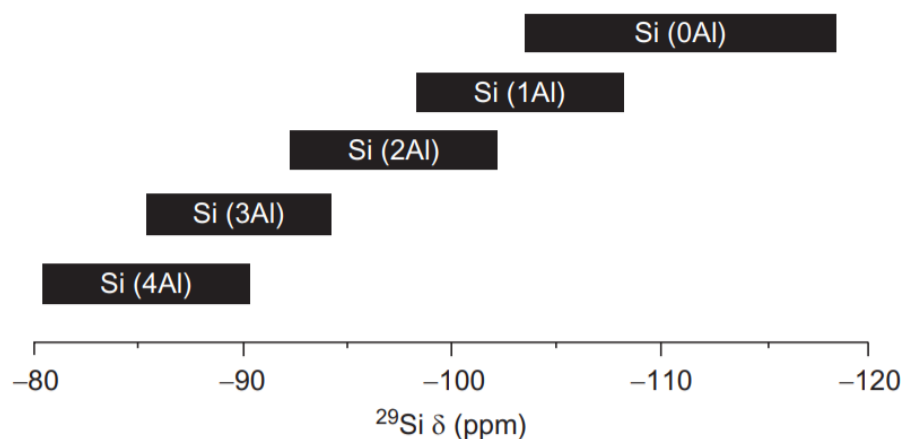


Figure 2.12. ^{29}Si NMR chemical shifts range of Si (nAl) species.³⁷

The ^{29}Si SP spectra were recorded with 128 scans and a recycle delay between scans of 20 s. The operating frequency was 79.51 MHz. Chemical shift was referenced to kaolinite secondary reference with a ^{29}Si peak signal at -92.0 ppm.

2.6.10.5 Cross Polarisation ^{13}C MAS NMR spectroscopy

A normal ^{13}C ($I = 1/2$) chemical shift spans from 0 to 250 ppm and corresponds to various functional groups in the structure. Carbon NMR tables and charts of chemical shifts are easily found online.

In this work, ^{13}C spectra were obtained in order to investigate the carbon positions and to assign resonances resulting from chemisorbed solvents. The ^{13}C CP-MAS NMR spectra were recorded with 512 scans and a recycle delay 5 s. The operating frequency was 100.63 MHz. The chemical shift was referenced to glycine with the main peak at 176.5 ppm.

2.6.11 Microwave Plasma-Atomic Emission Spectrometer (MP-AES)

Microwave Plasma Atomic Emission Spectroscopy (MP-AES) is an atomic emission technique used to obtain the elemental composition of liquid samples. This technique utilises microwave energy to produce a plasma discharge using supplied nitrogen. Liquid samples pumped with a peristaltic pump are nebulised prior to contact with plasma, which causes excitation of electrons in order to emit light in a characteristic pattern of wavelengths.³⁸ The intensity of the emitted light, thus the spectrum, is proportional to the number of atoms of

the element detected. Microwave induced plasma (MP) is a high temperature (2000-3000 K) source of the atomic emission therefore excellent excitation source for efficient detection of most elements. Elements can be detected in a range of part per million (ppm) up to 1 wt. % (10000 ppm). MP-AES is a powerful tool, which allows identification and quantification of several dissolved metallic species simultaneously. What is more, the method allows atom detection at low operational cost and eliminates the need for flammable gases by running on air.

In this work, MP-AES was primarily used to determine the quantity of Si and Al present in the effluent water after treating the zeolite materials in water. The amounts of leached Si and Al were of high importance in understanding the hydrothermal stability of selected zeolites at elevated temperatures and pressures.

MP-AES was performed on an Agilent 4100 MP-AES. The average concentration was taken from results at the wavelengths of 251.611 and 288.158 nm for silicon (Si) and 394.401 and 396.152 nm for aluminium (Al). MP-AES was used to determine the wt. % of Al and Si in the effluent water. The results were compared against the values obtained for fresh water before passing the catalysts. Silicon and aluminium reference standard solution (1000 ppm \pm 1%) were used for determining Si and Al calibration curves. In order to be confident about the outcome of the Si analysis, a blank experiment with only glass wool packed in the reactor was performed (24 h, 110°C). No Si leaching was observed, as the values of Si in effluent water were no different from the blank sample (deionised water).

2.7 References

- 1 C. Hammond, M. M. Forde, M. H. Ab Rahim, A. Thetford, Q. He, R. L. Jenkins, N. Dimitratos, J. A. Lopez-Sanchez, N. F. Dummer, D. M. Murphy, A. F. Carley, S. H. Taylor, D. J. Willock, E. E. Stangland, J. Kang, H. Hagen, C. J. Kiely, G. J. Hutchings, *Angew. Chem. Int. Ed.* 2012, **51**, 1-6
- 2 D. Ma, G. Han, S. B. Peh, S. B. Chen, *Ind. Eng. Chem. Res.*, 2017, **56**, 12773-12782
- 3 J. Bae, B. Hong, *Chem. Commun.*, 2018, **54**, 10997-11000
- 4 D. Padovan, S. Tolborg, L. Botti, E. Taarning, I. Sadaba, C. Hammond, *React. Chem. Eng.*, 2018, **3**, 155-163
- 5 D. Padovan, L. Botti, C. Hammond, *ACS Catal.*, 2018, **8**, 7131-7140
- 6 M. Caiti, G. Tarantino, C. Hammond, *ChemCatChem*, 2020, **12**, 6393 – 6400
- 7 E. Tsalaporta, J.M. Don MacElroy, *Heliyon*. 2020, **6**, e04883
- 8 J. W. Niemantsverdriet, *Spectroscopy in Catalysis: An Introduction*, Third Edition; Wiley-VCH Verlag GmbH & Co. KGaA, 2007. pp I
- 9 G. Hübschen, I. Altpeter, R. Tschuncky, H. G. Herrmann, *Materials Characterization Using Nondestructive Evaluation (NDE) Methods*, Woodhead Publishing, Cambridge, 2016
- 10 <http://www.iza-structure.org/databases/> [Accessed: 01 Nov. 2020]
- 11 M. Nasrollahzadeh, M. Atarod, M. Sajjadi, S. M. Sajadi, Z. Issaabadi, *Interface Sci. Technol*, 2019, **28**, 199-322
- 12 S. Lowell, J. E. Shields, M. A. Thomas, M. Thommes, *Characterization of Porous Solids and Powders: Surface Area, Pore Size and Density*, Springer Netherlands, 2004
- 13 K. S. W. Sing, D. H. Everett, R. A. W. Haul, L. Moscou, R. A. Pierotti, J. Rouquerol, T. Siemieniewska, *Pure Appl. Chem.*, 1982, **54**, 2201
- 14 P. Llewellyn, F. Rodriguez-Reinoso, J. Rouquerol, N. Seaton, *Stud. Surf. Sci. Catal.*, 2007, **160**, 49-56
- 15 J. M. Castillo, J. Silvestre-Albero, F. Rodriguez-Reinoso, T. J. H. Vlught, S. Calero, *Phys. Chem. Chem. Phys.*, 2013, **15**, 17374
- 16 A. W. Coats, J. P. Redfern, *Analyst.*, 1963, **88**, 906-924
- 17 A. Auroux, *Calorimetry and Thermal Methods in Catalysis*, Springer-Verlag, Berlin-Heidelberg, 2013
- 18 D. A. Skoog, F. J. Holler, S. R. Crouch, *Principles of Instrumental Analysis*, Sixth edition; Thomson Brooks/Cole, Belmont, 2006
- 19 J. G. Santaclara, F. Kapteijn, J. Gascon, M. A. van der Veen, *CrystEngComm*, 2017, **19**, 4118-4125
- 20 X. Mu, J. Jiang, F. Chao, Y. Lou, J. Chen, *Dalton Trans.*, 2018, **47**, 1895-1902
- 21 B. Stuart, *Modern Infrared Spectroscopy*, John Wiley & Sons Ltd, West Sussex, 1996
- 22 P. J. Larkin, *Infrared and Raman Spectroscopy*, Elsevier, 2018
- 23 F. S. Parker, *Applications of Infrared Spectroscopy*, Plenum Press, 1971
- 24 I. D. H. F. Williams, *Spectroscopic methods in organic chemistry*, McGraw-Hill, London and New York, 1995
- 25 J. H. Nelson, *Nuclear Magnetic Resonance Spectroscopy*, Pearson Education, 2003
- 26 G. Anbalagana, G. Sivakumarb, A. R. Prabakaranc, S. Gunasekaranc, *Vib. Spectrosc.* 2010, **52**, 122-127
- 27 G. Renner, T. C. Schmidt, J. Schram, *Compr. Anal. Chem.*, 2017, **75**, 67-118

-
- 28** B. Hafner, *Scanning Electron Microscopy Primer*, Characterization Facility, University of Minnesota-Twin Cities, 2007
- 29** D. J. Stoke, *Principles and Practice of Variable Pressure Environmental Scanning Electron Microscopy (VP-ESEM)*, John Wiley & Sons, Chichester, 2008
- 30** B. D. Cullity, S. R. Stock, *Elements of X-ray Diffraction, Third Edition*, Prentice-Hall, New York, 2001
- 31** J. B. Lambert, E. P. Mazzola, *Nuclear Magnetic Resonance Spectroscopy: An Introduction to Principles, Applications, and Experimental Methods*, Pearson Education, 2004
- 32** Fourier transformation of Free Induction Decay (FID). Scheme. Retrieved from <http://www2.chem.uic.edu/nmr/downloads/bruker/en-US/html/Avance%20Beginners%20Guide/en-US/index.html>
- 33** A. N. Garroway, *J. Magn. Reson.*, 1982, **49**, 168-171
- 34** D. Courtier-Murias, H. Farooq, J. G. Longstaffe, B. P. Kelleher, K. M. Hart, M. J. Simpson, A. J. Simpson, *Geoderma*, 2014, **226–227**, 405–414
- 35** Y. Yin, Y. Lu, *Handbook of Synthetic Methodologies and Protocols of Nanomaterials*, Vol. 1, World Scientific, 2019
- 36** Z. Wang, Y. Jiang, O. Lafon, J. Trébosc, K. D. Kim, C. Stampfl, A. Baiker, J.-P. Amoureux, J. Huang, *Nat Commun.*, 2016, **7**, 13820
- 37** G. Webb, *Annual Reports on NMR Spectroscopy, First Edition, First Edition*, Vol. 77, Academic Press, 2012
- 38** J. A. C. Broekaert, *Analytical Atomic Spectrometry with Flames and Plasmas*, Wiley-VCH Verlag GmbH, Weinheim, Germany, 2001

3 Hydrothermal stability of selected commercial zeolites

3.1 Introduction

Microporous crystalline aluminosilicates are widely used in industry due to their strong acid sites, good thermal stability, high surface area, well-defined porosity, adsorption capacity and ion exchange abilities.¹ As described in Chapter 1 (see Section 1.1.2), zeolite frameworks possess various pore sizes and dimensions, making them favourable for catalytic shape selective reactions and molecular sieving, *e.g.*, desalination.

Most of the commonly used commercial zeolites can be produced synthetically on a large scale and in a wide range of $\text{SiO}_2/\text{Al}_2\text{O}_3$ molar ratios.² Aluminium (Al) atoms are typically located in the lattice, or less commonly form extra-framework Al (EFAl) species, which results in formation of Lewis acid sites. These sites are key elements in catalytic activity as they introduce the negative charge into the framework. Furthermore, Al defects might be desirable in the framework as their appearance tunes the hydrophilicity of the zeolite.³ When the negative charge is counterbalanced by proton (H^+) this leads to the formation of Brønsted acid sites. This was described in more detail in Chapter 1 (see Section 1.1.3).

Maintaining and protecting drinking water has become one of the main challenges of modern times. In some parts of the world, freshwater shortages have resulted in the need of building seawater desalination plants.⁴ Nowadays, search for new desalination solutions and water stable membrane materials is crucial. In addition, green chemistry focuses on the use of environmentally friendly solvents that do not cause groundwater pollution.⁵ Water itself is an environmentally friendly solvent to be considered for green catalysis.

Hence, hydrothermal stability of the zeolite is a key parameter to its molecular sieving and catalytic performance. However, it can be expected that several parameters can have an influence on its lifetime, such as the $\text{SiO}_2/\text{Al}_2\text{O}_3$ molar ratio, framework density (FD_{Si}), ion exchange, particle size etc. In particular, the amount of Al and presence of alkaline cations in the framework can have a profound impact on the stability and resistance to framework failure in contact with water and steam.⁶ It was previously shown that in the MFI framework, ($\text{Si}/\text{Al} < 20$), the presence of high Al concentrations prevented Si from being extracted which limited pore formation.⁷ Consequently, the stability of zeolite structure is an important topic

of wide research interest due to the important role of zeolites in industrial applications, such as *e.g.*, desalination, catalysis and gas separation.⁸

In general, as described in Chapter 1 (Section 1.1.5.1), desilication and dealumination are thought to be equally causing framework failure in water. However, it was not yet confirmed which of the processes progresses faster and which of them is the starting point of framework failure.

Although many present studies^{9,10,11,12,13,14,15,25} discussed the stability of zeolites in water, none of these were performed near actual catalytic reaction conditions *e.g.*, at elevated temperature and/or at high pressure. Most of the studies concentrated on stability in boiling water under reflux, under autogenous pressure in Teflon-lined autoclaves or after treatment in steam.

In work by Lutz *et al.*, different behaviours of densely structured (MFI, MOR) and open-structured (BEA, FAU) framework types in water and steam were studied.²⁴ The authors have found that after 72 h at 240°C two destruction mechanisms took place – an acid (H⁺) attack on the Si-O-Al bonds and an alkaline (OH⁻) attack on the terminal Si-OH (silanol) group on the zeolite surface. What is more, the dense structure lost a maximum of 20% crystallinity, whereas the open-structured, lost up to 80%. However, there was a significant difference in framework damage between the zeolites; the experimental outcomes were not clearly explained by the authors.

Another recent study, by Reule *et al.*, focused on the effect of nitric acid treatment on Mordenite (MOR).¹⁶ The authors of this study suggested that the dealumination process was coupled with the removal of Al sites from the 4-membered rings (T3 and T4) in the 8- and 12-membered channels. Another study focused on hot liquid water treatment of zeolite β (BEA), indicated that the Al T-sites, including Al-O-Si angles and bonds, remained unaffected.⁹ At the same time, XRD and STEM analysis of the crystal structure have shown disruptions in the framework. The authors concluded that the degradation occurred due to hydrolysis of the siloxane T-O-T bridges, which were located in the 4-membered rings of the zeolite β structure.

Consequently, at the outset of this work there was no reported available data on the stability of zeolites in presence of water in fixed-bed continuous flow reactors (CFR). Such tests provide valuable information for not only the rapidly growing flow chemistry catalysis but also membrane separation technology where high pressure and high temperatures play

important roles.¹⁷ The aim of this Chapter was to obtain fundamental data and present a detailed study on the stability of commercially available zeolites. Belonging to the so called ‘big five’ group (*i.e.*, MFI, BEA, FAU, MOR and FER framework types) and zeolite A (LTA framework) are all structures of high interest in the petrochemical and desalination industry. Zeolites of high and low Al content were chosen for tests in in continuous water flow regime under mild inlet pressure and varying water temperatures. The outcomes of these tests were examined in detail with the use of powder X-Ray Diffraction (pXRD), N₂-physisorption, water vapour sorption, Energy-Dispersive X-ray spectroscopy (EDX), Single Pulse ²⁹Si and ²⁷Al MAS NMR and Microwave Plasma - Atomic Emission Spectroscopy (MP-AES).

3.2 Results and discussion

3.2.1 Characterisation of untreated parent zeolites

To gain an initial understanding of water impact, a number of commercial zeolites provided by Zeolyst were explored. The zeolites used in this study had a very similar chemical composition but were of different frameworks. All initial materials possessed similar SiO₂/Al₂O₃ molar ratios of 20-30. Powder X-ray Diffraction (pXRD) was used to verify the crystallinity of the initial samples, prior to testing. Diffraction patterns of all initially tested zeolites are presented in Figure 3.1. The Integrated Peak Areas of these samples were later used to determine the relative crystallinity.

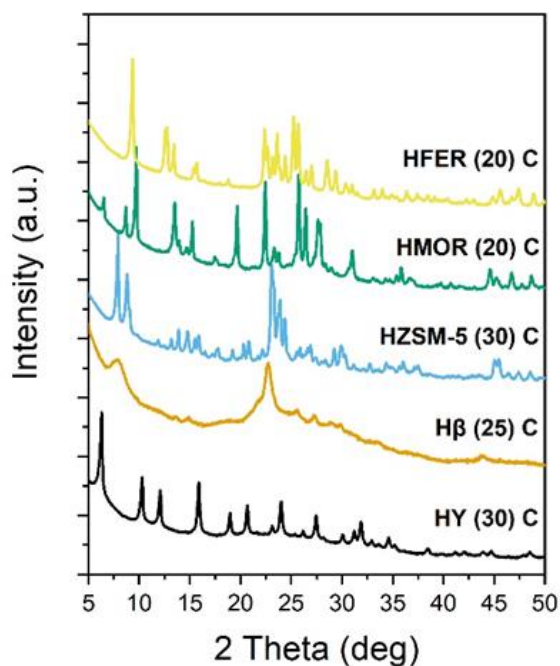


Figure 3.1 The pXRD patterns of pelletised commercial zeolite samples used for hydrothermal stability tests.

The diffractograms of all untreated zeolites in the preliminary screening were compared with the IZA Structure Commission database available online.¹⁸ Presented pXRD patterns matched the reference patterns found in the database. As an example, for untreated Y zeolite the major reflection peaks were located at (2θ) 6.3° , 10.3° , and 15.9° corresponding to the (111), (220), and (331) lattice planes, respectively.¹⁹

The peak broadening arises from two features, crystallite size and strain (change of d -spacing).²⁰ As defined by the Scherrer equation; the smaller the crystal, the broader the peak. This is due to decreased number of diffracting lattice planes of a crystal. Strain is caused by defects, such as dislocations, which disrupt the atomic arrangement of a crystal. Sharp peaks are due to the crystalline phase and broad features due to the amorphous phase.

It was observed that all the patterns exhibited intense diffraction reflections, except for H β (25) C sample, which was of lower intensity and exhibited peak broadening. This was due the fact that commercial zeolite β was synthesised as a polymorph of at least two, up to three, distinctive structures – polymorph A, polymorph B and much less often, Polymorph C. Polymorph A is chiral, whereas polymorph B is achiral.²¹ These two polymorphs are built equally in terms of building units and create a random stacking sequence that makes the

pXRD pattern look somewhat disordered.²¹ This gives an impression of a large amorphous phase. Up to now, there was still no existing characterisation method to determine the exact proportions of the polymorphs in the zeolite β . Recently, a synthesis of all pure silica Polymorph C and nearly pure Polymorph B were achieved, however it was still not possible to obtain a pure Polymorph A zeolite β .²²

3.2.2 Pre-screening of high aluminium content commercial zeolites

In order to understand the differences in framework behaviour in the presence of hot (110°C) pressurised water zeolites were examined for hydrothermal stability. Zeolites, of similar Al content ($\text{SiO}_2/\text{Al}_2\text{O}_3$ molar ratio of 20-30) were chosen for these tests. Powders were pelletised and sieved prior to packing and testing. Samples (0.2 g) were packed into fixed-bed continuous flow reactors (CFR) and tested under mild inlet (25-50 bar) pressure. The deionised water flow was set to 0.3 ml min^{-1} . The reactor was immersed in an oil bath and all initial tests were carried out for 24 h at 110°C. However, further tests were carried out in time and temperature ranging 6-24 h and at 80-110°C, respectively. Conditions are stated before each experiment description. The whole setup was described in detail in Chapter 2, Section 2.5.1.

The testing system was kept under stable outlet pressure (10 bar) by the means of a backpressure regulator. By this, the operations above the water boiling point were possible to proceed. It must be mentioned here that all samples were abbreviated by their origin – here, C for commercial zeolite, *i.e.*, commercial BEA type zeolite β sample after activation, possessing a $\text{SiO}_2/\text{Al}_2\text{O}_3$ molar ratio of 25, was denoted as H β (25) C.

Continuous flow experiments were chosen due to ease of performing, collecting and analysing the sample and the effluent. In contrast to batch operation, the powder was packed into the CFR. Furthermore, continuous flow is preferred in industrial scale catalytic chemistry due to practical and economic reasons, as high productivity and low costs are desirable.¹⁷

After running the CFR experiment for a required amount of time the fixed-bed reactor was dried overnight in a benchtop oven (16 h, 110°C, air), opened and the dried sample was collected for further characterisation.

The pXRD analysis was used to gather diffraction patterns of initial and tested powders. The relative crystallinity (X_{rel} , %) after water treatment was evaluated by comparison of the Integrated Peak Areas of characteristic peaks before (X_{untr}) and after (X_{tr}) water treatment, following the method presented in Chapter 2 (Section 2.4.1), and described by the equation:

$$X_{\text{rel}} = \frac{X_{\text{tr}}}{X_{\text{untr}}} \times 100\%$$

In addition, N₂-physisorption was used to determine micropore volume (pores < 2nm) of the samples. Total pore volume (V_t), mesopore volume (V_{ms}), micropore volume (V_{mc}), pore size distribution and specific surface area (S_{DFT}) values were determined with the use of the non-local density functional theory (NLDFT) as described in Section 2.6.2.

The relative microporosity (V_{mc} , %) was determined by comparing micropore volumes of tested (V_{mctr}) samples to untreated (V_{mcuntr}) ones, following the method presented in Chapter 2 (Section 2.4.2), and described by the equation:

$$V_{\text{mc}} = \frac{V_{\text{mctr}}}{V_{\text{mcuntr}}} * 100\%$$

Results of all initial tests (24 h, 110°C), relative microporosity and crystallinity for each sample, as well as relative total porosity values (V_{trel}) are presented in Figure 3.2.

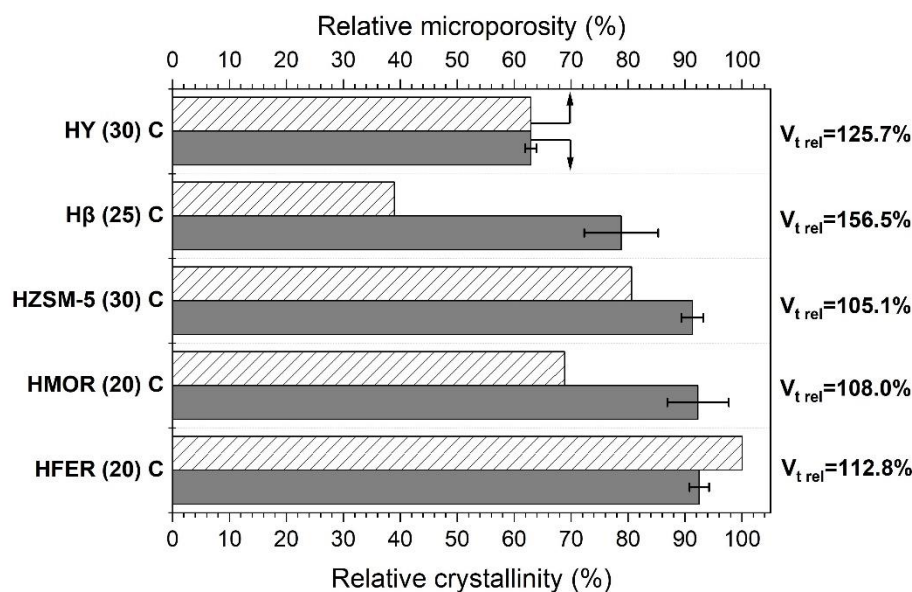


Figure 3.2 Screening of various structure type zeolites with high Al content in pressurised water at 110°C for 24 h (CFR). SiO₂/Al₂O₃ ratios are noted in parenthesis. Relative total porosity values ($V_{t,rel}$) were also added. Relative crystallinity error bars represent the standard deviation of the Integrated Peak Area after 5 samples examination.

First preliminary tests gave an overall idea of zeolite stability proving that different frameworks behave differently under same experimental conditions. The pXRD analysis confirmed changes in peak intensities after contact with water, and reduction of initial crystallinity was observed in all samples. The error bars represent the standard deviation of the Integrated Peak Areas of five measurements for each sample.

Out of 5 tested samples, an average of 92% of crystallinity after treatment maintained in the HZSM-5 (30) C, HMOR (20) C and HFER (20) C samples. In opposition to HY (30) C and H β (25) C, these three structures are considered as zeolites possessing higher framework densities (FD_{Si}). However, in the case of the zeolite β framework (BEA) accurate crystallinity measurements are difficult because of polymorph stacking and the structure being already partially disordered in the c-direction.²³ This complicated building structure, here stacking faults, lead to complex pXRD patterns that made the analysis of the zeolite β framework very difficult.²¹

In all tested cases, substantial decrease in micropore volume (V_{mc}) was accompanied by increase in mesopore volume (V_{mp}) and overall total pore volume (V_t). Out of the five samples, the increase in total pore volume followed the trend of HZSM-5 < HMOR < HFER < HY < H β . Indeed, the MFI structure presented the lowest increase

in relative total porosity (by 5.1%) among all examined samples. The zeolite H β (25) C sample showed a decrease of micropore volume of around 60% and increase of overall total pore volume of 56.5%. In contrast, the structural changes of the HY (30) C zeolite were severe and the drastic as well. The decrease in the micropore volume indicated a partial dissolution or amorphisation of the zeolite, in agreement with existing literature.^{24,25,26} The FAU structure is also known for its low density, resulting from the wide pore diameter of 7.4 Å defined by 12-member oxygen rings. Low density is also associated with the void volume, which in this case of FAU structures is around 48%.²⁷

Based on the relative total pore volume ($V_{t\text{rel}}$) data, in all cases pore volume has increased with lowest change of only 5.1% in the HZSM-5 (30) C. Also, in the case of HMOR (20) C and HFER (20) C, these changes were relatively small, 8.0% and 12.8% increase, respectively. However, a significant change was acknowledged in the case of the H β (25) C zeolite sample where the total pore volume increased by 56.5%. To highlight the differences, a complete surface area (S_{DFT}) and porosity (micropore and total pore volume) dataset of the two samples (HZSM-5 and H β), of opposite $V_{t\text{rel}}$ values, are listed in Table 3.1.

Table 3.1 Complete surface area (S_{DFT}), microporosity (V_{mc}) and total porosity (V_{t}) data obtained for H- β (25) C and H-ZSM-5 (30) C samples before and after water treatment (24 h at 110°C, CFR).

Sample type	Sample ID	S_{DFT} (m ² /g) ^(a)	V_{t} (cm ³ /g) ^(b)	V_{mc} (cm ³ /g) ^(c)
Untreated	H β (25) C	540	0.498	0.121
24 h test		397	0.779	0.047
Untreated	HZSM-5 (30) C	844	0.301	0.153
24 h test		696	0.317	0.123

^(a) Specific surface area obtained from NLDFT

^(b) Total pore volume from NLDFT

^(c) Micropore volume from NLDFT

In the case of HZSM-5 (30) C, the pore volumes after treatment did not significantly change in comparison with the untreated sample. However, microporosity decreased by 19.6% in favour of mesopores formation, while total pore volume increased by 5.1%. On top of that, specific surface area (S_{DFT}) has decreased by 17.5%. Contrarily, the H β (25) C sample was

much more impacted by the water, with a drastic decrease in micropore volume and increase of total pore volume of 63.5% and 56.5%, respectively. Although, the specific surface area decreased only by 26.5%.

Therefore, it was noticed that the more structurally dense MFI, FER and MOR structures are less influenced by water in comparison to structures that are disordered *i.e.*, BEA and of low framework density *i.e.*, FAU.

3.2.3 General effect of aluminium content

It was shown above, in Figure 3.2, that the type of framework has an influence on the zeolite behaviour when in contact with water. To expand the screening, more samples provided by Zeolyst were chosen in order to understand the Al content role. Zeolites from the HY, H β and HZSM-5 groups of much wider SiO₂/Al₂O₃ molar ratios (5.1-280) were chosen for this screening. Powder X-ray Diffraction (pXRD) was used to verify the crystallinity of all the initial samples. Diffraction patterns are presented in Figure 3.3.

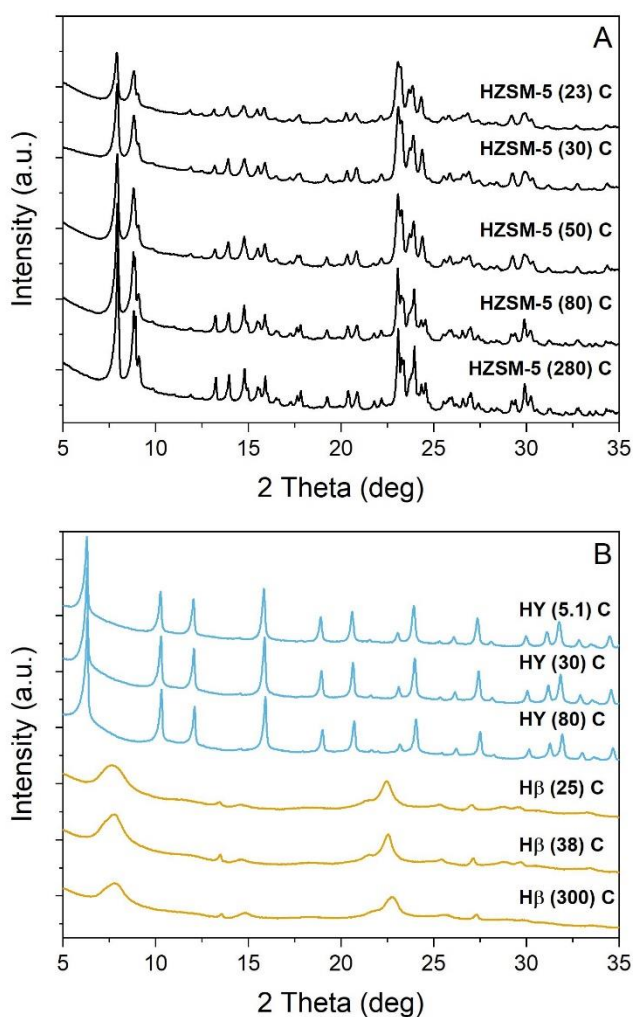


Figure 3.3 Powder X-ray Diffraction patterns were grouped and labelled; black for HZSM-5, MFI structure type (A, top); light blue for HY, FAU structure type and light yellow for H β , BEA structure type (B, bottom).

Presented pXRD patterns of each group match their reference patterns found in IZA Structure Commission database.¹⁸ Following the screening from section 3.2.1, tests were performed for the expanded group of samples. The study was carried out under same experimental conditions, in pressurised water for 24 h at 110°C (CFR). Results of relative crystallinity and microporosity of the expanded screening are presented in Figure 3.4.

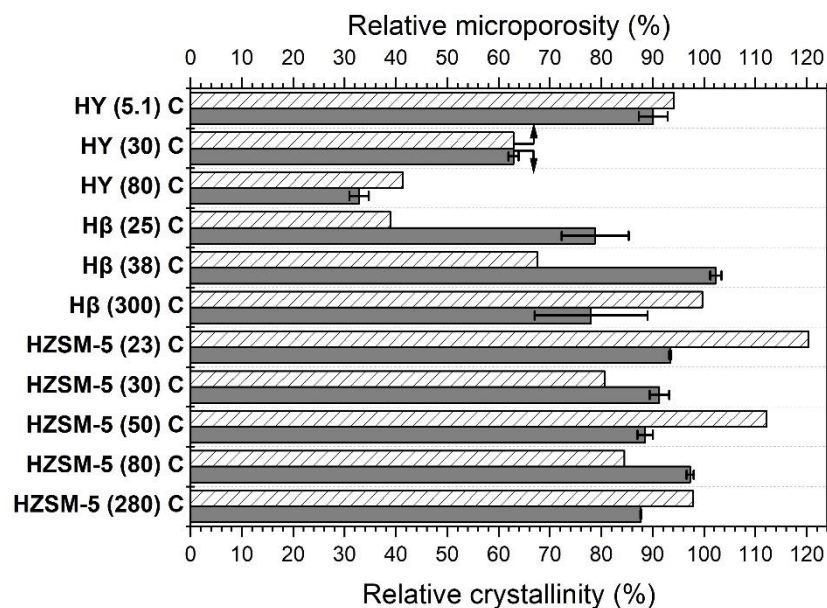


Figure 3.4 Expanding the screening of selected structure type zeolites under pressurised water (24 h at 110°C, CFR). Relative crystallinity error bars represent the standard deviation of the Integrated Peak Area after 5 samples examination.

The study carried out in presence of water at 110°C showed that the general microstructure changes are different for each framework. There was not a uniform trend for all samples, but specific trends within the same group of zeolite frameworks. The error bars represent the standard deviation of the Integrated Peak Areas of five measurements for each sample. For instance, it was observed that as the silicon (Si) content of the low density HY zeolite increased, the relative crystallinity decreased linearly. An opposite observation was seen for the Hβ structure, where more crystallinity retained in the high Si content sample. However, as described before, BEA type structures are more complex structures. Therefore, the determination of crystallinity was subject to a wider standard deviation due to polymorph stacking. Because of this particular zeolite group nature, further examination will be only considered in section 3.2.5 of this Chapter, where the Hβ (38) C sample is tested for ion exchange and possible applications are considered.

On the other hand, the zeolites belonging to the MFI framework showed relatively good stability across the entire range. Here, the MFI showed excellent water stability with a decrease of only 6-13% in crystallinity and still high percentage of relative microporosity. What is more, in the case of the MFI structure, the decrease in crystallinity based on the Al content was not linear. Moving from HZSM-5 (23) C to HZSM-5 (280) C there is a small

change in crystallinity and the overall changes were not as drastic as in the case of the FAU and BEA structure.

In all samples, substantial decrease in micropore volume (V_{mc}) was acknowledged. In the case of HY samples, the loss of microporosity followed the loss of crystallinity while the $\text{SiO}_2/\text{Al}_2\text{O}_3$ molar ratio value increased. The trend was exactly reversed in the case of H β , where the highest silica content sample retained most micropore volume. In the HZSM-5 group, lower microporosity loss was observed in samples of lower $\text{SiO}_2/\text{Al}_2\text{O}_3$ molar ratio. However, in the MFI group the fluctuation in relative microporosity was present as well. This indicated that the possible amorphisation or internal framework collapse might be proceeding. Although, these processes were progressing much slower than in the case of other zeolite groups.

A review article on mesoporosity in zeolites explained that mesopores are created as a consequence of internal micropore fouling and most probably the migration of framework Al into extra-framework sites or extraction of silica at high temperatures.²⁸ Therefore, this suggested that in the case of this study the mesoporosity was formed out of the existing micropores and the possible dissolution of a zeolite is rather internal than external.

3.2.4 Influence of temperature and time on FAU type zeolite

Given that the pre-screening has shown a major influence of water on the FAU framework type group, a more focused investigation on was carried out. The gathered information from previous sections have made it clear that this structure went through most structural changes. The influence of water on the framework stability was presented before on Figure 3.4. The commercial HY ($\text{SiO}_2/\text{Al}_2\text{O}_3$ molar ratio of 5.1-80) samples were chosen for testing in pressurised water (CFR) for the influence of varying time (6-24 h) and temperature (80-110°C). Results are presented in Figure 3.5.

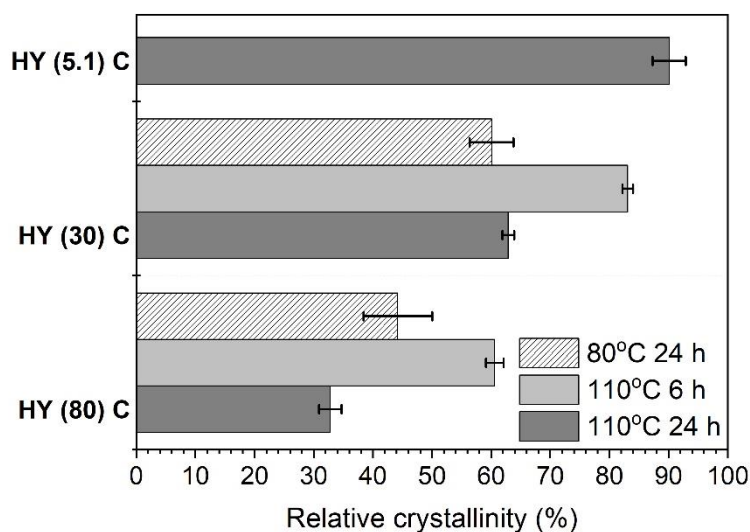


Figure 3.5 Behaviour of FAU type zeolite Y evaluated by pXRD spectra relative crystallinity analysis in temperature of 80°C and 110°C, and time of 6-24 h in CFR. Relative crystallinity error bars represent the standard deviation of the Integrated Peak Area after 5 samples examination.

By decreasing the temperature of water from 110°C to 80°C, higher stability of both lower Al content ($\text{SiO}_2/\text{Al}_2\text{O}_3$ molar ratio 30 and 80) zeolites was observed. It is clear that by decreasing the Al content, a decrease in overall endurance results. Furthermore, the change in water temperature indicated that water had an impact on the zeolite structure. By increasing the temperature, the modification and dissolution of the zeolite framework is accelerated. The obtained results showed that both parameters, time and temperature, have a destructive effect on crystallinity. Interestingly, a clear change in relative crystallinity, after analysing with pXRD, was noticed after only 6 h of water treatment.

Studies on stability of high Al content and dealuminated Y-zeolite in presence of aqueous media^{10,25} and steam²⁴ are already presented in the literature. Yet, these studies were done under autogenic pressure in Teflon lined stainless steel autoclaves. An article by Buttersack *et al.*, explored the stability of a Y zeolite with much higher $\text{SiO}_2/\text{Al}_2\text{O}_3$ molar ratio of 130, and reported that although the zeolite underwent amorphisation, there was no loss in mass after direct contact with water at 130°C.²⁵ According to the authors, the micropore volume loss was paralleled with a formation of mesopores and amorphous phase starting on the outer surface.

Physical properties of the analysed HY zeolites; specific surface area (S_{DFT}), total pore volume (V_t), micropore volume (V_{mc}) and relative crystallinity (X_{rel}) are presented in Table 3.2. These quantifications were done on the tested samples before and after treatment.

Table 3.2 Physical properties of zeolite samples used in this work before and after water treatment (24 h at 110°C, CFR).

Sample ID	Untreated sample			Treated 24 h at 110°C in water			$V_{mc\ rel}^{(d)}$ (%)	$X_{rel}^{(e)}$ (%)
	$V_t^{(b)}$	$V_{mc}^{(c)}$	$S_{DFT}^{(a)}$	$V_t^{(b)}$	$V_{mc}^{(c)}$	$S_{DFT}^{(a)}$		
	(cm^3/g)	(cm^3/g)	(m^2/g)	(cm^3/g)	(cm^3/g)	(m^2/g)		
HY (5.1) C	0.252	0.225	909	0.440	0.212	669	94.2	90.1
HY (30) C	0.317	0.267	919	0.398	0.168	644	62.9	63.0
HY (80) C	0.299	0.246	815	0.394	0.102	581	41.5	32.8

^(a) Specific surface area obtained from NLDFT

^(b) Total pore volume from NLDFT

^(c) Micropore volume from NLDFT

^(d) Relative microporosity calculated according to protocol in Chapter 2 Section 2.4.2

^(e) Relative crystallinity calculated according to protocol in Chapter 2 Section 2.4.1

In all cases, crystallinity (X_{rel}) and micropore volume ($V_{mc\ rel}$) values gradually decreased while the SiO_2/Al_2O_3 molar ratio increased. While the high Al content HY (5.1) C maintained the initial crystallinity at a level of 90.1%, this significantly dropped to 32.8% for the low Al content sample HY (80) C. Total pore volume values increased by 74.6% for the HY (5.1) C versus only 31.8% for HY (80) C sample. In all cases, a decrease in specific surface area (S_{DFT}) and micropore volume (V_{mc}) were observed as well. The secondary mesopore system formation is in good agreement with the observations described and given by Buttersack *et al.*²⁵

Nevertheless, it was previously shown that the commercial Y zeolites provided by Zeolyst and used in this study were post-synthetically modified.²⁹ The zeolites were previously ion exchanged, steamed and acid treated to achieve dealumination and consequently higher SiO_2/Al_2O_3 molar ratios. It was also previously shown that post-modified FAU framework type is much more sensitive to alkaline media.³⁰ After treatment in alkaline solutions, the ultra-stable zeolite Y underwent dissolution and became substantially amorphous.³¹

Furthermore, formation of mesopores and a decrease in specific surface area was directly linked to the ongoing process of material amorphisation.

To verify possible ongoing amorphisation hypothesis, pXRD and N₂-physisorption analysis were performed. Figure 3.6 presents pXRD patterns of the HY (80) C sample before and after treatment in water at 110°C after 6 h and 24 h. A inside graph presents how the relative microporosity compares to relative crystallinity loss.

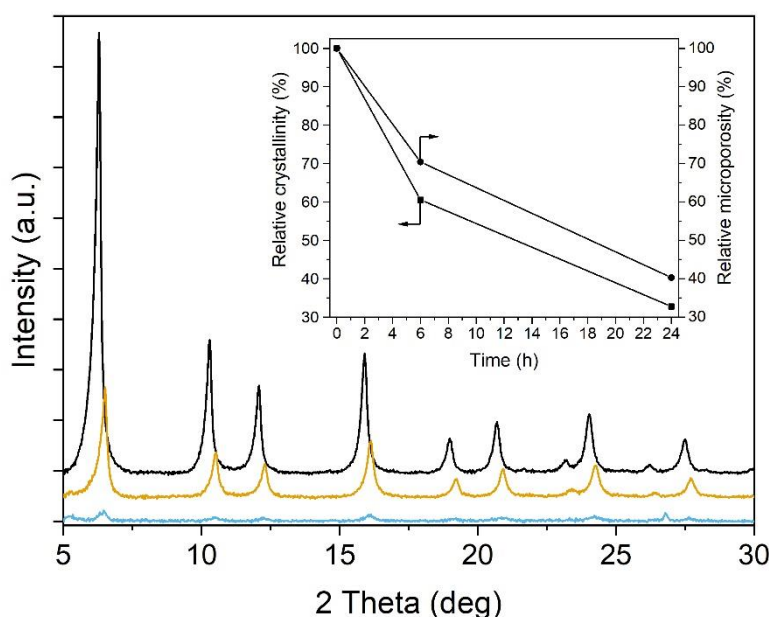


Figure 3.6 The diffraction patterns of commercial zeolite HY (80) C treated in CFR at 110°C: untreated (black), 6 h (yellow) and 24 h (blue). Comparison of relative microporosity and crystallinity of H-Y (80) C sample before and after treatment.

Presented data revealed that a significant internal transformation took place in the FAU type zeolite of SiO₂/Al₂O₃ molar ratio 80. The smaller inside graph, showed linear and parallel tendency of relative crystallinity and microporosity loss as a function of time. Treating the sample with water flow (110°C) resulted in a significant loss in relative crystallinity after only 6 h, and the signal was further decreased after 24 h of treatment. Broadening and peak shifting indicated the decreasing crystallite size as well as changes in the d-spacing. This indicated partial structure disordering, amorphisation or dissolution of the material. After 24 h, the loss of crystallinity was followed by the increase of total pore volume by 31.8%.

To further support and investigate the framework collapse presented in relation to the FAU type zeolite sample, both – DRIFTS FTIR spectra and Quantitative EDX microanalysis were

conducted. The data provided by the EDX analysis on the HY (80) C samples before and after 24 h at 110°C water flow experiment is presented in Table 3.3.

Table 3.3 Data from the quantitative EDX microanalysis performed on the HY (80) C sample before and after water treatment (24 h at 110°C, CFR). Standard deviations represent the distribution of atoms after ten measurements for each sample.

Sample ID	SiO ₂ /Al ₂ O ₃ ^(a)	SD (σ) ^(b)
HY (80) C Untreated	80.03	5.54
HY (80) C 24 h at 110°C	22.80	4.61

^(a) SiO₂/Al₂O₃ molar ratio was determined with EDX analysis; values are an average of 10 different areas of the sample. ^(b) Standard deviation

According to EDX data, the SiO₂/Al₂O₃ molar ratio decreased by 71.5%. This clearly shows that after the 24 h water treatment at 110°C the framework is destroyed due to Si and Al leaching. Although, the amount of initial Al is too low to definitely state that main degradation mechanism is desilication. Apparently, metal leaching is one of the permanent deactivation mechanisms that involve zeolite materials.³²

However, changes in the zeolite framework were easily detected by the DRIFTS FTIR analysis. The spectra of the untreated and treated HY (80) C samples are presented in Figure 3.7. The most important vibrations are annotated with asterisks.

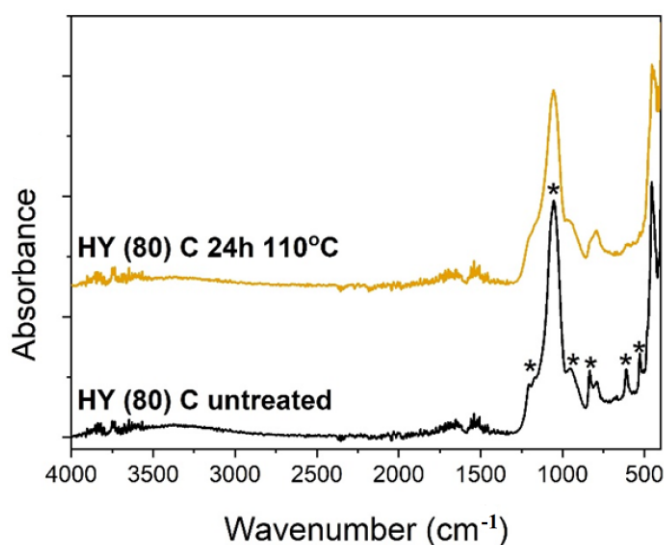


Figure 3.7 DRIFTS FTIR spectra of the untreated and water treated (24 h at 110°C, CFR) HY (80) C samples.

The spectrum of the untreated sample showed intensive bands at 1050 cm^{-1} , with two weaker sideband at 1205 cm^{-1} and 950 cm^{-1} , all attributed to the Si-O and Al-O asymmetrical stretching vibrations of the internal Si and Al exchanged tetrahedra.³³ Band located at 830 cm^{-1} , 610 cm^{-1} and 528 cm^{-1} were all assigned with stretching and bending vibrations Si-O-Al bonding and octahedral group, *i.e.* extra-framework Al species.³⁴ The difference between the untreated and treated spectra is the disappearance of bands assigned to EFAl. This meant that most likely EFAl species were no longer present in the sample after water treatment. Yet, this observation needs additional confirmation by ^{27}Al MAS NMR studies. However, bands assigned to framework positions remained unchanged meaning that framework Al positions remained stable in the sample.

Even though the EDX microanalysis confirmed that the material lost majority of its Si, this was not sufficient to prove how the remaining Si environment rearranged in the sample after water treatment. With the help of MAS NMR, it is possible to possibly confirm that the EFAl was removed from the sample and the Si and Al environment changed. In order to prove those assumptions, both ^{29}Si and ^{27}Al MAS NMR were conducted.

The Single Pulse ^{29}Si and ^{27}Al MAS NMR spectra of the untreated and water treated (24 h, 110°C) HY (80) C samples are presented in Figure 3.8.

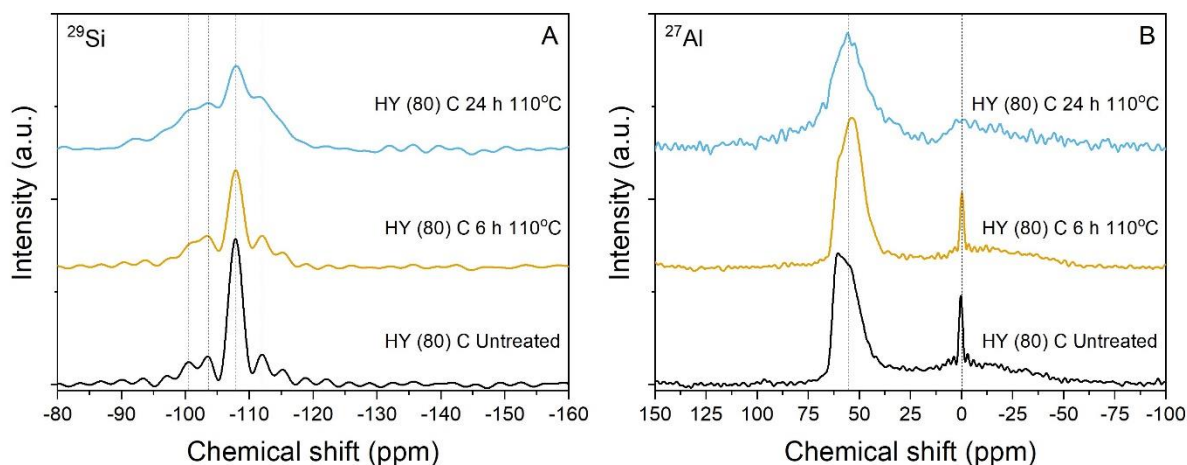


Figure 3.8 Single Pulse ^{29}Si (left, A) and ^{27}Al (right, B) MAS NMR spectra for the untreated (black), 6 h at 110°C (yellow) and 24 h at 110°C (blue) water treated HY (80) C samples.

Significant changes were observed in both, the Si and Al environment. As described in Chapter 2 (see section 2.6.10.4), in a zeolite Si can occur in five possible coordination environments. The most common distribution is the so-called Q^4 coordination, which is

linked to the SiO₄ tetrahedron building the framework. The region assigned to this coordination falls between -105 and -120 ppm. In the Single Pulse ²⁹Si NMR spectra (left, A) of the untreated sample, a strong resonance peak at -107 ppm was observed. The resonance was attributed to the highly ordered Q⁴ [Si(OSi)₄] coordination.³⁵ A small peak, also associated with the Q⁴ was observed at -112 ppm. The Q³ coordination peaks of much lower intensity were observed at -103 ppm and -100 ppm. The spectra of the treated in water samples were much different. It was observed, that only after 6 h of treatment, the main peak intensity has lowered and the Q³ increased. However, after 24 h, the arising of the Q³ was significant. The appearance of the Q³ signal is associated with formation of mostly [(SiO)₃SiOH] units. This indicated that the framework became significantly defective and degradation propagated as leaching took place.

As described in Chapter 2 (see section 2.6.10.3), most often Al occurs in a zeolite framework in two distinctive coordinations. This is the tetrahedral framework Al (between 100 ppm and 50 ppm) and octahedral extraframework Al (between 20 ppm and -10 ppm). In the case of the ²⁷Al (right, B) NMR, the spectrum of the untreated sample presented a tetrahedrally coordinated Al resonance peak located at 55 ppm and octahedral extraframework (EFAl) coordination peak located at 0 ppm. After 6 h of water treatment, the 0 ppm peak was still intense. Although, after 24 h the resonance was no longer observed. This confirmed the previous considerations derived from the DRIFTS FTIR spectra, where bands assigned to EFAl were no longer detected. The main framework Al peak was much broader, but still of high intensity.

The mesopore formation is associated with the removal of the octahedral Al, which is accompanied by the process of Si dissolving. However, while the Si leaches out of the framework positions, Al was found to be more stable in the lattice. The extraction of Al generated hydroxyl defects on the surface of the framework.³⁶ It seems that the hydrolysis occurs on the Si-O-Si bridges while EFAl species are extracted from the sample.

3.2.5 Influence of Na ion exchange on commercial ZSM-5

Even though the protonated forms of zeolites were the most employed in applications in the oil-refining and petrochemical industries, there were cases in which the negative charge of the structure was balanced by with an alkali cation, such as sodium (Na).³⁷

A partial exchange of Mo/ZSM-5 ($\text{SiO}_2/\text{Al}_2\text{O}_3 = 30$) catalysts with the Na^+ cation was reported to neutralize strong acid sites associated with the framework Al atoms.³⁸ The alkali exchange helped decreasing coke formation and improved the stability of the Mo/ZSM-5 catalyst in the non-oxidative methane dehydroaromatisation (MDA) reaction. Therefore, Na^+ ion exchange could be employed as additive for enhancing zeolite stability and higher anti-coke capability.

In terms of membrane stability, earlier studies found that ZSM-5 nanosheets of medium Al content ($\text{SiO}_2/\text{Al}_2\text{O}_3 = 50$) exhibited outstanding stability of at least 1 month performance in pervaporation desalination of brines, with saline concentrations up to 24 wt. %.³⁹ It was explained that the high hydrophilicity resulted from high Al surface content and Na^+ as extra-framework ion compensator ($[\text{AlO}_2]-\text{Na}^+$).

According to Buttersack *et al.*, Na^+ counter ions had a strong negative impact on the stability of siloxane bonding in a zeolite Y after contact with water.²⁵ However, the statement that H-forms were more stable than Na-form was valid only for dealuminated zeolites. It was also acknowledged that the behaviour of the non-dealuminated zeolite of high Al content was completely reversed.

Water vapour sorption isotherms of commercial untreated zeolite HZSM-5 (23) C and HZSM-5 (280) C samples before and after Na^+ ion exchange is presented in Figure 3.9. Ion exchange was performed according to the protocol described in detail in Chapter 2, Section 2.3.4.

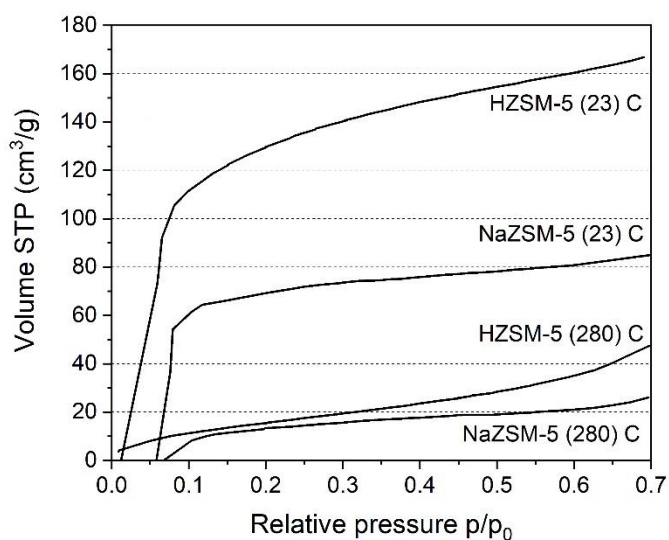


Figure 3.9 Water vapour sorption isotherms of commercial protonated and Na ion-exchanged HZSM-5 (23) C and HZSM-5 (280) C samples.

The effect of preferential neutralising the acidic H sites associated with Al atoms by partial Na exchange led to a drastic change in water vapour uptake of the zeolite. In both cases the protonated and Na⁺ ion exchanged ZSM-5 samples have presented a type I isotherm which is characteristic for microporous hydrophilic solids. However, in both cases, after Na ion exchange the water vapour sorption ability was decreased by 50% compared to the protonated forms. Water vapour sorption in presence of Na extra-framework counter-ion was considerably much lower compared to HZSM-5 analogues with silanol surface defects. The phenomenon was studied back in the 1980s and was considered as an adsorption of isolated water molecules on the alkali metal cation and a second shell build-up at higher equilibrium pressures.⁴⁰

To further explore the effect of Na⁺ as counter-ion, sodium exchanged commercial ZSM-5 were compared with their protonic forms. Relative crystallinity and microporosity data derived from H⁺ and Na⁺ samples are presented in Figure 3.10.

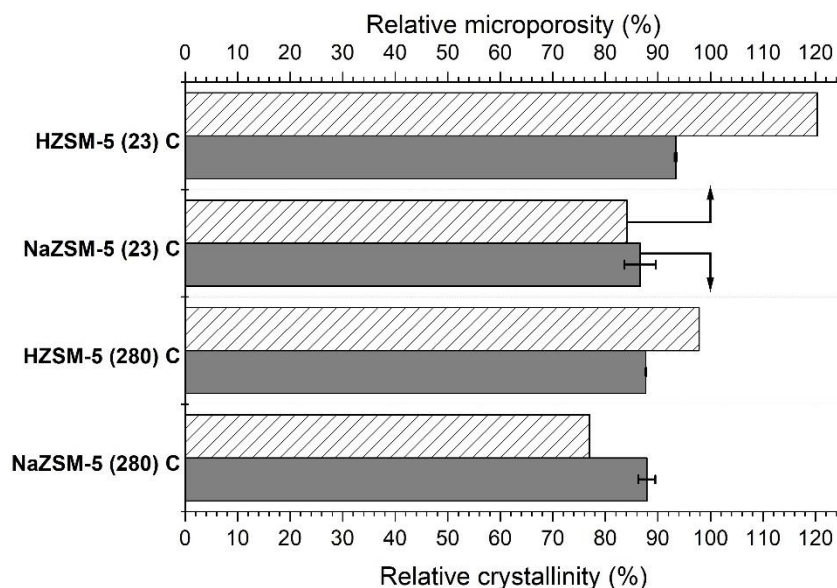


Figure 3.10 Influence of Na- ion exchange on commercial HZSM-5 (23) and (280) samples treated with water (24 h at 110°C, CFR) – relative crystallinity and microporosity comparison between H⁺ and Na⁺ samples. Relative crystallinity error bars represent the standard deviation of the Integrated Peak Area after 5 samples examination.

It was acknowledged that the addition of Na to the zeolite did not significantly modify the overall water stability. Only minor changes in relative crystallinity and microporosity were observed after water treatment (24 h, at 110°C, CFR). The error bars represent the standard deviation of the Integrated Peak Areas of five measurements for each sample. In the case of the Na⁺ and HZSM-5 (23) C sample, the protonated material shows much higher relative microporosity. The additional micropore volume might as well originate from the structure dissolution and be created instead of mesopores.

To confirm SiO₂/Al₂O₃ and Na₂O/SiO₂ ratios, EDX analysis was performed and the dataset is presented in Table 3.4. Due to EDX selectivity and dynamic range limitations, data is shown only for HZSM-5 (23) C and NaZSM-5 (23) C samples.

Table 3.4 EDX analysis on HZSM-5 (23) C and NaZSM-5 (23) C samples before and after water treatment (24 h at 110°C, CFR). Standard deviations represent the distribution of atoms after ten measurements for each sample.

Sample ID	Untreated				Treated 24 h at 110°C in water			
	SiO ₂ /Al ₂ O ₃ ^(a)	SD	Na ₂ O/SiO ₂ ^(b)	SD	SiO ₂ /Al ₂ O ₃ ^(a)	SD	Na ₂ O/SiO ₂ ^(b)	SD
HZSM-5 (23) C	20.65	0.29	0.01	0.00	17.92	0.43	0.01	0.00
NaZSM-5 (23) C	21.55	1.75	0.21	0.02	21.33	0.47	0.14	0.00

^(a) SiO₂/Al₂O₃ molar ratio was determined with EDX analysis; values are an average of 10 different areas of the sample.

^(b) Na₂O/SiO₂ molar ratio was determined with EDX analysis; values are an average of 10 different areas of the sample.

In terms of the SiO₂/Al₂O₃ molar ratio of HZSM-5 (23) C, the sample had a much higher decrease in the molar ratio. This means, that desilication took place to a much higher extent than in terms of the alkali-exchanged sample. What is more, it was acknowledged that hydrophobicity did affect the overall stability of the zeolite. Therefore, the presence of Na⁺ in the structure is preserving the crystallinity to some extent confirming previous assumptions.

3.2.6 Alkali ion exchange on commercial β (38) zeolite

Data gathered in the previous section (see Section 3.2.5) of this Chapter, indicated the probability of enhancing stability of zeolites in water by alkali ion exchange. Such stability would find applications in separation processes or aqueous environment catalysis. A recent study⁴¹ speculated the use of alkali-exchanged β zeolite as Lewis-acid catalysts. The study compared a commercial zeolite NH₄β (25) with ion exchanged (Li⁺, Na⁺ and K⁺) and a commercial Snβ (38) sample. According to the authors, the alkali-exchanged samples were not active for alcohol dehydration or reductive etherification of HMF. Although, all of them were equally stable during the reaction.

In terms of CO₂ adsorption, a Naβ zeolite (SiO₂/Al₂O₃ = 15) after ion exchange showed an increase in adsorption capacity in the sequence of K⁺>Na⁺>Li⁺>Ba²⁺>Ca²⁺>Mg²⁺. The performance of K⁺ exchanged β zeolite was confirmed by adsorption isotherms and corresponding heats of adsorption for CO₂.⁴²

To explore the effect of alkali counter-ions, alkali-exchanged commercial H β (38) C samples were compared with its protonic form and the results are shown in Figure 3.11. Ion exchange was performed according to the protocol described in detail in Chapter 2, Section 2.3.4.

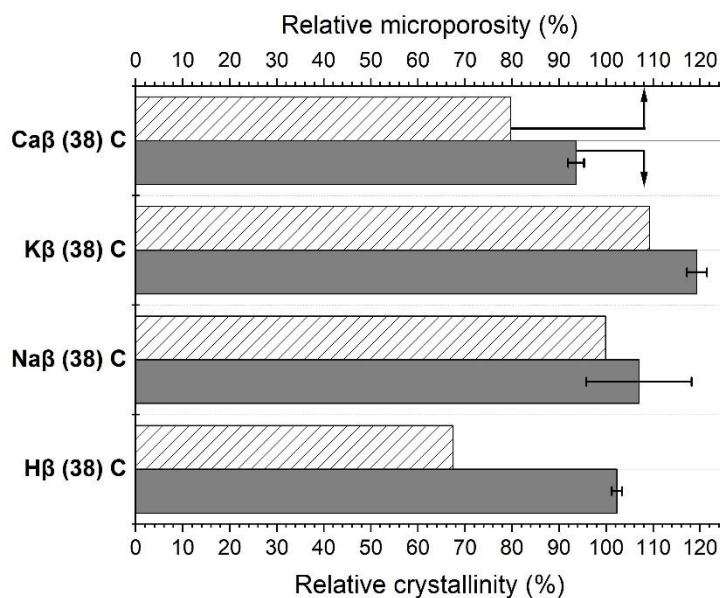


Figure 3.11 Influence of alkali ion exchange on commercial H β (38) C samples treated with water (24 h at 110°C, CFR) – relative crystallinity and microporosity comparison between H⁺ and alkali exchanged samples. Relative crystallinity error bars represent the standard deviation of the Integrated Peak Area after 5 samples examination.

The test resulted in an increased relative microporosity in alkali exchanged zeolite in the K⁺>Na⁺>H⁺>Ca²⁺ sequence. Which is in line with previously discussed CO₂ adsorption capacity. Samples exchanged with K⁺ and Na⁺ gave better results in terms of relative crystallinity. Studies have shown that by customising the hydrophobicity of zeolite channels, inner active sites may be protected in aqueous environment.⁴³ This is the case, since Na ion exchange of HZSM-5 zeolite has already confirmed that water vapour sorption abilities decreased by 50% compared to its protonated forms (See Figure 3.9). To make a clearer view, Table 3.5 summarises all of the textural details of examined samples before and after water treatment.

Table 3.5 Textural properties of ion exchanged H β (38) C zeolite samples used in this work before and after water treatment (24 h at 110°C, CFR).

Sample ID	Untreated sample			Treated 24 h at 110°C in water			X _{rel} ^(d) (%)
	V _t ^(b) (cm ³ /g)	V _{mc} ^(c) (cm ³ /g)	S _{DFT} ^(a) (m ² /g)	V _t ^(b) (cm ³ /g)	V _{mc} ^(c) (cm ³ /g)	S _{DFT} ^(a) (m ² /g)	
Ca β (38) C	0.307	0.197	729	0.459	0.157	685	93.6
K β (38) C	0.227	0.117	460	0.430	0.128	593	119.3
Na β (38) C	0.305	0.199	722	0.623	0.199	929	107.2
H β (38) C	0.298	0.200	755	0.755	0.135	799	102.3

^(a) Specific surface area obtained from NLDFT

^(b) Total pore volume from NLDFT

^(c) Micropore volume from NLDFT

^(d) Relative crystallinity calculated according to protocol in Chapter 2 Section 2.4.1

In terms of total pore volume, the Ca β (38) C samples had the lowest increase of total pore volume, by 49.5%. Compared to the H β (38) C sample, which resulted in highest increase of 153.3%. The K β (38) C and Na β (38) C samples have shown an increase of 89.4% and 104.3% increase, respectively. Although, K β (38) C and Na β (38) C samples showed best results in terms of minimal micropore volume increase of 9.4% and 0%, respectively. The two other samples, Ca β (38) C and H β (38) C, lost 20.3% and 32.5% of their micropore volume. Overall, the largest change was noticed for the H β (38) C sample, where the largest pore changes were recorded.

All samples were examined by EDX to investigate the possible change in SiO₂/Al₂O₃ and X/Al ratios (where X is the alkali ion). Data was gathered in Table 3.6.

Table 3.6 EDX analysis of ion exchanged H β (38) C sample before and after water treatment (24 h at 110°C, CFR). X refers to the counter ion. (*) In the case of H β (38) C sample, the X is Na⁺ ion. Standard deviations represent the distribution of atoms after ten measurements for each sample.

Sample ID	Untreated				Treated 24 h at 110°C in water			
	SiO ₂ /Al ₂ O ₃ ^(a)	SD	X/Al ^(b)	SD	SiO ₂ /Al ₂ O ₃ ^(a)	SD	X/Al ^(b)	SD
Ca β (38) C	34.28	1.77	0.42	0.04	27.58	3.32	0.40	0.01
K β (38) C	33.29	0.54	1.04	0.05	25.37	0.74	0.67	0.05
Na β (38) C	33.29	1.88	0.91	0.13	23.68	1.11	0.66	0.13
H β (38) C	34.30	1.25	0.10 ^(*)	0.05	22.32	1.27	0.07 ^(*)	0.02

^(a) SiO₂/Al₂O₃ molar ratio was determined with EDX analysis; values are an average of 10 different areas of the sample.

^(b) X/Al molar ratio was determined with EDX analysis; values are an average of 10 different areas of the sample.

The H β (38) C sample presented a higher decrease in SiO₂/Al₂O₃ molar ratio, than its alkali-exchanged derivatives. This means that desilication took place to a much higher extent in the protonated sample than in the alkali-exchanged ones. Lowest decrease in the molar ratio was observed in the case of the Ca β (38) C sample. What is interesting, in contrast to other ions, the calcium (Ca²⁺) ion remained in the internal channels. The negative charge introduced by aluminium in the framework is compensated by calcium. Meaning that one divalent Ca²⁺ ion compensates for two aluminium atoms, instead of two monovalent K⁺ or Na⁺ ions. The Ca²⁺ ion occupies a space within the channel between two adjacent aluminium atoms and remains within this region. In contrast to the K⁺ and Na⁺, Ca²⁺ ions are difficult to move and are not diffusing through the zeolite.⁴⁴ This also might explain the lowest increase of total pore volume since the ion is not removed from the framework as easily as Na⁺ and K⁺. The EDX analysis confirmed that the untreated and treated samples had same wt. % of Ca²⁺.

It was observed that the framework degradation under aqueous phase conditions is similar to the protonated and sodium exchanged MFI structure discussed in previous section (Section 3.2.5). This allows the conclusion that alkali ion exchange on zeolites limits the excessive degradation of the internal zeolite framework.

3.2.7 LTA zeolite stability

The 5 Å molecular sieves are produced by cation exchange of calcium (Ca) for sodium (Na) in zeolite A. Commercial desiccants are in a form of beads or pellet. The LTA zeolite used in this study was a CaA zeolite (LTA, Linde type A framework), a Ca^{2+} exchanged sodium aluminium silicate (BCR-705, provided in form of beads with 1-2 % clay as binder). Further information about LTA structure and its properties can be found in Chapter 1 (see section 1.1.1).

In general, the zeolite A (LTA framework) is an important zeolite widely used in solvent dehydration, as described in Chapter 1 (see Section 1.1.4.2). It is characteristic for its superior properties such as a 3-dimensional channel system of small pores, low FD_{Si} of 14.2 and significant water uptake possibilities. Herein, the LTA framework was used due to its low $\text{SiO}_2/\text{Al}_2\text{O}_3$ molar ratio of 2, which means that the distribution of Si and Al is equal in the structure.

The pXRD analysis was used to verify the crystallinity of the zeolite A untreated and water treated samples. Conditions were kept the same, as for previous samples, *i.e.*, the test was performed in pressurised water (CFR) for 24 h at 110°C. Figure 3.12 presents diffraction patterns of both samples.

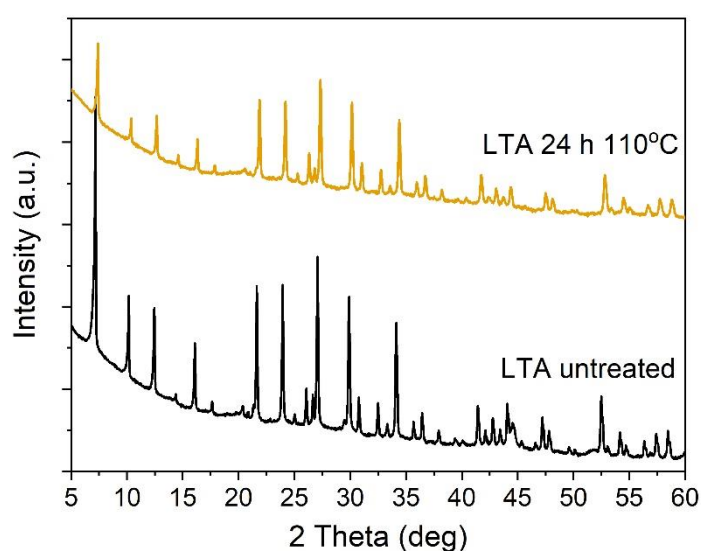


Figure 3.12 The pXRD patterns of untreated and treated in water (24 h at 110°C, CFR). Comparison of diffraction patterns before and after treatment with water.

The diffraction patterns were compared to IZA Structure Commission database available online. Presented pXRD patterns matched the reference the patterns corresponding to the LTA framework. The major reflection peaks were located at (2θ) 7.2°, 10.2°, 12.5°, 16.2°, 21.7°, 24.0°, corresponding to the (200), (220), (222), (420), (442) and (622) lattice planes, respectively.¹⁸ The pXRD peak intensity for the treated sample is much less intense than the untreated one. After water treatment, the Integrated Peak Area was only of 46.9% of the untreated sample.

Values presented in Table 3.7 are the textural properties of the zeolite A samples before and after treatment. Data is derived from N₂-physisorption and water vapour sorption analysis.

Table 3.7 Textural properties of LTA samples used in this work before and after water treatment (24 h at 110°C, CFR).

Sample ID	V _t ^(b) (cm ³ /g)	V _{mc} ^(c) (cm ³ /g)	S _{DFT} ^(a) (m ² /g)	Vapour sorption capacity (cm ³ /g)
LTA Untreated	0.378	0.220	1168	245
LTA 24 h 110°C	0.391	0.210	1106	-

^(a) Specific surface area obtained from NLDFT

^(b) Total pore volume from NLDFT

^(c) Micropore volume from NLDFT

A small reduction in porosity after testing was attributed to the increase in mesoporosity as the volume of micropores decreased. The high surface area of the untreated sample remained nearly unchanged, indicating that even if framework damage is propagating, the core of structure is still intact. However, water vapour sorption capacity was highest among all tested samples, reaching 245 mL g⁻¹.

Quantitative EDX microanalysis was conducted to assess the elemental composition of the samples. The analysis was done in order to understand how the elemental composition changes after water treatment. Table 3.8 presents a summary of wt. % composition of the untreated and water treated sample.

Table 3.8 LTA sample wt. % composition conducted by EDX before and after water treatment (24 h at 110°C, CFR). The SiO₂/Al₂O₃ molar ratios, standard deviations and relative crystallinity are given. Standard deviations represent the distribution of atoms after ten measurements for each sample.

Sample ID	O Wt. %	Si Wt. %	Al Wt. %	Na Wt. %	Ca Wt. %	Mg Wt. %	SiO ₂ / Al ₂ O ₃ ^(a)	SD (σ)	X _{rel} ^(b) (%)
LTA Untreated	59.16	17.01	12.94	3.51	5.72	1.66	2.53	0.08	100.0
LTA 24 h 110°C	57.25	17.81	14.21	0.15	8.82	1.75	2.41	0.11	46.9

^(a) SiO₂/Al₂O₃ molar ratio was determined with EDX analysis; values are an average of 10 different areas of the sample.

^(b) Relative crystallinity calculated according to protocol in Chapter 2 Section 2.4.1

According to the EDX quantitative analysis, the average elemental composition was 17.01 wt. % of Si and 12.94 wt. % of Al. These values after treatment were 17.81 wt. % of Si and 14.21 wt. % of Al. This means that higher wt. % of Si and Al remained in the sample after treatment and the SiO₂/Al₂O₃ molar ratio has not changed in a significant way, by only 4.3%. As mentioned before, crystallinity of the treated samples has decreased by 53.1% in comparison with the untreated one.

On the other hand, Na was extracted nearly completely from the sample after water treatment in the CFR. The larger alkali ions (Mg²⁺ and Ca²⁺) remained in the structure. This phenomenon was previously observed in the alkali ion exchanged H β samples (see Section 3.2.6).

The MP-AES analysis was used to determine the Si and Al concentrations in the effluent water, which was collected after passing through the sample. The amounts Si and Al that leached from the solid sample were approximately 17.40 wt. % and 20.77 wt. % of the total Si and Al in the sample, respectively. This means that the MP-AES analysis is in good agreement with the EDX and the observed loss of crystallinity derived by XRD.

In order to understand the Si and Al distribution before and after treatment both MAS NMR was conducted. The Single Pulse ²⁹Si and ²⁷Al MAS NMR spectra of both untreated and treated with water (24 h, 110°C) LTA samples are presented in Figure 3.13.

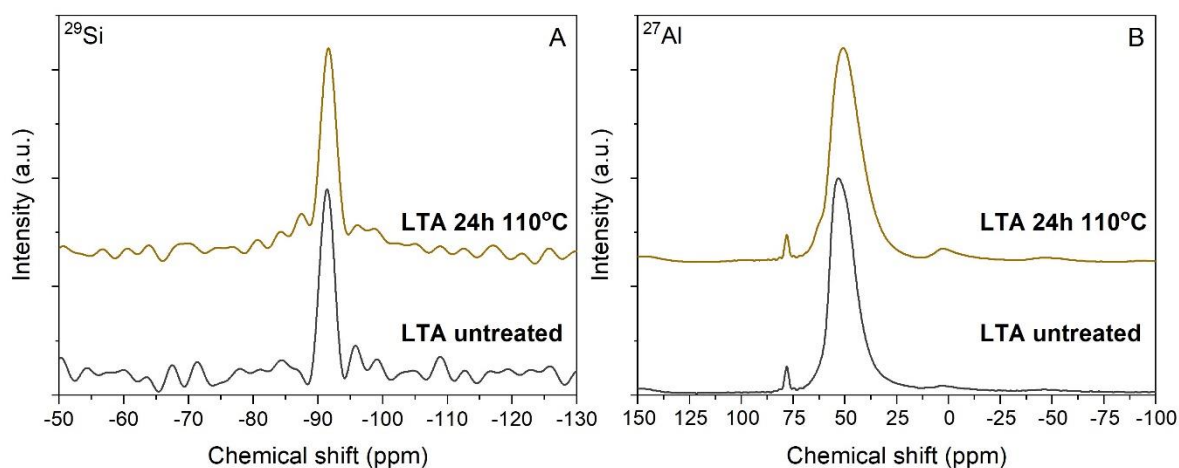


Figure 3.13 Single Pulse ^{29}Si (left, A) and ^{27}Al (right, B) MAS NMR spectra for the untreated (black) and water treated (yellow) for 24 h at 110°C , LTA samples.

In comparison to previously presented Solid State NMR spectra, here (left, A) the Si Q^4 coordination is not observed. Instead, both of the samples exhibited sharp resonance peaks at -91.5 ppm, attributed to the Q^0 $[\text{Si}(\text{OAl})_4]$ units coordination at the usual shifts for zeolite A which is in line with previous studies on the LTA zeolite.^{45,46} The spectrum of the treated sample is no different than the untreated. This means that the Si leaches out of the sample and not *e.g.* undergoes phase transition.

However, minor changes were observed in the Single Pulse ^{27}Al NMR (right, B) spectra. While the untreated sample resonance spectrum exhibited framework Al in tetrahedral coordination (51.3 ppm), the resonance was much broader in the water treated sample, only after 24 h of water treatment. What is more, a small amount of octahedral coordinated EFAl was detected. The well separated signal located at 78 ppm could be assigned to the tetrahedrally coordinated calcium aluminosilicate (framework or extra-framework) groups or the clay binder (most likely calcium aluminate CaAl_2O_4).⁴⁷

3.2.8 Framework density considerations

The results presented so far demonstrated the water impact on the stability of various zeolite frameworks and their internal degradation. The comparison of a wide variety of commercial zeolites gave insight into the water stability of different structures of similar chemical composition. For the purpose of the work, Table 3.9 summarises all structural details for

analysed zeolites. Presented data is based on the information found in Database of Zeolite Structures.¹⁸

Table 3.9 Summary of structural parameters of examined zeolites.

Zeolite structure	MOR	FER	FAU	BEA	MFI	LTA
Type of rings	12, 8, 5, 4	10, 8, 6, 5	12, 6, 4	12, 6, 5, 4	10, 6, 5, 4	8, 6, 4
SBU	5-1	5-1	6-6 or 6-2 or 6 or 4-2 or 1-4-1 or 4	N/A	5-1	8 or 4-4 or 6-2 or 6 or 1-4-1 or 4
Framework density (FD _{Si}) (T/1000 Å ³)	17.0	17.6	13.3	15.3	18.4	14.2

The secondary building units (SBU) are formed from [SiO₄] and [AlO₄]⁻ tetrahedra linked by oxygen bridges. Framework density (FD_{Si}) is a number of tetrahedral atoms per 1000 Å³, calculated for an idealised SiO₂ composition in the highest possible space group. Therefore, the higher the number, the denser the structure and lower the inner pore volume. As described in Chapter 1 (see Section 1.1.2), frameworks with lower FD_{Si} are predominantly built of 4-membered rings. The higher the FD, the larger the rings and smaller pores and more compact structure.

The same table with corresponding relative crystallinity for each tested sample, gathered from Figure 3.2 and 3.4, and Table 3.7 of this Chapter, is presented on Figure 3.14.

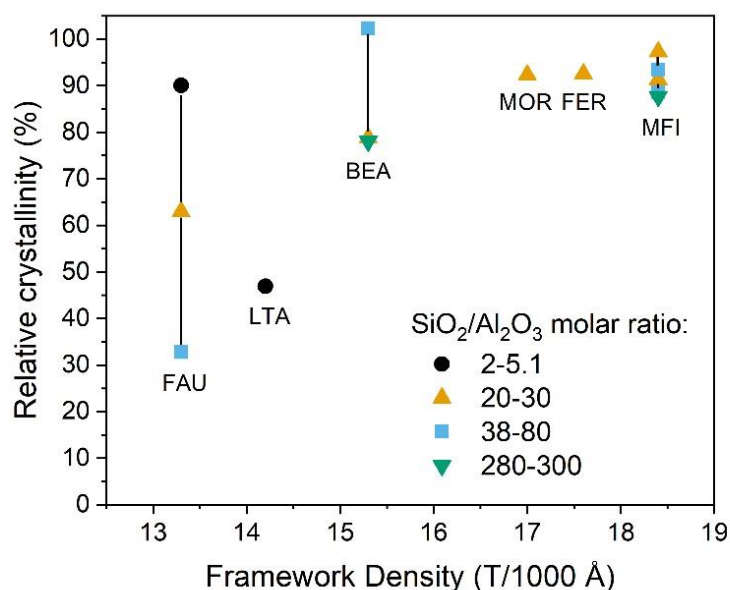


Figure 3.14 Relative crystallinity of different zeolite samples after water treatment (24 h at 110°C, CFR) versus Framework Density (FD_{Si}) of the analysed structures. All samples were divided into groups, according to the aluminium content and the SiO₂/Al₂O₃ molar ratio: ultrahigh 2-5.1 (black circle), high 20-30 (yellow triangle), medium 38-80 (blue square) and low 280-300 (green reversed triangle).

All tested zeolites were divided into groups, according to the SiO₂/Al₂O₃ molar ratio and therefore higher Al content: ultrahigh (2-5.1 ratio), high (20-30 ratio), medium (38-80 ratio) and low (280-300 ratio). As presented on the Figure, there is a general trend of higher relative crystallinity for denser zeolite structures (higher FD_{Si}). What is more, inside every framework group, zeolites with higher Al content showed higher relative crystallinity values. This means that Al might play an important role in the overall zeolite structure stability, when in contact with water.

3.3 Conclusions

In this chapter, stability tests were done on a variety of commercial zeolites. In particular, a different approach, focusing on representing real industrial processes and detailed spectroscopic studies before and after water treatment was employed. The investigation of water impact started from measuring the relative crystallinity and microporosity of selected zeolites. These comparisons were used as a first descriptor of the stability of the materials. Maintaining initial crystallinity is often crucial for the activity and performance of the material in catalysis, sorption and membrane processes.

The general aim was to achieve better understanding of the processes that undergo in the internal framework of zeolites while use of pressurised water flow. A range of detailed comparison between different structures (MFI, BEA, FAU, MOR and FER) and wide $\text{SiO}_2/\text{Al}_2\text{O}_3$ molar ratios was explored in order to have a better insight of the hydrothermal stability among these structures. To generate relations a variety of studies were conducted, including, powder X-Ray Diffraction (pXRD), vapour sorption isotherms, N_2 -physisorption isotherms, Energy-Dispersive X-ray spectroscopy (EDX) and ^{29}Si and ^{27}Al MAS NMR.

This study resulted in a conclusion, that the zeolites of the MFI framework (ZSM-5 zeolite) were most hydrothermally stable among all tested structures. Micropore analysis suggested that in most cases, under the influence of water, mesopores were formed and the structures lost their initial crystallinity. Quantitative EDX analysis confirmed that the HY as well as HZSM-5 and alkali-exchanged zeolites underwent desilication, but to a different extent. DRIFTS analysis on H-Y (80) C sample gave an idea of the sequence of processes undergoing in the structure – EFAl removal, desilication and finally a possible framework Al removal. A partial exchange of the HZSM-5 (23) C sample with a Na^+ counter ion led to drastic change in hydrophilicity. The desilication process was not as drastic as in the case of the protonated sample. A partial ion exchange of H β (38) C with K^+ , Na^+ and Ca^{2+} showed that the Ca^{2+} exchanged sample was least affected by water. Furthermore, after water treatment Ca^{2+} remained in the structure, opposite to K^+ and Na^+ , which leached out.

By exploring the 5 Å zeolite A (LTA structure) by comparing data generated from ^{29}Si and ^{27}Al MAS NMR and MP-AES it became clear that Si and Al leaching happen both at the same time. As previously shown, larger alkali ions such as calcium remained in the structure, while those of smaller atomic radius (sodium) leached out.

From the data obtained so far, it can be concluded that desilication as well as dealumination are equally the main cause of structure failure. Most likely, Si-O-Si bridges underwent hydrolysis after EFAl removal, starting from the smallest rings building the zeolite internal channels. In all cases, the micropore volume and overall total porosity were affected.

The framework density was directly related to the pore volume and rings subunits in the zeolite structure. The research presented in this work shows that zeolites with higher values of FD_{Si} are much more stable in water environment than those with lower FD_{Si} . What is more, structures with higher Al content among all tested frameworks, were more resistant to textural damage.

3.4 References

- 1 T. W. Wong, *Handbook of Zeolites: Structure, Properties and Applications*, Nova Science Publishers, 2009
- 2 K. Muraoka, W. Chaikittisilp, T. Okubo, *J. Am. Chem. Soc.*, 2016, **138**, 6184–6193
- 3 M. Fasano, T. Humplik, A. Bevilacqua, M. Tsapatsis, E. Chiavazzo, E. N. Wang, P. Asinari, *Nat Commun*, 2016, **7**, 12762
- 4 Y. H. Teow, A. W. Mohammad, *Desalination*, 2019, **451**, 2–17
- 5 T. Welton, *Proc. R. Soc. A*, 2015, **471**, 20150502
- 6 C. J. Heard, L. Grajciar, F. Uhlík, M. Shamzhy, M. Opanasenko, J. Čejka, P. Nachtigall, *Adv. Mater.*, 2020, **32**, 2003264
- 7 J. C. Groen, J. C. Jansen, J. A. Moulijn, J. Pérez-Ramírez, *J. Phys. Chem. B*, 2004, **108**, 13062-13065
- 8 M. Dusselier, M. E. Davis, *Chem. Rev.*, 2018, **118**, 5265-5329
- 9 A. Vjunov, J. L. Fulton, D. M. Camaioni, J. Z. Hu, S. D. Burton, I. Arslan, J. A. Lercher, *Chem. Mater.*, 2015, **27**, 3533–3545
- 10 R. M. Ravenelle, F. Schüßler, A. D’Amico, N. Danilina, J. A. van Bokhoven, J. A. Lercher, C. W. Jones, C. Sievers, *J. Phys. Chem. C*, 2014, **114**, 19582-19595
- 11 H. Xiong, H. N. Phama, A. K. Datye, *Green Chem.*, 2014, **16**, 4627-4643
- 12 T. Ennaert, J. Geboers, E. Gobechiya, C. M. Courtin, M. Kurttepel, K. Houthoofd, C. E.A. Kirschhock, P. C. M. M. Magusin, S. Bals, P. A. Jacobs, B. F. Sels, *ASC Catal.*, 2015, **5**, 754-768
- 13 D. W. Gardner, J. Huo, T. C. Hoff, R. L. Johnson, B. H. Shanks, J. P. Tessonnier, *ACS Catal.*, 2015, **5**, 4418–4422
- 14 L. Zhang, K. Chen, B. Chen, J. L. White, D. E. Resasco, *J. Am. Chem. Soc.*, 2015, **137**, 11810-11819
- 15 S. Proding, H. Shi, S. Eckstein, J. Z. Hu, M. V. Olarte, D. M. Camaioni, M. A. Derewinski, J. A. Lercher, *Chem. Mater.*, 2017, **29**, 7255-7262
- 16 A. A. C. Reule, J. A. Sawada, N. Semagina, *J. Catal.*, 2017, **349**, 98-109
- 17 C. Willes and P. Watts, *Green Chem.*, 2012, **14**, 38-54
- 18 IZA Structure Commission database <http://www.iza-structure.org/databases/>
- 19 M. M. J. Treacy, J. B. Higgins, *Collection of Simulated XRD Powder Patterns for Zeolites*, Elsevier Science B.V., 2007
- 20 P. S. Prevey, *X-Ray Diffraction Residual Stress Techniques*. In ASM Handbook: Materials Characterization, vol. 10; R. E. Whan, Ed.; ASM International, 1986, 380–392
- 21 T. Lu, W. Yan, R. Xu, *Inorg. Chem. Front.*, 2019, **6**, 1938-1951
- 22 M. Tong, D. Zhang, W. Fan, J. Xu, L. Zhu, W. Guo, W. Yan, J. Yu, S. Qiu, J. Wang, F. Deng, R. Xu, *Sci Rep*, 2015, **5**, 11521
- 23 L. B. McCusker and C. Baerlocher, *Stud Surf Sci Catal*, 2001, **137**, 37-67
- 24 W. Lutz, H. Toufar, R. Kurzhals, M. Suckow, *Adsorption*, 2015, **11**, 405-413
- 25 C. Buttersack, A. König, R. Gläsera, *Micropor. Mesopor. Mat.*, 2019, **281**, 148-160
- 26 W. Lutz, *Adv. Mater. Sci. Eng.*, 2014, **1**, 1-20
- 27 S. Bhatia, *Zeolite catalysis: principles and applications*, CRC Press, 1990
- 28 K. Möller and T. Bein, *Chem. Soc. Rev.*, 2013, **42**, 3689-3707
- 29 R. Zhang, S. Xu, D. Raja, N. B. Khusni, J. Liu, J. Zhang, S. Abdulridha, H. Xiang, S. Jiang, Y. Guan, Y. Jiao, X. Fan, *Micropor. Mesopor. Mat.*, 2019, **278**, 297-306
- 30 D. Verboekend, N. Nuttens, R. Locus, J. Van Aelst, P. Verolme, J. C. Groen, J. Pérez-Ramírez, B. F. Sels, *Chem. Soc. Rev.*, 2016, **45**, 3331-3352

-
- 31 D. Verboekend, G. Vilé, J. Pérez-Ramírez, *Adv. Funct. Mater.*, 2012, **22**, 916-928
- 32 J. A. Moulijn, A. E. van Diepen, F. Kapteijn, *Appl Catal A Gen*, 2001, **212**, 3-16
- 33 J. Madejova, *Vibr. Spectrosc.*, 2003, **31**, 1-10
- 34 A. Beran, *Rev Mineral Geochem.*, 2002, **46**, 351-369
- 35 G. Webb, *Annual Reports on NMR Spectroscopy, First Edition*, First Edition, **77**, Academic Press, 2012
- 36 P. P. Man, M. J. Peltre, D. Barthomeuf, *J. Chem. Soc. Faraday Trans.*, 1990, **86**, 1599-1602
- 37 Y. Li, L. Li, J. Yu, *Chem*, 2017, **3**, 928-949
- 38 A. Martínez, E Peris, *Appl Catal A Gen*, 2016, **515**, 32-44
- 39 Z. Cao, S. Zeng, Z. Xu, A. Arvanitis, S. Yang, X. Gu, J. Dong, *Sci. Adv.*, 2018, **4**, eaau863
- 40 A. Jentys, G. Warecka, M. Derewinski, J. A. Lercher, *J. Phys. Chem.*, 1989, **93**, 4837-4843
- 41 J. Yu, J. Luo, Y. Zhang, J. Cao, C. C. Chang, R. J. Gorte, W. Fan, *Micropor. Mesopor. Mat.*, 2016, **225**, 472-481
- 42 S. T. Yang, J. Kim, W. S. Ahn, *Micropor. Mesopor. Mat.*, 2010, **135**, 90-94
- 43 R. Gounder, M. E. Davis, *AIChE J.* 2013, **59**, 3349-3358
- 44 J. Perez-Carbajo, D. Dubbeldam, S. Calero, P. J. Merkling, *J. Phys. Chem. C*, 2018, **122**, 29274-29284
- 45 K. L. Morana, P. D. Barker, J. E. Readman, P. P. Edwards, R. Dupree, P. A. Anderson, *Chem. Commun.*, 2000, **1**, 55-56
- 46 J. Shi, M. W. Anderson, S. W. Carr, *Chem. Mater.*, 1996, **8**, 369-375
- 47 C. E. Hughes, B. Walkley, L. J. Gardner, S. A. Walling, S. A. Bernal, D. Iuga, J. L. Provis, K. D.M. Harris, *Solid State Nucl. Magn. Reson.*, 2019, **99**, 1-6

4 Influence of aluminium content on the stability of high framework density zeolites

4.1 Introduction

Aluminosilicate zeolites are widely used in research and chemical industry, including catalysis, heavy metal sorption and membrane separation processes.¹ Conventional hydrothermal synthesis method of zeolites has several advantages over post-synthesis treatment methods (*i.e.*, acid dealumination). These are bottom-up incorporation of various tri- and tetravalent metals into the framework, controlled pore size distribution, introduction of intentional defects or defect free synthesis.

In Chapter 3, various commercially available zeolites were tested for their water stability. In that chapter, it was demonstrated that higher aluminium (Al) content of the zeolite structure led to a corresponding increase in material stability when in direct contact with hot water. What is more, it was found that high Framework Density (FD_{Si}) structures such as Mordenite (MOR), Ferrierite (FER) and ZSM-5 (MFI) are much more stable in water than the structures of low FD_{Si} , such as zeolite β (BEA), zeolite Y (FAU) and zeolite A (LTA). However, the commercially available zeolite materials possess a limited range of available SiO_2/Al_2O_3 molar ratios. Therefore, the final results derived from Chapter 3 prohibited a conclusive discussion regarding the impact of Al content in terms of zeolite stability.

To overcome this, herein the focus is directed more deeply on the role of Al in the zeolite structure, particularly as the Al content can strongly influence performance and catalytic activity in addition to the stability of the zeolite. Previous investigations by Sazama *et al.* have shown that local Al distribution in the ZSM-5 framework can be controlled by the conditions of the zeolite synthesis.² Hence, the Al distribution strongly affected the product composition during olefins cracking. A higher concentration of single Al atoms (one Al atom in the six- or five-membered rings) in the material resulted in higher yields of propene, ethene and pentene and lower yields of aromatics.

High aluminium content ZSM-5 zeolites were also reported to be excellent catalysts for butene cracking reaction.³ A study by Jiao *et al.*, explored the role of a hollow structure of a

mesoporous ZSM-5 zeolite ($\text{SiO}_2/\text{Al}_2\text{O}_3 = 32$).⁴ It was found that the good accessibility of Lewis acid sites, associated with EFAl species, originated in higher catalytic performance.

In addition to catalytic activity, the hydrophilicity of a zeolite and its water uptake abilities strongly depend on the $\text{SiO}_2/\text{Al}_2\text{O}_3$ molar ratio. The higher the content of Al the more hydrophilic the structure and more water molecules occupying the internal void spaces as presented in Chapter 3. Additionally, water is mobile within the framework and can undergo an unlimited number of reversible de- and rehydration cycles under ambient conditions.⁵ However, high Al content might make the zeolite unsuitable for use under acidic conditions.⁶ Consequently, the Al content may also affect the stability of the zeolite in a pressurised, continuous flow reactor (CFR). A water stability study by Jamil *et al.* reported that in a medium aluminium content ZSM-22 ($\text{SiO}_2/\text{Al}_2\text{O}_3 = 60$) Al leached from framework to EFAl positions when hot water was applied.⁷ However, it was shown that the EFAl species have created a protective layer for silicon bonds. As a result, the framework was more resistant to failure at elevated water temperatures (up to 250°C) than when its analogues with a lower Al content ($\text{SiO}_2/\text{Al}_2\text{O}_3 = 160\text{-}200$) was exposed. The overall stability of the zeolite was strongly dependent on the temperature of applied water. Furthermore, a study by Ravenelle *et al.* reported similar observations in a study on water stability of Y and ZSM-5 zeolites in temperatures up to 200°C.⁹

Due to the potential importance of Al content in terms of zeolite stability, many previously reported studies focused on the hydrothermal stability of different aluminosilicate zeolites.^{8,9,10,11,12,13} Many experimental studies are also supported by DFT calculation models and a large number of relevant theoretical papers that can be found in the literature as well.¹⁴ However, in line with the data presented in Chapter 3, these previous studies have almost exclusively focused on commercially available zeolites and were done under static conditions.

The screening of commercial materials, which was discussed in Chapter 3, gave a first insight on the differences in stability, depending on the framework density and aluminium content. However, analysis on commercial materials had limitation due to the fact that most of the samples had an unknown history of synthesis, were prepared by post synthetic modifications of the parent structure, and were only available in limited $\text{SiO}_2/\text{Al}_2\text{O}_3$ molar ratios (23, 30, 50, 80 and 280).^{15,16,17} Consequently, there is a need for comparisons to be made between post-treated commercial zeolites and synthesised zeolites prepared under

strict, analogous conditions, in order to better study how their chemical composition and topology influence zeolite stability. An improved understanding of zeolite hydrolysis and the role of Al would be highly beneficial for prospect applications in liquid phase operations.

It was demonstrated in Chapter 3 that the MFI framework, in particular the ZSM-5 zeolite, was among the most water stable frameworks. This chapter presents a more in-depth study of how the aluminium content of the MFI framework impacts its stability, by preparation of own-pot laboratory synthesised ZSM-5 materials. Subsequently, comparison of its stability to zeolites of similar FD_{Si} materials is covered.

4.2 Results and discussion

4.2.1 Characterisation of one-pot synthesised H-ZSM-5 zeolites

It must be mentioned here that all the samples discussed in this chapter are abbreviated by their origin – a one-pot laboratory synthesised MFI type ZSM-5 zeolite sample after activation, possessing a SiO_2/Al_2O_3 molar ratio of 30, was denoted as HZSM-5 (30) HT. Synthesis of each zeolite was done according to the protocols given in Chapter 2 (see Sections 2.2.1.1 and 2.2.1.2).

To understand in better detail the stability of the MFI structure, a range of new H-ZSM-5 zeolites of SiO_2/Al_2O_3 molar ratios ranging from 30 to infinity (*i.e.*, no Al) was successfully hydrothermally synthesised with the use of hydroxide medium. The powder X-ray Diffraction (pXRD) was used in order to verify the crystallinity of the synthesised samples. The diffraction patterns of calcined samples are presented in Figure 4.1.

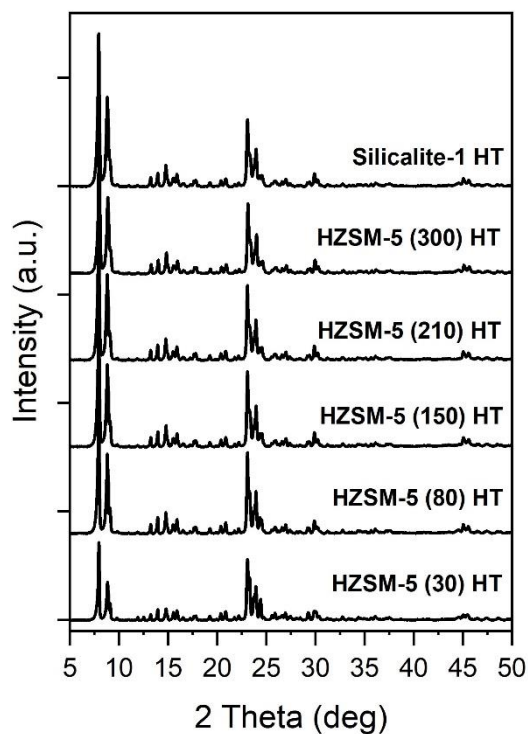


Figure 4.1 pXRD patterns of all one-pot synthesised and calcined zeolites H-ZSM-5 (30-300) and pure silica Silicalite-1 (MFI type) samples.

The sharp and well-defined diffraction patterns of the MFI structures were observed in the case of all the synthesised samples. All diffractograms were compared with the IZA Structure Commission database available online.¹⁸ The presence of intense characteristic diffraction peaks at $2\theta = 7.98^\circ$, 8.82° , 23.14° , 23.96° and 24.44° clearly indicated that the collected diffractograms corresponded to highly crystalline H-ZSM-5 and Silicalite-1 zeolites. In addition, no other diffraction peaks corresponding to undesired impurities were observed.

Single Pulse ^{29}Si and ^{27}Al MAS NMR spectra were recorded to further investigate the content and coordination environment of Si and Al in the synthesised materials. The spectra presented on Figure 4.2 show differences in Si (left, A) and Al (right, B) distributions between the high (30), medium (80) and low (300) aluminium content MFI frameworks.

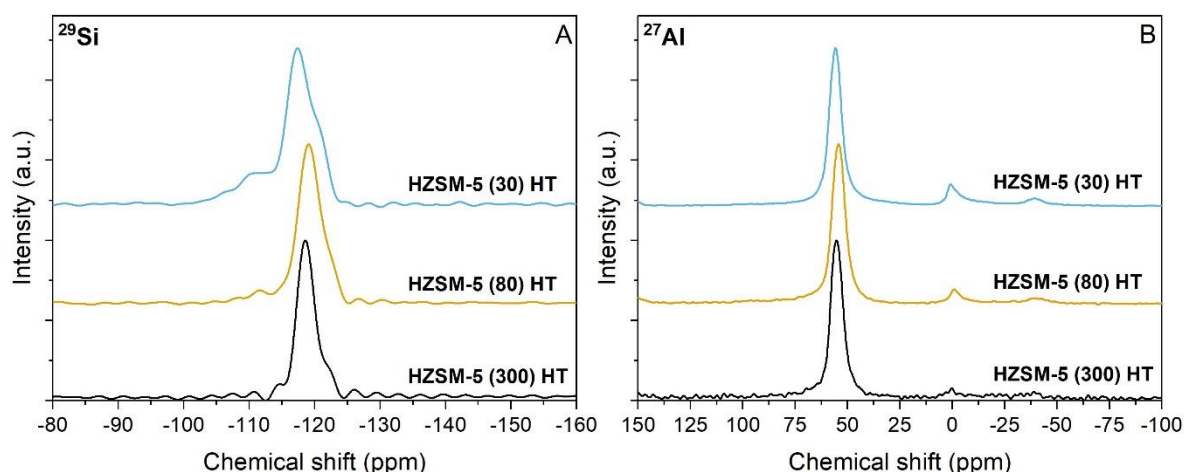


Figure 4.2 Comparison of Single Pulse ^{29}Si (left, A) and ^{27}Al (right, B) Solid State MAS NMR spectra of untreated HZSM-5 (30) HT (blue), HZSM-5 (80) HT (yellow) and HZSM-5 (300) HT (black) zeolite samples.

In the three measured samples, the vast majority of framework Si is located in the Q^4 (-118 ppm) coordination, which is confirmed by the ^{29}Si spectra (left, A). This is clearly visible, especially in the case of the HZSM-5 (300) HT sample. When the Al content increases, the Q^4 resonance becomes broader and eventually in the case of the HZSM-5 (30) HT sample, a new resonance appears at -110 ppm. This peak is associated with the Q^3 coordination. The Q^3 resonance is usually associated with two types of species, *i.e.* $[\text{Si}(\text{OSi})_3(\text{OAl})]$ and $[\text{Si}(\text{OSi})_3(\text{OH})]$ ones, indicating that the Al is exchanging Si in the framework tetrahedra. The ^{27}Al spectra (right, B) confirm these observations. In all cases, the majority of the Al atoms were located in the tetrahedral framework sites (55 ppm), with only a minor part as EFAl (0 ppm) which was increasing with the Al content increase in the material. In the case of the HZSM-5 (300) HT sample, the signal located in the EFAl region is so insignificant that it is most likely noise from the analysis background.

The amount of Al in the framework, as well as surface defects associated with the silanol nests, have a great influence on the hydrophilicity of the zeolite. Water vapour sorption analysis (Figure 4.3) was performed at room temperature (25°C) on chosen one-pot synthesised samples in order to confirm the differences in hydrophilicity, which are directly related to the zeolite chemical composition.

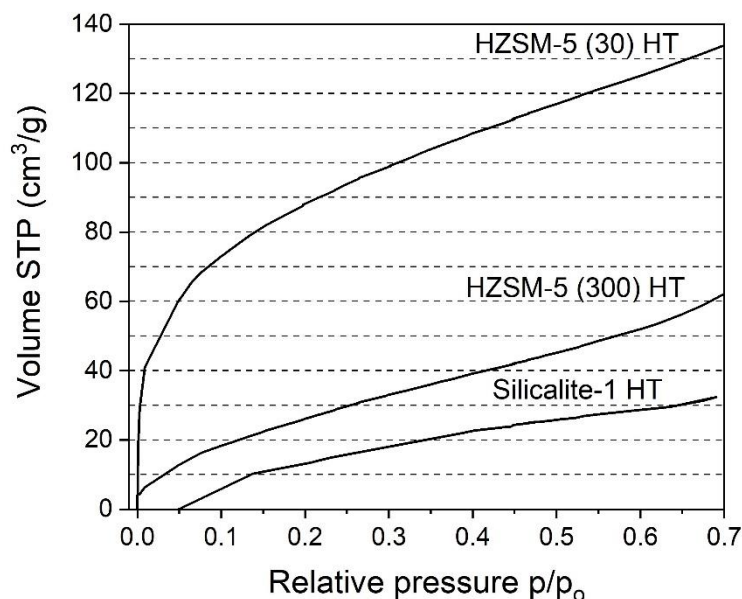


Figure 4.3 Water vapour sorption isotherms on synthesised MFI type zeolites of $\text{SiO}_2/\text{Al}_2\text{O}_3$ molar ratio 30-300 and pure silica Silicalite-1. Isotherms were recorded at temperature of 25°C .

As a result, the obtained water vapour sorption isotherms were as expected and represented the hydrophilicity and hydrophobicity of selected samples, depending on the aluminium content. In line with expectations, the higher the aluminium content the vapour uptake was higher. Furthermore, the HZSM-5 (30) HT isotherm shape (type I) was typical for hydrophilic microporous materials. However, HZSM-5 (300) HT and Silicalite-1 HT samples were represented by type V isotherms, which are distinctive for more hydrophobic materials. The vapour sorption abilities resulted in volumes of 135 mL g^{-1} , 62 mL g^{-1} and 32 mL g^{-1} for HZSM-5 (30) HT, HZSM-5 (300) HT and Silicalite-1 HT samples, respectively.

4.2.2 Influence of water on crystallinity and porosity

To extend the study from Chapter 3, the one-pot synthesised set of HZSM-5 zeolites was investigated for water stability. In line with the research presented in Chapter 3, water stability tests were performed in order to understand how the Al content might affect the properties and overall durability of the HZSM-5 zeolites. Similar as previously presented, these tests were performed in fixed-bed continuous flow reactors (CFR) with deionised water flow (0.3 mL min^{-1}) under moderate inlet pressure (25-50 bar). The packed stainless-steel

reactor was immersed in an oil bath and all tests were carried out for 24 h at 110°C as described in detail in Chapter 2 (see Section 2.5.1).

The results of the tests in a form of relative crystallinity are presented in Figure 4.4. The relative value determination was done according to the protocol given in Chapter 2 (see Section 2.4.1).

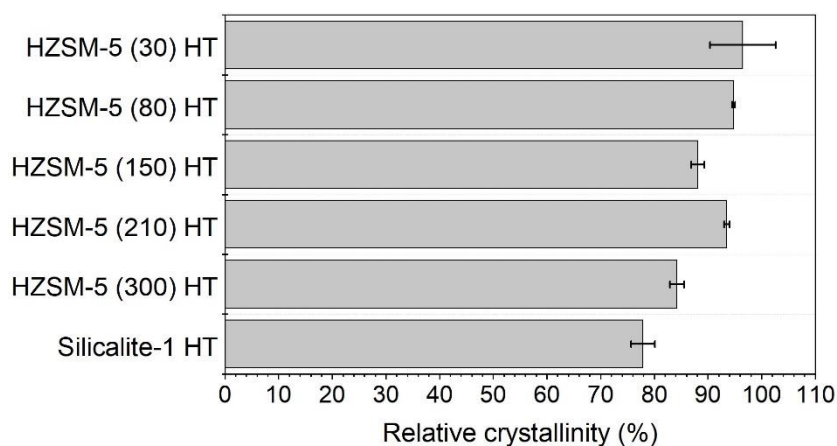


Figure 4.4 Relative crystallinity of HZSM-5 zeolite materials of $\text{SiO}_2/\text{Al}_2\text{O}_3$ molar ratios 30-300 and pure silica, Silicalite-1. Relative crystallinity error bars represent the standard deviation of the Integrated Peak Area after 5 samples examination.

A good level of crystallinity, between 88-96%, remained within the whole range of 30 to 210 with a slight decrease of crystallinity for the low aluminium content HZSM-5 (300) and pure silica Silicalite-1. However, it was acknowledged that a progressive loss of crystallinity occurred among all the series with the highest loss for HZSM-5 (300) HT (84%) and in pure Silicalite-1 HT (78%) samples, where a low content and no aluminium are present, respectively.

Changes of textural properties, especially specific surface area (S_{DFT}) and porosity, in form of relative values are given in Table 4.1. As presented in Chapter 3, changes in micropore volume and total pore volume were the first indicator of internal changes happening after direct contact with water at elevated temperatures. The relative value determinations were done according to the protocol given in Chapter 2 (see Section 2.4.2).

Table 4.1 Summary of changes to the textural properties in a form of relative values, all based on NLDFT calculations.

Sample ID	$S_{DFT}^{(a)}$ (rel. %)	$V_t^{(b)}$ (rel. %)	$V_{mc}^{(c)}$ (rel. %)	$V_{mp}^{(d)}$ (rel. %)
HZSM-5 (30) HT	92.9	109.1	82.1	138.6
HZSM-5 (80) HT	96.2	106.5	92.9	124.6
HZSM-5 (150) HT	106.5	104.7	84.6	104.2
HZSM-5 (210) HT	90.5	120.6	95.4	88.4
HZSM-5 (300) HT	85.7	97.5	85.2	88.7
Silicalite-1	93.1	94.3	88.8	114.2

^(a) Specific surface area (m^2/g) obtained from NLDFT

^(b) Total pore volume (cm^3/g) from NLDFT

^(c) Micropore volume (cm^3/g) NLDFT

^(d) Mesopore volume (cm^3/g) NLDFT

As an addition to relative crystallinity, changes in pore volumes were observed as well. Interestingly, Silicalite-1 exhibited the highest loss of crystallinity but did not lose much of its micropore volume and retained 88.8% of its initial micropore volume value. In all cases, micropore volume loss was observed. Although, higher mesopore volumes were found in high Al content zeolites (30, 80 and 150), compared to high Si ones (210 and 300). Total pore volume increased by 4.7-20.6 % in samples of 30-210 molar ratio values and decreased in high silica ones (300 and Silicalite-1).

4.2.3 Comparison study between post-synthetic treated and one-pot synthesised HZSM-5 zeolites

This study investigated the similarities in performance of commercially available (presented in Chapter 3) and materials prepared via the one-pot synthesis method (hydrothermal route). The textural properties were analysed by powder X-ray diffraction, N_2 -physisorption, water vapour sorption experiments and ATR-FTIR analysis.

Figure 4.5 presents a comparison of commercial (C) and one-pot synthesised (HT) HZSM-5 zeolite samples with similar aluminium content treated for in water for 24 h at 110°C (as described in Section 4.2.1). Additionally, relative total pore volume ($V_{t\ rel}$) of each sample was added on the right-hand side of the figure.

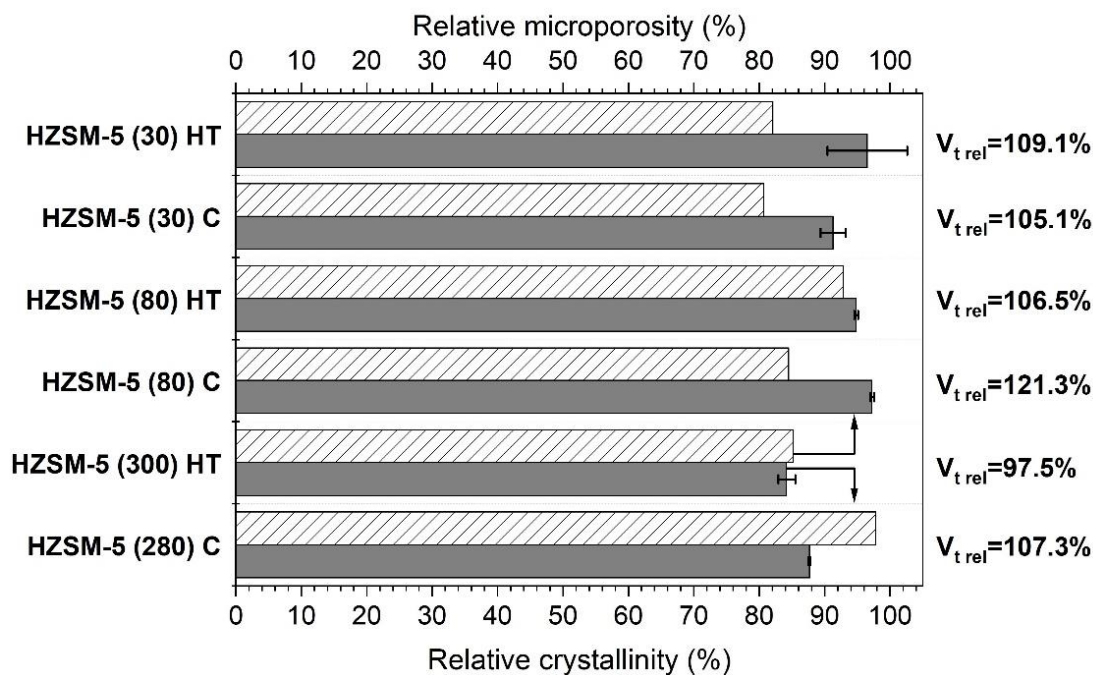


Figure 4.5 Comparison of relative crystallinity and microporosity among commercial (C) and one-pot synthesised (HT) materials of similar aluminium content treated with water at 110°C for 24 h. Relative crystallinity error bars represent the standard deviation of the Integrated Peak Area after 5 samples examination.

Values of relative crystallinity and microporosity were similar with slight differences along the comparison set. This indicates that the commercial post-synthetic modified and one-pot synthesised structures had comparable tolerance upon exposure to hot water flow. At 110°C, the relative crystallinity of all samples decreased by 2-18% with a highest crystallinity loss for the HZSM-5 (300) HT sample. Materials with higher aluminium content (30 and 80) retained >90% of their original crystallinity. No additional crystalline phases have been observed on the pXRD diffraction patterns of treated samples, meaning that no new phases or phase transition happened after treatment with water.

Furthermore, the total pore volumes ($V_{t,rel}$) estimated from the N_2 -physisorption isotherms were only a bit higher in terms of the HZSM-5 (80) C sample, with an increase of 21.3%. However, the increasing total pore volume values, by 5.1-9.1%, confirmed formation of internal mesopores, which was observed to happen in every tested sample. The appearance of mesopores is mainly associated with the partial collapse of micropore or internal dissolution.

ATR-FTIR analysis was conducted on untreated and treated HZSM-5 (300) HT samples in order to confirm the pore collapse in treated samples. The HZSM-5 (300) HT was used as

an example, to determine the effect of water on the internal structure and Si-O and Al-O bonds. The spectra are presented on presented on Figure 4.6.

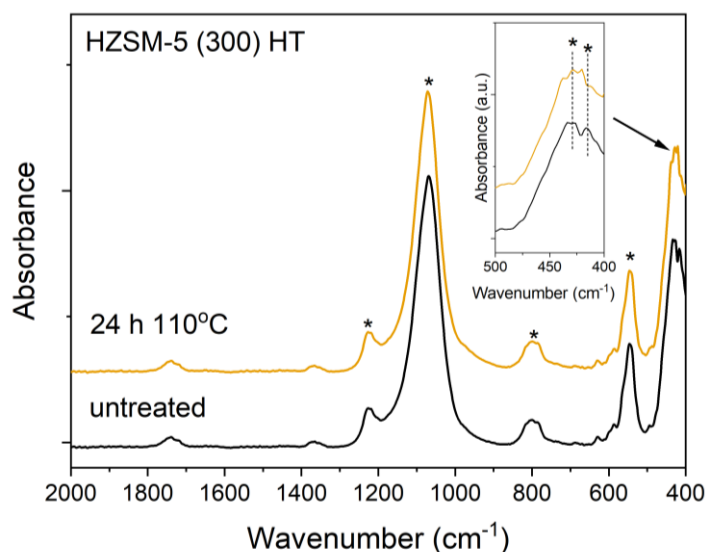


Figure 4.6 ATR-FTIR spectra of a treated (dark yellow) and untreated (black) HZSM-5 (300) HT. Asterisks point out bands described in text.

The spectra of the untreated and treated samples presented a characteristic intense band at a wavenumber of 1070 cm^{-1} , and a shoulder at 1250 cm^{-1} , attributed to the asymmetric stretching vibrations of the internal silicon (Si-O(Si)) and aluminium exchanged (Si-O(Al)) tetrahedra.¹⁹ The bands of symmetric stretching vibration of the T-O bonds occur in the wavenumber region of $790\text{--}800\text{ cm}^{-1}$. The bands located at $430\text{--}450\text{ cm}^{-1}$ were associated with the internal T-O bending, which can be assigned with Al-O bands.²⁰ The intense band at 550 cm^{-1} was found to be typical for the MFI-structured material and is associated with the pentasil framework vibration.²¹ However, the only change (highlighted in the box) in the spectra was around 420 cm^{-1} and this region has been assigned to pore opening vibrations.²² However, in the case of the spectrum below 500 cm^{-1} , the equipment is not very accurate and there is a possibility of making an error by interpreting this region. From these IR spectra, it is seen that the disappearing pore opening band might be associated with the undergoing changes in the internal channels as the micropore volume decreases in favour of mesopores formation.

4.2.4 Medium aluminium content HZSM-5 (80) HT stability with time

In order to explore the structural stability a medium Al content HZSM-5 (80) HT structure was examined. The HZSM-5 (80) was chosen due to several reasons, including the detection and linear dynamic range limitations of the MP-AES technique and the EDX elemental analysis. Out of all synthesised zeolites, this structure had the lowest Al content (40 times less than Si content) but could still be easily detected by EDX. The detection limit for bulk materials is 0.1 wt.% therefore EDX cannot detect trace elements, concentrations below 0.01 wt.%.²³

In order to test the stability, prolonged tests on the HZSM-5 (80) HT zeolite samples were conducted. A set of experiments was carried out for 24, 51 and 120 h in a fixed-bed continuous flow reactor (CFR) in water at 110°C. The deionised water flow was set to 0.3 mL min⁻¹. To clarify, for every test a new untreated sample was packed into the CFR.

To verify the changes in the texture, the collected data was compared by means of pXRD, N₂-physisorption, Pore Size Distribution (NLDFT), EDX, MAS NMR and MP-AES. The results from conducting pXRD, N₂-physisorption and EDX analysis were gathered and presented in Table 4.2.

Table 4.2 Summary of SiO₂/Al₂O₃ molar ratio, pore size volumes, surface areas for the untreated and treated in different amount of time HZSM-5 (80) HT samples. Standard deviations (SD) represent the distribution of atoms after ten measurements for each sample.

Sample ID	SiO ₂ /Al ₂ O ₃ ^(a)	SD (σ)	S _{DFT} ^(b) (m ³ /g)	V _t ^(c) (cm ³ /g)	V _{mc} ^(d) (cm ³ /g)	X _{rel} ^(e) (%)
HZSM-5 (80) HT untreated	77.08	2.08	762	0.279	0.134	100.00
HZSM-5 (80) HT 24h 110°C	70.18	1.53	733	0.297	0.125	94.80
HZSM-5 (80) HT 51h 110°C	65.40	3.25	770	0.353	0.126	88.35
HZSM-5 (80) HT 120h 110°C	63.90	4.20	711	0.341	0.118	79.77

^(a) SiO₂/Al₂O₃ molar ratio was determined with EDX analysis; values are an average of 10 different areas of the sample.

^(b) Specific surface area obtained from NLDFT

^(c) Total pore volume from NLDFT

^(d) Micropore volume from NLDFT

^(e) Relative crystallinity calculated according to protocol in Chapter 2 Section 2.4.1

The N₂-physisorption analysis showed that the micropore volume (V_{mc}) did change for all samples, with the highest decrease of approximately 12% after 120 h of treatment. Additionally, the total pore volume (V_t) of the 120 h sample increased by 22.2%, which was a second largest change just after the 51 h treatment sample. The decrease in micropore volume and increase of total pore volume again indicates formation of new mesopores at the expense of micropore retention. What is interesting is that treatment with hot water might be an alternative method of introducing mesoporosity to the MFI structure other than treating it in alkaline aqueous media, as is typically followed.²⁴

Furthermore, EDX analysis of the materials indicated that silicon leaching indeed occurred. The difference in SiO₂/Al₂O₃ molar ratio before treatment and after 120 h was significant - a drop of 17.1%. This indicates that silicon leaching might be the main mechanism of framework degradation. At the same time, the relative crystallinity decreased by ~20%. There was a clear correlation between the change of SiO₂/Al₂O₃ molar ratio and relative crystallinity as they both changed gradually, with elapsing time, as presented on Figure 4.7.

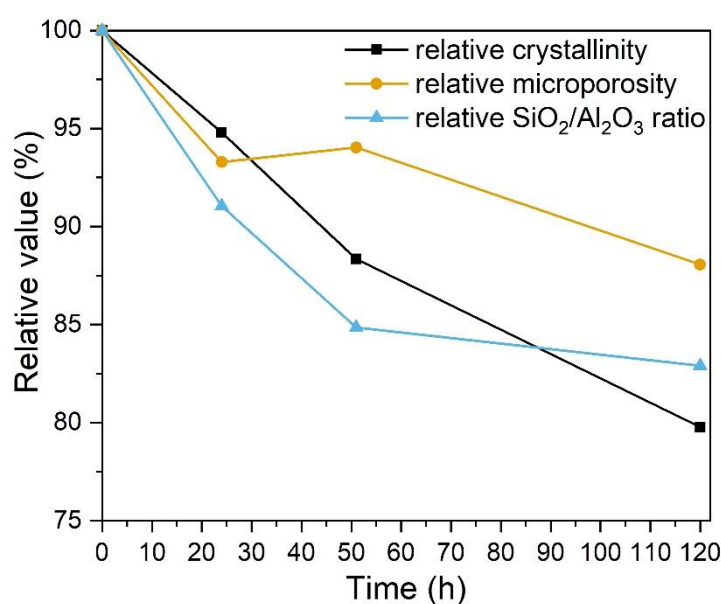


Figure 4.7 Visual representation of change in relative crystallinity (black line, squares), microporosity (yellow, circles) and the SiO₂/Al₂O₃ molar ratio (blue, triangles) after HZSM-5 (80) HT sample treatment with water for 24 h, 51 h and 120 h at 110°C.

In order to understand changes undergoing in the MFI framework Solid State NMR was conducted on the untreated and water treated HZSM-5 (80) HT samples. Figure 4.8 presents Single Pulse ^{29}Si and ^{27}Al MAS NMR spectra of the untreated and treated HZSM-5 (80) HT.

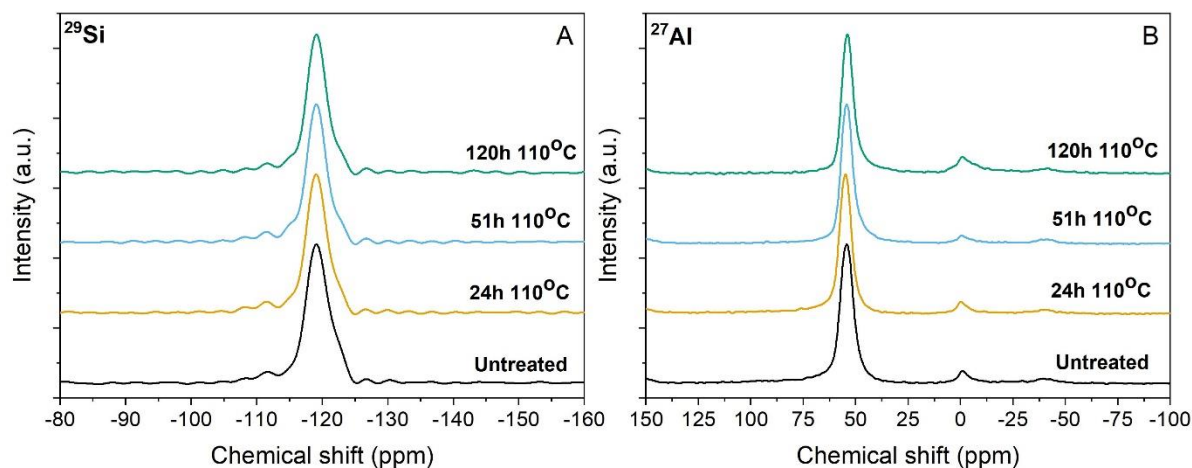


Figure 4.8 Comparison of Single Pulse ^{29}Si (left, A) and ^{27}Al (right, B) Solid State MAS NMR spectra of untreated and treated HZSM-5 (80) HT zeolite samples – untreated and after 24 h (yellow), 51 h (blue) and 120 h (green) treatment in water.

In the case of the ^{29}Si spectra (left, A), the untreated and treated zeolites show one main peak at -119 ppm, corresponding to the tetrahedral Q^4 coordination. The intensity did not vary significantly among the series; therefore, it was decided to normalise to peaks to show that the shape remained the same for among all samples. No additional resonances and peak broadening were observed in the presented spectra.

No significant changes were observed for the Al environment (right, B) as well. The 55 ppm and 0 ppm resonance peaks corresponding to the tetrahedral coordinated and octahedral Al atoms remained nearly unchanged. However, the octahedral resonance peak was slightly broader in the case of the 51 h and 120 h treated samples. This would mean that the EFAl species might have leached out from the sample or that a minor amount of framework Al was moving into EFAl positions. Spinning side bands are observed around -38 ppm.

Silicon and aluminium leaching are important descriptor of the framework stability, as this characteristic was often crucial for the activity of the material in catalytic applications.²⁵ Thus, to support the observation of silicon leaching, Microwave Plasma - Atomic Emission Spectroscopy (MP-AES) analysis was carried out on the effluent water after passing the

fixed-bed CFR. According to EDX analysis, the average Al and Si content of an untreated HZSM-5 (80) HT sample was 1.16 wt. % and 46.38 wt. %, respectively. As three separate samples were analysed for the treatment with water, all data was adjusted to appropriate sample weights and data was presented on Figure 4.9 exposing a rather linear trend for both Al and Si extraction from the samples.

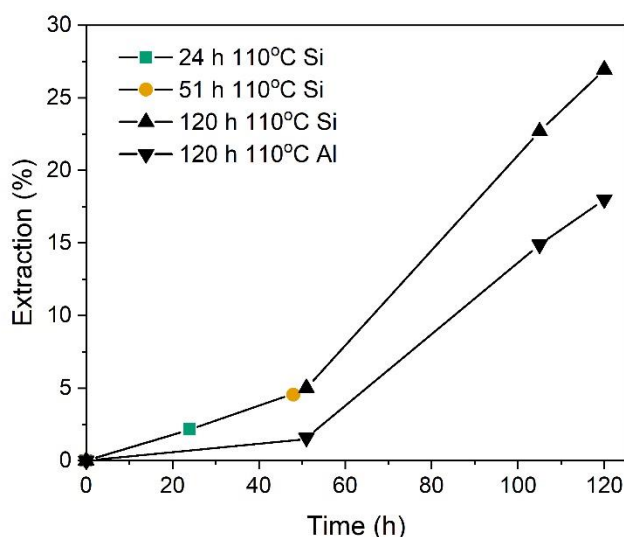


Figure 4.9 Amount of extracted (%) Si and Al from HZSM-5 (80) HT samples in time, compared to the total weight of all the sample packed in the reactor. Green square – sample 24 h at 110°C; yellow dot – sample 51 h at 110°C; black triangles – sample 120 h at 110°C treatment with water. Al was not detected in effluent in the case of 24 h and 51 h samples. Black reversed triangles – Al extraction from sample 120 h at 110°C.

In the case of the sample treated for 24 h, Si was present in effluent water with an average concentration of 5.63 ppm. This concentration corresponded to approximately 2.14 wt. % of the total Si present in the untreated sample. However, the analysis showed no presence of aluminium in effluent.

The same experiment was conducted after 48 h for the 51 h treated sample giving the average Si concentration of 6.06 ppm concentration, corresponding to 4.55% of total Si and yet no presence of Al. However, for the sample treated for 120 h three separate effluent samples were analysed. The results for Si and Al, respectively were as follows: 51 h (Al 1.58 wt. %, Si 5.00 wt. %), 105 h (Al 13.31 wt. %, Si 17.68 wt. %) and 120 h (Al 3.11 wt. %, Si 4.26 wt. %). Giving a total of 18.00 wt. % Al and 29.94 wt. % Si extracted from the parent zeolite sample after 120 h.

The data derived from MP-AES method confirmed that the entire set of samples underwent desilication and to a lesser extent dealumination, which is in line with the data presented previously. Furthermore, it is clear that dealumination occurred to a much lower extent than desilication. It is also noticed that desilication occurred from the first hours of testing and is followed by framework dealumination, which is eventually expected, since the framework loses quite a significant number of framework Si.

4.2.5 High aluminium content HZSM-5 (30) stability

4.2.5.1 Influence of extended water contact on stability

As presented previously (Section 4.2.3), the one-pot synthesised and commercial samples of the high aluminium content MFI structure showed only little differences in relative crystallinity and microporosity after 24 h of testing. This section focused on comparing textural differences after extending the tests to 120 h. Table 4.3 summarises differences in pore volumes and $\text{SiO}_2/\text{Al}_2\text{O}_3$ molar ratios of untreated and treated samples with water at 110°C for 120 h.

Table 4.3. Summary of $\text{SiO}_2/\text{Al}_2\text{O}_3$ molar ratio, pore size volumes, surface areas for the untreated and treated in different amount of time HZSM-5 (30) HT and HZSM-5 (30) C samples. $\text{SiO}_2/\text{Al}_2\text{O}_3$ molar ratio was determined with EDX analysis. Standard deviations (SD) represent the distribution of atoms after ten measurements for each sample.

Sample ID	Untreated				After 120h at 110°C in water (CFR)			
	$V_t^{(a)}$ (cm^3/g)	$V_{mc}^{(b)}$ (cm^3/g)	$\text{SiO}_2/\text{Al}_2\text{O}_3^{(c)}$	SD (σ)	$V_t^{(a)}$ (cm^3/g)	$V_{mc}^{(b)}$ (cm^3/g)	$\text{SiO}_2/\text{Al}_2\text{O}_3^{(c)}$	SD (σ)
HZSM-5 (30) C	0.301	0.153	28.79	0.39	0.304	0.105	21.90	0.76
HZSM-5 (30) HT	0.344	0.147	31.25	1.40	0.384	0.132	23.03	0.67

^(a) Total pore volume from NLDFT

^(b) Micropore volume from NLDFT

^(c) $\text{SiO}_2/\text{Al}_2\text{O}_3$ molar ratio was determined with EDX analysis, values are an average of 10 different areas of the sample

The one-pot synthesised HZSM-5 (30) HT sample exhibited similar stability compared to the post-synthetic modified HZSM-5 (30) C sample (explanation of description in Section 2.3.2 and Section 2.3.3). In both cases a similar change in $\text{SiO}_2/\text{Al}_2\text{O}_3$ molar ratio was observed, which decreased by 23.9% and 26.3% for the commercial and one-pot synthesised sample, respectively. In terms of pore volume, the HT sample retained more microporosity – 91.7% vs 68.6% commercial one, but the HT sample was more prone to formation of mesoporosity and increase of overall total pore volume (111.6% vs 101.0% commercial).

All samples were analysed by Single Pulse ^{29}Si and ^{27}Al MAS NMR and compared after 120 h treatment in water (at 110°C), in order to see possible differences in the Si and Al environments (Figure 4.10).

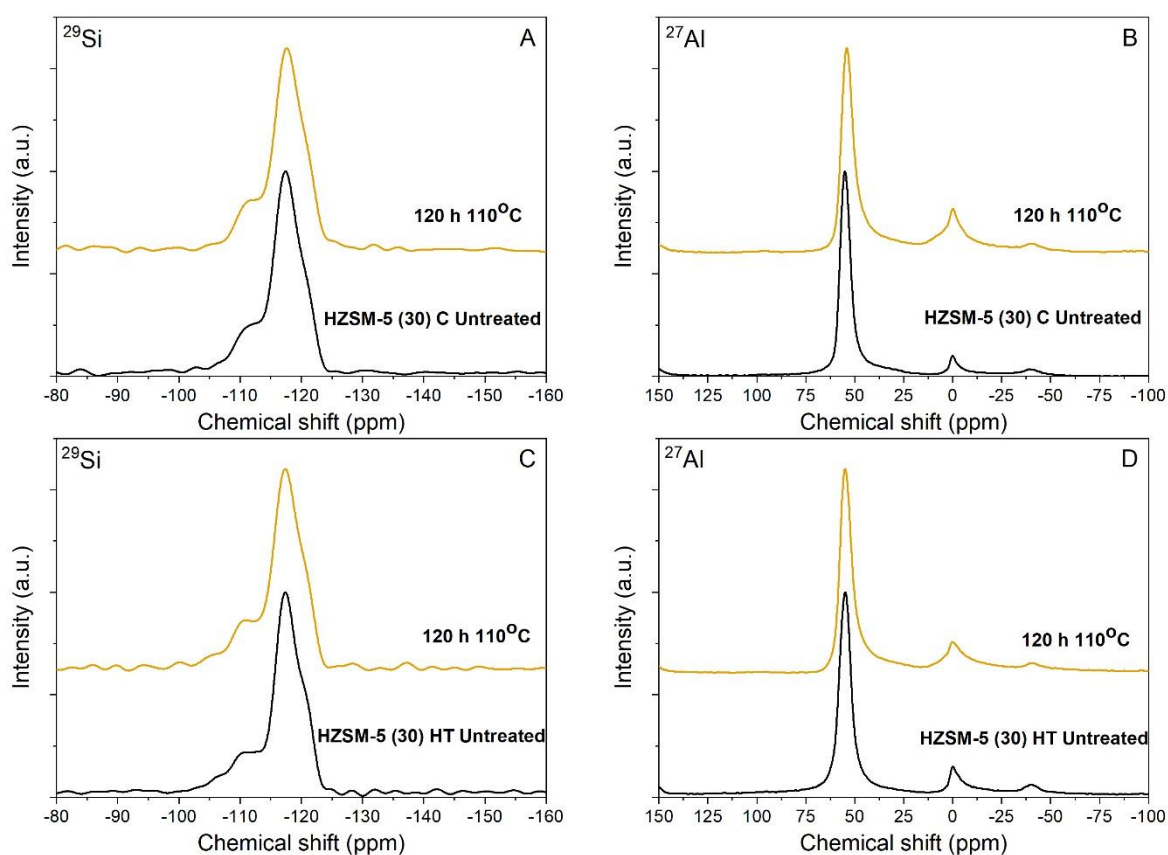


Figure 4.10 Comparison of Single Pulse ^{29}Si MAS NMR spectra of untreated and treated HZSM-5 (30) C (top left, A) and HZSM-5 (30) HT (bottom left, C) zeolite samples 120 h in water. Comparison of Single Pulse ^{27}Al MAS NMR spectra of untreated and treated HZSM-5 (30) C (top right, B) and HZSM-5 (30) HT (bottom right, D) zeolite samples for 120 h in water.

The difference in Si environment depending on the $\text{SiO}_2/\text{Al}_2\text{O}_3$ molar ratio of the MFI structure was previously discussed in more detail in Section 4.2.1. While the Single Pulse

^{29}Si MAS NMR spectrum of HZSM-5 (80) HT sample presented only Q^4 coordination (Figure 4.8), a different Si environment is observed in the HZSM-5 (30) samples. Here, as presented on Figure 4.10, the HZSM-5 (30) commercial (left, A) and one-pot synthesised (left, C) samples resulted in same shape spectra and chemical shift of Si nuclei. The peak centred at -117 ppm corresponds to the highly ordered Q^4 species. In contrast, the resonance at -110 ppm were attributed to the Q^3 species, corresponding to $[(\text{SiO})_3\text{SiOH}]$ and $[\text{Si}(\text{OSi})_3(\text{OAl})]$ units. After 120 h of testing, no major changes were observed in both spectra.

In terms of the aluminium environment (right B and D), the Single Pulse ^{27}Al MAS NMR spectra presented sharp resonance peak at 55 ppm, attributable to tetrahedrally coordinated Al atoms. The small fraction of Al signal located at 0 ppm confirmed the existence of EFAl. Both spectra were comparable, but the C sample resulted in shifting a small amount of the framework Al into EFAl positions. This is observed by the change in peak intensity and its broadening.

Silicon leaching was also observed by MP-AES measurements by measuring the effluent solution from the fixed-bed CFR. The results of these measurements obtained from the HZSM-5 (30) C and HZSM-5 (30) HT samples are presented in Figure 4.11.

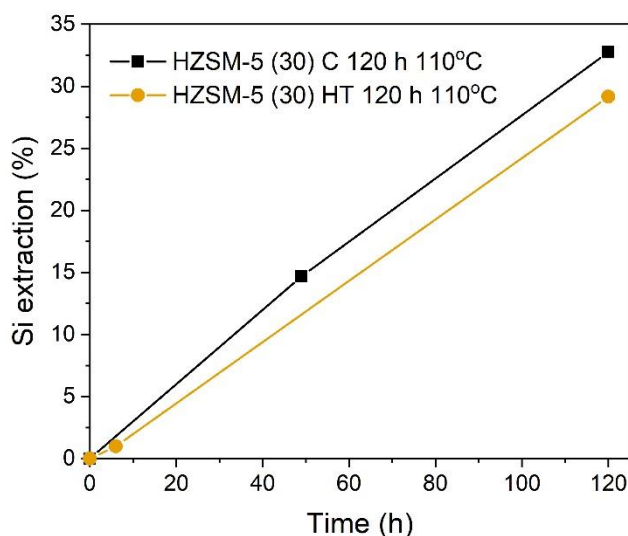


Figure 4.11 Amount of extracted (%) Si from HZSM-5 (30) HT and HZSM-5 (30) C samples in time, compared to the total weight of all the sample packed in the reactor. Al was not detected in effluent in the case of all samples. The Al concentration was same as in the blank.

According to EDX analysis, the average Al and Si content of the untreated commercial (C) and one-pot synthesised (HT) samples was 2.63 wt. % and 2.52 wt. % (Al), and 39.42 wt. % and 40.77 wt. % (Si), respectively. In the case of the HZSM-5 (30) HT sample, silicon was present in the effluent water (116 mL) after just 6 h, with an average concentration of 6.98 ppm (SD \pm 0.01 ppm). This means that about 0.81 mg of Si leached from the sample. Since the total mass of the sample packed into CFR was 200 mg and the total wt. % of Si was 40.77%, this equalled to approximately 0.99 wt. % of total Si of the sample Si content that leached out after only 6 h. After 120 h of testing the amount of extracted Si reached 28.16 wt. %. Giving a total of 29.15 wt. % of the total Si content that leached out from the initial packed sample.

In the case of the commercial HZSM-5 (30) C sample, after 49 h the average concentration of Si in the effluent water was 13.95 ppm (SD \pm 0.14 ppm), resulting in approximately 14.68 wt. % Si that leached. After 120 h of testing the amount attained an additional 18.05 wt. % resulting in a total of 32.73 wt. % extracted from the sample.

Both analysed samples presented similar results with a slightly better result for the HZSM-5 (30) HT sample. The final values were 32.73 wt. % and 29.15 wt. % of total Si extraction for the commercial and hydrothermal sample, respectively. In contrast to the HZSM-5 (80) HT sample analysed in Section 4.2.4, Al was not present in the effluent water at any stage. The MP-AES system did not detect higher aluminium concentrations compared to the blank sample. Again, same as in the case of the HZSM-5 (80) HT sample, the MP-AES analysis confirmed undergoing desilication but not dealumination. The results of the tests performed under same experimental conditions were similar for samples presented in this and previous section.

4.2.5.2 Influence of water temperature on stability

To determine the influence of water temperature on the stability of the HZSM-5 (30) HT, the sample was tested at room temperature (22°C) for 120 h and compared with a sample tested at 110°C for 120 h. From the previous stability test of the two sample analogues, it appeared that similar level of desilication was present in both – commercial and hydrothermal sample in the same temperature and testing time. As such, only HZSM-5 (30) HT was explored at lower temperature. Table 4.4 summarises differences in pore volumes

and $\text{SiO}_2/\text{Al}_2\text{O}_3$ molar ratios of untreated and treated HZSM-5 (30) HT samples with water in CFR at 110°C and 22°C for 120 h.

Table 4.4 Summary of $\text{SiO}_2/\text{Al}_2\text{O}_3$ molar ratio, pore size volumes, surface areas for the untreated and treated HZSM-5 (30) HT samples in different temperatures. The $\text{SiO}_2/\text{Al}_2\text{O}_3$ molar ratio was determined with EDX analysis. Standard deviations (SD) represent the distribution of atoms after ten measurements for each sample.

HZSM-5 (30) HT	$V_t^{(a)}$ (cm^3/g)	$V_{mc}^{(b)}$ (cm^3/g)	$\text{SiO}_2/\text{Al}_2\text{O}_3^{(c)}$	SD (σ)
Untreated	0.344	0.147	31.25	1.40
After 120h at 110°C in water (CFR)	0.384	0.132	23.03	0.67
After 120h at 22°C in water (CFR)	0.344	0.142	26.61	0.24

^(a) Total pore volume from NLDFT

^(b) Micropore volume from NLDFT

^(c) $\text{SiO}_2/\text{Al}_2\text{O}_3$ molar ratio was determined with EDX analysis, values are an average of 10 different areas of the sample.

An interesting difference in porosity was acknowledged, while the total pore volume increased by 11.6% for the treated at 110°C sample, the room temperature one showed no difference in values. What is more, the microporosity dropped by only 3.6% for the 22°C one, in comparison to a drop of 26.3% for the high temperature tested sample. However, the $\text{SiO}_2/\text{Al}_2\text{O}_3$ molar ratio changed in the case of both samples by 26.3% and 14.8% in the case of the samples treated at 110°C and 22°C , respectively, suggesting that some desilication possibly took place even at room temperature. Figure 4.12 presents the ATR-FTIR analysis data.

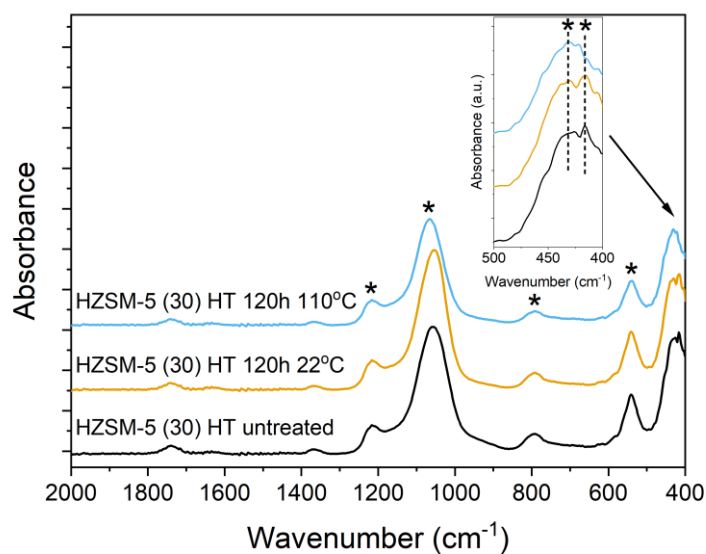


Figure 4.12 ATR-FTIR spectra of untreated HZSM-5 (30) HT (black) and treated at 22°C (light yellow) and 110°C (light blue) for 120 h.

The spectra of the samples presented characteristic bands, which were previously described in detail in section 4.2.2 of this Chapter. However, again the only change (pointed with the box) was around the 420 cm⁻¹ band region, assigned to pore opening vibrations.²² The room temperature treated sample showed no difference in comparison to the untreated sample. This proves that the water did not affect the micropore volume. From data gathered in Table 4.4 it was understood that room temperature water had nearly no influence on the porosity of the high aluminium zeolite. Again, ATR-FTIR analysis confirmed that changes to the structure were observed after contact with hot (110°C) water.

All samples were analysed by Single Pulse ²⁹Si and ²⁷Al MAS NMR and compared after 120 h treatment in elevated and room temperature water. Single Pulse MAS NMR spectra are presented in Figure 4.13.

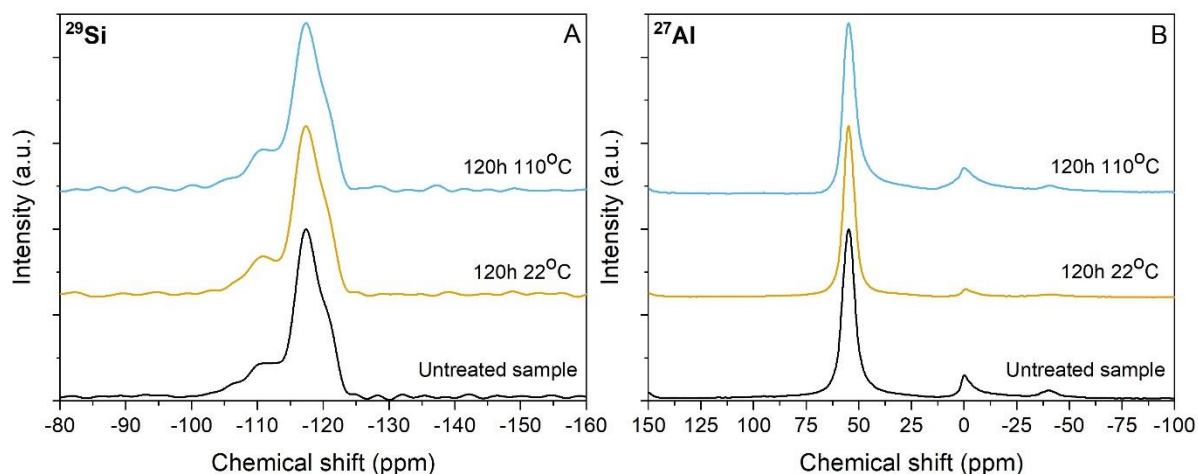


Figure 4.13 Comparison of Single Pulse ^{29}Si (left, A) and ^{27}Al (right, B) MAS NMR spectra of untreated (black) and treated HZSM-5 (30) HT samples 120 h in water at 110°C (yellow) and 22°C (blue).

In all cases, the ^{29}Si (left, A) the resonance at -117 ppm corresponded to Q^4 highly ordered species. The resonance at -110 ppm were attributed to Q^3 species and in the case of the room temperature treated sample, the peak was slightly more intense, although it was decided to normalise the peaks to show that the shape remained the same for among all samples.

All the ^{27}Al spectra (right, B) presented two clear resonances. One very sharp and intense centred at 55 ppm and the second one located at 0 ppm. The sharp resonance peak at 55 ppm was assign to tetrahedral coordinated Al atom. The small fraction of Al signal located at 0 ppm confirmed the existence of extra-framework aluminium in all samples. In the case of room temperature treated sample, the EFAl peak is slightly less intense as if the EFAl would leach out of its positions or the Al was reinserted into framework positions.²⁶

Figure 4.14 presents results obtained by MP-AES analysis. These measurements were conducted to observe differences in silicon and possible aluminium leaching.

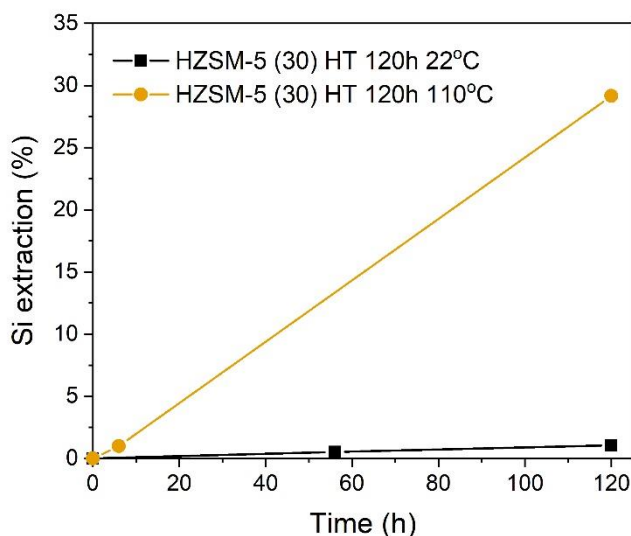


Figure 4.14 Amount of extracted (%) Si from HZSM-5 (30) HT samples after treatment at room temperature (22°C) and 110°C. Al was not detected in effluent in the case of all samples. The Al concentration was same as in the blank sample.

Noticeably, the samples presented opposite results in terms of Si leaching. The room temperature (22°C) treated sample resulted in a final value of 1.05 wt. % of the total extracted Si. However, this was 28 times lower than in the case of the sample treated at 110°C. The final values for both samples were approximately 1.05 wt. % and 29.15 wt. % of total sample Si content that leached after 120 h at 22°C and at 110°C, respectively. What is more, in both cases the levels of extracted aluminium were omitted, as the concentration level was no different as the blank sample.

To summarise, the room temperature treated sample has shown to be nearly completely unmodified after 120 h of treatment in the CFR. The HZSM-5 (30) HT sample was observed to have no change in total pore volume and only a negligible decrease of 3.4% of micropore volume. This change can be associated with the very small amount of leached silicon (1.05 wt. %). However, the lack of pore collapse was confirmed by the existing pore opening bands observed by ATR-FTIR analysis. These results confirm that the EDX analysis might not always be the most reliable in terms of the $\text{SiO}_2/\text{Al}_2\text{O}_3$ molar ratio calculations. The initial calculation shown in Table 4.4 suggested much larger changes of the internal structure. On the other hand, the sample treated at 110°C suffered internal damage. The micropore volume decreased by 10.2% in favour of mesopore formation. The total pore volume had increased by 11.6% and ATR-FTIR analysis confirmed pore modification at higher temperature.

Desilication was confirmed by MP-AES analysis, with 29.15 wt. % of total Si that leached from the sample. However, in both cases the ^{29}Si MAS NMR spectra were similar, and only a small difference was observed in the ^{27}Al MAS NMR spectra. Interestingly, the amount of octahedrally coordinated Al (EFAI) species was shown to decrease in the 22°C treated sample, which might mean that the EFAI might be reattached to framework positions. This may in fact be possible since it was already demonstrated that in some cases the EFAI might revert into the tetrahedral coordination after heating the zeolite above 100°C.²⁷

4.2.5.3 Influence of testing conditions on stability

In the final test, it was to investigate whether the water contact volume over the zeolite and testing conditions may have an influence on the framework damage. Two different extreme testing conditions, focused on different processes, were chosen for the HZSM-5 (30) HT sample – flow (CFR) and static (Batch) conditions. The static test was done in a simple round bottom flask under stirring and reflux to avoid water evaporation (as described in Chapter 2, Section 2.5.2). The flask was filled with 250 mL of distilled water and heated to 110°C. The water contact volume over the zeolite here refers to the water volume per weight of the zeolite sample and therefore the lower the volume, the higher the water contact interaction. In both cases 0.2 g of zeolite was used. To clarify, in the case of the static test (Batch), the sample was in static contact with 250 mL of water during 120 h. However, in the flow test (CFR), when water flow of 0.3 ml min⁻¹ was used, 8.64 times more water volume has passed through the sample during 120 h.

After static testing, the Batch sample was dried overnight in a benchtop oven (110°C, static air) and compared to the sample tested in CFR (110°C, 120 h). The EDX and pore size analysis of untreated and treated samples are presented in Table 4.5.

Table 4.5 Summary of SiO₂/Al₂O₃ molar ratio, pore size volumes, surface areas for the untreated and treated HZSM 5 (30) HT samples. The samples were treated for 120 h at 110°C CFR and 120 h at 110°C Batch. Standard deviations (SD) represent the distribution of atoms after ten measurements for each sample.

HZSM-5 (30) HT	V _t ^(a) (cm ³ /g)	V _{mc} ^(b) (cm ³ /g)	SiO ₂ /Al ₂ O ₃ ^(c)	SD (σ)
Untreated	0.344	0.147	31.25	1.40
After 120 h at 110°C in water (CFR)	0.384	0.132	23.03	0.67
After 120 h at 110°C in water (Batch)	0.309	0.200	23.51	0.81

^(a) Total pore volume from NLDFT

^(b) Micropore volume from NLDFT

^(c) SiO₂/Al₂O₃ molar ratio was determined with EDX analysis, values are an average of 10 different areas of the sample

The difference between the SiO₂/Al₂O₃ molar ratios was very similar, indicating a decrease of 26.3% and 24.8% for the CFR and Batch samples, respectively. The sample treated in the CFR showed an increase in total pore volume and decrease in micropore volume by 11.6% and 10.2% respectively. In contrast, the sample treated in a round bottom flask (Batch) lost 10.2% of total pore volume and gained 36.1% in microporosity. This might happen due to two different mechanisms undergoing in the samples, since two different testing conditions are considered here. The change in observations might be due to different water contact interaction. Since the longer water contact might influence the generation of extra micropore volume due to longer times of water penetration.

Figure 4.15 presents the ATR-FTIR analysis data of both CFR and Batch samples. As was done previously, the analysis was performed to confirm the possible disappearance of pore opening bands.

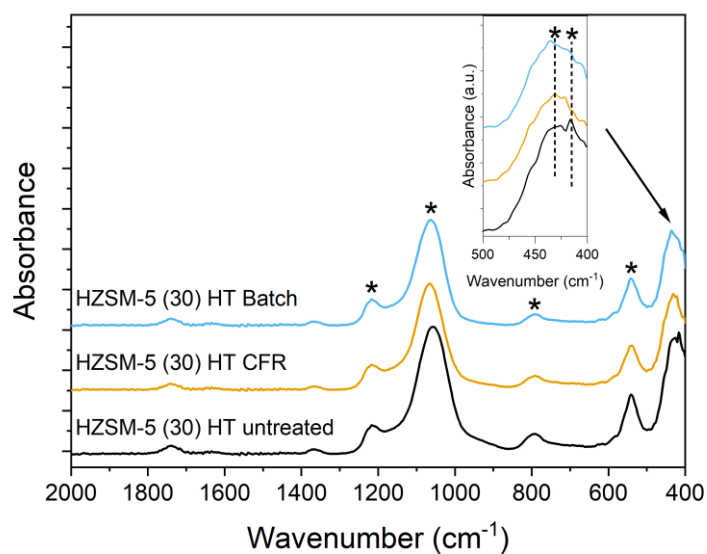


Figure 4.15 ATR-FTIR spectra of untreated HZSM-5 (30) HT (black) and treated for 120 h at 110°C in CFR (yellow) and Batch (blue).

Again, as expected the spectra of the samples presented specific bands which were described in detail in Section 4.2.2 of this chapter. However, again the only change (pointed with the box) was around 420 cm⁻¹ region assigned to pore opening vibrations. Both treated samples were similar and lacked the band. This means that despite the different testing conditions, both samples underwent similar structural changes, indicating that the temperature of water has a major impact on the stability of the zeolite.

Samples were analysed by Single Pulse ²⁹Si and ²⁷Al MAS NMR after the 120 h treatment under different testing conditions. Single Pulse MAS NMR spectra are presented in Figure 4.16.

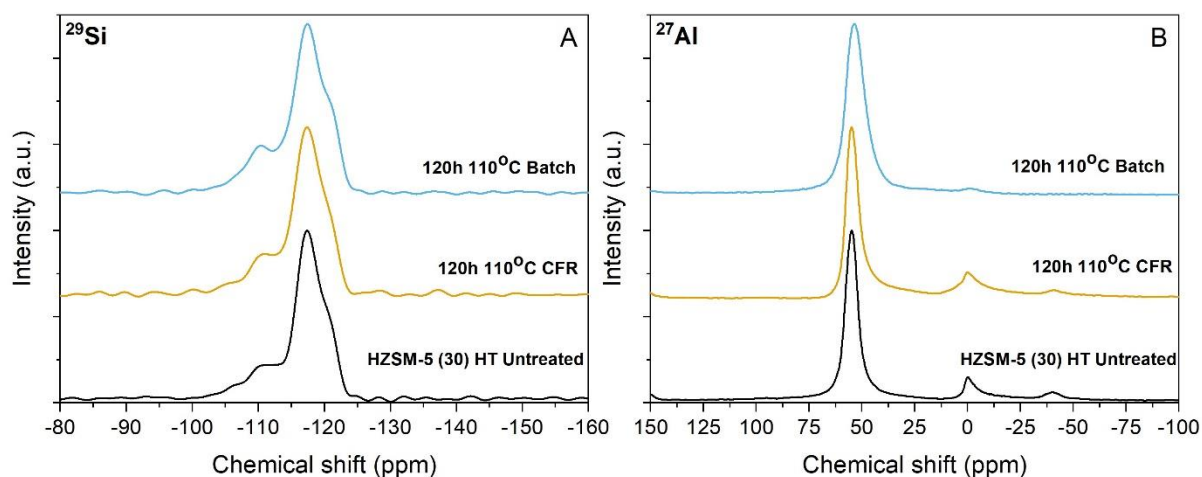


Figure 4.16 Comparison of Single Pulse ^{29}Si (A) and ^{27}Al (B) MAS NMR spectra of untreated (black) and treated HZSM-5 (30) HT samples 120 h in water at 110°C in CFR (light yellow) and at 110°C in Batch (light blue).

The ^{29}Si spectra (left, A) presented a sharp resonance peak at -117 ppm corresponding to Q^4 highly ordered species. For the Batch sample, the Q^4 peak was a bit broader. The resonance at -110 ppm, attributed to Q^3 was better defined for the Batch sample than in the case of the CFR sample, indicating that rearrangement of atoms might have taken place after boiling the sample in water to a greater degree in the Batch reactor.

The ^{27}Al spectra (right, B) were a bit different from the samples analysed before. The Batch sample lacked the Al signal located at 0 ppm, which meant that EFAl was removed from the sample after treatment. The sharp resonance peak at 55 ppm, assign to tetrahedral coordinated Al atom, had also broadened which meant that the aluminium environment had definitely changed. The CFR spectrum remained unchanged in comparison to the untreated sample. This can mean that the water contact has an impact on the Al environment. This might be the extraction from framework or rearrangement from EFAl to framework positions.

It was confirmed that testing conditions have a major influence on leaching or dissolution of the zeolite framework, and in particular the stability of EFAl sites. A study by Ravenelle *et al.* presented similar observations, concluding that siloxane hydrolysis plays a dominant role in framework dissolution, after testing HZSM-5 (MFI) samples of high Al content under autogenic pressure in a Teflon-lined autoclave.⁹

4.2.5.4 High density frameworks and water contact

As presented in the previous section (Section 4.2.5.3), different observations on the stability of Al in the MFI structure were observed. The HZSM-5 (30) HT sample has demonstrated a decrease in EFAl species after boiling it in water for 120 h (Batch). It was assumed that there is a relationship between the water contact and the removal of framework and/or extra-framework aluminium from the zeolite under static conditions. To verify the assumption, CFR and Batch tests were performed on a high Al content commercial zeolite. Tests were performed in order to determine whether the results between the MFI, FER and MOR structures could be comparable.

The HFER (20) C and HMOR (20) C samples were tested in CFR (0.2 g, 0.3 mL min⁻¹, 120 h, 110°C) and boiled (0.2 g, 250 mL water, 120 h, 110°C, heated under reflux) as described in detail in Chapter 2, Sections 2.5.1 and 2.5.2). The treated samples were analysed by Single Pulse ²⁹Si and ²⁷Al MAS NMR after 120 h and spectra are presented in Figure 4.17.

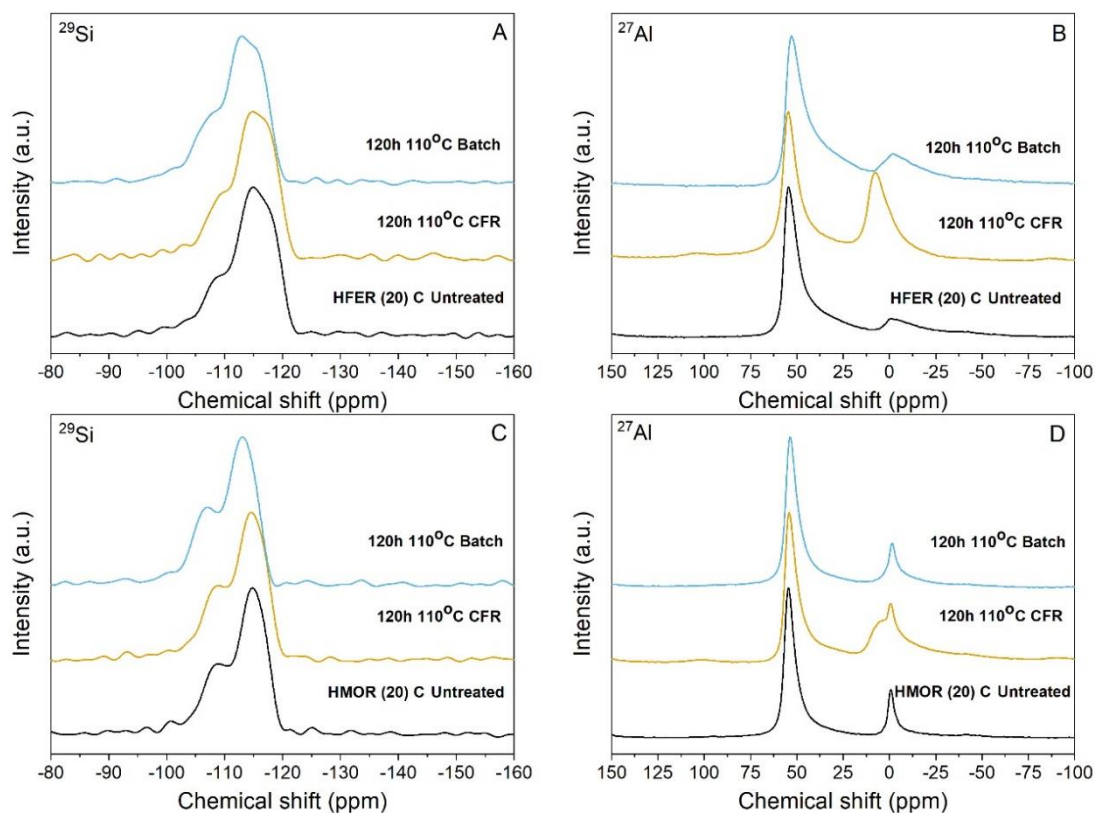


Figure 4.17 Comparison of Single Pulse ²⁹Si (left) and ²⁷Al (right) MAS NMR spectra of untreated and treated at 110°C water in CFR and boiled ('Batch') HFER (20) C (top left, A and top right, B) and HMOR (20) C (bottom left C and bottom right D) samples.

In the case of HFER (20) C, the ^{29}Si resonance (top left, A) presented no visible differences in peak shape and chemical shift for both CFR and Batch samples. Similar observations were made for the HMOR (20) C (bottom left, C) samples. No visible differences were observed in the ^{29}Si spectra, where the resonance of -115 ppm corresponded to Q^4 and -108 ppm was attributed to Q^3 species.

On the other hand, for both tested zeolites, the ^{27}Al MAS NMR (top right, B and bottom right, D) spectra presented a main peak at 55 ppm that was ascribed to tetrahedral Al in zeolite framework. The HMOR (20) C (right, D) and HFER (20) C (right, B) Batch sample spectra were no different from the untreated materials. However, the HFER (20) C (right, B) spectrum after treatment in CFR presents a shift of the extra-framework Al resonance peak from 0 ppm to 7 ppm. The peak was much broader, which would mean that Al species might have rearranged in the structure by formation of five-coordinated extra-framework Al or are a subject to leaching.

However, in the case of HMOR (20) C (bottom right, D) the CFR treated sample, the EFAl resonance is much more intensive and broader in comparison to the untreated sample, indicating an increase in concentration of EFAl species, their rearrangement in the sample and their possible extraction.

In both cases, HMOR (20) C and HFER (20) C samples, the change in EFAl environment might not be observed on the spectra, due to the possibility that Al leaches better in Batch than in CFR. Since 8.64 times more water volume passes the sample in CFR, and the time of water interaction is different under both conditions, as specified previously. In order to confirm the ongoing dealumination and/or desilication of both samples while testing in the CFR (Figure 4.18) and Batch (Figure 4.19), the MP-AES analysis was performed on the effluents. Samples were taken during the continuous process and after finishing the experiment. Test results of the HFER (20) C and HMOR (20) C samples were compiled with the HZSM-5 (30) C and HT samples tested previously and added as reference, and are presented in Figure 4.18.

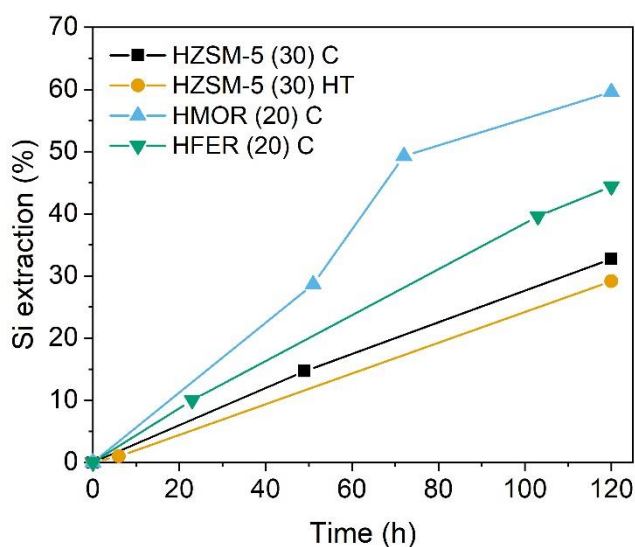


Figure 4.18 Percentage of extracted Si out of total Si from HMOR, HFER and HZSM-5 samples tested in CFR. Aluminium extraction has been omitted as the concentration level was same as blank sample. Water temperature of 110°C.

After analysing 4 similar aluminium content zeolites under the same testing conditions and temperature, one main thing was acknowledged. Even though the MFI samples contained less Al in the framework, these materials still presented better results in long-term water stability than MOR and FER, which possess higher Al content in their structures.

In the case of the HFER (20) C and HMOR (20) C samples, Si extraction reached 44.40 wt. % and 59.60 wt. % of the total Si content respectively. These numbers are much higher than in the case of the MFI structure. However, in all cases, Al was not detected by the MP-AES system, meaning that no framework and/or EFAl species leached out of the samples. However, when exposed to water for a shorter time, aluminium located in the framework positions might undergo partial or total relocation to extra-framework positions, as observed by solid state NMR.

After 120 h of Batch testing, samples were recovered by centrifugation. Both HMOR (20) C and HFER (20) C samples were dried in a benchtop oven (110°C, 16 h, static air) and it was observed that approximately 53.3% and 85.6% of the initial sample weights were recovered, respectively. Following separation from the samples, the water effluent (250 mL) was also analysed by MP-AES for the presence of aluminium and silicon. The results are presented on Figure 4.19.

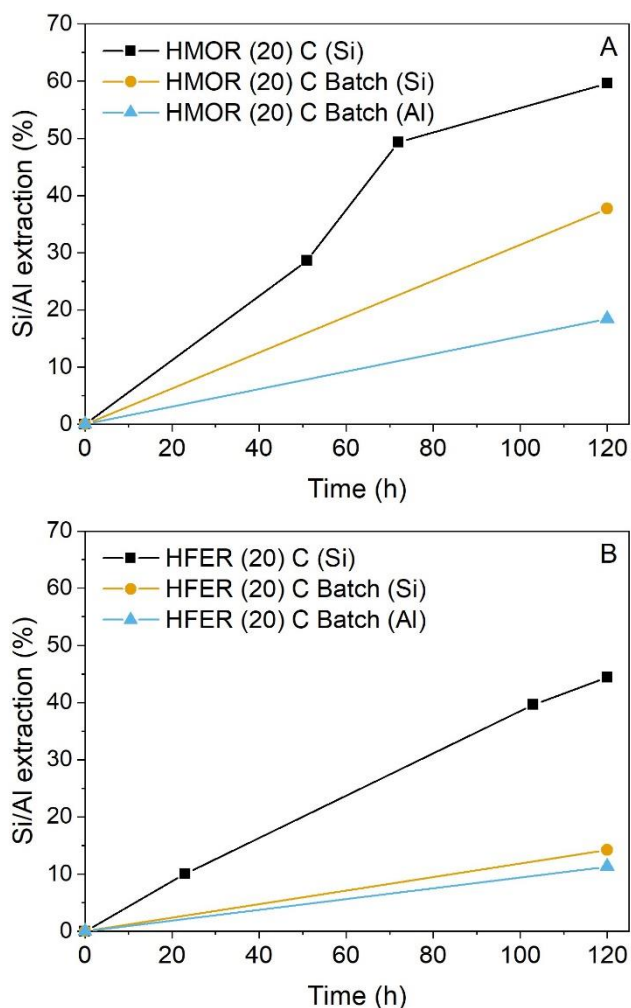


Figure 4.19 Percentage of extracted Si/Al out of total Si/Al from HMOR (top, A) and HFER (bottom, B) samples tested in Batch compared to samples tested in CFR. Water temperature of 110°C. CFR tested sample and Si leaching (black line, squares); Batch tested and Si leaching (yellow, circles); Batch tested and Al leaching (blue, triangles).

Interestingly, here in both cases the leaching study showed the presence of Si and Al in the water recovered by centrifugation after the Batch tests. The percentages of leached Si (amount of Si leached out of total Si in the sample) are much lower than after testing the samples in CFR (HFER: 44.40 wt. % vs. 14.23 wt. %; HMOR: 59.60 wt. % vs. 37.71 wt. %). It might mean that when in constant contact of the zeolite with water under static conditions, the silicon leaching is reduced as the system reaches a solubility equilibrium. However, aluminium leaching was observed as well. In the case of the HMOR (20) C and HFER (20) C samples the percentages of leached Al were 18.41 wt. % and 11.30 wt. % of total Al content in the samples, respectively. In this case, the continuous flow of water can inhibit the

leaching of Al and have a huge impact on the stability of the zeolite sample. This observations also confirm that Al leaches much easier under static conditions (Batch) than in CFR.

Looking at the results from both CFR and Batch tests, it can be concluded that the shorter water contact in CFR inhibits dealumination. Whereas longer water contact, in Batch, means limited desilication but also dealumination of the zeolite. This phenomenon was not only reported for one high-density zeolite structure, but for 3 different frameworks, which makes this observation even more interesting. However, the lack of leached Al was observed only in high Al content zeolites (MFI, MOR, FER), since Al was previously detected in the effluent after testing the medium content MFI structure in CFR (see Figure 4.9 in Section 4.2.4), which would confirm the stabilising role of Al in the framework.

In line with other publications, degradation of the zeolite structure occurs rather through hydrolysis of Si–O–Si bonds than dealumination.⁹ Al atoms stay in their tetrahedral and octahedral coordination positions in the zeolite framework, however since Si is leaching out micropore volume decreases in favour of micropore formation. The Si leaching seems to be more prone in structures with increasing Si/Al ratio. Testing conditions have a huge influence on the stability. It is concluded that in closed systems (here: batch), in which the zeolite is in contact with a known volume of water, at the beginning the Si leaching happens at the same rate as in the flow system. However, in a closed system, leaching of Si reaches a dissolution equilibrium and the water becomes saturated with Si ions from the zeolite framework which causes drop the system pH. The solubility of Si limits the extent to which the framework can be hydrolysed.²⁸ Since stability of zeolites at low pH is widely known, it is expected that Al atoms will be progressively leached from the zeolite.²⁹ This is observed on Figure 4.19, where Si reached solubility equilibrium and the drop in pH caused dealumination. On the other hand, in a continuous flow system, saturation of Si is not possible, as there is constant new flow of deionized water and Si is moved from its framework position and removed from the system without causing dealumination.

4.3 Conclusions

The aim of this chapter was to achieve a better understanding of the role of aluminium in high-density framework zeolites. The MFI structure is of great industrial interest as it may

find use in different aqueous environment application, such as catalytic biomass conversion and desalination processes. Herein, a focused study on the stability of various MFI zeolites of different aluminium content during treatment with hot water flow (CFR) was undertaken. Zeolites were tested for longer times of 120 h, at low and high temperatures (22°C and 110°C) and different testing conditions (flow and static) were applied.

For this purpose, a set of new MFI materials was prepared via the standard hydrothermal method with use of TPAOH OSDA. A range of detailed comparisons between different similar one-pot synthesised and commercial zeolites structures was explored. Different studies were conducted and relations presented. As a result, similar stability was observed for samples of different origin but same $\text{SiO}_2/\text{Al}_2\text{O}_3$ molar ratio within the MFI structure.

Observing and preventing silicon and aluminium leaching is important in terms of framework stability and is often crucial for the material catalytic activity and performance in membrane sieving. At this stage of the study, it was shown that in MFI structure zeolite silicon and aluminium leaching occurred when the medium aluminium content zeolite *i.e.* HZSM-5 (80) HT was exposed to water at 110°C. However, Si leaching was observed from the very beginning of CFR testing, whereas Al leaching happened much later in the process.

A high Al content MFI zeolite was chosen for further tests. It was confirmed that both of the MFI type zeolites lost similar amounts of framework silicon *i.e.*, for HZSM-5 (80) HT and HZSM-5 (30) HT the values of total extracted Si were 29.94 wt. % and 29.15 wt. %, respectively. On the other hand, no aluminium was present in effluent after testing the HZSM-5 (30) HT sample, while the aluminium extraction was approximately 18.00% of total Al extracted from the HZSM-5 (80) HT sample. This reconfirmed that aluminium played a great role in effective prevention of framework degradation and that desilication was mainly generating secondary mesoporosity in the high Al content MFI framework.

Moreover, it was found that water temperature plays a significant role. This was confirmed by exposing the HZSM-5 (30) HT zeolite sample to water flow in CFR at room (22°C) and elevated temperatures (110°C) for 120 h. The amount of Si extracted from the room temperature treated sample was 28 times lower than in the case of the high temperature treated one. Also, the micropore volume and overall total porosity were not affected after testing in room temperature. What is more, no Al was present in the effluent water after both samples were tested, meaning that no dealumination was observed.

Different testing conditions were implemented as well. Since the HZSM-5 (30) HT sample was already tested under flow conditions (CFR), it was decided to compare it to a sample tested under static conditions (Batch). The static conditions were implemented in a form of a simple round bottom flask under stirring and reflux to avoid water evaporation of water at 110°C. Both samples were tested for 120 h. The Batch sample had similar SiO₂/Al₂O₃ molar ratio after the experiment, but the ²⁷Al MAS NMR revealed extraction of EFAl and framework aluminium peak broadening which was not observed in any other sample before. This indicated that the method of testing had an influence as well on the level and the mechanism of the zeolite framework degradation.

To confirm these observations, two other high density and high aluminium content zeolite structures were used – Ferrierite (FER type) and Mordenite (MOR type). These samples, of similar SiO₂/Al₂O₃ molar ratio of 20, were tested under same conditions of time and temperature in Batch and CFR. It was concluded that the level of framework degradation depends on the testing conditions and therefore the water interaction with the zeolite. Here, two extreme methods were used. Under static conditions (Batch) the longer contact means longer water penetration of the zeolite but also reaching solubility equilibrium since stable water volume was used. This is an opposite situation to the flow conditions (CFR), where the volume of water passing through the sample is much greater, but also the water-zeolite interaction is shorter and solubility equilibrium is not reached. It was also observed that in Batch conditions Si and Al leaching happened simultaneously for both Mordenite and Ferrierite structures, whereas in CFR no aluminium was present in the effluent water. However, the desilication level was much higher when the zeolites were tested in flow (CFR).

The research presented in this chapter has confirmed that zeolites with higher Al content in their framework are less prone to framework damage when exposed to direct contact with water at high temperature. The fact that no dealumination was present and observed in the H-ZSM-5 zeolite for such a prolonged time in the CFR is interesting from a catalytic point of view. This means that Lewis acid sites might not be affected and under some suitable conditions (mainly related with choosing the appropriate reaction temperature) the zeolite could behave as water-tolerant catalysts for prolonged periods of time.

4.4 References

- 1 M. Dusselier, M. E. Davis, *Chem. Rev.* 2018, **118**, 5265-5329
- 2 P. Sazama, J. Dedecek, V. Gábová, B. Wichterlová, G. Spoto, S. Bordiga, *J. Catal.*, 2008, **254**, 180–189
- 3 C. Auepattana-aumrung, V. Márquez, S. Wannakao, B. Jongsomjit, J. Panpranot, P. Prasertthdam, *Sci Rep*, 2020, **10**, 13643
- 4 Y. Jiao, L. Forster, S. Xu, H. Chen, J. Han, X. Liu, Y. Zhou, J. Liu, J. Zhang, J. Yu, C. D'Agostino, X. Fan, *Angew. Chem. Int. Ed.*, 2020, **59**, 19478-19486
- 5 D. W. Breck, *Zeolite Molecular Sieves: Structure, Chemistry and Use*, John Wiley & Sons, New York-London-Sydney-Toronto, 1974
- 6 I. G. Wenten, P. T. Dharmawijaya, P. T. P. Aryanti, R. R. Mukti, Khoiruddin, *RSC Adv.*, 2017, **7**, 29520–29539
- 7 A. K. Jamil, O. Muraza, R. Osuga E. N. Shafei, K-H. Choi, Z. H. Yamani, A. Somali, T. Yokoi, *J. Phys. Chem. C*, 2016, **120**, 22918-22926
- 8 W. Lutz, H. Toufar, R. Kurzhals, M. Suckow, *Adsorption*, 2015, **11**, 405-413
- 9 R. M. Ravenelle, F. Schüßler, A. D'Amico, N. Danilina, J. A. van Bokhoven, J. A. Lercher, C. W. Jones, C. Sievers, *J. Phys. Chem. C*, 2014, **114**, 19582-19595
- 10 A. Vjunov, J. L. Fulton, D. M. Camaioni, J. Z. Hu, S. D. Burton, I. Arslan, J. A. Lercher, *Chem. Mater.*, 2015, **27**, 3533–3545
- 11 L. Zhang, K. Chen, B. Chen, J. L. White, D. E. Resasco, *J. Am. Chem. Soc.*, 2015, **137**, 11810-11819
- 12 P. A. Zapata, Y. Huang, M. A. Gonzalez-Borja, D. E. Resasco, *J. Catal.*, 2013, **308**, 82-97
- 13 A. R. Maag, G. A. Tompsett, J. Tam, C. Aik Ang, G. Azimi, A. D. Carl, X. Huang, L. J. Smith, R. L. Grimm, J. Q. Bond, M. T. Timko, *Phys. Chem. Chem. Phys.*, 2019, **21**, 17880-17892
- 14 C. J. Heard, L. Grajciar, F. Uhlik, M. Shamzhy, M. Opanasenko, J. Čejka, P. Nachtigall, *Adv. Mater.*, 2020, **32**, 2003264
- 15 R. Zhang, S. Xu, D. Raja, N. B. Khusni, J. Liu, J. Zhang, S. Abdulridha, H. Xiang, S. Jiang, Y. Guan, Y. Jiao, X. Fan, *Micropor. Mesopor. Mat.*, 2019, **278**, 297-306
- 16 M. J. Remy, D. Stanica, G. Poncelet, E. J. P. Feijen, P. J. Grobet, J. A. Martens, P. A. Jacobs, *J. Phys. Chem.*, 1996, **100**, 12440-12447
- 17 Zeolyst, standard zeolite powders, accessed 1 March 2021, <http://zeolyst.com>
- 18 IZA Structure Commission, Database of Zeolite Structures, accessed 1 March 2021, <http://www.iza-structure.org/databases/>
- 19 D. Coutinho, R. A. Orozio-Tevan, R. F. Reidy, K. J. Balkus, *Micropor. Mesopor. Mat.*, 2002, **54**, 229–248
- 20 S. M. Auerbach, K. A. Carrado, P. K. Dutta, *Handbook of Zeolite Science and Technology*, CRC Press, 2003
- 21 D. Lesthaeghe, P. Vansteenkiste, T. Verstraelen, A. Ghysels, C. E. A. Kirschhock, J. A. Martens, V. Van Speybroeck, M. Waroquier, *J. Phys. Chem. C*, 2008, **112**, 9186–9191
- 22 L. Shirazi, E. Jamshidi, M. R. Ghasemi, *Cryst. Res. Technol.*, 2008, **43**, 1300-1306
- 23 J. I. Goldstein, J. R. Michael, N.W.M. Ritchie, J. H. J. Scott, D. C. Joy (2018) SEM Image Interpretation. In: Scanning Electron Microscopy and X-Ray Microanalysis. Springer, New York, NY.
- 24 A. Palizdar, S. M. Sadrameli, *Renewable Energy*, 2020, **148**, 674-688

-
- 25** P. Sudarsanam, E. Peeters, E. V. Makshina, V. I. Parvulescu, B. F. Sels, *Chem. Soc. Rev.*, 2019, **48**, 2366-2421
- 26** R. Mokaya, *Chem. Commun.*, 2000, 1891-1892
- 27** J. A. van Bokhoven, A. M. J. van der Eerden, D. C. Koningsberger, *Stud. Surf. Sci. Catal.*, 2002, **142**, 1885-1890
- 28** S. Prodingier, M. A. Derewinski, *Pet. Chem.*, 2020, **60**, 420-436
- 29** X. Liu, P. Mäki-Arvela, A. Aho, Z. Vajglova, V. M. Gun'ko, I. Heinmaa, N. Kumar, K. Eränen, T. Salmi, D. Y. Murzin, *Molecules* 2018, **23**, 946.

5 Stability of MOFs

5.1 Introduction

For the last 25 years, academic and industrial perspective has focused on the development of alternative materials to zeolites and other porous inorganic solids. This interest resulted in discovery and research of Metal-Organic Frameworks (MOFs) which are a subclass of coordination polymers.¹ These materials are built of metal ions or metal-oxo clusters coordinated with organic linkers forming 3-dimensional ultraporous structures. MOFs are often compared to zeolites as they possess similar features such as porosity, high adsorption abilities and solvent sorption capacities.² However, unlike zeolites, MOFs are characterised by open metal sites (OMS), coordinatively unsaturated sites (CUS) or open coordination sites (OCS)³ while T-atoms (*i.e.*, Al, Si) in zeolites are of lower accessibility due to large oxygen ions surrounding the heteroatom.²

MOFs show great potential for a variety of applications, including thin film devices, catalysis, biosensor, drug delivery agents and high-capacity adsorbents.^{4,5,6} First known MOF structures were unstable and exhibited poor hydrothermal or even steam stability.⁷ Zeolites, as purely inorganic materials, were expected to present excellent hydrothermal stability. However, they have also been shown to suffer from some limitations in water of elevated temperatures. These observations were demonstrated throughout the two previous chapters, where zeolites presented internal structural damage due to partial desilication and dealumination mechanisms after contact with hot water.

Several recent publications focused on stability and improving stability of MOFs in water. Batra *et al.* built a machine learning-based model to classify MOFs accurately and instantly towards stability depending on target application, or the amount of water exposed.⁸ Ding *et al.* summarised recent advances in the design and synthesis of stable MOFs and MOF-based materials through synthesis or by post synthetic structural processing.⁹ It was shown that a well-design of MOFs synthesis route can provide extraordinary performance for targeted application. UiO-66 (Figure 5.1) is considered to be a stable material for applications in aqueous environment.^{10,11}

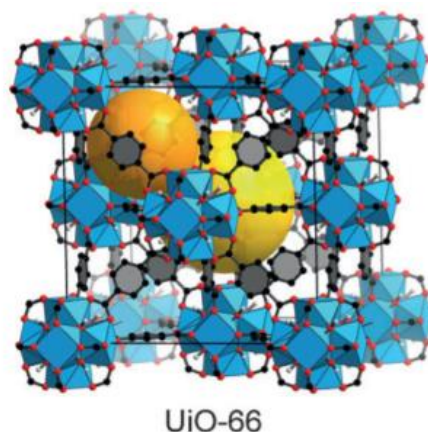


Figure 5.1 A representation of the UiO-66 MOF framework.

Hydrothermally stable MOFs could be potentially used for applications in liquid phase operations. Thermogravimetric analysis (TGA) gives an initial idea of a material stability, providing information about thermal decomposition and the rate of weight loss as function of temperature or time. According to a review paper from 2014, a most common method for determining the water stability of a MOF is to expose it to steam and compare the pXRD patterns and BET surface area measurements of a post treated powder to the untreated one.²² However, liquid phase operations require much advanced testing methods. This is mainly because certain structures might show good stability under steam but degrade completely when in direct contact with liquid water, particularly at elevated pressure. Another testing condition proposed, is immersion and stirring under relevant aqueous conditions. Such studies might suggest high stability due to static conditions. However, as presented in Chapter 4, the choice of experimental setup has a great influence on the stability test outcomes.

As mentioned previously, there is a certain number of MOF structures which are potentially stable in water. HKUST-1 structure was confirmed to be stable at 40% relative humidity for 7 days in air.¹² A solid state NMR study has presented that the material maintains structural integrity when in contact with water content up to 0.5 mol equivalent with respect to copper.¹³ Water adsorption cycles performed for a UiO-66 have shown that the structure maintains unchanged porosity and surface area after 6 cycles at 25°C.¹⁴ What is more, due to excellent adsorption properties materials such as UiO-66, MIL-53, and ZIF-8 have been studied extensively for removal of toxic metals due to their high chemical stability.^{15,16} UiO-66 was reported to be stable in a broad pH range of 1 to 10 and was found to be superior

for removal of arsenic (arsenate) from water.¹⁶ Similarly, the capability was observed in ZIF-8.¹⁷ MIL-53 membranes have been successfully used for the dehydration of a water-ethyl acetate mixture (7 wt.% water) by pervaporation at 60°C.¹⁸ Another paper studied water stability of MIL-53(Al) by immersing in different solutions of varying pH values (*i.e.*, 2, 7, and 14) at different temperatures (*i.e.*, at room temperature, 50 °C and 100 °C).¹⁹ The crystallinity maintained unchanged for over 7 days at temperatures below 50 °C. However, slight degradation was observed by pXRD for samples immersed at 100 °C for the same amount of time.

All these mentioned studies present great potential for the use of MOFs in liquid phase operations. Yet none of the review papers published so far (up to 2020) mentioned structural stability studies done in continuous flow regime (CFR).^{10,22,23} However, publications related to the use of MOFs in membrane applications show greater potential for use for *e.g.* desalination.²⁰

A need for CFR studies has arisen as a consequence of these observations. The aim of this Chapter is to obtain fundamental data on water and solvent stability of selected MOF structures. Shorter times of 24-48 h were chosen for the initial studies, with a possibility for further tests to be extended for up to 120 h, not only in water, but also ethanol and methanol for comparison of the outcomes. These types of studies are not yet published in literature.

5.2 Initial MOF screening

Based on detailed literature reviews, four MOFs were chosen for stability tests in CFR in order to screen out the most water stable framework.^{10,21,22,23} Previous reported studies on those materials have shown that these MOF structures are considered in catalytic perspective due to their unique porosity, potential stability under high temperature conditions, scale-up possibilities, and Lewis and/or Brønsted acidity.²³

Three out of four MOFs were obtained from BASF, and UiO-66(Zr)-H was synthesised according to the procedure described in Chapter 2, Section 2.2.2.1. Table 5.1 summarises the chosen MOF structures, focusing on the MOF name, metal ion and linker source.

Table 5.1 Selection of MOF structures used in the study.

MOF ID ^(a)	Commercial name ^(b)	Metal ion/cluster	Linker source
MIL-53(Al)	Basolite [®] A100	Al ³⁺	Terephthalic acid (H ₂ BDC)
HKUST-1 (or MOF-5)	Basolite [®] C300	Cu ²⁺	Trimesic acid (H ₃ BTC)
ZIF-8	Basolite [®] Z1200	Zn ²⁺	2-Methylimidazole (HMiM)
UiO-66(Zr)-H	-	Zr ⁴⁺	Terephthalic acid (H ₂ BDC)

(a) All structures schemes are presented in Chapter 1, Section 1.2.1

(b) Produced by BASF

Further details on the structure, characterisation and properties of these MOF structures are presented in Chapter 1. Samples of the commercial HKUST-1, ZIF-8, MIL-53(Al) and synthesised UiO-66(Zr)-H were subjected to thermal analysis in order to establish the nature of the coordinated components and to validate the thermal stability of these materials. The MOF powders were not pelletised prior to analysis, as it was previously reported that specific surface area, pore sizes and crystallinity were severely affected by the pelletisation process.²⁴ TGA analysis was performed in order to confirm that the textural properties and thermal decomposition points were consistent with previous studies. The TGA–DTG curves of four unmodified samples were recorded and are presented on Figure 5.2.

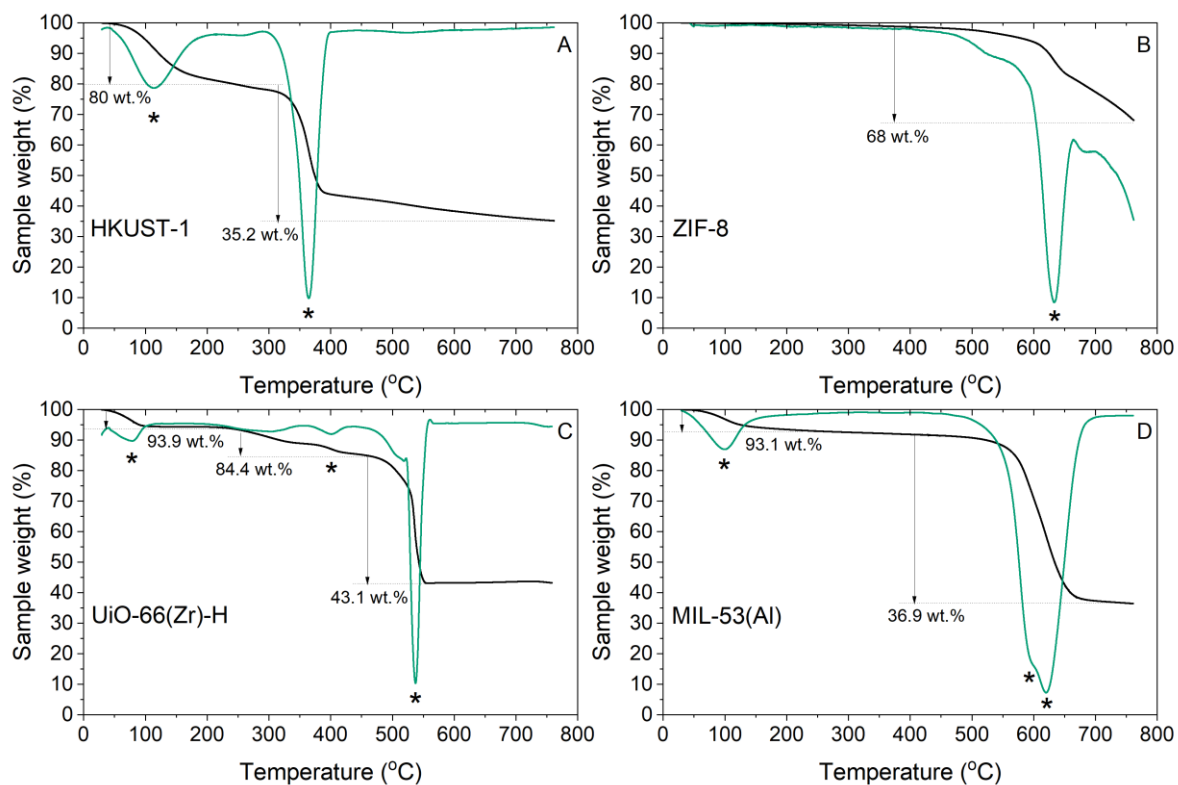


Figure 5.2 TGA (black) and the DTG (green) curves of HKUST-1 (top, A); ZIF-8 (top, B); UiO-66(Zr)-H (bottom, C); MIL-53(Al) (bottom, D) samples. The asterisks point the peak calculation of the largest change in sample weight defined by the 1st derivative of the weight loss curve (black line).

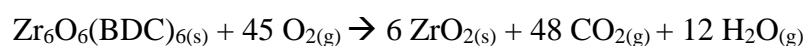
The samples were heated with a controlled ramp rate ($10^{\circ}\text{C min}^{-1}$) under constant nitrogen purge and flow rate of 30 mL min^{-1} in order to record their thermal response in temperature range of $25\text{--}800^{\circ}\text{C}$. Thermal stability studies revealed that all frameworks are stable up to at least 350°C . All structures, except for ZIF-8 (Figure 5.2, top, B), had water or other solvent trapped inside the pores, which evaporated at 100°C .

In the case of the HKUST-1 (Figure 5.2, top, A) sample, in the first step of the TGA curve, a weight loss of almost 20 wt. % indicates dehydration of the adsorbed water or solvent inner the material. This loss corresponds to 3 water molecules per each copper centre in the framework.²⁵ At 365°C , HKUST-1 underwent complete decomposition, involving around 45 wt. %, loss and the remaining (35.2 wt.%) structure converted to inorganic copper oxide phase (Cu_2O and CuO).²⁶ The weight loss and the overall thermogravimetric analysis is in line with previously reported TGA curves of this material.²⁷

The thermal decomposition of UiO-66(Zr)-H is presented on Figure 5.2 (bottom, C). The decomposition started by a weight loss of 6.1 wt.%, which was associated with evaporation

of adsorbed solvent (DMF) molecules at around 100°C and later by dehydroxylation of zirconium oxoclusters which was assigned to the small weight change at 400°C (total loss of 15.6 wt.%).²⁸ The large weight loss at 536°C is most likely due to the linker volatilisation.²⁹ UiO(Zr)-66-H decomposes to zirconia (ZrO₂), which is the final remaining solid material (43.1 wt.%).

An ideal hydroxylated UiO(Zr)-66-H has a molar mass of 1664.06 g mol⁻¹. In an ideal case scenario a defect-free dehydroxylated UiO(Zr)-66-H is denoted as Zr₆O₆(BDC)₆. When heating procedure is applied, the final decomposition of a dehydroxylated UiO(Zr)-66-H is considered as follows:³⁰



Knowing that the final product is solid ZrO₂ (6 moles = 739.34 g mol⁻¹), the expected weight loss is 55.56%, while the recorded weight loss was 56.9%. This can indicate remaining impurities in form of acetic acid or ethanol trapped in the UiO-66 pores. The shape of the TGA curve and observations of weight changes are in line with other TGA studies of similar UiO-66 structures.³¹

The MIL-53(Al) (Figure 5.2, bottom, D) was stable up to 620°C. Similar as in the case of other samples, the first step and weight loss of 6.9 wt.% is associated with the evaporation of adsorbed water. The ZIF-8 (Figure 5.2, top, B) framework decomposed at 633°C, and a weight loss of 32 wt.% is observed. These values are as expected and in line with previous reports.^{32,33} Since ZIF-8 exhibits hydrophobic properties, no initial weight loss was observed at ~100°C.³⁴

Samples were examined for hydrothermal stability in stainless steel continuous flow reactors (CFR) with deionised water flow according to procedure given in Chapter 2, Section 2.5.1 (0.2 g packed sample, 35 bar inlet pressure, 10 bar back pressure, water flow 0.3 mL min⁻¹, 110°C). After running the continuous flow experiments the fixed-bed reactors were dried in a benchtop oven overnight (16 h, 110°C, air), opened and the samples were collected for further characterisations. Shorter testing times of 24-48 h were chosen for the initial studies, in order to determine the extent of pressure build up in the system. If this pressure is not relieved, the CFR system may be damaged.

Powder X-ray Diffraction (pXRD) was used to verify the crystallinity of all of the initial samples and those after water treatment. These studies give important information about

possible changes in the crystal structure after contact with water. In an ideal situation, no change should be observed. Diffraction patterns of untreated and water treated HKUST-1 and ZIF-8 samples are presented in Figure 5.3. Due to structural similarities and ease of presenting and discussing the data the UiO-66(Zr)-H and MIL-53(Al) samples are presented on a separate figure, Figure 5.4.

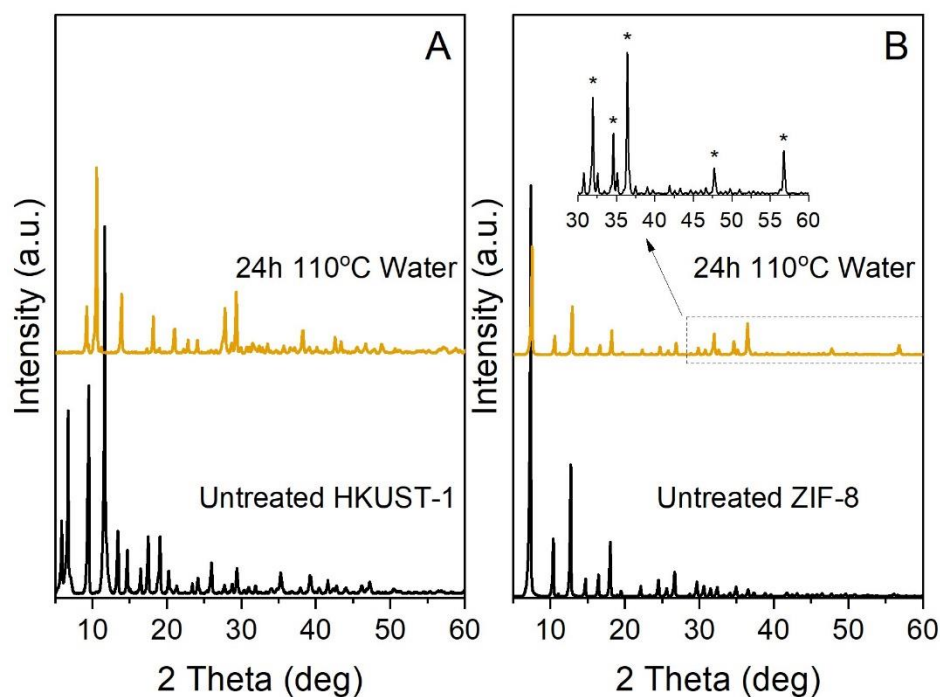


Figure 5.3 A comparison of untreated (black) and water treated (light yellow) for 24 h at 110°C (CFR) A) HKUST-1; B) ZIF-8 samples.

HKUST-1 (Figure 5.3, left, A) is known not to be stable in water.³⁵ Here, the MOF was used to present an example of MOF instability in water, as the structure underwent a complete structural transformation only after 24 h of treatment. The diffraction pattern of the HKUST-1 exposed to hot water did not reveal the presence of the BTC linker.³⁶ The completed degradation of the MOF crystal structure arose most likely by the hydrolysis of the metal-linker bond and transformation into another unique crystal structure. Consequently, the framework resulted in, most possibly, a mixture of or a material built of copper hydroxide $\text{Cu}(\text{OH})_2$ and a protonated carboxylic linker.³⁷ However, $\text{Cu}(\text{OH})_2$ can be used for HKUST-1 synthesis (room temperature, aqueous ethanolic solution), therefore the degradation of MOF could be possibly reversed.³⁸

In the case of the ZIF-8 (right, B) the MOF main peak intensities (7.3° , 10.4° and 12.9°) decreased significantly after water treatment. Furthermore, additional new peaks were observed in the $30\text{--}60^\circ$ region (highlighted by the box). After water treatment, five small peaks located at 32.6° , 34.7° , 36.5° , 47.8° , 57.2° (highlighted by asterisks) appeared, all associated with formation of ZnO.³⁹ Differently than HKUST-1, ZIF-8 underwent moderate hydrolysis and at a much slower pace.

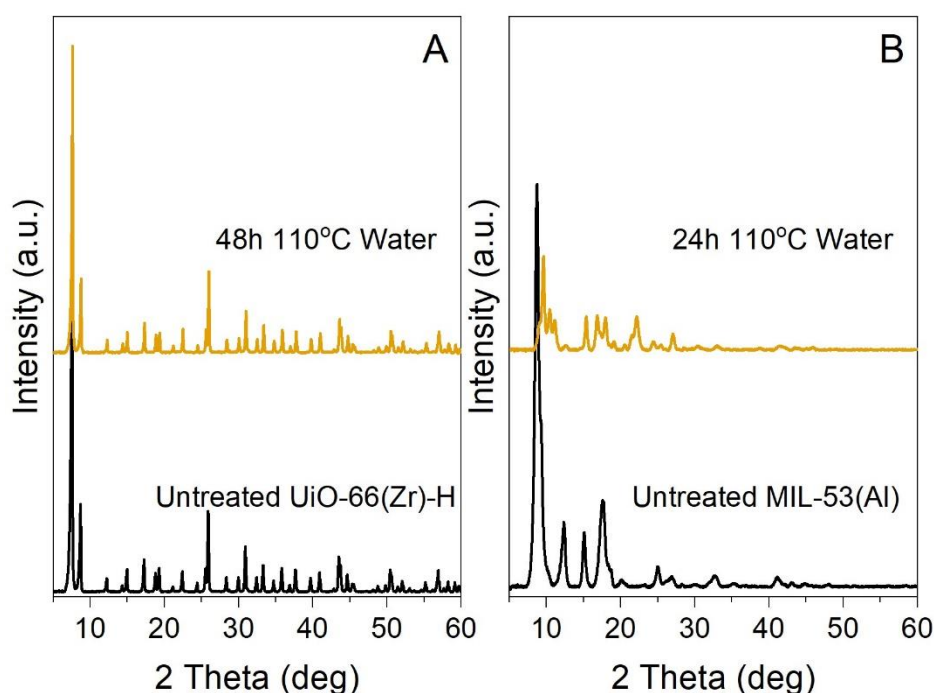


Figure 5.4 A comparison of untreated (black) and water treated (light yellow) for 24 or 48 h at 110°C (CFR) A) UiO-66(Zr)-H; B) MIL-53(Al) samples.

The UiO-66(Zr)-H (left, A) and MIL-53(Al) (right, B) presented on Figure 5.4 are much more comparable as these materials possess the same linker (H_2BDC), but different metal ions; Zr and Al, respectively. The UiO-66(Zr)-H structure (left, A) is widely considered as a structure stable under static water conditions. Here, the diffraction patterns after 48 h presented no change in comparison to the untreated sample. No additional phases were detected and the intensities of all peaks remained the same.

In contrast to UiO-66(Zr)-H, the MIL-53(Al) (left, B) structure underwent complete framework transformation only after 24 h of treatment. The diffraction pattern of the untreated sample presented 2 peaks associated with the H_2BDC linker – an intense peak at

17.4° and a smaller one at 25.1°. ⁴⁰ These peaks are still visible in the treated sample pattern, although are of much lower intensities. In general, the diffraction pattern after water treatment fails to follow the untreated sample pattern. A new unique crystalline phase was formed, most likely in form of γ -AlO(OH) and/or γ -Al₂O₃. ⁴¹ However, further characterisation of the new phase is recommended.

In order to confirm changes in textural properties a complete N₂-physisorption analysis on the untreated and treated materials was also performed in order to see how the specific surface area (S_{DFT}) and total pore volume (V_t) changes after water treatment (Table 5.2).

Table 5.2 Complete textural properties; specific surface area (S_{DFT}) and total porosity data (V_t) of MOF untreated and water treated samples (24-48 h at 110°C, CFR).

MOF ID	Sample type	S_{DFT} (m ² g ⁻¹) ^(a)	V_t (cm ³ g ⁻¹) ^(b)
MIL-53(Al)	Untreated	565	0.800
	24 h 110°C	66	0.008
HKUST-1	Untreated	1338	0.602
	24 h 110°C	15	0.016
ZIF-8	Untreated	1234	0.625
	24 h 110°C	838	0.427
UiO-66(Zr)-H	Untreated	1591	0.618
	48 h 110°C	1518	0.611

(a) Specific surface area obtained from NLDFT

(b) Total pore volume from NLDFT

As can be seen, all samples demonstrated different levels of specific surface area and total pore volumes, with the untreated UiO-66(Zr)-H presenting highest S_{DFT} value (1591 m² g⁻¹) of all the tested MOFs. However, both HKUST-1 and MIL-53(Al) presented significant decreases in the S_{DFT} and V_t values due to both structures being converted to inorganic phases, as presented previously with pXRD diffraction patterns. Inorganic nonporous phases present very low values of specific surface area and are characterised by the lack of pore volume. Whereas ZIF-8 presented a significant decrease in both S_{DFT} and V_t values by 32%. In the case of UiO-66(Zr)-H these changes were very slight, with a decrease in specific

surface area of 4.5% and pore volume of only 1% after 48 h, which proves that this structure exhibits unprecedented hydrothermal stability beyond all tested MOFs.

However, looking at Figure 5.3 and Figure 5.4, it is not easy to verify if commercial materials are just less stable than synthesised ones, since the synthesis route of the commercial materials is unknown. As an example, a study by Lee *et al.* presented differences in ZIF-8 physicochemical properties after using 7 different synthesis routes and concluded that smaller particles were more stable and active in Knoevenagel condensation reactions.⁴² Moreover, the choice of zinc source might also be significant. Stability of ZIF-8 was a topic of a research study by Sheng *et al.*, who explored the influence of zinc source on the MOF stability by immersing each prepared ZIF-8 at 80°C water for up to 10 days.⁴³ This work presented that a higher framework stability might be achieved by using zinc acetate instead of other zinc salts as the main metal source in the synthesis.

Since the synthesis of ZIF-8 is relatively straightforward, a stability comparison was made between commercial ZIF-8 and laboratory synthesised ZIF-8. Accordingly, ZIF-8 was prepared via a simple solvothermal route following the procedure described by Tian *et al.*, using $\text{Zn}(\text{NO}_3)_2 \cdot 6\text{H}_2\text{O}$ as zinc source and 2-methylimidazole as linker source.⁴⁴ Both were dissolved in methanol prior mixing and left stirring at room temperature in a round bottom flask. After 24 h the ZIF was collected by centrifugation, washed and dried. A detailed preparation method is described in Chapter 2, Section 2.2.2.4.

The commercial material (henceforth ZIF-8 C) was compared to a room temperature synthesised material (henceforth ZIF-8 RTS) in terms of crystallinity after 24 h in stainless steel continuous flow reactors (CFR) with deionised water flow at 110°C. Diffraction patterns of untreated and water treated samples are presented on Figure 5.5.

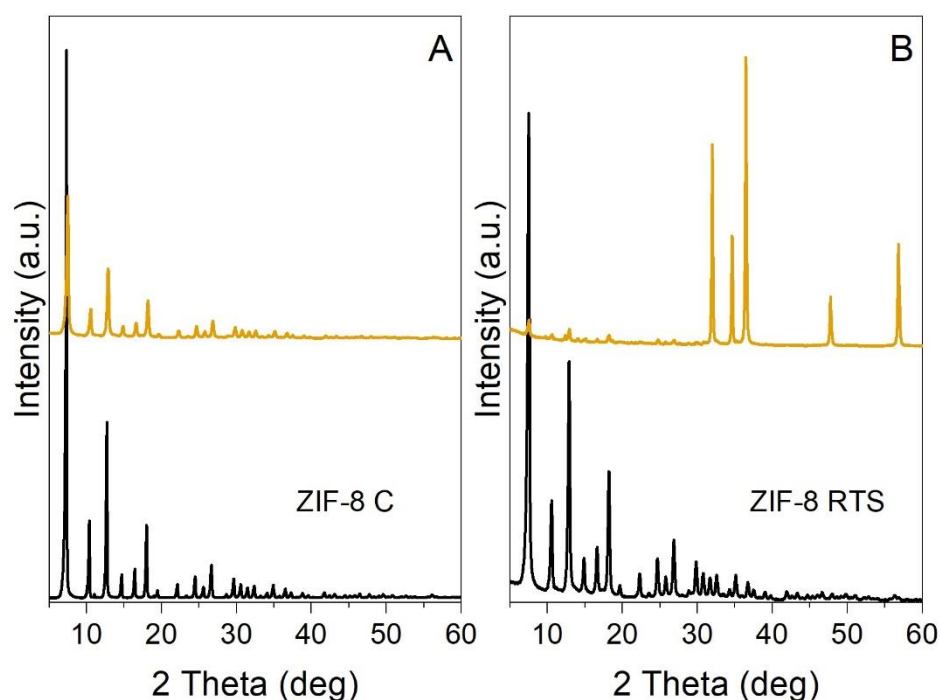


Figure 5.5 A comparison of commercial ZIF-8 (ZIF-8 C, left A) versus room temperature synthesised one (ZIF-8 RTS, right, B, magnification x2) samples. Untreated (black) and 24 h at 110°C (CFR) water treated (light yellow).

In order to present the results in a readable way and emphasise the differences, the scale of the B graph was magnified 2 times. The untreated ZIF-8 RTS sample (right, B) presented much lower initial peak intensity than its commercial equivalent, ZIF-8 C (left, A). In contrast to the commercial ZIF-8 C sample, the synthesised sample (RTS) nearly completely transformed into ZnO after only 24 h of treatment. As previously described, the ZnO peaks are located at 32.6°, 34.7°, 36.5°, 47.8°, 57.2°. However, the small peaks between 5 and 30° indicate that a small amount of the metal-imidazole-metal structure still remained in the treated sample. The overall outcome has proved, that both of the samples, prepared most likely by two different methods, were unstable under water flow conditions but to a different extent. These results clearly show that the choice of synthesis route and zinc source have a determining influence on the stability of a MOF structure, as suggested previously.

However, all of the tested commercial samples underwent partial or complete hydrolysis and/or transformed into unique crystal structures only after 24 h treatment in water at 110°C. This strongly implies that HKUST-1, ZIF-8 and MIL-53(Al) are materials that in present

forms could be ruled out from the use under pressurised liquid water conditions for extended periods of time.

It was observed that the own-synthesised UiO-66 structure possesses good thermal stability with a final decomposition point at 536°C. No change in the pXRD diffraction patterns occurred after 48 h of water treatment. Importantly, the structure exhibited nearly no loss in specific surface area and total pore volumes over 48 h of treatment at 110°C in the CFR. Therefore, further exploration of UiO-66 structure and its stability was undertaken since promising and interesting stability results have been obtained.

5.3 UiO-66(Zr)-H and its amino analogue, UiO-66(Zr)-NH₂

5.3.1 Materials characterisation

After initial testing of HKUST-1, ZIF-8, MIL-53(Al) and UiO-66(Zr)-H, it was concluded that only UiO-66(Zr)-H was stable in CFR after 48 h of testing at 110°C. The morphology of the structure remained unchanged after direct contact with hot water as confirmed by pXRD analysis. This zirconium (Zr) containing structure is a porous material in which the terephthalate linker choice can be controlled, and dictates the structure and hence properties of the material.⁴⁵ Several different UiO-66 analogues have been synthesised so far by using various functionalised terephthalate linkers, including groups such as -NH₂, -(NH₂)₂, -NO₂, -Br, -OH, -(OH)₂, -SO₃H, -COOH, -I and -(SH)₂.^{46,65} In order to understand the linker choice on its framework stability, two analogue frameworks (-H and -NH₂) were synthesised according to procedures presented in Chapter 2, Section 2.2.2.1. The only difference in the procedure, was the choice of linker source (terephthalic acid and 2-aminoterephthalic acid). Figure 5.6 presents Scanning Electron Microscopy (SEM) images of the surface morphology of both UiO-66(Zr) materials.

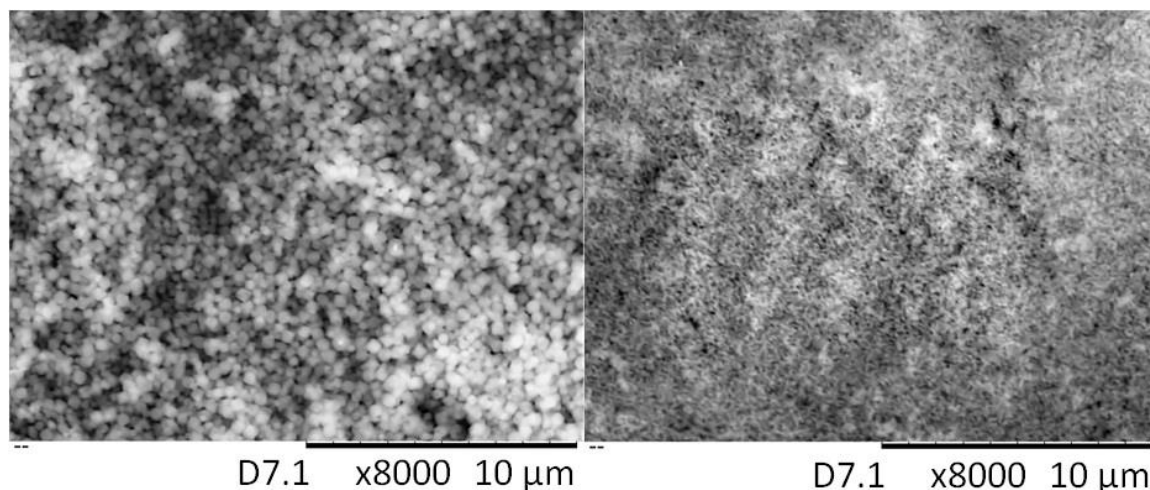


Figure 5.6 SEM images of UiO-66(Zr)-H (left) and UiO-66(Zr)-NH₂ (right). Magnification: 8000x, BSE 15 kV.

The SEM image of UiO-66(Zr)-H (left) gives a clear view of cubic intergrown crystals. However, the UiO-66(Zr)-NH₂ (right) crystals are much smaller in sizes. Both materials present a high crystallinity and possess specific surface areas of up to 1600 m² g⁻¹, which is in line with previous findings in the existing literature.⁶⁵

The untreated UiO-66(Zr)-H and UiO-66(Zr)-NH₂ samples were probed by Thermogravimetric analysis (TGA) and presented in Figure 5.7. It is interesting, that with such a slight difference in linker choice, these materials differ significantly in thermal stability.

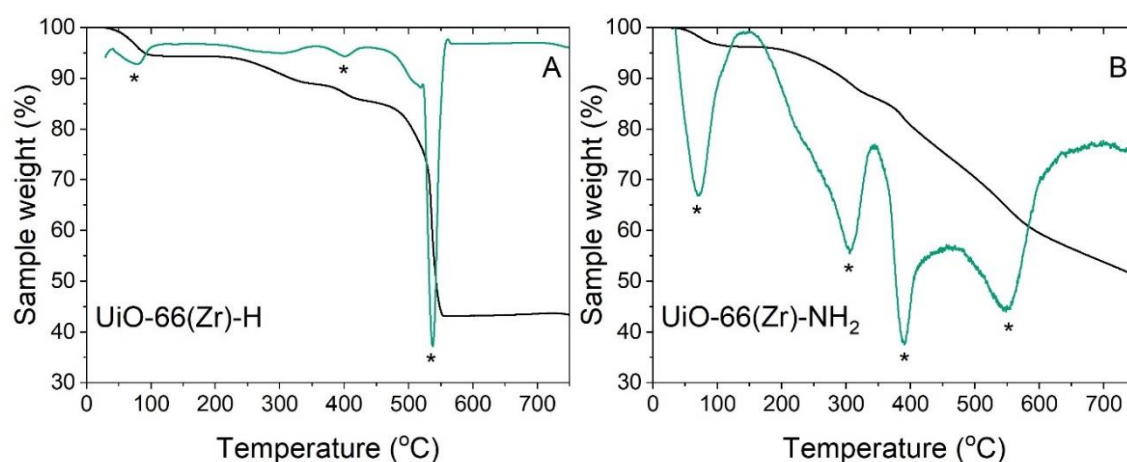


Figure 5.7 TGA (black) and the DTG (green) curves of untreated UiO-66(Zr)-H (left, A) and UiO-66(Zr)-NH₂ (right, B) samples.

The TGA analysis was run in order to understand the thermal decomposition of the materials. A slower temperature ramp rate would provide more detailed steps for mass loss. In the case of UiO-66(Zr)-H (left, A), most likely water and/or solvents trapped in the pores evaporated at 100°C, while partial dehydroxylation of the zirconium oxoclusters took place at 400°C.⁴⁵ Based on the 1st derivative (DTG), complete structural decomposition due to the linker volatilisation and/or loss of the benzene ring was observed at 536°C. The final residue was formation of non-porous ZrO₂ product.⁴⁷ In the case of UiO-66(Zr)-NH₂ (right, B) the first step at 70°C is associated with the evaporation of residue ethanol trapped in the pores after the postsynthetic centrifugation. Same as in the case of the non-amino sample, dehydroxylation took place at around 390°C. The initial decomposition of NH₂-BDC linker occurred at 305°C,⁴⁸ which means that framework collapse started much earlier than in the case of the UiO-66(Zr)-H material. As in the case of the protonated sample, formation of final ZrO₂ product occurred at 545°C.

Among different Lewis acids, the Zr-doped zeolites had shown excellent catalytic performances for the transformation of cellulosic biomass.⁴⁹ According to Corma *et al.*, Zr-BEA can actively catalyse the transfer hydrogenation and etherification reactions.⁵⁰ Since the UiO-66(Zr) materials are promising in terms of catalytic applications, this leads to a need for the total ammonia sorption capacity examination and Lewis/Brønsted acidity strength determination. These were evaluated by the means of ammonia temperature-programmed desorption (NH₃-TPD). The analysis was performed mainly due to the potential use of various UiO-66 structures as new functional materials in catalysis, especially in aqueous environment. The procedure was described in detail in Chapter 2, Section 2.6.5. The NH₃-TPD profiles are presented in Figure 5.8.

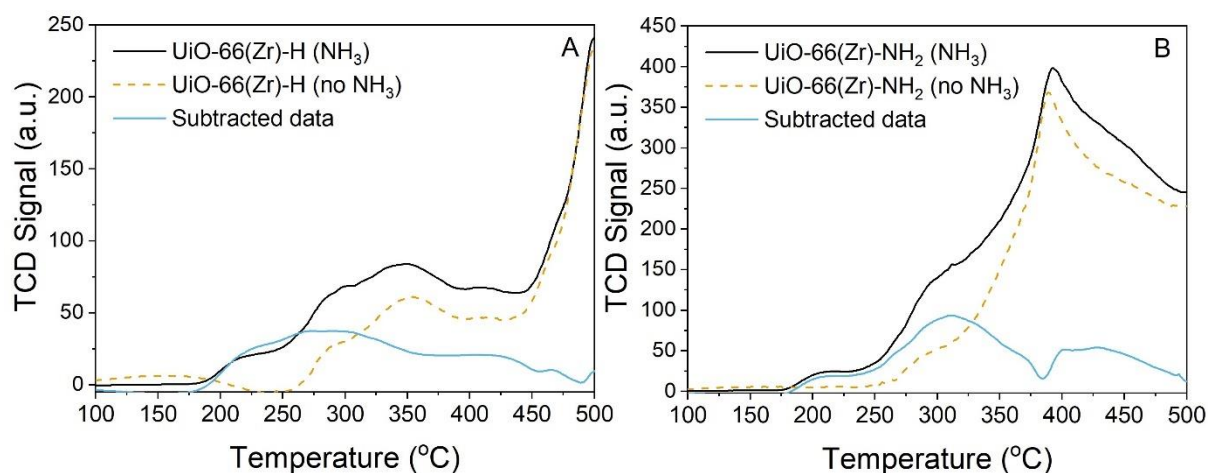


Figure 5.8 NH_3 -TPD profiles of UiO-66(Zr)-H (left, A) and UiO-66(Zr)- NH_2 (right, B) samples. TCD signal for sample analysis without NH_3 saturation (yellow dash line) and sample analysis with NH_3 saturation (black solid line). The subtracted data is shown as a solid blue line.

The chemisorbed ammonia (NH_3) was desorbed from the samples by heating the materials up to 500°C , as suggested in existing literature.⁵¹ In order to obtain the ammonia sorption capacity two different measurements on the same structure were performed. First, measurement was done with the chemisorbed ammonia and the second one, without. From the data obtained through analysis with NH_3 saturation (black solid line) the nonchemisorbed data (yellow dash line) was subtracted (blue solid line) and this data was used to calculate the total ammonia sorption capacity. This subtraction was performed so that NH_3 generated by linker desorption did not misrepresent the results. Complete identification of the chemisorbed NH_3 on different acid sites was accomplished by deconvolution of all significant TPD peaks, which are presented on Figure 5.9.

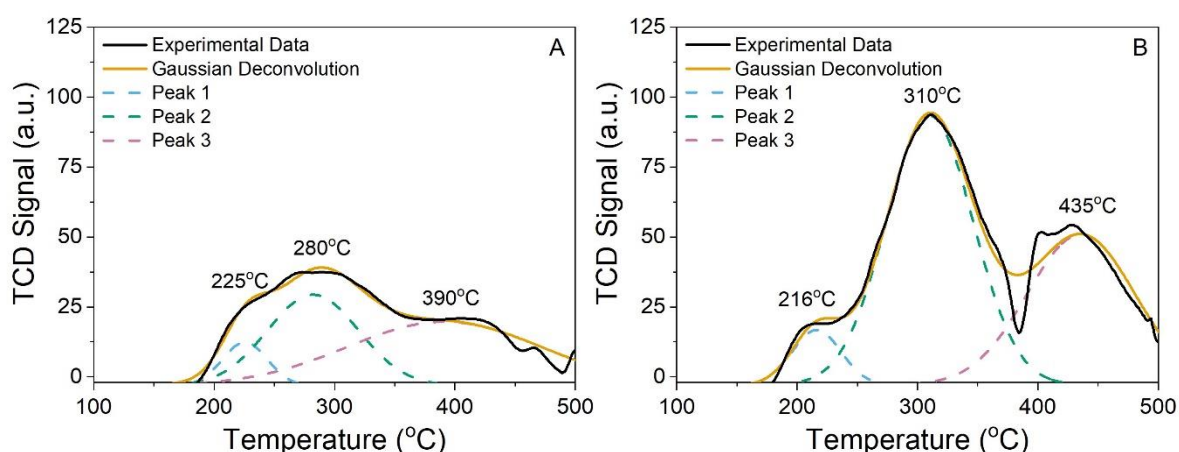


Figure 5.9 NH_3 -TPD profiles of UiO-66(Zr)-H (left, A) and UiO-66(Zr)- NH_2 (right, B) samples (solid black line) with their Gaussian deconvolution profiles (solid yellow line) and fitted peaks (dashed lines).

Figure 5.9 present three types of data. The black solid lines represent the original experimental data obtained by subtracting chemisorption profiles, as described previously. The yellow solid lines represent the NH_3 -TPD profiles deconvoluted by fitting with the Gaussian function. The dashed lines (blue, green and violet) are the fitted peaks, with corresponding temperatures located above each peak centre. The deconvolution of the desorption plots for the UiO-66(Zr)-H and UiO-66(Zr)- NH_2 sample was done using Gaussian function to present each acid site contribution.

TPD analysis on the UiO-66(Zr)-H (left, A) resulted in 3 main peaks associated with weak, medium and strong acid sites. The weak acid sites were detected at 225°C and were assigned to the evaporation of residual DMF solvent trapped in the pores.⁵³ The medium acid sites with the peak centred at 280°C were assigned with Lewis acid sites, which are Zr^{4+} nodes.⁵² The third area, at around 390°C, was associated with adsorption on the zirconia oxo-clusters (μ_3 -OH groups), which are associated with the Brønsted acid sites.

In the case of UiO-66(Zr)- NH_2 (right, B) the acidity resulted from desorption of ammonia from 3 different acid sites. A very weak peak at 216°C was attributed to weak acid sites. This corresponded most likely to evaporation of residual DMF solvent and the physical adsorption of NH_3 on weak Lewis acid sites.⁵³ The second desorption peak at 310°C was assigned to medium acid sites, which meant ammonia adsorption on strong Lewis acid sites. These sites are the accessible amino groups of the NH_2 -BDC linker. The last peak, which was found at around 435°C, was assigned to strong acid sites. Same as in the case of the

protonated analogue, associated with NH₃ adsorbed on Brønsted acid sites, the zirconia oxo-clusters (μ_3 -OH groups).

The details and corresponding quantitative values obtained from the NH₃-TPD analysis are specified in Table 5.3.

Table 5.3 Ammonia sorption capacity per unit mass of adsorbent.

MOF ID	Sample Weight (g)	Total NH ₃ capacity (mmol/g)	Peak of desorption temperature (°C) and corresponding peak area contribution (%)		
UiO-66(Zr)-H	0.055	0.133	225 (8.6)	280 (36.7)	390 (54.7)
UiO-66(Zr)-NH ₂	0.084	0.187	216 (6.3)	310 (55.4)	435 (38.3)

In general, in both cases strong acidity resulted from desorption of the zirconia oxo-clusters (μ_3 -OH groups). However, the larger NH₃ capacity resulted for the UiO-66(Zr)-NH₂ structure. This was due to stronger adsorption of NH₃ on the amine-functionalised part of the framework, the amino groups of the NH₂-BDC linker. This means that the amine UiO-66 structure might be of greater catalysis potential, if stable in aqueous environment.

5.3.2 CFR stability testing

When thinking about stability, it is essential to understand how the frameworks reacts to different liquid solvents. In order to advance the knowledge generated in previous sections and investigate to which extent both UiO-66 materials are stable, additional CFR tests were performed for longer periods of time (120 h). In particular, different liquid solvents were used. Similar as in the case of zeolites tested in Chapter 3 and 4, herein all tests were carried out for in CFR in solvent (*i.e.*, H₂O, MeOH, EtOH) flow (0.2 g, 0.3 mL min⁻¹, 120 h, 110°C, 35 bar inlet pressure). Tests were conducted on the both UiO-66(Zr) materials, the UiO-66(Zr)-H and its amino analogue UiO-66(Zr)-NH₂. Interestingly, such test were not performed and have not yet been published in literature. The outcomes of the pXRD analysis are presented on Figure 5.10.

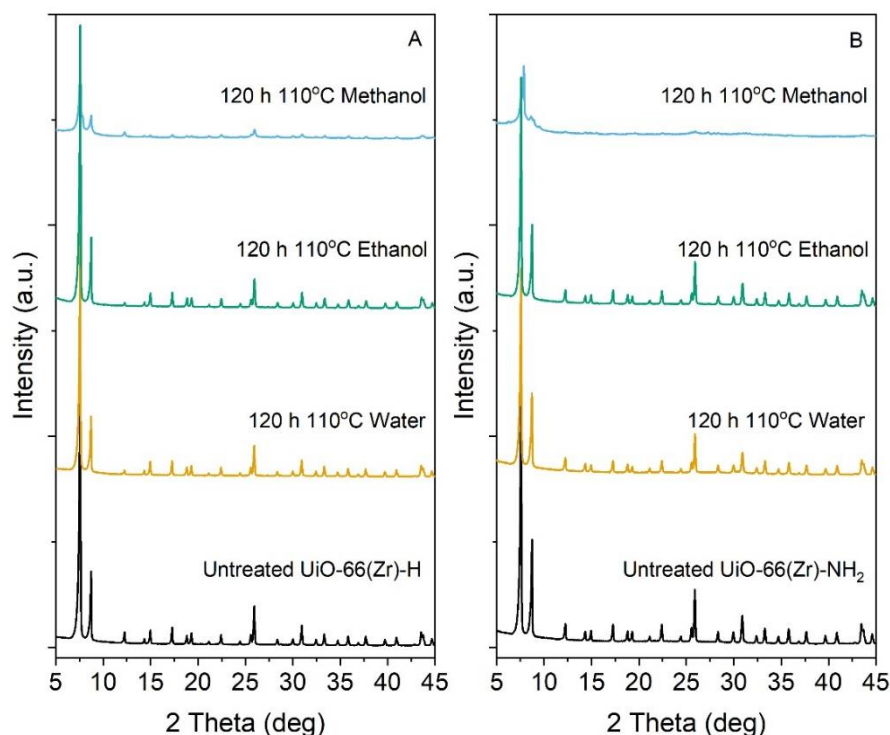


Figure 5.10 The pXRD spectra of UiO-66(Zr)-H (left, A) and UiO-66(Zr)-NH₂ (right, B) after solvothermal treatment (at 110°C, 120 h, CFR).

The untreated pXRD diffractograms of both tested MOFs presented high crystallinity patterns. All patterns were consistent with previously reported XRD of this framework,⁴⁵ having no impurities or secondary phases, as well as having the two most intense peaks located at 2θ 7.5° and 8.6°, corresponding to the (111) and (200) crystal planes, respectively.⁴⁵ A slight decrease in the 2θ 7.5° peak intensity was observed for the functionalised UiO-66(Zr)-NH₂. This could be due to the altering of the original organic scaffolding, that is the terephthalic acid (H₂BDC).

Water and ethanol treated MOFs, of both -H and -NH₂ samples, showed negligible changes in their crystallinity and maintained their single phase even under elevated temperature and high-pressure conditions. Methanol, on the other hand, had a severe detrimental effect in terms of the framework crystallinity. Although it has been shown in literature that methanol can play a crucial role in the creation and stabilisation of dangling linkers in the UiO-66(Zr)-H material,⁵⁴ here methanol had a damaging effect on the structure. Interestingly, according to the same paper, by Marreiros *et al.*, a considerable linker leaching was observed after suspending UiO-66(Zr)-H in 10 mL of MeOH (at 40°C, 72 h).⁵⁴ Methanol

seemed to generate missing-linker defects capped with methoxide ligands. However, the paper did not focus on this phenomenon.

To further investigate the textural changes of both materials after treatment, N_2 -physisorption analysis was performed. The data gathered for both synthesised UiO-66 untreated and treated samples in a fixed-bed CFR at 110°C for 120 h are presented in Figure 5.11.

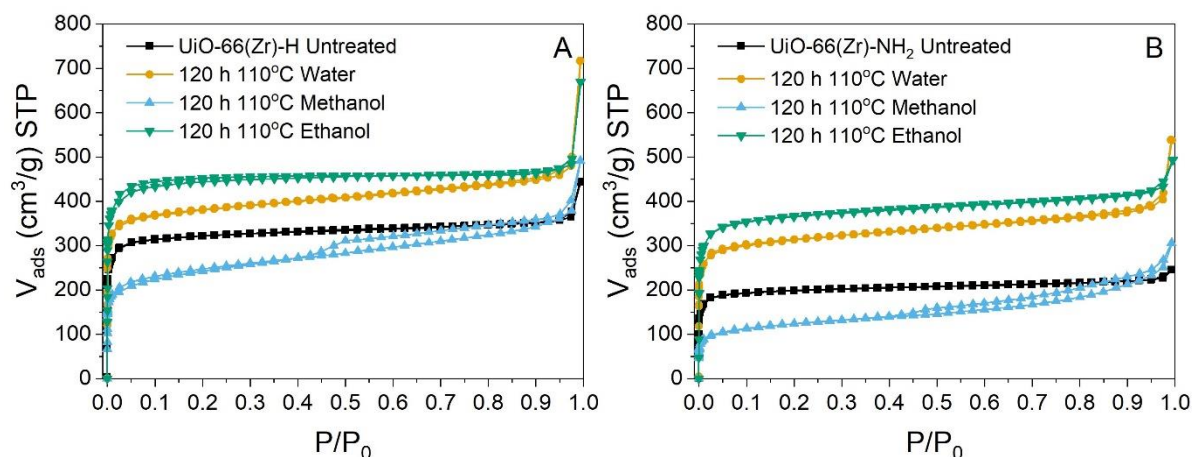


Figure 5.11 Nitrogen physisorption of UiO-66(Zr)-H (left, A) and UiO-66(Zr)-NH₂ (right, B) and their respective after HTS treatment; untreated (black), water (yellow), ethanol (green), methanol (blue).

The untreated, water and ethanol treated samples of both UiO-66 structures showed similarities, as all were characterised with a type I adsorption isotherm, which is as expected.⁵⁵ No hysteresis loop is to be observed for these UiO-66 samples, which indicated these are microporous structures. The high volume of absorbed nitrogen is correlated to the total surface area of the particles including pores at the surface and shows that samples possess very large surface areas. However, the isotherms of methanol treated samples belonged to the type IV adsorption isotherm. The presence of hysteresis is typical for the type IV isotherms and here is indicative of mesoporosity generated after the contact with methanol.⁵⁶ The hysteresis appearance might be due to the benzene ring opening, Zr leaching, ZrO₂ formation or formation of a completely different mesoporous structure. Since pXRD analysis did not give a completely clear answer on the crystal structure, as mentioned before, there is a possibility of formation of a new mesoporous structure due to the NH₂-BDC linkers being exchanged with methoxide ligands. To better highlight the differences across the samples, a complete surface area (S_{DFT}), microporosity (V_{mc}) and total porosity (V_{t}) dataset are listed in Table 5.4.

Table 5.4 Complete specific surface area (S_{DFT}), total porosity data (V_t) and micropore volume (V_{mc}) data of UiO-66(Zr)-H and UiO-66(Zr)-NH₂ samples before and after water, ethanol and methanol treatments (120 h, 110°C, CFR).

MOF ID	Sample type	S_{DFT} (m ² g ⁻¹) ^(a)	V_t (cm ³ g ⁻¹) ^(b)	V_{mc} (cm ³ g ⁻¹) ^(c)
UiO-66(Zr)-H	Untreated	1593	0.544	0.459
	Water	1991	0.728	0.512
	Ethanol	2270	0.719	0.623
	Methanol	1179	0.587	0.229
UiO-66(Zr)-NH ₂	Untreated	1235	0.562	0.325
	Water	1647	0.615	0.394
	Ethanol	1841	0.651	0.472
	Methanol	592	0.393	0.096

(a) Specific surface area obtained from NLDFT

(b) Total pore volume from NLDFT

(c) Micropore volume from NLDFT

The specific surface areas (S_{DFT}) of both UiO-66(Zr)-H and UiO-66(Zr)-NH₂ varied quite significantly, with the original one (-H) exhibiting the largest area. Interestingly, when analysed after solvent tests, both parent samples shared same trends in how their specific surface area (SSA) becomes modified; SSA after ethanol is observed to increase, followed by water and thirdly the untreated sample. The methanol post-treated samples not only show the lowest surface areas, as those were the only samples to show hysteresis, which is attributed to the presence of mesoporosity. These higher values for ethanol and water treated samples can be associated with the presence of missing cluster defects, which decreases the framework density and increases the total porosity.

Mesopore formation and possible reorganisation of active sites are primary causes of the MOF degradation. To further evaluate the impact of solvents on the samples UV-VIS spectroscopic studies were thus performed. UV-VIS spectroscopy analysis is another powerful way to analyse the metal and linker stability. The appearance of certain bands can give answers on the interaction of the metal nodes with the linker in the structure.⁵⁷ The UV-VIS absorption spectra of untreated and treated UiO-66(Zr)-H and UiO-66(Zr)-NH₂ samples in the CFR at 110°C are presented in Figure 5.12.

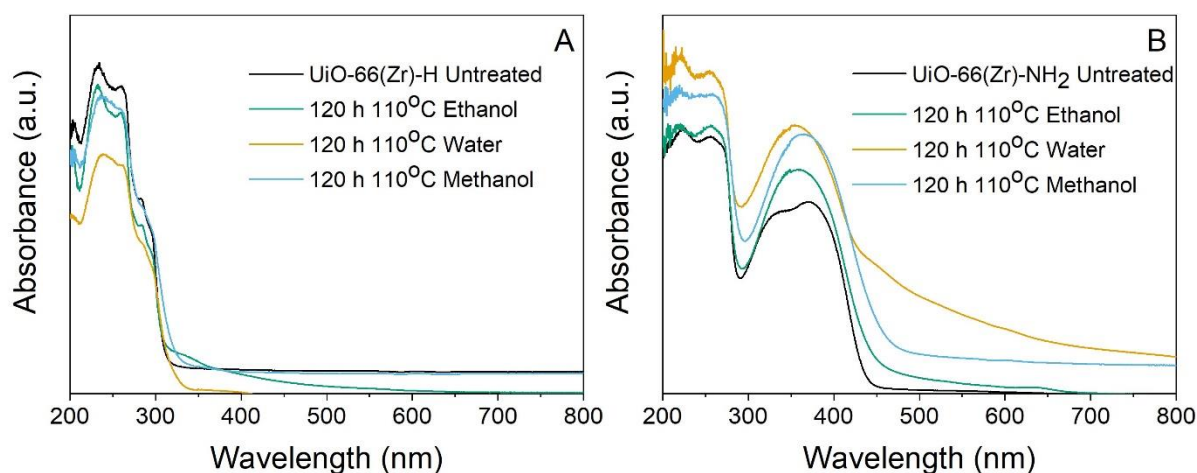


Figure 5.12 DRUV-VIS spectra of UiO-66(Zr)-H (left, A) and UiO-66(Zr)-NH₂ (right, B) samples; untreated (black), water treated (yellow), ethanol treated (green), methanol treated (blue).

In both cases, the UV-VIS absorption spectra showed peaks at 233 nm and 262 nm which were related to UV adsorption of Zr-O oxo-clusters in both UiO-66(Zr) structures.⁵⁸ Additionally, in the case of UiO-66(Zr)-H (left, A), the band peak at 285 nm with a shoulder at 300 nm was attributed to the terephthalate linker.⁵⁹ It was observed that the H₂BDC linker showed no absorption in the visible region. However, the untreated amino-functionalised sample (right, B) presented additional peaks spanning between 350-450 nm with two maxima at ca. 335 nm and 370 nm that were ascribed to linker-based absorption influenced by the nearby metal centres.

The profiles after treatment were similar but not identical to the untreated samples. For the UiO-66(Zr)-H, it was observed that the 285 nm band disappeared after testing the sample in methanol. However, the bands related to the linker and oxo-clusters were unchanged after ethanol use and slightly affected by water. The amino-functionalised sample oxo-clusters remained unmodified after solvent treatment.

In the case of the UiO-66(Zr)-NH₂ samples, the powder changed their colours after treatment. These changes are presented on Figure 5.13. For clarity, the UiO-66(Zr)-H untreated sample is white and remains white after treatment with all tested solvents.



Figure 5.13 UiO-66(Zr)-NH₂ samples before treatment (fresh, A) and after treatment with methanol (B), ethanol (C), and water (D), 120 h at 110°C. Photographs taken by Ricardo Navar.

For the four UiO-66(Zr)-NH₂ samples, the colour changed from pale yellow (A, untreated) to dark yellow (B, methanol), beige (C, ethanol) and brown (D, water). The change in colour might be due to chemical grafting of the solvents on the linker ring, the NH₂ group or the Zr-oxo cluster itself.

Solid state MAS NMR spectra were performed in order to confirm the presence of organic linkers and the nature of any organic guest inclusions in the untreated and treated samples. These residuals can be only physisorbed in the pores or chemisorbed and even change the character of the whole structure.⁶⁰ Prior to MAS NMR analysis samples were placed in an oven at 110°C overnight to remove the excess solvent prior to testing. The ¹³C CP-MAS NMR spectra for untreated and treated UiO-66(Zr)-H and UiO-66(Zr)-NH₂ samples in a fixed-bed CFR (120 h, at 110°C), are presented in Figure 5.14.

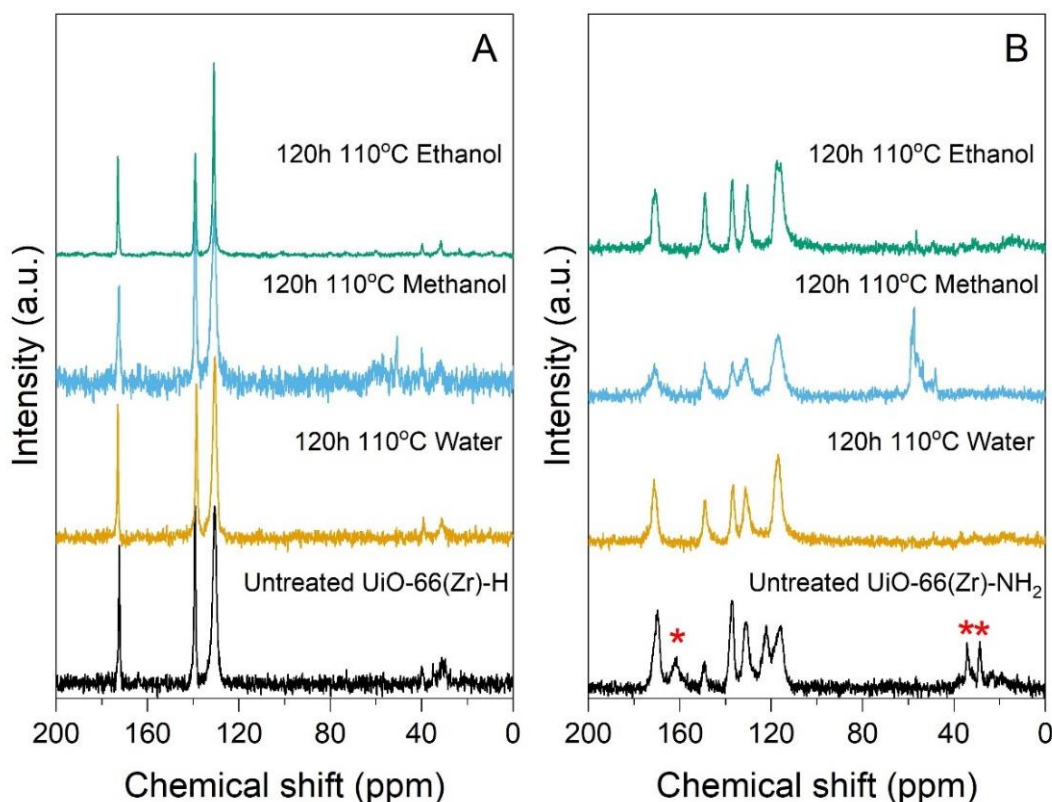


Figure 5.14 The ^{13}C CP-MAS NMR of UiO-66(Zr)-H (left, A) and UiO-66(Zr)-NH₂ (right, B). Red asterisks indicate residual DMF.

The untreated UiO-66(Zr)-H (left, A) ^{13}C CP-MAS NMR spectrum presented the three standard peaks,⁶¹ one at 172 ppm attributed to the carboxylic group carbon (C=O) atoms. The second one at 138 ppm, assigned to the quaternary carbon (C_{quat}) atoms, *i.e.*, no protons attached to carbon atoms and last one at 130 ppm, which consists of phenyl ring -CH groups.⁶¹ All spectra of solvent treated UiO-66(Zr)-H samples were no different in terms of new or absent signals.

Primarily in UiO-66(Zr)-NH₂ (right, B), residual dimethylformamide (DMF) from the synthesis preparation was detected in the untreated sample spectrum (28 ppm, 34 ppm and 161 ppm). While having the three standard resonances from the original UiO-66, three additional peaks were detected for all untreated and treated UiO-66(Zr)-NH₂.⁵⁴ The 150 ppm was attributed to the C atom attached to the functionalised amino group. Furthermore, 116 ppm and 122 ppm comprise the surrounding carbon atoms of the former amino-attached carbon.⁶¹ However, the untreated and its subsequent post-treated catalysts appear to be relatively broad, no significant changes except for the methanol-treated MOF could be observed. There was a significant decrease in terms of intensity on the carboxylic resonance

(at ~170 ppm) in the methanol treated $\text{NH}_2\text{-MOF}$. Additional peaks can be seen as well within the range of 45-60 ppm, which can be attributed to the chemisorbed methanol.⁵⁴

Since stability in water is of main interest, here DRIFTS spectroscopy analysis was used to investigate the possibility of hydrolysis undergoing in the sample. DRIFTS spectra of untreated UiO-66(Zr)-H and UiO-66(Zr)- NH_2 samples are illustrated in Figure 5.15.

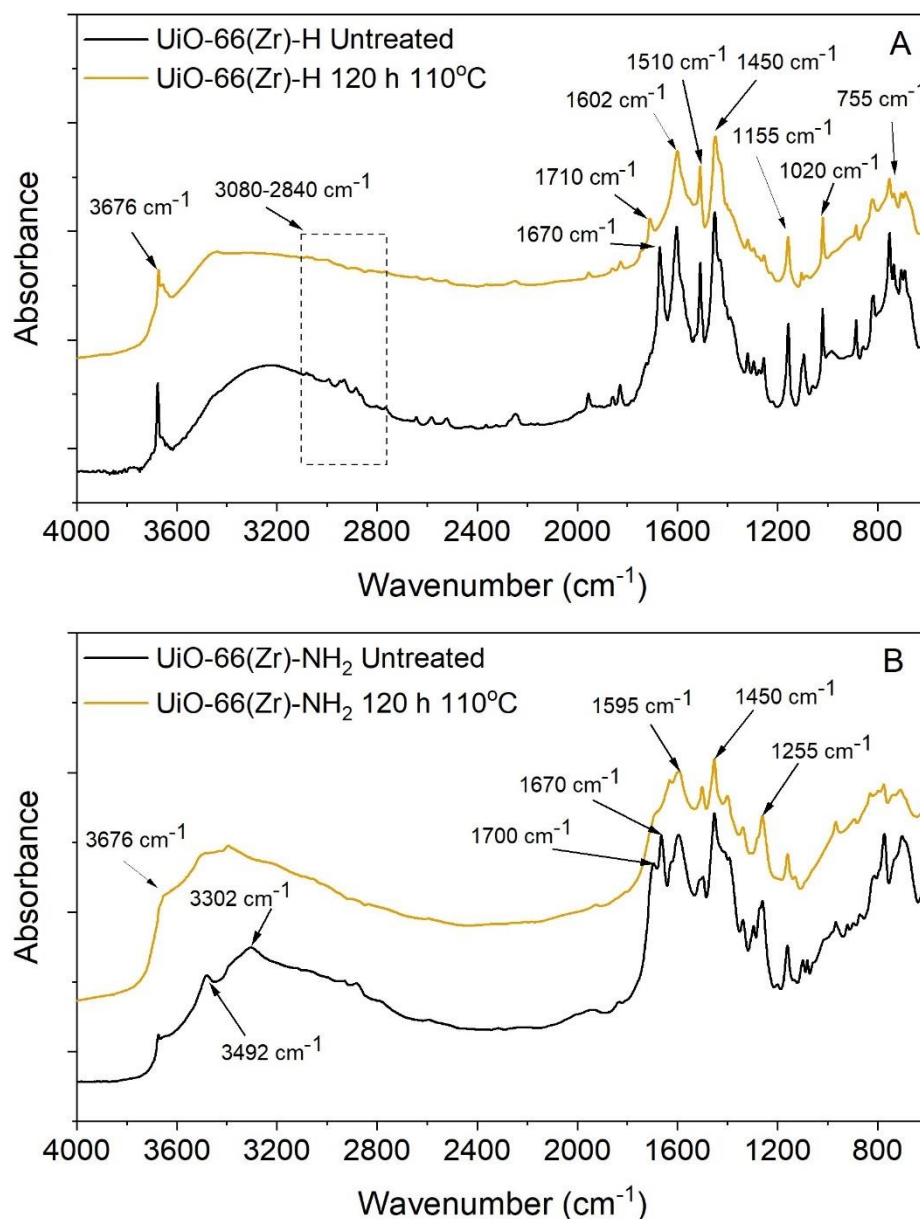


Figure 5.15 DRIFTS spectra of untreated (black solid line) and water treated (yellow solid line) UiO-66(Zr)-H (top, A) and UiO-66(Zr)- NH_2 (bottom, B) samples. Analysis conditions: range 4000-600 cm^{-1} ; resolution of 2 cm^{-1} ; 16 scans. Analysis run by Dr Giulia Tarantino.

Similarities of the untreated (black solid line) UiO-66(Zr)-H (top, A) and UiO-66(Zr)-NH₂ (bottom, B) spectra lay in a few regions, specifically 3676 cm⁻¹ band attributed to Zr-OH (bonding hydroxyl group of the SBU), 3080-2840 cm⁻¹ region of the symmetric and asymmetric vibrations of the aliphatic and aromatic modes. The bands of this region disappear after treatment, which may be due to group rearrangement and OH group bonding to the ring. Symmetric and asymmetric ν(-COO) groups were located at 1450 cm⁻¹ and 1602 cm⁻¹.

The strong absorption peak located at 1710 cm⁻¹ arises in the UiO-66(Zr)-H sample after treatment with water. This band indicates the C=O stretching vibration of free carboxylic acid,⁶² which might be associated with the hydrolysis process. Other bands that were attributed to both metal-organic frameworks were located at 1510 cm⁻¹ and 1595 cm⁻¹ and ascribed to C=C stretching vibration of the phenyl ring. In the lower energy (fingerprint) region, O-M-O vibrations were observed and band located at 755 cm⁻¹, representing the symmetric vibration peak of O-Zr-O clusters, which indicated the metal bounding to the linkers.⁶³ Residual DMF vibrations were identified with a sharp peak at 1670 cm⁻¹. Both bands at 1020 cm⁻¹ and 1155 cm⁻¹ are attributed to the H₂BDC linker.

In the case of the amino-functionalised MOF extra bands were found, such as 3492 cm⁻¹ and 3302 cm⁻¹ attributed to the N-H symmetric and asymmetric stretch of the amine, respectively. The band located at 1255 cm⁻¹ was ascribed to C-N bond in the linker.⁶⁴

In summary, the two UiO-66 structures were tested for solvent stability in CFR for extended periods of time (120 h, 110°C). With a slight difference in linker choice, materials differed significantly in thermal stability, specific surface area and pore volume in favour of the UiO-66(Zr)-H sample. However, it is clear that both structures were significantly stable in water and ethanol, but underwent transformation in methanol. It is possible that the linkers are being exchanged with methoxide ligands, since the ¹³C CP-MAS NMR analysis confirmed chemisorbed methanol on the UiO-66(Zr)-NH₂ structure. Hence, further studies in higher temperatures and structures with different metal clusters are required.

5.4 High temperature testing of Hf and Zr UiO-66

5.4.1 UiO-66(Hf)-H

5.4.1.1 Material characterisation

The stability testing focused on the UiO-66(Zr)-H sample confirmed that the structure is of significant hydrothermal stability at 110°C. General MOF functionality properties are derived from the metal cluster and linker. Therefore, it is highly important to understand the role of the main active centres (metal cluster) in order to design a material superior for the desired application. In order to understand the metal cluster choice on framework stability, a different metal analogue, but same topology, framework was synthesised. Here, the UiO-66(Hf)-H is compared to the UiO-66(Zr)-H structure. However, it was decided not to prepare the amino-functionalised version to avoid data complications. The synthesis of UiO-66(Hf)-H was prepared according to procedures presented in Chapter 2, Section 2.2.2.1. The ionic radius of both ions, Hf⁴⁺ and Zr⁴⁺, are similar (0.84 Å and 0.83 Å, respectively).

As undertaken in the previous section, the determination of the thermal stability and acidity of parent UiO-66(Hf)-H was done by the means of TGA/DTG and NH₃-TPD. The outcomes of both analyses are presented on Figure 5.16.

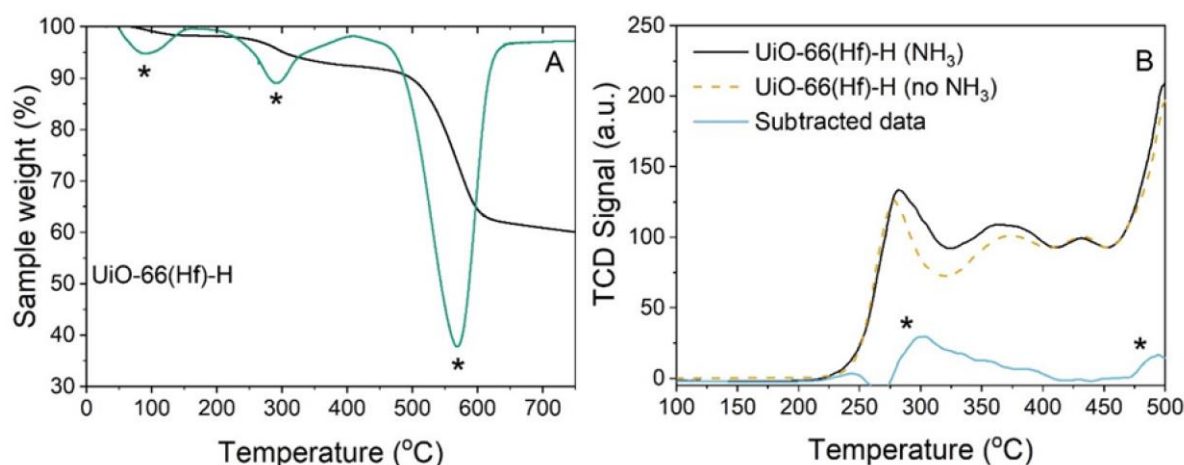


Figure 5.16 (left, A) TGA (black) and the DTG (green) curves of UiO-66(Hf)-H; (right, B) NH₃-TPD profiles of UiO-66(Hf)-H. TCD signal for sample analysis without NH₃ saturation (yellow dash line) and sample analysis with NH₃ saturation (black line). The subtracted data is shown as a solid blue line.

The thermal decomposition (Figure 5.16 left, A) of the UiO-66(Hf)-H sample was characterised by final decomposition peak, associated with the linker decomposition, at 570°C. The weight loss observed below 100°C was from the loss of absorbed solvent residue

or water molecules. The small peak around 290°C was associated with the dehydration of the Hf [Hf₆O₄(OH)₄] clusters.⁶⁵

In order to obtain the ammonia sorption capacity two different measurements on the same structure were performed (Figure 5.16 right, B). First measurement was done with the chemisorbed ammonia and the second one, without. From the data obtained through analysis with NH₃ saturation (black solid line) the nonchemisorbed data (yellow dash line) was subtracted (blue solid line) and this data was used to calculate the total ammonia sorption capacity. Similar to the Zr-MOF sample, here the TPD analysis (right, B) resulted in 2 main ammonia adsorption peaks associated with medium and strong acid sites. The medium acid sites with the peak centred at around 300°C were assigned with Lewis acid sites, which are exposed metal nodes.⁵² The second area, located at around 480°C, was associated with adsorption on the hafnia oxo-clusters (μ_3 -OH groups), which are Brønsted acid sites. The calculated NH₃ capacity was approximately 0.026 mmol g⁻¹, which is more than 5 times less than in the case of the UiO-66(Zr)-H sample reported earlier (Table 5.3).

5.4.1.2 CFR stability testing

The possibility of high temperature testing and long term stability would make the Hf and Zr MOF materials even more interesting from a catalytic prospective. Herein, CFR tests were carried out on the UiO-66(Hf)-H samples in pure solvent flow (0.2 g, 0.3 mL min⁻¹, 120 h, 160°C, 30 bar inlet pressure). Since, the testing temperature was raised from 110°C to 160°C, the backpressure regulator was set to 20 bar to allow processes above the normal boiling point. Solvents used in this study were as previously used; water, ethanol and methanol. The outcomes of the pXRD and ¹³C CP-MAS NMR analysis are presented on Figure 5.17.

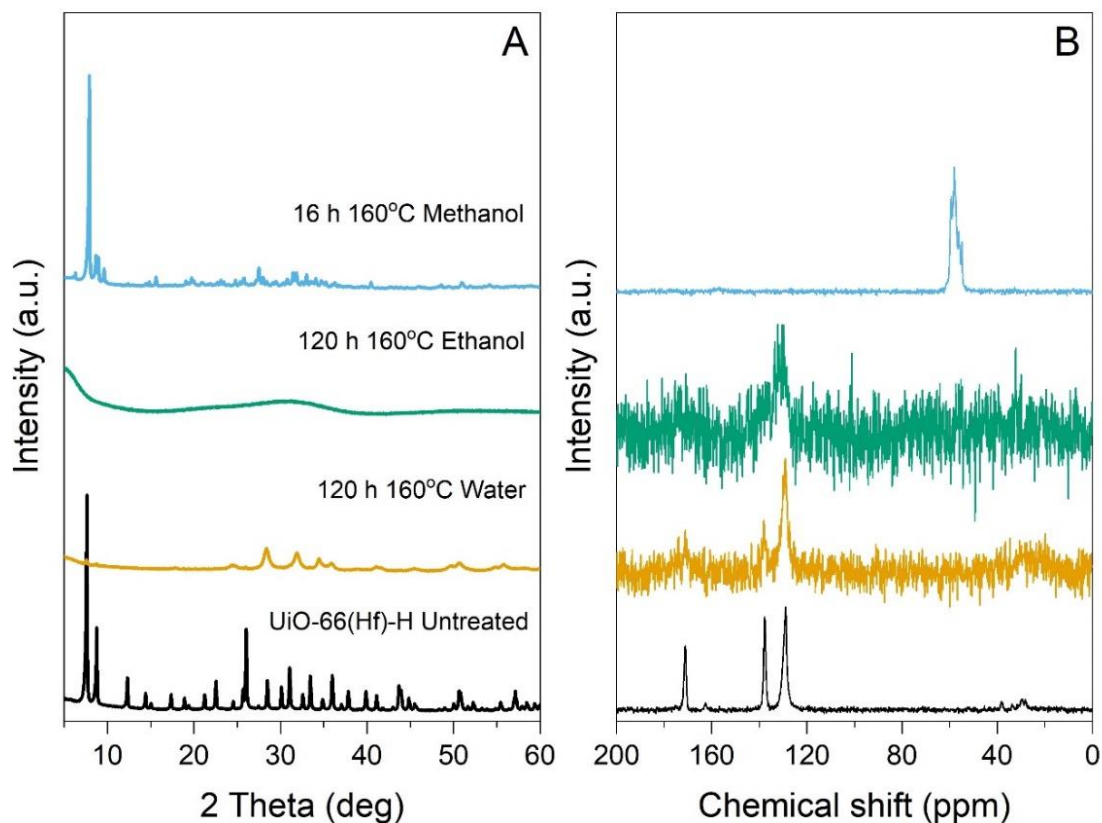


Figure 5.17 The pXRD diffraction patterns (left, A) and their corresponding ^{13}C CP-MAS NMR spectra (right, B) of untreated UiO-66(Hf)-H and after treatment at 160°C for 120 h with water (yellow); 120 h with ethanol (green); 16 h with methanol (blue).

The diffraction pattern (left, A) of the untreated UiO-66(Hf)-H shows a well-defined pattern of a crystalline MOF. Although, much different than in the case of its Zr analogue treated, at 110°C , here the differences after treatment are significant. In the case of the water treated sample (yellow), all pXRD peaks ($25\text{--}37^\circ$) corresponded to pure monoclinic hafnia reflections (JCPDS 34-0104),⁶⁶ with no evidence of any second phases. Although, the corresponding ^{13}C CP-MAS NMR spectrum (right, B) shows peaks associated with the H_2BDC linker. The methanol experiment had to be terminated after only 16 h of testing, due to the system being overpressurised. The pressure build-up might be a result of mechanical alternation of the material as explained in Section 1.1.5.2.

The recovered sample (blue) resulted in an unknown inorganic phase with absorbed methanol (50-60 ppm) on or in its internal structure. The UiO-66 after treatment with ethanol, was completely amorphous, even though the NMR spectrum shows a single carbon signal associated with the phenyl ring -CH groups.

Since UV-VIS was earlier used as a method to check the interaction of the metal nodes with the linker in the structure, consequently here the data is presented as well. The UV-VIS absorption spectra of untreated and treated UiO-66(Hf)-H samples in the CFR are presented in Figure 5.18.

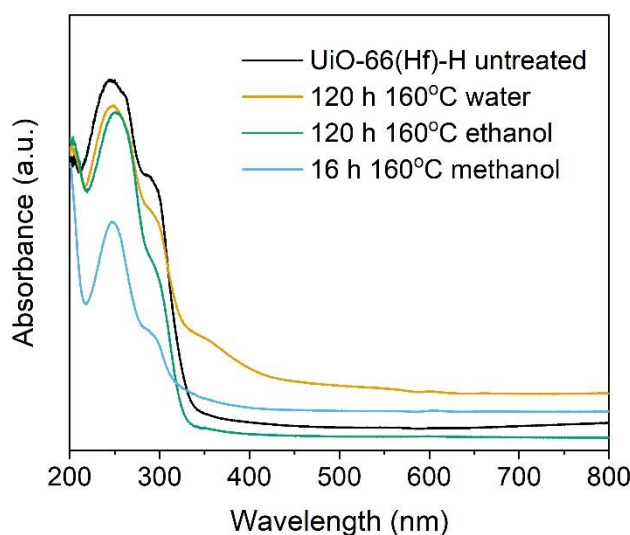


Figure 5.18. DRUV-VIS spectra of untreated and UiO-66(Hf)-H samples after treatment at 160°C for 120 h with water (yellow); 120 h with ethanol (green); 16 h with methanol (blue).

Similar as in previously analysed UiO-66 samples, the untreated UiO-66(Hf)-H sample (black) spectrum shows two peaks at 233 nm and 265 nm which are ascribed to the absorption of Hf-O clusters. The 300 nm peak was attributed to the terephthalate linker. The water (yellow) and ethanol (green) treated samples show similarities in the 225-280 nm region, even though the methanol sample is completely different. The 300 nm peak is still visible in the water treated sample and solid-state NMR confirmed the presence of the linker in the sample, although pXRD confirms only hafnia reflections. The DRIFTS spectroscopy analysis was used to follow the internal change to the material while water treatment at 160°C. The DRIFTS spectra of untreated UiO-66(Hf)-H and samples treated in water and methanol are illustrated in Figure 5.19.

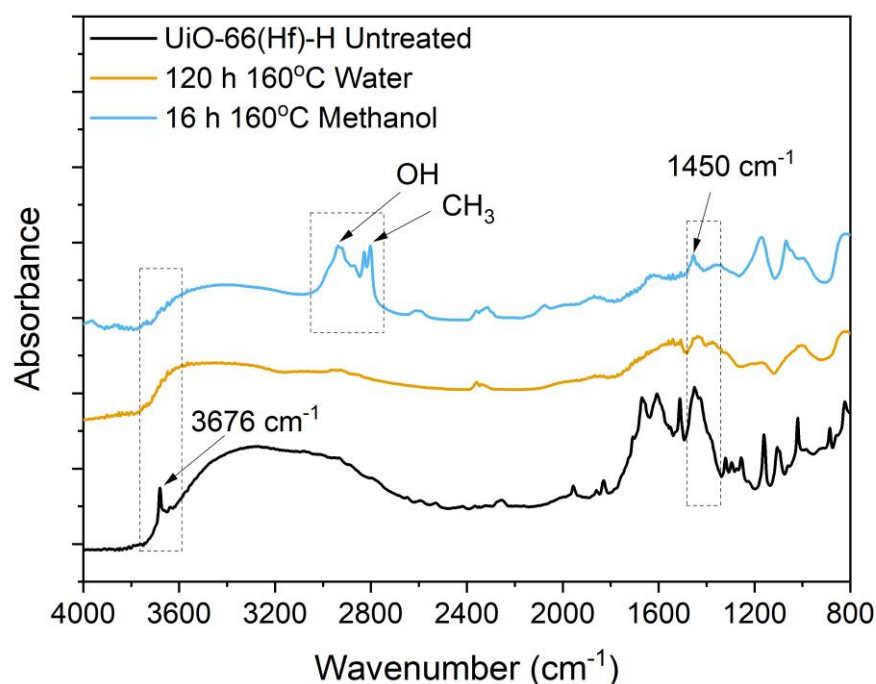


Figure 5.19 DRIFTS spectra of untreated (black solid line), water treated (yellow solid line) and methanol treated (blue solid line) UiO-66(Hf)-H samples. Analysis conditions: range 4000-600 cm⁻¹; resolution of 2 cm⁻¹; 16 scans.

Interestingly, the spectrum of the untreated UiO-66(Hf)-H is nearly identical to the spectrum of UiO-66(Zr)-H described above. Therefore, the description would be same as in the case of Figure 5.15.

In the case of both treated samples the dehydration of bridging μ_3 -OH of the hafnium clusters (loss of the 3676 cm⁻¹ mode) is observed. In the case of the water treated sample, the transition is into HfO₂, with some remains of the original framework as the XRD analysis suggested. In the case of the methanol treated sample the absorbed methanol region, highlighted with a dashed box, spans from 2750 cm⁻¹ to 3050 cm⁻¹ with typical two sharp peaks associated with the CH₃ vibrations and a broad peak associated with the OH vibrations. Surprisingly, after only 16 h, the only similarity with the untreated sample is the 1450 cm⁻¹ vibration band, associated with some of the H₂BDC linker. Unfortunately, the changes in both treated frameworks are so extensive that analysing the spectra does not give a clear and strict answer about how the damage propagated in the structure.

Surprisingly, the UiO-66(Hf)-H structure presented no stability in any of the solvents at prolonged times (120 h) and at elevated temperatures (160°C). Unfortunately, it was

impossible to evaluate the stability in methanol for longer than 16 h. According to the ^{13}C CP-MAS NMR spectrum, most likely the linker was completely exchanged with methoxide ligands.

5.4.2 UiO-66(Zr)-H

5.4.2.1 CFR stability testing

Since the UiO-66(Hf)-H has proved not to be stable at 160°C for 120 h in any of the solvents, additional CFR tests were carried out on the UiO-66(Zr)-H samples. Due to high interest of stability in water, only this solvent was used in the testing (0.2 g , 0.3 mL min^{-1} , 160°C , 30 bar inlet pressure, 20 bar backpressure). The outcomes of the pXRD and ^{13}C CP-MAS NMR analysis after 24 h, 72 h and 120 h tests are presented on Figure 5.20.

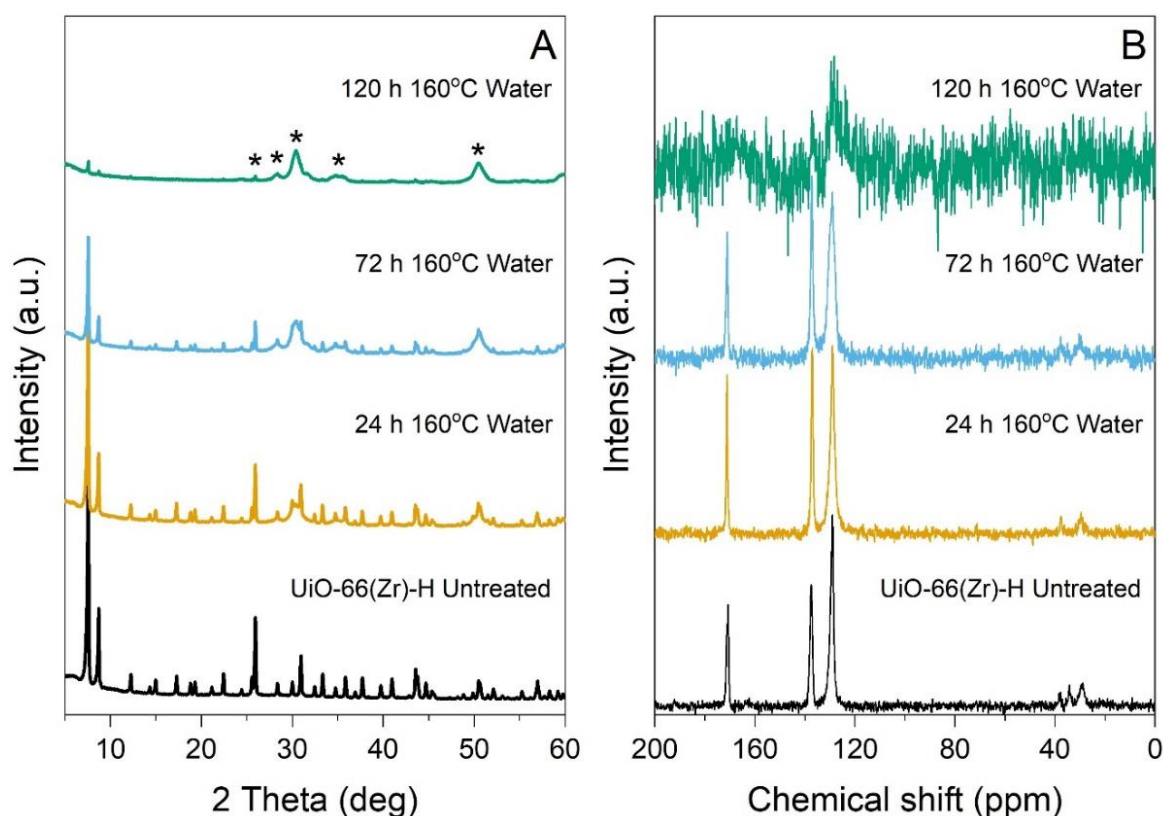


Figure 5.20 The pXRD diffraction patterns (left, A) and their corresponding ^{13}C CP-MAS NMR spectra (right, B) of untreated UiO-66(Zr)-H and after treatment at 160°C in water for 24 h (yellow), 72 h (blue) and 120 h (green). Asterisks indicate the ZrO_2 monoclinic phase.

Here, the pXRD diffraction patterns (left, A) are much more promising. However, the analysis revealed that after 24 h a secondary ZrO_2 inorganic phase is present (31.5° , 50.1°).

This phase arises after 72 h and the peaks associated with the general UiO-66 structure decrease in intensity. After 120 h the diffraction peaks of 24.1° , 28.2° , 31.5° , 35.3° , 50.1° belonged to the crystal planes of ZrO_2 with monoclinic phase,⁶⁷ confirming the complete transformation of the MOF.

The corresponding ^{13}C CP-MAS NMR spectra support the pXRD observations of crystalline (24 h and 72 h) and amorphous (120 h) samples. UV-VIS analysis was used to confirm the changes in interaction of the metal nodes with the linker. The UV-VIS absorption spectra of untreated and water treated UiO-66(Zr)-H samples in the CFR are presented in Figure 5.21.

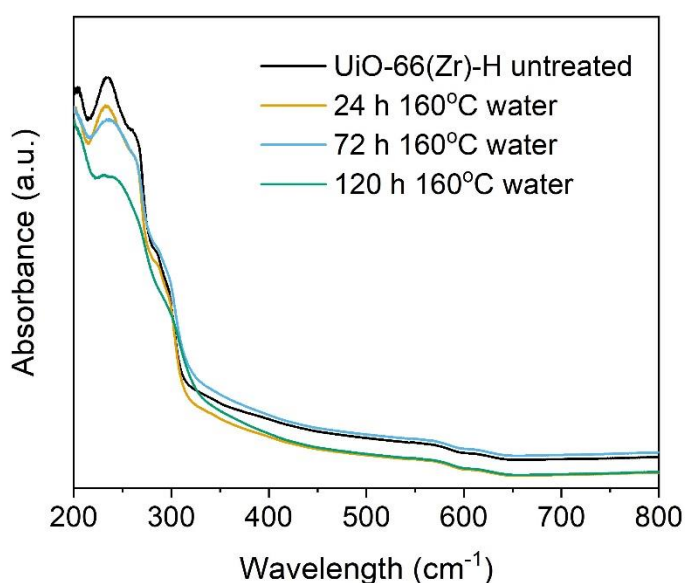


Figure 5.21 UV-VIS spectra of untreated and UiO-66(Zr)-H samples after treatment at 160°C in water for 24 h (yellow), 72 h (blue) and 120 h (green).

As expected, the untreated UiO-66(Zr)-H sample (black) spectrum shows two peaks at 233 nm and 265 nm which are ascribed to the absorption of Zr-O clusters. The 300 nm peak was attributed to the terephthalate linker. The intensity of the bands gradually decreased with time. While the 24 h (yellow) and 72 h (blue) treated samples show similarities in the 225-280 nm region, the 120 h one is of less intensity.

DRIFTS spectroscopy analysis was used to follow the internal change to the material while water treatment at 160°C . The DRIFTS spectra of untreated UiO-66(Zr)-H, 24 h, 72 h and 120 h treated samples are illustrated in Figure 5.22.

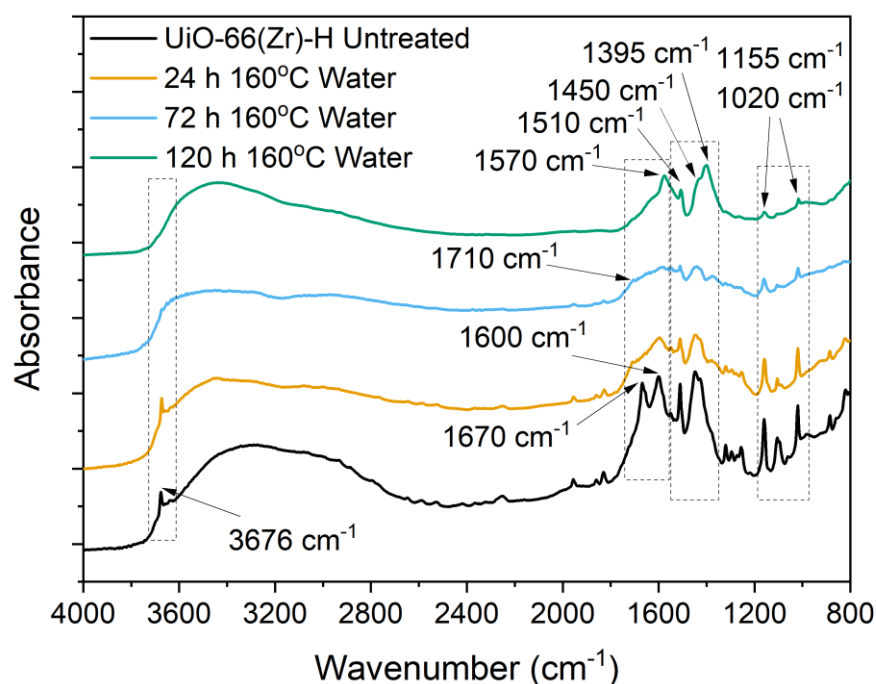


Figure 5.22 DRIFTS spectra of untreated (black) and water treated UiO-66(Zr)-H samples for 24 h (yellow), 72 h (blue) and 120 h (green) at 160°C water (CFR). Analysis conditions: range 4000-800 cm^{-1} ; resolution of 2 cm^{-1} ; 16 scans.

Four significant areas were highlighted with dashed boxes in order to understand the role of temperature and water in the decomposition of UiO-66(Zr)-H at 160°C. However, most significant changes were observed after 72 h of water treatment. First vibration that disappears after 24 h is the residual DMF identified with a sharp peak at 1670 cm^{-1} . Subsequent adsorption of water leads to appearance of OH groups, which are observed by arising of the 1710 cm^{-1} band. The same band is again no longer observed in the 120 h treated sample. The representative vibrations that subsequently disappear and are no longer observed after 120 h are the asymmetric $\nu(-\text{COO})$ groups identified by the peak at 1600 cm^{-1} . Since the intense band gradually disappears after 24 h and 72 h, this would clearly mean that the linker slowly separates itself from the oxo-cluster.

After 120 h bands associated with the H₂BDC linker (1020 cm^{-1} , 1155 cm^{-1} , 1395 cm^{-1} , 1450 cm^{-1} , 1510 cm^{-1} , 1570 cm^{-1}) are still observed, and the remains of the original framework were still detectable by XRD and solid state ¹³C CP-MAS NMR. The last step is the dehydration of vibrations of terminal and bridging $\mu_3\text{-OH}$ of Zr₆O₄(OH)₄ (loss of the 3676 cm^{-1} mode), observed after 72 h, with a transition to a Zr₆O₆ cluster⁶⁸ and further into

ZrO₂, as the XRD analysis suggested. To add, in the UiO-66(Zr)-H tested previously at a lower temperature of 110°C band associated with the bridging μ_3 -OH was still present after 120 h.

The UiO-66(Zr)-H structure tested at 160°C has presented remarkable stability in water up to 72 h of treatment in the CFR. With the DRIFTS, XRD and solid-state NMR analysis, it was possible to identify the steps of framework degradation.

5.5 Conclusions

In this chapter, solvothermal stability tests of potentially water stable MOFs were demonstrated. It is important to remember that a solvent stable MOF structure must be strong enough to withstand the intrusion of the solvent molecules into the framework, and consequently retain crystallinity and overall porosity at elevated temperatures.

Chosen structures, *i.e.*, HKUST-1, ZIF-8, MIL-53 and UiO-66 were selected due to significant interest in prospective liquid phase operation use. The first presented tests focused on water stability of the selected MOFs. Out of all initial structures, only UiO-66(Zr)-H has presented exceptional water stability, with nearly no change in specific surface area and total porosity after treatment for 48 h at 110°C. While the rest of the samples underwent partial or total hydrolysis after only 24 h at 110°C. However, the comparison of stability between commercial and synthesised ZIF-8 has shown that the metal source and method of synthesis have a significant effect on the hydrothermal stability of the final MOF structure.

Two UiO-66 structures, with different functionalised BDC linker but the same metal nodes, were chosen for further tests. This is, UiO-66(Zr)-H and UiO-66(Zr)-NH₂, synthesised with terephthalic acid (H₂BDC) and 2-aminoterephthalic acid (NH₂-BDC), respectively. Both synthesised materials, protonated and amino analogue, were thermally stable up to 536°C and 545°C, respectively and possessed Lewis and Brønsted acid sites. Detailed spectroscopic studies before and after treatment for 120 h at 110°C in water, ethanol and methanol flow in a CFR were employed. The main conclusion is that methanol has a destructive impact on both frameworks, which was confirmed first by pXRD and N₂-physisorption. Crystallinity has decreased significantly and formation of mesopores was confirmed by N₂-physisorption analysis. The ¹³C CP-MAS NMR suggested that methanol might be chemisorbed on the

structure. Methanol exchanges the original linker within the framework with methoxide ligands or grafts on the Zr-oxo clusters. However, when ethanol and water were used, crystallinity remained unchanged. No phase transition was observed. Furthermore, N₂-physisorption showed increase in the specific surface area, micropore and total pore volumes. The ¹³C CP-MAS NMR did not present any significant changes in the carbon environment. Although, in the case of water treated samples, DRIFTS FTIR confirmed that bands associated with hydrolysis process were present. In the case of both samples, the free carboxylic acid (C=O) stretch was the band that appeared on the spectra. What is more, a colour change of the treated samples was observed for the UiO-66(Zr)-NH₂ sample. It was concluded that the change is associated with the MeOH solvent reacting with the linker, the NH₂ groups or the Zr-oxo cluster itself.

Section 5.4 focused on the UiO-66(Hf)-H structure, which has the same linker as UiO-66(Zr)-H but a different metal node. Since UiO-66(Zr)-H presented superb stability at 110°C, the UiO-66(Hf)-H structure was treated at a higher temperature of 160°C. This was done, since stability at even higher temperatures would be even more interesting from a catalytic perspective. Unfortunately, the UiO-66(Hf)-H structure was found to be completely amorphous after 120 h in ethanol, and only a hafnia phase was found after the water treatment at elevated temperatures. It was impossible to evaluate the stability in methanol, due to system being overpressured. According to the DRIFTS studies the terephthalate linker was exchanged with methoxide ligands leading to formation of a completely new structure only after 16 h.

Since the presented data gave interesting results, the UiO-66(Zr)-H was subsequently extensively tested in water at 160°C, due to high interest of its hydrothermal stability. According to the XRD analysis, the arising of the zirconia phase was observed just after 24 h, however the structure was still stable up to 72 h, which is an outstanding result for a MOF structure.⁹ The ¹³C CP-MAS NMR and DRIFTS spectra have confirmed a clear footprint of the H₂BDC linker even after 120 h. The DRIFTS also confirmed that the linker slowly separates itself from the oxo-cluster causing further dehydration of the bridging μ₃-OH of the oxo-cluster. The transition into an inorganic oxide was parallel to the linker separation. These findings allowed to understand the slow framework transformation in water and how the final damage to the structure proceeded. However, further developments

and spectroscopic studies are needed to fully understand the stability in ethanol and methanol.

In summary, this chapter gave a strong understanding of the MOF solvothermal stability with a main focus on the UiO-66 structure. A metal-linker coordination might be the key to the MOF hydrolytic stability in elevated temperatures, since the strength of this bond might be the weakest point of its structure. This was specifically observed in the UiO-66 structure when Hf replaced Zr in the cluster. However, unlike zeolites, both of the UiO-66(Zr) structures (-H and -NH₂) have presented excellent hydrothermal stability at 110°C for at least 120 h of liquid phase operation in CFR. Due to their active acid sites these structures could be potentially used in water phase catalysis.

5.6 References

- 1 S. R. Batten, N. R. Champness, X-M. Chen, J. Garcia-Martinez, S. Kitagawa, L. Öhrström, M. O’Keeffe, M. P. Suh, J. Reedijk, *CrystEngComm*, 2012, **14**, 3001-3004
- 2 N. Rangnekar, N. Mittal, B. Elyassi, J. Caro, M. Tsapatsis, *Chem. Soc. Rev.* 2015, **44**, 7128-7154
- 3 Ü. Kökçam-Demir, A. Goldman, L. Esrafilı, M. Gharib, A. Morsali, O. Weingart, C. Janiak, *Chem. Soc. Rev.*, 2020, **49**, 2751-2798
- 4 H. C. Zhou, J. R. Long, O. M. Yaghi, *Chem. Rev.*, 2012, **112**, 673–674
- 5 A. Kirchon, L. Feng, H. F. Drake, E. A. Josepha, H. C. Zhou, *Chem. Soc. Rev.*, 2018, **47**, 8611-8638
- 6 V. Rao Bakuru, S. R. Churipard, S P. Maradur, S. Babu Kalidindi, *Dalton Trans.*, 2019, **48**, 843-847
- 7 M. De Toni, R. Jonchiere, P. Pullumbi, F-X. Coudert, A. H. Fuchs, *ChemPhysChem* 2012, **13**, 3497-503
- 8 R. Batra, C. Chen, T. G. Evans, K. S. Walton, R. Ramprasad, *Nat Mach Intell.* 2020, **2**, 704–710
- 9 M. Ding, X. Cai, H-L. Jiang, *Chem. Sci.*, 2019, **10**, 10209-10230
- 10 C. Wang, X. Liu, N. K. Demir, J. P. Chen, K. Li, *Chem. Soc. Rev.* 2016, **45**, 5107-5134
- 11 D. Buzek, J. Demel, K. Lang, *Inorg. Chem.* 2018, **57**, 14290–14297
- 12 Y. Li, R. T. Yang, *AIChE J.*, 2008, **54**, 269-279
- 13 F. Gul-E-Noor, B. Jee, A. Poppl, M. Hartmann, D. Himsl, M. Bertmer, *Phys. Chem. Chem. Phys.* 2011, **13**, 7783-7788
- 14 E. Soubeyrand-Lenoir, C. Vagner, J. W. Yoon, P. Bazin, F. Ragon, Y. K. Hwang, C. Serre, J.-S. Chang, P. L. J. Llewellyn, *Am. Chem. Soc.*, 2012, **134**, 10174- 10181
- 15 Y. Chen, X. Bai, Z. Ye, *Nanomaterials* 2020, **10**, 1481
- 16 C. Wang, X. Liu, J. P. Chen, K. Li, *Sci. Rep.*, 2015, **5**, 16613
- 17 J. Li, Y.-N. Wu, Z. Li, B. Zhang, M. Zhu, X. Hu, Y. Zhang, F. Li, *J. Phys. Chem. C*, 2014, **118**, 27382-27387
- 18 Y. Hu, X. Dong, J. Nan, W. Jin, X. Ren, N. Xu, Y. M. Lee, *Chem. Commun.*, 2011, **47**, 737-739
- 19 X. Qian, B. Yadian, R. Wu, Y. Long, K. Zhou, B. Zhu, Y. Huang, *Int. J. Hydrog. Energy*, 2013, **38**, 16710-16715
- 20 B-M. Jun, Y. A. J. Al-Hamadani, A. Son, C. Min Park, M. Jang, A. Jang, N. Chan Kim, Y. Yoon, *Separation and Purification Technology*, 2020, **247**, 116947
Volume 247, 15 September 2020, 116947
- 21 M. Mon, R. Bruno, J. Ferrando-Soria, D. Armentano, E. Pardo, *J. Mater. Chem. A*, 2018, **6**, 4912-4947
- 22 N. C. Burtch, H. Jasuja, K. S. Walton, *Chem. Rev.*, 2014, **114**, 10575–10612
- 23 B. Liu, K. Vikrant, K. Kim, V. Kumar and S. K. Kailasa, *Environ. Sci.: Nano*, 2020, **7**, 1319-1347
- 24 E. Tsalaporta, J.M. Don MacElroy, *Heliyon*. 2020, **6**, e04883
- 25 N. Al-Janabi, P. Hill, L. Torrente-Murciano, A. Garforth, P. Gorgojo, F. Siperstein, X. Fan, *Chem. Eng. J.*, 2015, **281**, 669–677
- 26 K. Yao, Y. Xia, J. Li, N. Wang, J. Han, C. Gao, M. Han, G. Shen, Y. Liu, A. Seifitokaldani, X. Sun, H. Liang, *J. Mater. Chem. A*, 2020, **8**, 11117-11123

- 27 L. Qun-xing, A. Bo-wen, J. Min, P. Sang-Eon, H. Ce, L. Yan-qin, *J Porous Mater* 2015, **22**, 247-259
- 28 J. Hafizovic Cavka, S. Jakobsen, U. Olsbye, N. Guillou, C. Lamberti, S. Bordiga, K. P. Lillerud, *J. Am. Chem. Soc.* 2008, **130**, 13850-13851
- 29 Q. Yang, H. Y. Zhang, L. Wang, Y. Zhang, J. Zhao, *ACS Omega*, 2018, **3**, 4199-4212
- 30 J. Winarta, B. Shan, S. M. McIntyre, L. Ye, C. Wang, J. Liu, B. Mu, *Cryst. Growth Des.* 2020, **20**, 1347-1362
- 31 S. J. Garibay, S. M. Cohen, *Chem. Commun.*, 2010, **46**, 7700-7702
- 32 M. Sánchez-Sánchez, N. Getachew, K. Díaz, M. Díaz-García, Y. Chebude, I. Díaz, *Green Chem.*, 2015, **17**, 1500-1509
- 33 T. Tian, J. Velazquez-Garcia, T. D. Bennett, D. Fairen-Jimenez, *J. Mater. Chem. A*, 2015, **3**, 2999-3005
- 34 E. E. Sann, Y. Pan, Z. Gao, S. Zhan, F. Xia, *Separation and Purification Technology*, 2018, **206**, 186-191
- 35 H. V. Doan, A. Sartbaeva, J.-C. Eloi, S. A. Davis, V.P. Ting, *Sci Rep* 2019, **9**, 10887
- 36 J. Raziél Álvarez, E. Sánchez-González, E. Pérez, E. Schneider-Revueltas, A. Martínez, A. Tejeda-Cruz, A. Islas-Jácome, E. González-Zamora, I. A. Ibarra, *Dalton Trans.* 2017, **46**, 9192-9200
- 37 G. Majano, O. Martin, M. Hammes, S. Smeets, C. Baerlocher, J. Pérez-Ramírez, *Adv. Funct. Mater.* 2014, **24**, 3855-3865
- 38 G. Majano, J. Pérez-Ramírez, *Adv. Mater.*, 2013, **25**, 1052-1057
- 39 W. Li, X. Wu, H. Liu, J. Chen, W. Tang, Y. Chen, *New J. Chem.* 2015, **39**, 7060-7065
- 40 D. Prochowicz, K. Sokołowski, I. Justyniak, A. Kornowicz, D. Fairen-Jimenez, T. Frišćić, J. Lewiński, *Chem. Commun.* 2015, **51**, 4032-4035
- 41 I. Bezverkhyy, G. Ortiz, G. Chaplais, C. Marichal, G. Weber, J-P. Bellat, *Micropor. Mesopor. Mat.* 2014, **183**, 156-161
- 42 Y.-R. Lee, M.-S. Jang, H.-Y. Cho, H.-J. Kwon, S. Kim, W.-S. Ahn, *Chemical Engineering Journal*, 2015, **271**, 276-280
- 43 L. Sheng, F. Yang, C. Wang, J. Yu, L. Zhang, Y. Pan, *Materials Letters*, 2017, **197**, 184-187
- 44 H. Tian, S. Wang, C. Zhang, J. Veder, J. Pan, M. Jaroniec, L. Wang, J. Liu, *J. Mater. Chem. A*, 2017, **5**, 11615-11622
- 45 J. H. Cavka, S. Jakobsen, U. Olsbye, N. Guillou, C. Lamberti, S. Bordiga, K. P. Lillerud, *J. Am. Chem. Soc.*, 2008, **130**, 13850-13851
- 46 M. Lammert, M. T. Wharmby, S. Smolders, B. Bueken, A. Lieb, K. A. Lomachenko, D. De Vosc, N. Stock, *Chem. Commun.*, 2015, **51**, 12578-12581
- 47 N. Lu, F. Zhou, H. Jia, H. Wang, B. Fan, R. Li, *Ind. Eng. Chem. Res.* 2017, **56**, 14155-14163
- 48 Y. Cao, H. Zhang, F. Song, T. Huang, J. Ji, Q. Zhong, W. Chu, Q. Xu, *Materials*, 2018, **11**, 589-603
- 49 G. Yang, L. Zhou, *Scientific Reports*, 2017, **7**, 16113
- 50 A. Corma, F. X. Llabrés I Xamena, C. Prestipino, M. Renz and S. Valencia, *J. Phys. Chem. C*, 2009, **113**, 11306-11315
- 51 K. Wang, Y. Liu, W. Wu, Y. Chen, L. Fang, W. Li, H. Ji, *Catal. Lett.*, 2020, **150**, 322-331
- 52 M. H. Beyzavi, C. J. Stephenson, L. Yangyang, O. Karagiari, J. T. Hupp, O. K. Farha, *Front. Energy Res.*, 2015, **2**, 63

- 53** M. Stawowy, M. Roziewicz, E. Szczepanska, J. Silvestre-Albero, M. Zawadzki, M. Musiol, R. Luzny, J. Kaczmarczyk, J. Trawczynski, A. Lamacz, *Catalysts* 2019, **9**, 309
- 54** J. Marreiros, C. Caratelli, J. Hajek, A. Krajnc, G. Fleury, B. Bueken, D. E. De Vos, G. Mali, M. B. J. Roeffaers, V. Van Speybroeck, R. Ameloot, *Chem. Mater.*, 2019, **31**, 1359-1369
- 55** S. M. Chavan, G. C. Shearer, S. Svelle, U. Olsbye, F. Bonino, J. Ethiraj, K. Petter Lillerud, S. Bordiga, *Inorg. Chem.* 2014, **53**, 9509–9515
- 56** M. Thommes, K. Kaneko, A. V. Neimark, J. P. Olivier, F. Rodriguez-Reinoso, J. Rouquerol, K. S. Sing, *Pure Appl. Chem.*, 2015, **87**, 1051-1069
- 57** K. Hendrickx, J. J. Joos, A. De Vos, D. Poelman, P. F. Smet, V. Van Speybroeck, P. Van Der Voort, K. Lejaeghere, *Inorg. Chem.*, 2018, **57**, 5463–5474
- 58** D. Sun, W. Liu, M. Qiu, Y. Zhang, Z. Li, *Chem. Commun.*, 2015, **51**, 2056–2059
- 59** K. G. M. Laurier, E. Fron, P. Atienzar, K. Kennes, H. Garcia, M. Van der Auweraer, D. E. De Vos, J. Hofkens, M. B. J. Roeffaers, *Phys. Chem. Chem. Phys.*, 2014, **16**, 5044-5047
- 60** A. M. Ploskonka, J. B. DeCoste, *ACS Appl. Mater. Interfaces*, 2017, **9**, 21579–21585
- 61** S. Devautour-Vinot, G. Maurin, C. Serre, P. Horcajada, D. Paula da Cunha, V. Guillerme, E. de Souza Costa, F. Taulelle, C. Martineau *Chem. Mater.*, 2012, **24**, 2168–2177
- 62** Y. Luan, Y. Qi, Z. Jin, X. Peng, H. Gao, G. Wang, *RSC Adv.*, 2015, **5**, 19273–19278
- 63** W. Xu, M. Dong, L. Di, Z. Zhang, *Nanomaterials*, 2019, **9**, 1432
- 64** G. W. Peterson, M. McEntee, C. R. Harris, A. D. Klevitch, A. W. Fountain, J. R. Soliz, A. Balboa, A. J. Hauser, *Dalton Trans.*, 2016, **45**, 17113-17116
- 65** M. J. Katz, Z. J. Brown, Y. J. Colón, P. W. Siu, K. A. Scheidt, R. Q. Snurr, J. T. Hupp, O. K. Farha, *Chem. Commun.*, 2013, **49**, 9449-9451
- 66** S. A. Eliziário, L. S. Cavalcante, J. C. Sczancoski, P. S Pizani, J. A. Varela, J. W. M. Espinosa, E. Longo, *Nanoscale Res Lett*, 2009, **4**, 1371–1379
- 67** T. Xu, D. Ma, C. Li, Q. Liu, S. Lu, A. M. Asiri, C. Yang, X. Sun, *Chem. Commun.*, 2020, **56**, 3673-3676
- 68** L. Feng, S. Yuan, L-L. Zhang, K. Tan, J-L. Li, A. Kirchon, L-M. Liu, P. Zhang, Y. Han, Y. J. Chabal, H.-C. Zhou, *J. Am. Chem. Soc.*, 2018, **140**, 2363–2372

6 Conclusions and prospective challenges

6.1 Conclusions

Stability of porous materials in liquid phase processes such as solvent-based catalysis and water purification systems has become of high importance in recent years. Since zeolites are already widely used in the petrochemical industry for decades, there is a surge in interest to apply them in liquid phase operations. Also Metal Organic Framework (MOF) structures are attracting a great deal of the scientific interest due to their high crystallinity, unique porosity and novel functionality. However, despite their academic attention, MOFs have not yet become widely commercialised. In 2017, for the first time ever, NuMat Technologies has started using MOFs to capture toxic gases produced in the electronics sector.¹

After detailed research among the existing literature found in Chapter 1, the delay in commercialisation has been associated with the lack of knowledge and analytical evaluation of the solvothermal stability of these materials. Even though zeolites and MOFs were subject to water stability tests, these kinds of experiments were done only in steam or under static conditions. Not enough emphasis has been placed on the stability evaluation in continuous flow regime systems, where elevated temperature and pressure play a great role. Therefore, in this thesis, the solvothermal stability of chosen zeolite and metal organic materials under these conditions has been studied.

It has been confirmed that zeolites and MOF materials possess extraordinary properties and could possibly be used in various industrial applications such as continuous flow catalysis. The synthesis of these materials is relatively straightforward and reproducible. In the case of aluminosilicate zeolites, the synthesis is done under hydrothermal conditions from reactive alkaline gels at temperatures up to 200°C. The same conditions can be applied for MOFs synthesis, however, most of these structures (*i.e.*, ZIF-8) do not require special hydrothermal treatment, as they can be even simply synthesised in a round bottom flask under stirring even at room temperature. Also, these materials show superior possibilities of potential scale-up and mass production which makes them even more interesting from an industrial point of view.

Initial studies (Chapter 3) on the water impact on the zeolite framework have focused on high content Al zeolites of various framework types, *i.e.*, MFI, BEA, MOR, FAU, FER ($\text{SiO}_2/\text{Al}_2\text{O}_3$ molar ratios of 20-30). The evaluation of the tests started from measuring the relative crystallinity and microporosity values of these structures since these were first descriptors of the stability of the materials. It has been observed that a certain reduction of initial crystallinity occurred in all tested samples. However, zeolite structures possessing higher framework densities (FD_{Si}) such as MOR, FER and MFI withstand the water damage much better than the lower FD_{Si} structures (FAU and BEA types). Also, it was observed that the increase in total pore volume has followed the trend of $\text{MFI} < \text{MOR} < \text{FER} < \text{FAU} < \text{BEA}$.

An in-depth screening of the FAU type framework has provided interesting results on the time and temperature stability of the HY zeolite. By testing zeolites of different Al content ($\text{SiO}_2/\text{Al}_2\text{O}_3 = 5.1, 30$ and 80) it has become clear that the high content Al HY zeolite structure maintains its microporosity and crystallinity much better than its lower Al content analogues. A linear relationship was observed between the Al content, and the decrease of these parameters. However, when the lowest Al content HY sample was treated at a lower temperature its crystallinity was less affected, meaning that the higher the temperature the more significant the structural damage. The ^{29}Si and ^{27}Al MAS NMR spectra of the sample has revealed that EFAl species were still present after 6 h of treatment, while the degradation propagated by mainly Si leaching. However, after 24 h no EFAl was detected and the concentration of silanol surface defects was significant.

The study was further expanded in order to investigate changes in structure damage, within same frameworks, but varying $\text{SiO}_2/\text{Al}_2\text{O}_3$ molar ratios (between 5.1-280). This part led to a conclusion that the zeolites (HZSM-5) belonging to the MFI structure type were most stable among all tested structures. However, these materials still exhibited some similar, but not extreme, damage over the whole $\text{SiO}_2/\text{Al}_2\text{O}_3$ range of 23-280. Micropore analysis led to the understanding that under the influence of water, internal mesopores are formed and the zeolite loses its initial crystallinity. A partial exchange of an H-ZSM-5 zeolite sample with a Na^+ counter ion led to drastic change in hydrophilicity of the material. The initial vapour sorption ability dropped by 50% and the damage caused to the sample was not as severe as in the case of the protonated sample.

To relate this observed stability behaviour within different structural zeolites, a BEA type zeolite sample was ion exchanged with Na^+ , K^+ and Ca^{2+} counter ions. The study resulted in

an increased relative microporosity in the order of $K^+ > Na^+ > H^+ > Ca^{2+}$ after CFR testing and it was observed that K^+ and Na^+ exchanged samples retained more crystallinity after treatment. This allowed the conclusion that the alkali ion exchange on zeolites limits the degradation of the internal framework.

For the final study of this chapter a zeolite A (LTA type) of SiO_2/Al_2O_3 molar ratio 2 was chosen. The zeolite A is the only one among zeolites that found application in industrial desalination and organic dehydration systems. However, after testing the sample and comparing data generated from ^{29}Si and ^{27}Al MAS NMR and MP-AES it has become clear that leaching of Si and Al is observed and overall total porosity and crystallinity are severely affected. At the end of this chapter a wide range of FD_{Si} zeolite structures was compared and presented a general correlation of higher relative crystallinity for denser zeolite frameworks. Furthermore, it was observed that for each structure, frameworks of higher Al content were less prone to damage, meaning that Al plays an important role in the zeolite stability when in contact with water.

Understanding the role of Al in the zeolite framework stability has led to subsequent, more in depth study. Since testing of only commercial samples with an unknown synthesis route has its limitations, it was decided to prepare a one-pot synthesised set of MFI type zeolites - HZSM-5 (SiO_2/Al_2O_3 molar ratio range of 30-300) and pure silica Silicalite-1. Therefore, Chapter 4 focused on the comparison of these zeolites with the commercial materials, studied in continuous flow and under static conditions at varying temperatures. The studies were done to better understand the role of aluminium in the MFI structure. Tests were carried out for extended times of 120 h at $110^\circ C$ in CFR. The characterisation of the materials was carried out employing several spectroscopic methods. These demonstrated that the medium Al content MFI sample is subject to crystallinity and microporosity loss and general desilication. After testing the sample for 51 h no presence of Al was detected by MP-AES in the effluent water. This was a promising observation, confirming conclusions from Chapter 3 about the stabilising role of Al in the framework. However, evidence of internal degradation by desilication were found by microporosity analysis and MP-AES. Surprisingly, the ^{29}Si MAS NMR spectra of 120 h treated sample were no different than the untreated ones.

Even more interesting observations were made after investigating the high Al content HZSM-5 samples. It was found that the high Al content in the framework plays an even a

more important role. The material was subject to testing at 110°C in two different setups – CFR and under static conditions (*i.e.*, Batch, boiled in a round bottom flask under reflux). These tests have provided valuable data showing that the desilication of the sample was similar, however different pore volumes after testing were observed. In the case of the CFR tested sample, total pore volume increased while microporosity decreased. An opposite observation was made for the Batch sample. It was concluded that under static conditions the generation of extra micropore volume might have been due to longer water contact and water penetration of the structure. ATR analysis confirmed the lack of characteristic bands assigned to pore opening vibrations. Another difference was observed when ^{29}Si and ^{27}Al MAS NMR spectra were compared. The Batch sample Q^4 peak, assigned to the tetrahedral Si was a bit broader, while the EFAl resonance peak was no longer observed. The CFR spectra remained unchanged in comparison to the untreated sample. Furthermore, the combination of ATR, MAS NMR and MP-AES methods confirmed that at room temperature the water does not affect the microstructure in CFR. The level of desilication was insignificant with just over 1 wt. % of total Si extracted and no extracted Al.

Encouraged by the interesting results of the effect of static conditions of the high FD_{Si} frameworks, similar structures, *i.e.*, Mordenite and Ferrierite zeolites were subject to similar tests. The CFR and Batch tests were carried out under similar conditions in water at 110°C. When testing the MFI, MOR and FER type structured samples in CFR, one main observation was done - no Al was present in the effluent water after 120 h of testing. However, after testing the same materials under static conditions (*i.e.*, Batch) the same phenomenon was not observed. In the case of FER and MOR samples, both desilication and dealumination were observed to happen simultaneously at similar leaching level. The MP-AES analysis have confirmed that Si and Al were present in the effluent water, however Si was detected in much lower concentrations that in the case of the CFR tested samples. The lower amount of leached Si might be associated with the solubility equilibrium since stable volume of water was used. Nevertheless, this led to a final conclusion, that the testing condition setup has a huge influence on the zeolite stability in water at elevated temperatures. While much larger volumes of water pass the sample, the water-zeolite interaction is shorter in the pressurised CFR system, dealumination does not occur. When the zeolite structure is in constant contact with water under static conditions, at standard atmospheric pressure, both phenomena, *i.e.*, desilication and dealumination were observed.

Since MOF structures characteristics make them prospect candidates for a wide number of applications including liquid phase catalysis, Chapter 5 focused on an extensive stability evaluation. It was found in existing literature that several commercially available structures are confirmed to be stable in steam and water. Selected MOF structures – HKUST-1, ZIF-8, MIL 53 and UiO-66 were therefore selected for tests in water, ethanol and methanol for comparison of the outcomes. Since these materials are already well established over the last 25 years, it is surprising that continuous flow regime (CFR) studies were not yet subjected to wider consideration.

Herein, out of 4 tested structures, only UiO-66 has shown outstanding stability, with nearly no change in initial diffraction patterns, specific surface area and total porosity after 48 h in CFR. Yet, it was decided to prepare the UiO-66 structure in form of 3 analogues with different metal clusters (Zr and Hf) and linkers (H₂BDC and NH₂BDC). These materials were subject to further tests in water, ethanol and methanol for extended periods of time and varying temperature. While the UiO-66(Zr)-H and UiO-66(Zr)-NH₂ samples were stable in water and ethanol, it was surprisingly observed that methanol exchanges the original linker or might be chemically grafted to the Zr-oxo clusters. This observation was also confirmed when UiO-66(Hf)-H sample was tested. Testing both Hf and Zr analogues at a temperature of 160°C has led to an observation, that that both structures slowly transform into corresponding metal oxides upon contact with water. The in detailed study of the Zr UiO-66 has confirmed that the structure was stable up to 72 h at 160°C in water. A metal-linker coordination was found to be the key to the structure stability.

6.2 Challenges and final remarks

This thesis has provided a good insight into the solvothermal stability of chosen zeolites and MOF structures. However, despite the fact that many challenges have been addressed, many new queries came to attention. As presented in Chapter 3, ion-exchanging the zeolite counter ion had a huge impact on its hydrophilicity and overall structure stability. One of the questions raised is the stability of zeolites doped with other metals. Hence, these types of structures are highly desired in catalysis, due to obtaining different acidity and catalytic activity of the zeolite. Since high FD_{S_i} structures were confirmed to be much stable, the question is how the density of the structure and Al content would impact or tune the metal loading and its activity.² Such materials could be further explored in order to probe their

hydrothermal stability. In particular, techniques such as DRIFTS, Raman and TEM could be employed in order to follow and understand the process of incorporation of the metal in the framework. Since the calcination step is also crucial it would be important to develop optimisation of the overall synthesis steps.

In Chapter 4 the stability of zeolite materials synthesised via the alkaline route was evaluated. It has been shown that the bottom-up approach can lead to a controlled and successful synthesis of a wide range of zeolites of the same topology. However, these materials are defined by a high concentration of surface defects, *i.e.*, external and/or internal silanol groups. As the existing literature suggests mineralising agents may be used instead of alkaline organic OSDAs in zeolite synthesis. This change in approach may lead to more defect free structures and a lower concentration of silanol nests on the zeolite surface. However, the aluminium incorporation into the zeolite framework is limited under acidic pH conditions due to the high isoelectric point (IEP) of alumina with respect to silica.³ The introduction of new heteroatoms to the structure will depend on their IEP, *i.e.*, the surface charge of their species in acidic medium. Therefore, the high content Al zeolites are not able to be produced this way. In addition, no zeolite formation is possible below IEP of silica.

However, it is widely known that other aluminium free Lewis acid (*i.e.*, Sn, Zr, Hf, Ti) zeolites can be synthesised by using fluoride ions as mineralising agent.^{4,5} Hence, the main challenge here is the removal of defect sites which are destabilising zeolites under aqueous conditions. One of the methods might be silylation treatment which is the attachment of mono-, di-, and trichlorosilanes with different alkyl chain lengths on the surface silanol groups in order to enhance the hydrothermal stability of high Al zeolite structures.⁶

Chapter 5 gave a great set of new information and data on the stability of UiO-66 another MOF structures in direct contact with water. However, the synthesis of many MOFs is still done with the use of many harsh solvents such as DMF or methanol. Due to the need of fulfilling the green chemistry principles, the large-scale production for industrial purposes is required to focus on the use of safer and greener solvents.⁷ Therefore, future work associated with the synthesis field should provide a simpler and greener approach. Furthermore, the exploration of prospective MOF structures stable in water, should start from obtaining fundamental data and understanding on the strength and stability of the metal-linker coordination.

Yet the challenges and opportunities in prospect MOF applications continue to expand, with the growing fascination around these materials. There is an extremely impressive interest for the development of MOF based materials for liquid phase operations. It is even believed that MOF catalysts would perform even better than their inorganic alternatives, *i.e.*, zeolites.⁸ Therefore, the future is bright for MOF chemistry in the next years.

6.3 References

- 1 *Nature Chem* 2016, **8**, 987
- 2 M. Ravi, V. L. Sushkevich, J. A. van Bokhoven, *Nat. Mater*, 2020, **19**, 1047-1056
- 3 D. Shi, K-G. Haw, C. Kouvatas, L. Tang, Y. Zhang, Q. Fang, S. Qiu, V. Valtchev, *Angew. Chem. Int. Ed.*, 2020, **59**, 19576-19581
- 4 T. Blasco, M. A. Camblor, A. Corma, P. Esteve, J. M. Guil, A. Martinez, S. Valencia, A. Martinez, J. A. Perdigon-Melon, *J. Phys. Chem. B*, 1998, **102**, 75-88
- 5 P. Y. Dapsens, C. Mondelli, J. Perez-Ramirez, *Chem. Soc. Rev.*, 2015, **44**, 7025-7043
- 6 H-T. Vu, F. M. Harth, N. Wilde, *Front Chem.*, 2018, **6**, 143
- 7 D. M. Venturi, F. Campana, F. Marmottini, F. Costantino, L. Vaccaro, *ACS Sustain. Chem. Eng.*, 2020, **8**, 17154-17164
- 8 C. H. Hendon, A. J. Rieth, M. D. Korzynski, M. Dinca, *ACS Cent. Sci.*, 2017, **3**, 554-563